②

NAVAL POSTGRADUATE SCHOOL

Monterey, California

THESIS

A STUDY OF FILM COOLING DOWNSTREAM OF ONE AND TWO ROWS OF HOLES ORIENTED IN SPANWISE/NORMAL PLANES

by

Anthony Eldorado Ramsey

SEPTEMBER 1992

Thesis Advisor: Phillip M. Ligrani

Approved for public release; distribution is unlimited

Unclassified
SECURITY CLASSIFICATION OF THIS PAGE

REPORT DOCUMENTATION PAGE

1a. REPORT SECURITY CLASSIFICATION Unclassified	1b. RESTRICTIVE MARKINGS
2a. SECURITY CLASSIFICATION AUTHORITY	3. DISTRIBUTION/AVAILABILITY OF REPORT Approved for public release; distribution is unlimited.
2b. DECLASSIFICATION/DOWNGRADING SCHEDULE	
4. PERFORMING ORGANIZATION REPORT NUMBER(S)	5. MONITORING ORGANIZATION REPORT NUMBER(S)

6a. NAME OF PERFORMING ORGANIZATION Naval Postgraduate School	6b. OFFICE SYMBOL *(If applicable)* 55	7a. NAME OF MONITORING ORGANIZATION Naval Postgraduate School
6c. ADDRESS *(City, State, and ZIP Code)* Monterey, CA 93943-5000		7b. ADDRESS *(City, State, and ZIP Code)* Monterey, CA 93943-5000
8a. NAME OF FUNDING/SPONSORING ORGANIZATION	8b. OFFICE SYMBOL *(If applicable)*	9. PROCUREMENT INSTRUMENT IDENTIFICATION NUMBER

8c. ADDRESS *(City, State, and ZIP Code)*

10. SOURCE OF FUNDING NUMBERS

Program Element No.	Project No.	Task No.	Work Unit Accession Number

11. TITLE *(Include Security Classification)*
A STUDY OF FILM COOLING DOWNSTREAM OF ONE AND TWO ROWS OF HOLES ORIENTED IN SPANWISE/NORMAL PLANES

12. PERSONAL AUTHOR(S) RAMSEY, ANTHONY ELDORADO

13a. TYPE OF REPORT Master's Thesis	13b. TIME COVERED From To	14. DATE OF REPORT *(year, month, day)* SEPTEMBER 1992	15. PAGE COUNT 269

16. SUPPLEMENTARY NOTATION
The views expressed in this thesis are those of the author and do not reflect the official policy or position of the Department of Defense or the U.S. Government.

17. COSATI CODES

FIELD	GROUP	SUBGROUP

18. SUBJECT TERMS *(continue on reverse if necessary and identify by block number)*
compound angle injection , film cooling, turbulent boundary layer

19. ABSTRACT *(continue on reverse if necessary and identify by block number)*

Experimental results are presented which describe the development and structure of flow downstream of a single and two staggered rows of film-cooling holes with compound angle orientations. With the configuration studied, holes are inclined at 90 degrees with respect to the test surface when projected in the streamwise/normal planes, and 30 degrees with respect to the test surface when projected in the spanwise/normal plane. Within each row, holes are spaced 6.0 hole diameter apart in the spanwise direction which gives 3.0d spacing between adjacent holes for the staggered row arrangement. Spanwise average values of the adiabatic film-cooling effectiveness are depend mostly on four parameters: hole angle orientation, spanwise hole spacing, number of rows of film-cooling holes(one or two), and blowing ratio. Spanwise averaged values of the adiabatic film-cooling effectiveness are generally greatest at low x/d and decrease with increasing x/d values for any given blowing ratio. Spanwise averaged effectiveness values decrease with blowing ratio for x/d less than 40 except for data for m = 2.5. This trend generally reverses itself at higher x/d values. Spanwise averaged iso-energetic Stanton number ratios range between 1.0 and 1.5 and show little variation as x/d increases for each value of blowing ratio, howerver for each x/d, values increase with increasing blowing ratio.

20. DISTRIBUTION/AVAILABILITY OF ABSTRACT ☒ UNCLASSIFIED/UNLIMITED ☐ SAME AS REPORT ☐ DTIC USERS	21. ABSTRACT SECURITY CLASSIFICATION unclassified	
22a. NAME OF RESPONSIBLE INDIVIDUAL Phillip M. Ligrani	22b. TELEPHONE *(Include Area code)* 408-646-3382	22c. OFFICE SYMBOL ME/Li

DD FORM 1473, 84 MAR

83 APR edition may be used until exhausted
All other editions are obsolete

SECURITY CLASSIFICATION OF THIS PAGE
Unclassified

Approved for public release; distribution is unlimited.

A Study of Film Cooling Downstream of One and Two Rows of Holes Oriented in Spanwise/Normal Planes

by

Anthony Eldorado Ramsey
Lieutenant, United States Navy
B.S., Mississippi Valley State University, 1985

Submitted in partial fulfillment of the requirements
for the degree of

MASTER OF SCIENCE IN MECHANICAL ENGINEERING

from the

NAVAL POSTGRADUATE SCHOOL
September 1992

Author: Anthony Eldorado Ramsey
Anthony Eldorado Ramsey

Approved by: Phillip M Ligrani
Phillip M. Ligrani, Thesis Advisor

Matthew Kelleher
Matthew D. Kelleher, Chairman, Department of Mechanical Engineering

ABSTRACT

Experimental results are presented which describe the development and structure of flow downstream of a single row and two staggered rows of film-cooling holes with compound angle orientations. With the configuration studied, holes are inclined at 90 degrees with respect to the test surface when projected into the streamwise/normal plane, and 30 degrees with respect to the test surface when projected into the spanwise/normal plane. Within each row, holes are spaced 6.0 hole diameter apart in the spanwise direction which gives 3.0d spacing between adjacent holes for the staggered row arrangement. Also presented are plots showing the streamwise development of injectant distributions and streamwise development of mean velocity distributions. Spanwise averaged values of the adiabatic film-cooling effectiveness depend mostly on four parameters: hole angle orientation, spanwise hole spacing, number of rows of film-cooling holes (one or two), and blowing ratio. Spanwise averaged values of the adiabatic film-cooling effectiveness are generally greatest at low x/d and decrease with increasing x/d values for any given blowing ratio. Spanwise averaged effectiveness values decrease with blowing ratio for x/d less than 40 except for data for m=2.5. This trend generally reverses itself at higher x/d values. Spanwise averaged iso-energetic Stanton number ratios range between 1.0 and 1.5 and show little variation as x/d increases for each value of blowing ratio, however for each x/d, values increase with increasing blowing ratio.

TABLE OF CONTENTS

LIST OF FIGURES

LIST OF SYMBOLS

A	- heat transfer surface area
C_d	- coefficient of discharge
C_p	- specific heat
d	- injection hole diameter (0.925 cm)
F_{ij}	- radiation view factor
h	- heat transfer coefficient with film injection
h_o	- baseline heat transfer coefficient, no film injection
h_f	- iso-energetic heat transfer coefficient with film injection
I	- momentum flux ratio, $\rho_c U_c^2 / \rho_\infty U_\infty{}^2$
K	- thermal conductivity, W/m^oK
m	- blowing ratio, $\rho_c U_c / \rho_\infty U_\infty$
q	- heat flux
Re	- Reynolds number
s	- equivalent slot width
St	- Stanton number with film injection
St_o	- baseline Stanton number, no film injection
St_f	- iso-energetic Stanton number with film injection
$\overline{St_f}$	- spanwise-averaged iso-energetic Stanton number with film injection
T	- static temperature
T_{amb}	- ambient temperature
T_{plate}	- average plate temperature
T_c	- coolant temperature

T_{inj} - injectant temperature

T_{plenum} - plenum temperature

T_w - wall temperature

T_∞ - freestream temperature

T_{aw} - adiabatic wall temperature

U - streamwise mean (time-averaged) velocity

X - streamwise distance measured from the leading edge of the boundary layer trip

x - streamwise distance measured from the downstream edges of the injection holes

x/d - dimensionless streamwise distance

Y - distance normal to the test surface

Z - spanwise distance measured from the test surface centerline

α - thermal diffusivity, $K/\rho C_p$

β_1 - complete beta function

β_{u1} - incomplete beta function

ε - radiation emissivity

σ - Stefan-Bolzman constant

ξ - unheated starting length

η - adiabatic film cooling effectiveness, $(T_{aw} - T_\infty)/(T_c - T_\infty)$

$\bar{\eta}$ - spanwise-averaged adiabatic film cooling effectiveness

ρ - density

θ - non-dimensional injection temperature, $(T_c - T_\infty)/(T_w - T_\infty)$

Ω - injection hole angles with respect to the test surface as projected into the streamwise/normal plane

β - injection hole angle with respect to the test surface as projected into the spanwise/normal plane.

Subscripts

aw - adiabatic wall

c - injectant at exits of injection holes

o - stagnation

w - wall

∞ - freestream

cond - conduction heat transfer

conv - convection heat transfer

rad - radiation heat transfer

Superscripts

$\overline{\quad}$

time-average

ACKNOWLEDGMENTS

This research was sponsored by Naval Sea Systems Command, Code 56X3, Washington, D.C., and by the Wright Aeronautical Laboratories, Wright Patterson Air Force Base, Ohio. The Navsea program monitor was Dr. Dan Groghan and Dr. Sam Shepard. The Wright Patterson Air Force Base program monitor was Dr. Bill Troka.

I wish to express my deep appreciation to Professor Phillip Ligrani who was a very influential and important driving force behind this study. His patience, guidance and enthusiasm for this study was a source of inspiration to me.

In addition, I wish to thank the entire staff of the NPS Department of Mechanical Engineering, especially Thomas H. McCord, Thomas Christian, James T. Schofield, and Mardo Blanco who were always willing to assist in the manufacture and repair of equipment. Last, but not least, I am deeply appreciative of my wife, Arbeneater, whose support and understanding was an asset throughout this research.

I. INTRODUCTION

A. BACKGROUND/THEORY

The efficiency of gas turbine engines has improved to the point that inlet temperatures are reaching 2000 K. These high temperatures along with high rotational speeds place large amounts of stress on component materials, especially on the first stage turbine blades. For reduced stress levels and improved reliability of these blades, efficient means of cooling these components are needed. One cooling scheme which is used extensively to provide thermal protection of gas turbine component surfaces in commercial and military applications is film cooling. In the past, the film cooling arrangement most often employed on turbine blades, turbine endwalls, combustion chamber linings, and afterburner linings used injection holes with simple angle orientations. Simple angle holes are ones which inject cooling air at an angle inclined with respect to the test surface when viewed in the streamwise/normal plane, and in the streamwise direction when viewed in the streamwise/spanwise plane.

More recently, gas turbine components employ film cooling holes with compound angle orientations. Compound angle oriented film holes produce injectant which provides better protection and higher film cooling effectivenesses than injectant from film cooling holes with simple angle orientations. Compound angle holes are oriented with respect to the test surface such that the injectant is ejected with a spanwise velocity component relative to the mainstream flow. The present study focuses on the behavior of boundary layers with compound angle film cooling because of its wide use in cooling gas turbine components, and because very little compound angle film cooling data are available in the archival literature.

In the present study, adiabatic film cooling effectiveness, Stanton number, iso-energetic Stanton number, mean velocity, mean total pressure, and injectant distribution data are presented and analyzed from measurements downstream of a compound angle configuration not previously investigated at the Naval Postgraduate School. Adiabatic film cooling effectiveness values are determined using linear superposition theory applied to Stanton number ratios measured at different injection temperatures. This is possible since the three-dimensional energy equation which describes the flow field is linear and homogeneous in its dependent variable, temperature, for constant property flow. This equation is of the form:

$$\alpha\left(\frac{\partial^2 T}{\partial x^2}+\frac{\partial^2 T}{\partial y^2}+\frac{\partial^2 T}{\partial z^2}\right)=u\frac{\partial T}{\partial x}+v\frac{\partial T}{\partial y}+w\frac{\partial T}{\partial z} \qquad \text{(Equation 1.1)}$$

where $\alpha = \frac{k}{\rho c}$. (Equation 1.2)

The technique of superposition was first applied to film cooling by Metzger, Carper and Swank [Ref. 1]. This study examined the effect of secondary fluid injection through nontangential slots on the heat transfer in region near the injection site. In a comment on this paper, E.R.G. Eckert showed how local heat transfer coefficient ratios for different injection temperatures can be used to deduce the adiabatic wall temperature, T_{aw}, and the iso-energetic heat transfer coefficient, h_f. The adiabatic wall temperature is defined as the temperature which the film cooled wall assumes when the heat flux is zero. The iso-energetic heat transfer coefficient is defined as the heat transfer coefficient obtained under iso-energetic conditions in which the freestream and injectant recovery temperatures are the same. With these parameters, the heat flux with film cooling is given by :

$$q = h_f (T_w - T_{aw}) \qquad \text{(Equation 1.3)}$$

The same heat flux may also be expressed in terms of the variation between the actual wall temperature and the freestream recovery temperature using the equation given by :

$$q = h(T_w - T_\infty) \qquad \text{(Equation 1.4)}$$

Equating these two then produces an equation having the form :

$$h = h_f \frac{(T_w - T_{aw})}{(T_w - T_\infty)} \qquad \text{(Equation 1.5)}$$

or, after rearrangement,

$$h = h_f \left[1 - \frac{(T_{aw} - T_\infty)}{(T_w - T_\infty)} \right] \qquad \text{(Equation 1.6)}$$

This equation is then equivalent to :

$$h = h_f (1 - \theta \eta) \qquad \text{(Equation 1.7)}$$

where

$$\theta = \frac{(T_c - T_\infty)}{(T_w - T_\infty)} \qquad \text{(Equation 1.8)}$$

and;

$$\eta = \frac{(T_{aw} - T_\infty)}{(T_c - T_\infty)} \qquad \text{(Equation 1.9)}$$

θ is defined as the non-dimensional temperature and η is the definition of the adiabatic film-cooling effectiveness. Dividing each side of equation 1.7 by h_o, the heat transfer coefficient without film cooling, and then expressing heat transfer coefficients in terms of Stanton numbers then produces the form of this equation employed in the present study :

$$\frac{St}{St_o} = \frac{St_f}{St_o}(1 - \theta \eta) \qquad \text{(Equation 1.10)}$$

A plot of St/St_o versus θ, where θ is varied by changing the injection temperature, thus gives a straight line with a vertical axis intercept of iso-energetic Stanton number ratio St_f/St_o, and a horizontal axis intercept of the inverse of the adiabatic film cooling effectiveness$1/\eta$. This procedure applies only so long as temperature differences are small enough that fluid properties are reasonably invariant as θ is changed, and as long as fluid properties are reasonably invariant with respect to all three coordinate directions (Ligrani and Camci, [Ref. 2], and Ligrani, [Ref. 3]).

B. PRESENT STUDY

Results are presented which describe the development and structure of flow downstream of film-cooling holes with compound angle orientations. Results are given which were measured both downstream of one row of holes and downstream of two staggered rows of holes. Holes are inclined at 90 degrees with respect to the test surface when projected into the streamwise/normal plane, and 30 degrees with respect to the test surface when projected into the spanwise/normal plane. Within each row, holes are spaced 6.0d apart, where d is the hole diameter. This gives 3.0d spacing between adjacent holes when two staggered rows are employed. Results presented include distributions of surface Stanton numbers, adiabatic film cooling effectiveness deduced from heat transfer coefficients using superposition, iso-energetic Stanton numbers, and injectant distributions. The Stanton number data are presented for θ values ranging from 0 to 5.0 at x/d ratios of 6.8, 17.6, 33.8, 55.5, 77.1, and 98.7. Blowing ratios m range from 0.5 to 2.5 for one row of film cooling holes and 0.5 to 1.5 for two rows of holes. Also presented are plots showing the streamwise development of distributions of mean streamwise velocity.

C. EXPERIMENTAL OUTLINE

Three different types of measurements are made in the present study:

1. Stanton numbers, Stanton number ratios, and adiabatic film cooling effectiveness values at 21 spanwise locations at x/d ratios of 6.8, 17.6, 33.8, 55.5, 77.1, and 98.7.

2. Mean velocity and total pressure surveys in Y-Z planes at x/d values of 7.4, 43.8, and 85.6.

3. Mean temperature survey in Y-Z planes at x/d values of 7.4, 43.8, and 85.6 to provide information on injectant distributions.

These data are obtained for six different injection configurations: (1) one row of compound angle film-cooling holes with a blowing ratio of m=0.5, (2) one row of compound angle film-cooling holes with a blowing ratio of m=1.0, (3) one row of compound angle film-cooling holes with a blowing ratio of m=1.5, (4) two staggered rows of compound angle film-cooling holes with a blowing ration of m=0.5, (5) two staggered rows of compound angle film-cooling holes with a blowing ratio of m=1.0, (6) two staggered rows of compound angle film-cooling holes with a blowing ratio of m=1.5.

D. THESIS ORGANIZATION

The remainder of this thesis is organized as follows. Chapter II discusses the experimental apparatus and procedures. Chapter III contains experimental results. Chapter IV then presents a summary and conclusions. Appendix A contains all of the figures. Appendix B discusses all of the data acquisition programs, processing programs and plotting programs developed and used for this study. Appendix C contains a data file directory which gives the names of all data files contained on floppy disks.

II. EXPERIMENTAL APPARATUS AND PROCEDURES

A. WIND TUNNEL AND COORDINATE SYSTEM.

The wind tunnel is the same one used in the experiments of Ligrani, et al. [Refs. 4 and 5]. The facility is open-circuit, subsonic, and housed in the laboratories of the Department of Mechanical Engineering of the Naval Postgraduate School. A centrifugal blower is located at the upstream end, followed by a diffuser, a header containing a honeycomb and three screens, and then a 16 to 1 contraction ratio nozzle. The nozzle leads to the test section which is a rectangular duct 3.05 m long and 0.61 m wide, with a topwall having adjustable height to permit a zero pressure gradient to be set along the length of the test section (without the film cooling) to within 0.01 inches of water differential pressure. The initial duct height at the nozzle exit is 0.203 m. The freestream velocity is 10 m/s and the freestream turbulence intensity is approximately 0.13 percent based on the same velocity. The boundary layer is tripped using a 2 mm high spanwise uniform strip of tape close to the nozzle exit. It is 1.072 m upstream of the heat transfer surface and goes across the wind tunnel in the spanwise direction.

Schematics of the test section side view and top view are given in Figures 1 and 2, respectively. These figures also show the compound angle film-cooling geometry employed in this study, denoted configuration 4. Locations of the boundary layer trip, the film cooling holes, the heat transfer test surface, and the thermocouple rows are additionally labelled in Figures 1 and 2. With this arrangement, an unheated starting length exists when the heat transfer surface is at a temperature above that of the surrounding laboratory. Thus, the direction of heat transfer is from the wall to the gas. In regard to the coordinate system, Z is the spanwise coordinate measured from the test section spanwise centerline, X is measured from the upstream edge of the boundary layer trip, and Y is measured normal to the test surface. X is measured from the downstream edge of the injection holes and generally presented as x/d.

B. INJECTION HOLE CONFIGURATION

A schematic showing the compound angle film hole geometry (configuration 4) along the test surface is shown in Figure 3. Injection holes for configuration 4 are arranged in two rows which are staggered with respect to each other, with spanwise spacings between adjacent holes of 3.0d. Centerlines of holes in separate rows are separated by 4.0d in the streamwise direction. When one row of holes is employed, it is the one located nearest the heat flux surface and spanwise hole spacing is 6.0d. Each row of holes contains five injection cooling holes with a nominal inside diameter of 0.925 cm. The centerline of the middle hole of the downstream row is located on the spanwise centerline (Z=0.0 cm) of the test surface. The compound angle holes are used with Ω=90 degrees and β=30 degrees, where Ω is the angle of the injection holes with respect to the test surface as projected into the streamwise/normal plane, and β is the angle of the injection holes with respect to the test surface as projected into the spanwise/normal plane. Thus, as shown in Figure 3, holes are oriented so that the spanwise components of injectant velocity are directed in the negative-Z direction.

C. INJECTION SYSTEM.

The injection system is described by Ligrani, et al. [Ref. 5]. Air for the injection system originates one or two 1.5 horsepower DR513 Rotron Blowers, each capable of producing 30 cfm at 2.5 psig. From the blowers, air flows through a Fisher and Porter rotometer, a diffuser, and finally into the injection heat exchanger and plenum chamber. The exchanger provides means to heat the injectant above ambient temperature. With this system and test plate heating, the non-dimensional injection temperature parameter θ is maintained at values ranging from 0.0 to 5.0, which includes values within the range of gas turbine component operation. The upper surface of the plenum chamber is connected to the injection tubes which are 9.4 cm long, giving a length to diameter ratio of about 10.

Injection system performance was checked by measuring discharge coefficients at different Reynolds numbers based on injection hole diameter and mean injectant velocity. The results of these performance checks are given by Bishop [Ref. 6], who also gives procedures to measure discharge coefficients and blowing ratios.

All film cooling parameters, such as the blowing ratio, are calculated based on the temperature at the exits of the injection holes, (T_{inj}). This temperature T_{inj} is related to the injection plenum temperature, T_{plenum}, by an equation given by Bishop [Ref. 6]:

$$T_{inj}\left({}^{o}C\right) = 2.2907 + 0.85948 \times T_{plenum}\left({}^{o}C\right) \qquad \text{(Equation 2.1)}$$

This equation represents an empirical fit to experimental data for blowing ratios ranging from 0 to 1.5 and for injection temperatures from 0 to 100 degrees Celsius. With this orientation, injection temperatures may be determined from measurements of the plenum temperature.

When one row of holes is employed, the downstream row of injection holes is used. With this arrangement, the upstream holes are then plugged and covered with cellophane tape.

D. HEAT TRANSFER SURFACE

The heat transfer surface is designed to provide a heat flux distribution which is constant over its area. The test surface is inserted into the bottom wall of the wind tunnel next to the airstream. The upper face of this test surface is maintained level with the wind tunnel test surface using height adjustment screws mounted in the plexiglass support frame. The test surface is made of stainless steel foil painted flat black, with dimensions of 1.3 m x 0.476 m x 0.20 mm. Copper-constantan thermocouples are attached to the underside of the stainless steel foil in six rows of 21 thermocouples per row, with a spanwise spacing of 1.27 cm between individual thermocouples. Thermocouple lead wires are embedded in grooves cut into a triple sheet of 0.254 mm thick double sided tape. RTV epoxy is then used to fill spaces around thermocouple lead wires within these grooves. Electrobond epoxy is used to attach a wire wound heater, with dimensions of 1.0 mm x 1.118 m x 0.438 m and manufactured by Marchi Associates, to the underside of the double sided tape. The heater is rated at 120 volts and 1500 watts, and designed to maintain uniform dissipation of heat over its entire surface. Located below the heater are several layers of insulating materials including Lexan sheets, foam insulation, styrofoam and balsa wood. A plexiglass support frame then encases the bottom portion of the heat transfer test surface and provides support. This frame is then mounted on the underside of the wind tunnel. Surface temperature levels and convective heat transfer rates are controlled by adjusting power into the heater using a Standard Electric Co. Variac, type 3000B.

After the surface was completed, a variety of qualification tests were conducted to check the performance of the heat transfer test surface. These are described in detail by Ligrani, [Ref. 4], Bishop [Ref. 6], and Ciriello [Ref. 7], along with additional details on the measurement of local Stanton numbers.

E. STANTON NUMBER MEASUREMENTS

In past studies, local Stanton numbers were calculated based on local temperature measurements and global convective heat flux levels. The global convective heat flux levels were determined from a global energy balance which accounts for radiation, conduction and convection from the entire test surface. In the current study, this analysis is refined to also include energy balances for control volumes around individual thermocouples which account for local spanwise and streamwise conduction along the test surface. Figure 4 illustrates these local energy balances are made based on control volumes around each thermocouple. The corresponding energy balance equation is given by :

$$q_{conv} = q_{in} - q_{rad} - q_{cond} - q_{spanwise} - q_{streamwise} \quad \text{(Equation 2.2)}$$

The local heat transfer coefficient is then given by :

$$h = \frac{q_{conv}}{(T - T_\infty)} \qquad \text{(Equation 2.3)}$$

and the resulting Stanton number equation is :

$$St = \frac{h}{\rho U_\infty C_p} \qquad \text{(Equation 2.4)}$$

where q_{in}=I*V, which is the power into the heater. q_{rad} is a global radiation heat flux from the test surface. q_{cond} is a global conduction heat flux from the bottom and sides of the test surface. $q_{spanwise}$ is the local spanwise conduction between the thermocouple of interest and the adjacent thermocouples. $q_{streamwise}$ is the local streamwise conduction between the row of the thermocouple of interest and the adjacent rows of thermocouples. q_{in}, q_{rad}, and q_{cond} are global heat fluxes, and as such, are averaged over the heat transfer surface using the surface area of the heater which is 0.4897 m^2. The details of the heat transfer procedure for determination of the thermal contact resistance, conduction heat transfer, radiation heat transfer, and the spanwise/streamwise conduction heat transfer are described from Wigle [Ref. 8].

A total of 126 thermocouple are placed beneath the foil surface of the heat transfer test section for determination of local temperature values. When spanwise averages of measured quantities, like the Stanton numbers, are determined, 13 of the 21 thermocouples in each row are employed. These are located at Z ranging from -14 cm to 2.5 cm, and used as this portion of the wind tunnel test surface is always covered by film cooling as it spreads along it.

F. TEMPERATURE MEASUREMENTS

Temperature measurements are made utilizing calibrated copper-constantan thermocouples. These include heat transfer surface temperatures, the freestream temperature, local boundary layer temperatures, and the injection plenum temperature. The calibration equation used for the heat transfer surface temperatures is given by Ortiz [Ref. 9]:

$$T\left({}^{o}C\right) = 0.018205 + 0.025846 \times E - 0.000000581 \times E^2$$

(Equation 2.5)

where E is in microvolts. The surface temperature thermocouples are connected to channels 1 to 126 of the acquisition system.

The calibration equation employed for the freestream thermocouple is described by Williams [Ref. 10]. This thermocouple is connected to data acquisition channel 147. Its calibration equation is given by :

$$T\left({}^{o}C\right) = -2.602912 + 32.177745 \times E - 5.483059 \times E^2 + 1.24739 \times E^3$$

(Equation 2.6)

where E is in millivolts.

Thermocouples employed in the plenum chamber, used to measure film injectant temperatures in the boundary layer, were calibrated by Bishop [Ref. 6]. From this calibration, the polynomial representing temperature as a function of thermocouple output voltage is given by :

$$T\left({}^{\circ}C\right) = 0.0858454 + 26017.4569 \times E - 740382.8 \times E^2 + 35639480 \times E^3$$

(Equation 2.7)

where E is in millivolts. Two thermocouples of this type are used on channels 149 and 150 for measurement of plenum temperature. A thermocouple with the same calibration equation is used on channel 153 for measurement of boundary layer temperatures used to quantify injection distributions.

Temperature surveys to determine injectant distributions are performed using a thermocouple traversed through the boundary layer in conjunction with a thermocouple used to measure freestream temperature. For these tests, no heat applied to the heat transfer test plate, and freestream temperature is maintained at ambient temperature while injectant is heated to 50 degrees Celsius in the injection plenum. For each survey, local temperatures are taken at 800 (20 x 40) locations in the Y-Z plane at a particular x/d location. The spatial resolution between sampling points is 0.508 cm in each direction (Y and Z), and the overall sampling plane dimensions are 10.2 cm x 20.3 cm.

The traversing device consists of spanwise and vertical traversing blocks allowing two degrees of freedom. Each block is mounted on a separate assembly consisting of two steel case hardened support shafts and a 20 thread per inch pitch drive screw. Separate M092-FD310 stepping motors are used to drive each of the two shafts. A two-axis Motion Controller(MITAS), equipped with 2K bytes of memory and a MC68000 16 bit microprocessor controls a motor drive which runs the motors. The motors, controller, and the drive are manufactured by the Superior Electric Company. Software within a Hewlett-Packard Series 9000 Model 310 computer provides instructions which control operation of the controller and traversing device.

A Hewlett-Packard 3497A Data Acquisition/Control Unit with a Hewlett-Packard 3498A Extender is used to collect all voltages from the thermocouples used. These units are controlled by a Hewlett-Packard Series 9153C computer.

G. STREAMWISE MEAN VELOCITY MEASUREMENTS.

The streamwise mean velocity is measured using a five-hole pressure probe with a conical tip manufactured by United Sensors Corporation. Celesco transducers and Carrier Demodulators are used to sense pressures when connected to probe output ports. The same automated traverse used for injectant surveys was used to obtain these surveys. With this device, the pressure probe was traversed over 10.2 cm by 20.3 cm spanwise/normal planes at 800 locations spaced 0.51 cm apart in each direction. At each location, 50 samples of the output from each of the five pressure ports are aquisitioned for later processing. These devices, measurement procedures employed, as well as data acquisition equipment and procedures used are further detailed by Ligrani, et al. [Ref. 4 and 5], Bishop [Ref. 6], and Ciriello [Ref. 7].

H. BASELINE DATA MEASUREMENTS.

To provide a baseline data check, Stanton numbers, measured without film injection present, are compared to an empirical relationship given by Kays and Crawford [Ref. 11]. This relationship represents turbulent boundary layer flow in a zero pressure gradiant over a constant heat flux surface just downstream of an unheated starting length. The equation is given by :

$$\mathrm{StPr}^{0.4} = 0.03\mathrm{Re}^{-0.2} \times \frac{\beta_1\left(\frac{1}{9},\frac{10}{9}\right)}{\beta_{u1}\left(\frac{1}{9},\frac{10}{9}\right)} \qquad \text{(Equation 2.8)}$$

Here, β_1 and β_{u1} are the Beta function and the incomplete Beta function, respectively. The term u_1 is defined as :

$$u_1 = 1 - \left(\frac{\xi_1}{x}\right)^{\frac{9}{10}} \qquad \text{(Equation 2.9)}$$

Figures 5 and 6 compare the exact solution given by equation 2.2 to baseline data obtained when 4 amps and 6 amp of current are applied to the heat transfer test surface. Figure 5 is a plot of Stanton numbers versus x/d which shows that experimental data agree with the correlation for x/d greater than about 17. Figure 6 shows a plot of Stanton numbers versus Reynolds numbers with trends which are similar to the ones in Figure 5.

III. EXPERIMENTAL RESULTS

Experimental results are presented which were measured downstream of the compound angle angle injection configuration 4. Heat transfer data, mean velocity surveys, total pressure surveys, and injectant temperature distributions are presented from measurements downstream of both one row of film-cooling holes, and two staggered rows of film-cooling holes at various blowing ratios. Plots of St/St_o vs θ are presented for each blowing ratio. The measurements are given for X=1.12, 1.22, 1.37, 1.57, 1.77, abd 1,97 meters from the trip, which correspond to the x/d values of 6.8, 17.6, 33.8, 55.5, 77.1, and 98.7, respectively. These data demonstrate the linearity of the St/St_o vs θ data, which is important because it validates the use of the linear superposition technique to deduce the iso-energetic Stanton number ratio (St_f/St_o) and the adiabatic film-cooling effectiveness (η).

The next figures presented are plots of spanwise averaged adiabatic film-cooling effectiveness ($\overline{\eta}$) and iso-energetic Stanton number ratio ($\overline{St_f / St_o}$) vs x/d. As mentioned earlier, thirteen measurements across the span at each streamwise location are used to determine these spanwise averages. Also given is the Stanton number data as a function of Reynolds number for different values of non-dimensional temperature (θ). The next three figures are three-dimensional plots showing the spanwise variation of adiabatic film-cooling effectiveness (η) , iso-energetic Stanton number ratio (St_f/St_o), and Stanton number ratio (St/St_o) for a particular θ. Temperature surveys and mean velocity and total pressure surveys are subsequently presented for three different spanwise normal planes at streamwise locations of x/d=7.4, 43.8, and 85.6 for each blowing ratio.

A. PLATE 4, COMPOUND ANGLE, ONE ROW OF FILM-COOLING HOLES.

1. Heat Transfer Measurements

a. m=0.5

Figures 7-12 present St/St_o vs θ results for X=1.12, 1.22, 1.37, 1.57, 1.77, and 1.97 meters at a spanwise location of Z=0.0 cm for m=0.5. The data presented for these six X(or x/d) locations demonstrate the linearity of the St/St_o vs θ data. Figure 13 is a plot of spanwise-averaged $\overline{\eta}$ vs x/d and shows that $\overline{\eta}$ is largest at the value of x that corresponds to x/d=6.8 and that it decreases as x/d increases. Figure 14 is a plot of spanwise-averaged $\overline{St_f / St_o}$ vs x/d and shows that the values range between 1.0 and 1.2 and are generally independent of x/d at a particular m. In Figure 15, spanwise-averaged Stanton number data are given as a function of Reynolds number for θ =0.042, 0.67, 1.82, 2.74, 3.21, and 4.94. In general, at each Reynolds number, Stanton numbers decrease as θ increases, and at a particular θ, Stanton number values generally decrease with increasing Reynolds number, such that all sets of data show similar qualitative trends. Figures 16-18 show streamwise and spanwise variations of η , St_f/St_o, and St/St_o θ=1.82, respectively. The plots of η at x/d=6.8 and x/d=17.6 in Figure 16 show spanwise periodicity which becomes less pronounced with streamwise development. The spanwise periodicity of η is due to deficits (low η) and accumulations (high η) of injectant. The plots of St_f/St_o and St/St_o are spanwise periodic such that the higher values correspond to areas of high near-wall mixing, and the lower values correspond to areas of higher concentrations of injectant.

b. m=1.0

Figures 19-24 present St/St_o vs θ results for X=1.12, 1.22, 1.37, 1.57, 1.77, and 1.97 meters at a spanwise location of Z=0.0 cm for m=1.0. Figure 25 is a plot of spanwise-averaged $\overline{\eta}$ vs x/d. Figure 26 is a plot of spanwise-averaged $\overline{St_f / St_o}$ vs x/d. In Figure 27, spanwise-averaged Stanton number data are given as a function of Reynolds number for θ =0.075, 0.63, 1.51, 2.34, 2.86, and 4.25. Figures 28-30 show streamwise and spanwise variations of η , St_f/St_o and St/St_o for θ=1.51, respectively. The trends of the plots are qualitatively similar to ones present for m=0.5 and becomes more spanwise peroidic as x/d increases. Quantitative magnitudes of spanwise averaged $\overline{\eta}$ are somewhat lower than similar data for m=0.5 for values of x/d less than 30. For x/d values higher than 30, the magnitudes are higher. The quantitative magnitudes of local η are similar to m=0.5. Spatially resolved St_f/St_o and St/St_o distributions show larger spanwise periodic variations than the results for m=0.5.

c. m=1.5

Figures 31-36 present St/St_o vs θ results for X=1.12, 1.22, 1.37, 1.57, 1.77, and 1.97 meters at a spanwise location of Z=0.0 cm for m=1.5. Figure 37 is a plot of spanwise-averaged $\overline{\eta}$ vs x/d. Figure 38 is a plot of spanwise-averaged $\overline{St_f / St_o}$ vs x/d. In Figure 39, spanwise-averaged Stanton number data are given as a function of Reynolds number for θ =0.19, 0.61, 1.42, 2.17, 2.90, and 4.41. Figures 40-42 show streamwise and spanwise variations of η , St_f/St_o and St/St_o for θ=1.42, respectively. The trends of the plots are qualitatively similar to ones present for m=0.5 and m=1.0. Quantitative magnitudes of spanwise averaged $\overline{\eta}$ and are lower than similar results at m=0.5

and m=1.0 for x/d less than 60. The quantitative magnitudes of spanwise averaged $\overline{\eta}$ for m=0.5 are lower for x/d greater than 60. The quantitative magnitudes of local η are similar to the ones presented for m=0.5 and m=1.0. Quantitative magnitudes of $\overline{St_f / St_o}$ are higher than similar data for m=0.5 and m=1.0 except for x/d values higher than 60. At x/d greater than 60, the magnitudes are lower than the values for m=1.0. Spatially resolved plots of St_f/St_o and St/St_o show larger spanwise periodic variations than St_f/St_o and St/St_o data for m=0.5 and m=1.0.

d. m=2.0

Figures 43-48 present St/St_o vs θ results for X=1.12, 1.22, 1.37, 1.57, 1.77, and 1.97 meters at a spanwise location of Z=0.0 cm for m=2.0. Figure 49 is a plot of spanwise-averaged $\overline{\eta}$ vs x/d. Figure 50 is a plot of spanwise-averaged $\overline{St_f / St_o}$ vs x/d.. In Figure 51, spanwise-averaged Stanton number data are given as a function of Reynolds number for θ =0.35, 0.69, 1.37, 2.07, 2.72, and 3.86. Figures 52-54 show streamwise and spanwise variations of η , St_f/St_o and St/St_o for θ=1.37, respectively. Quantitative magnitudes of spanwise averaged $\overline{\eta}$ are lower than similar results at lower blowing ratios for x/d less than 60. At larger x/d greater than 60, spasnwise averaged $\overline{\eta}$ are equal to the values of m=1.5 and slightly higher than the values of m=0.5. The quantitative magnitudes of local η are lower than those of lower m. Quantitative magnitudes of $\overline{St_f / St_o}$ are higher than data at the lower blowing ratios except at x/d value less than 10, and spatially resolved plots of St_f/St_o and St/St_o show larger amplitude variations than are evident in data obtained with lower blowing ratios.

e. m=2.5

Figures 55-60 present St/St_o vs θ results for X=1.12, 1.22, 1.37, 1.57, 1.77, and 1.97 meters at a spanwise location of Z=0.0 cm for m=2.5. Figure 61 is a plot of spanwise-averaged $\overline{\eta}$ vs x/d. Figure 62 is a plot of spanwise-averaged $\overline{St_f / St_o}$ vs x/d. In Figure 63, spanwise-averaged Stanton number data are given as a function of Reynolds number for θ =0.43, 0.75, 1.25, 1.86, 2.70, and 3.78. Figures 64-66 show streamwise and spanwise variations of η , St_f/St_o and St/St_o for θ=1.86, respectively. Quantitative magnitudes of spanwise averaged $\overline{\eta}$ and local η are lower than results for lower blowing ratios for x/d less than 40 except for m=1.5 and m=2.0. At larger x/d, the values of $\overline{\eta}$ are slightly higher due to greater amounts of injectant over the test surface. Quantitative magnitudes of $\overline{St_f / St_o}$ are higher than data at lower blowing ratios, and spatially resolved plots of St_f/St_o and St/St_o show larger periodic amplitude variations across the span of the test surface than are present at lower m.

2. Streamwise Mean Velocity Surveys

The five hole pressure probe is used to obtain distributions of streamwise mean velocity and total mean pressure. These two types of distributions are qualitatively very similar for all experimental conditions examined.

a. m=0.5

Figures 67-69 present streamwise velocity distributions and Figures 70-72 present total pressure distributions for m=0.5 for streamwise locations x/d=7.4, 43.8, and 85.6. Distributions for the first streamwise location at x/d=7.4 are spanwise periodic near the wall. Accumulations of injectant correspond to streamwise velocity deficits at spanwise locations Z=-11 cm to -12 cm, -5 cm to -6 cm, 0 cm to -1.5 cm, and 3.5 cm to 6 cm. Surveys at x/d=43.8 and x/d=85.6 show more spanwise periodicity and thicker boundary layers with smaller quantitative variations near the wall compared to the survey at x/d=7.4.

b. m=1.0

Figures 73-75 present streamwise velocity distributions and Figures 76-78 present total pressure distributions for m=1.0 for streamwise locations x/d=7.4, 43.8, and 85.6. Accumulations of injectant correspond to streamwise velocity deficits at spanwise locations Z=-11.5 cm to -13 cm, -6 cm to -8 cm, -1 cm to -2.5 cm, and 2.5 cm to 4 cm. Individual deficits are also skewed such that they are not symetrical with respect to the spanwise direction. These results are qualitatively similar to ones for a blowing ratio m=0.5.

c. m=1.5

Figures 79-81 present streamwise velocity distributions and Figures 82-84 present total pressure distributions for m=1.5 for streamwise locations x/d=7.4, 43.8, and 85.6. Distributions for the first streamwise location at x/d=7.4 are spanwise periodic with high velocity regions corresponding to injectant accumulations, located at spanwise locations Z=-6 cm to -8 cm, -1 cm to -3 cm, and 3 cm to 5 cm. This behavior is different from results for lower blowing ratios due to the high injection velocities associated with this blowing ratio. Velocity distributions at x/d=43.8 and x/d=85.6 also show spanwise periodicity due to velocity deficits which correspond to accumulations of injectant.

3. Injectant Distributions

a. m=0.5

Figures 85-88 present mean temperature survey results which provide information on injectant distributions for m=0.5 for streamwise locations of x/d=7.4, 43.8, and 85.6. At the first streamwise location of x/d=7.4, the injectant distribution is spanwise periodic such that higher temperature regions correspond to accumulations of injectant. Individual accumulations of injectant are skewed and not symetrical with respect to the spanwise direction. As the injectant is convected downstream, it becomes more diffuse at streamwise locations of x/d=43.8 and x/d=85.6. The injectant distribution is still spanwise periodic at x/d=43.8 and x/d=85.6 but concentrations of injectant are moved farther from the wall.

b. m=1.0

Figures 89-92 present injectant distributions for m=1.0 for streamwise locations of x/d=7.4, 43.8, and 85.6. Qualitative trends are similar to surveys for m of 0.5. Injectant distributions are spanwise periodic at x/d=7.4 and become more diffuse as the injectant is convected downstream to x/d=43.8 and x/d=85.6.

c. m=1.5

Figures 93-96 show injectant distributions for m=1.5 for x/d=7.4, 43.8, and 85.6. Qualitative trends show some similarity to ones observed at lower m. In this case, injectant distributions begin to show spanwise unformity at x/d=85.6 especially 4-5 cm from the wall. Compared to results for the lower blowing ratios, injectant is pushed farther from the test surface at all three streamwise locations investigated.

B. PLATE 4, COMPOUND ANGLE, TWO STAGGERED ROWS OF FILM-COOLING HOLES

1. Heat Transfer Measurements

a. m=0.5

Figures 97-102 present St/St_o vs θ results for X=1.12, 1.22, 1.37, 1.57, 1.77, and 1.97 meters at a spanwise location of Z=0.0 cm for m=0.5. The data presented for these six X(or x/d) locations demonstrate the linearity of the St/St_o vs θ data. Figure 103 is a plot of spanwise-averaged $\overline{\eta}$ vs x/d and shows that $\overline{\eta}$ is largest at x/d=6.8 and decreases as x/d increases. Figure 104 is a plot of spanwise-averaged $\overline{St_f / St_o}$ vs x/d and shows that the values range between 1.0 and 1.10 and are generally independent of x/d. In Figure 105, spanwise-averaged Stanton number data are given as a function of Reynolds number for θ =0.22, 0.61, 1.33, 1.98, 2.52, and 3.46. In general, at each Reynolds number, Stanton numbers decrease as θ increases, and at a particular θ, Stanton number values generally decrease with increasing Reynolds number, such that all sets of data show similar qualitative trends. Figures 106-108 show spanwise variations of η , St_f/St_o, and St/St_o for θ=1.33, respectively. The plots of η at x/d=6.8 in Figure 106 show spanwise periodicity which becomes less evident with streamwise development. Measurements of η at larger x/d show spanwise uniformity . The plots of St_f/St_o and St/St_o in Figures 107-108 are spanwise periodic. The peaks of St/St_o are smaller compared to results measured downstream of one row of film-cooling holes.

b. m=1.0

Figures 109-114 present St/St_o vs θ results for X=1.12, 1.22, 1.37, 1.57, 1.77, and 1.97 meters at a spanwise location of Z=0.0 cm for m=1.0. Figure 115 is a plot of spanwise-averaged $\bar{\eta}$ vs x/d. Figure 116 is a plot of spanwise-averaged $\overline{St_f / St_o}$ vs x/d. Figure 117 presents spanwise-averaged Stanton number data as a function of Reynolds number for θ =0.28, 0.66, 1.18, 1.74, 2.07, and 2.80. Figures 118-120 show streamwise and spanwise variations of η , St_f/St_o and St/St_o for θ=1.18, respectively. The trends shown by data in these plots are qualitatively similar to trends observed for m=0.5. However, quantitative magnitudes of spanwise averaged $\bar{\eta}$ are higher than results for m=0.5. The quantitative magnitudes of local η are similar to thoses of m=0.5. Quantitative magnitudes of $\overline{St_f / St_o}$ are higher than $\overline{St_f / St_o}$ data for m=0.5 at all x/d.

c. m=1.5

Figures 121-126 present St/St_o vs θ results for X=1.12, 1.22, 1.37, 1.57, 1.77, and 1.97 meters at a spanwise location of Z=0.0 cm for m=1.5. Figure 127 is a plot of spanwise-averaged $\bar{\eta}$ vs x/d. Figure 128 is a plot of spanwise-averaged $\overline{St_f / St_o}$ vs x/d. Figure 129 presents spanwise-averaged Stanton number data as a function of Reynolds number for θ =0.56, 0.74, 1.17, 1.67, 2.21, and 2.90. Figures 130-132 show streamwise and spanwise variations of η , St_f/St_o and St/St_o for θ=1.17, respectively. The trends shown by data in these plots are qualitatively similar to trends observed for m=0.5 and m=1.0. However, quantitative magnitudes of spanwise averaged $\bar{\eta}$ and local η are higher than results for m=0.5 and m=1.0 except at x/d less than 10. Quantitative magnitudes of $\overline{St_f / St_o}$ are higher than $\overline{St_f / St_o}$ data for m=0.5 and m=1.0 at all x/d.

2. Streamwise Mean Velocity Surveys

The five hole pressure probe is used to obtain distributions of streamwise mean velocity and total mean pressure. These two types of distributions are qualitatively very similar for all experimental conditions examined.

a. m=0.5

Figures 133-135 present streamwise mean velocity distributions and Figures 136-138 present total mean pressure distributions for m=0.5 for streamwise locations x/d=7.4, 43.8, and 85.6. Velocity distributions for the first streamwise location at x/d=7.4 are spanwise periodic with velocity deficts located at spanwise locations Z=-11.5 cm to -12.5 cm, -6 cm to -7 cm, -0.5 cm to -1.5 cm, and 3.5 cm to 5 cm which correspond to locations where injectant from the downstream row of holes accumulates. Nearby velocity deficits correspond to accumulations of injectant which originated in the upstream row of holes. Velocity distributions at x/d=43.8 and x/d=85.6 show spanwise uniformity which results because injectant from the upstream row of holes merges and coalesces with injectant from the downstream row of holes.

b. m=1.0

Figures 139-143 present streamwise mean velocity distributions and Figures 144-148 present mean total pressure distributions for m=1.0 for streamwise locations x/d=7.4, 43.8, and 85.6. The velocity distributions at x/d=7.4 is spanwise periodic with velocity deficits which correspond to injectant accumulations located at spanwise locations Z=-7 cm to -8.5 cm, -1 cm to -3 cm, and 2 cm to 4 cm. These accumulations of injectant are more spanwise periodic than the ones for m=0.5 since the velocity deficits regions are larger due to the merging of injectant from the upstream and downstream rows. Velocity distributions for x/d=43.8 and x/d=85.6 are similar to the one in m=0.5. Velocity distribution were also measured with 2 rows of injection holes and a total of eight injection holes, instead of 10 which are nominally used. Such results for x/d=43.8 and for x/d=85.6 with m=1.0 are shown in Figures 142-143. The distributions are spanwise periodic for both x/d values. The velocity deficit at Z=-10 cm to -12 cm for x/d=43.8, and a velocity deficit at Z=-12 cm to -14 cm are both slightly skewed due to the merging of injectant from the upstream row of holes with the injectant from the downstream row of holes.

c. m=1.5

Figures 149-153 present streamwise mean velocity distributions and Figures 154-158 present mean total pressure distributions for m=1.5 for streamwise locations x/d=7.4, 43.8, and 85.6. Velocity distributions at x/d=7.4 are spanwise periodic with velocity deficits which correspond to injectant accumulations located at spanwise locations of Z=-7 cm to -9.5 cm, -2 cm to -4 cm, and 1.5 cm to 4 cm. These accumulations of injectant are similar to the ones for m=0.5 and m=1.0 since they seem to result from merging of injectant from the upstream and downstream rows of holes. The m=1.5 velocity distributions for x/d=43.8 and x/d=85.6 are similar to the ones for m=0.5 and m=1.0 with thicker boundary layer and some lift-off occuring about 4 to 5 cm from the wall for x/d=43.8. Velocity distributions for m=1.5 are also presented from measurements downstream of 2 rows of holes with a total of eight holes.

Distributions for x/d=43.8 and x/d=85.6 are spanwise periodic with a velocity deficit at Z=-10 cm to -12 cm for x/d=43.8, and a velocity deficit at Z=-12 cm to -14 cm for x/d=85.6.

3. Injectant Distributions

a. m=0.5

Figures 159-162 present mean temperature survey results which provide information on injectant distributions for m=0.5 for streamwise locations of x/d=7.4, 43.8, and 85.6. At x/d=7.4 individual injectant concentrations are non-circular and form a spanwise periodic pattern across the span of the measurement plane. As the injectant is convected downstream to x/d=44.3 and x/d=86.3, it is more diffuse and becomes more spanwise uniform.

b. m=1.0

Figures 163-168 present injectant distributions for m=1.0 for streamwise locations of x/d=7.4, 43.8, and 85.6. Qualitative trends are similar to the m=0.5 surveys. In both cases, injectant distributions are spanwise periodic at x/d=7.4 and become more diffuse and spanwise uniform as the injectant is convected downstream to x/d=43.8 and x/d=85.6. Extra accumulations of injectant on the left side of tunnel (looking downstream) are evident at x/d=86.3, as a consequence of spanwise convection of the injectant in the negative Z direction.

c. m=1.5

Figures 169-174 present injectant distributions for m=1.5 for streamwise locations of x/d=7.4, 43.8, and 85.6. Qualitative trends are similar to the m=0.5 and m=1.0 surveys. In both cases, injectant distributions are spanwise periodic at x/d=7.4 and become more diffuse and spanwise uniform as the injectant is convected downstream to x/d=43.8 and x/d=85.6. Figures 169-172 for x/d=7.4 show temperature ranges measured downstream of eight holes and downstream of ten holes.

C. COMPARISON OF RESULTS FROM SIMPLE ANGLE AND COMPOUND ANGLE FILM-COOLING HOLES

Experimental results for the compound angle injection systems, configuration 1, configuration 3, and configuration 4, and for the simple angle injection system, configuration 2, are compared in this section. To quantify the orientations of the film-cooling holes for the different configurations, angles Ω and β are employed. Ω is the angle of the injectant holes with respect to the test surface as projected into the streamwise/normal plane, and β is the angle of the injection holes with respect to the test surface as projected into the spanwise/normal plane. Configuration one is a compound angle injection arrangement with $\Omega=35^o$, $\beta=30^o$, and a hole spacing of 7.8d for one row of holes, and a hole spacing of 3.9d for two rows of holes. Configuration two is a simple angle injection arrangement with $\Omega=35^o$, $\beta=90^o$, and a hole spacing of 6.0d for one row of holes and a hole spacing of 3.0d for two rows of holes. Configuration three is a compound angle injection arrangement with $\Omega=35^o$, $\beta=30^o$, and a hole spacing of 6.0d for one row of holes and a hole spacing of 3.0d for two rows of holes. Configuration four is a compound angle arrangement with $\Omega=90^o$, $\beta=30^o$, and a hole spacing of 6.0d for one row of holes and a hole spacing of 3.0d for two rows of holes.

Spanwise-averaged values of adiabatic film-cooling effectiveness ($\overline{\eta}$) and spanwise-averaged values of the iso-energetic Stanton number ratio ($\overline{St_f / St_o}$)

for the various configuration are now presented from measurements at different blowing ratios and streamwise positions (x/d). Figures 175-178 present data from configurations one and four. Of these, Figures 175-176 give spanwise averaged $\overline{\eta}$ and spanwise averaged $\overline{St_f / St_o}$ data vs x/d for one row of holes, and Figures 177-178 present results obtained downstream of two staggered rows of holes. Figures 179-182 present data from configurations two and four. Spanwise-averaged $\overline{\eta}$ and spanwise-averaged $\overline{St_f / St_o}$ vs x/d data for one row of film-cooling holes are given in Figures 179-180. Similar data for two staggered rows of film-cooling holes are given in Figures 181-182. Figures 183-186 present results from configurations three and four. Of these, Figures 183-184 give results measured downstream of one row of film-cooling holes. Figures 185-186 then present data from configurations three and four measured downstream of two staggered rows of holes.

From these graphs, it is evident that, for a given blowing ratio, for all configurations tested, spanwise averaged $\overline{\eta}$ values are generally greatest at low x/d and decrease with increasing x/d as injectant is diffused and convected downstream. In addition, spanwise averaged $\overline{\eta}$ values decrease with increasing blowing ratio for x/d less than 20 - 40. This trend reverses at higher x/d because effectiveness is mostly dependent upon the amount of injectant along the test surface, and at lower blowing ratios, smaller amounts of injectant are spread across the test surface. Spanwise-averaged values of $\overline{\eta}$ measured downstream of two staggered rows of holes are higher than data measured downstream of one row of holes when compared at any given blowing ratio since twice as much injectant is present per unit area along the test surface.

Spanwise averaged iso-energetic Stanton number ratios $(\overline{St_f / St_o})$ downstream of one row of holes and downstream of two staggered rows of holes generally range between 1.0 and 1.5 and show little variation with x/d for each blowing ratio tested. The trend at any given x/d shows increasing $\overline{St_f / St_o}$ with blowing ratio except for x/d less than 50 for configuration one.

D. CORRELATIONS OF ADIABATIC FILM-COOLING EFFECTIVENESS DATA

Figure 187 shows a plot of data from all four configurations at all blowing ratios tested (measured downstream of one row of holes and down stream of two staggered rows of holes in) $\overline{\eta}/m$ vs xI/s coordinates. Figure 188 shows the same data in $\overline{\eta}/I$ vs xI/s coordinates. The data in the $\overline{\eta}/m$ vs xI/s plot collapse according to spanwise hole spacing and overall, show the least scatter. The data in the $\overline{\eta}/I$ vs xI/s plot seem to collapse according to blowing ratio.

IV. SUMMARY AND CONCLUSIONS

Experimental results are presented which describe the development and structure of flow downstream of a single row and two staggered rows of film-cooling holes with compound angle orientations. With the configuration studied, holes are inclined at 90 degrees with respect to the test surface when projected into the streamwise/normal plane, and 30 degrees with respect to the test surface when projected into the spanwise/normal plane. Within each row, holes are spaced 6.0 hole diameters apart in the spanwise direction which gives 3.0d spacing between adjacent holes for the staggered row arrangement. Results presented include distributions of iso-energetic Stanton numbers, and adiabatic film cooling effectiveness deduced from Stanton numbers using superposition. Also presented are plots showing the streamwise development of injectant distributions and streamwise development of mean velocity distributions. The effects of blowing ratio, injectant temperature and downstream position are discussed.

Results from eight different injection configurations are presented and discussed for compound angle configuration four: (1) one row of film-cooling holes with a blowing ratio of m=0.5, (2) one row of film-cooling holes with a blowing ratio of m=1.0, (3) one row of film-cooling holes with a blowing ratio of m=1.5, (4) one row of film-cooling holes with a blowing ratio of m=2.0, (5) one row of film-cooling holes with a blowing ratio of m=2.5, (6) two staggered rows of film-cooling holes with a blowing ratio of m=0.5, (7) two staggered rows of film-cooling holes with a blowing ratio of m=1.0, and (8) two staggered rows of film-cooling holes with a blowing ratio of m=1.5.

Spanwise averaged values of the adiabatic film-cooling effectiveness depend mostly on four parameters: hole angle orientation, spanwise hole spacing, number of rows of film-cooling holes (one of two), and blowing ratio. In general, for a given blowing ratio, spanwise averaged $\overline{\eta}$ values are greatest at low x/d and decrease with increasing x/d as injectant is diffused and convected downstream. In addition, spanwise averaged η values decrease with blowing ratio for x/d less than 40. This trend generally reverses at higher x/d because smaller amounts of injectant are spread across the test surface as the blowing ratio decreases. Spanwise averaged iso-energetic Stanton number ratios downstream of one row of holes and two staggered rows of holes generally range between 1.0 and 1.5 and show little variation with x/d for each blowing ratio tested. At any given x/d, iso-energetic Stanton number ratios generally increase with increasing blowing ratio. Spanwise-averaged values of effectiveness measured downstream of two staggered rows of holes are higher than values measured downstream of one row of holes when compared at the same blowing ratio, because twice as much injectant covers the test surface area.

APPENDIX A

Appendix A contains all of the figures generated for this thesis. The figures presented include: Test set-up; injection hole configuration, plots of spanwise-averaged adiabatic effectiveness and iso-energetic Stanton number ratios as dependent upon position; spatially resoved plots of local adiabatic effectiveness, iso-energetic Stanton number ratios, and Stanton number ratios for θ values near 1.0; and spanwise plots of mean velocity, total mean pressure and temperature for the eight configurations studied.

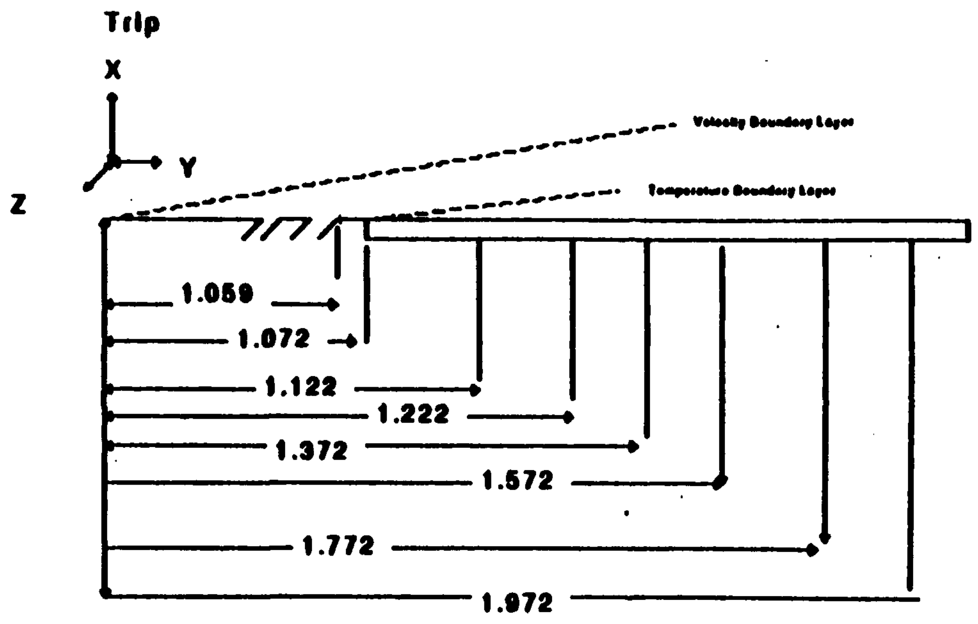

Figure 1. Test Section Coordinate System, Configuration 4, Compound Angle

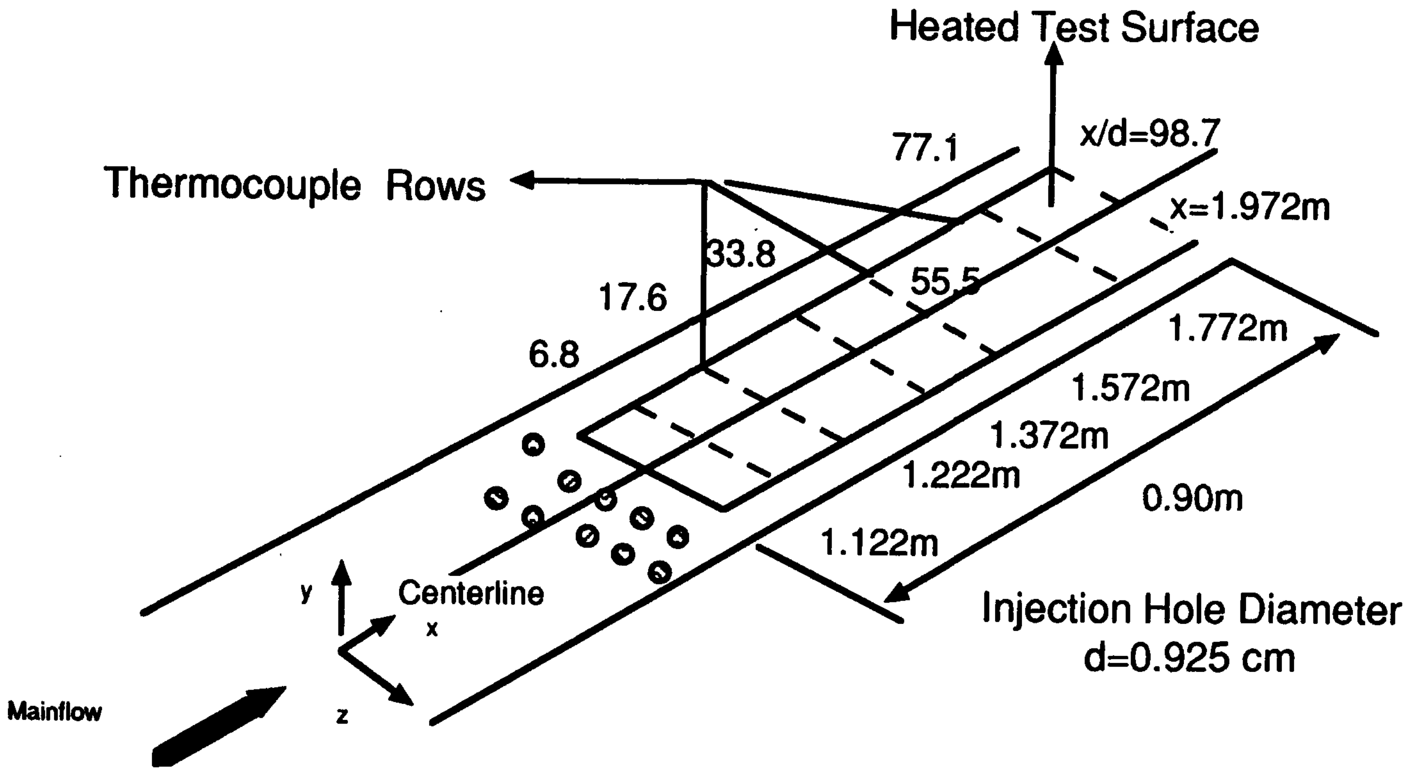

Figure 2. Top View Schematic of Wind Tunnel Test Section, Configuration 4, Compound Angle

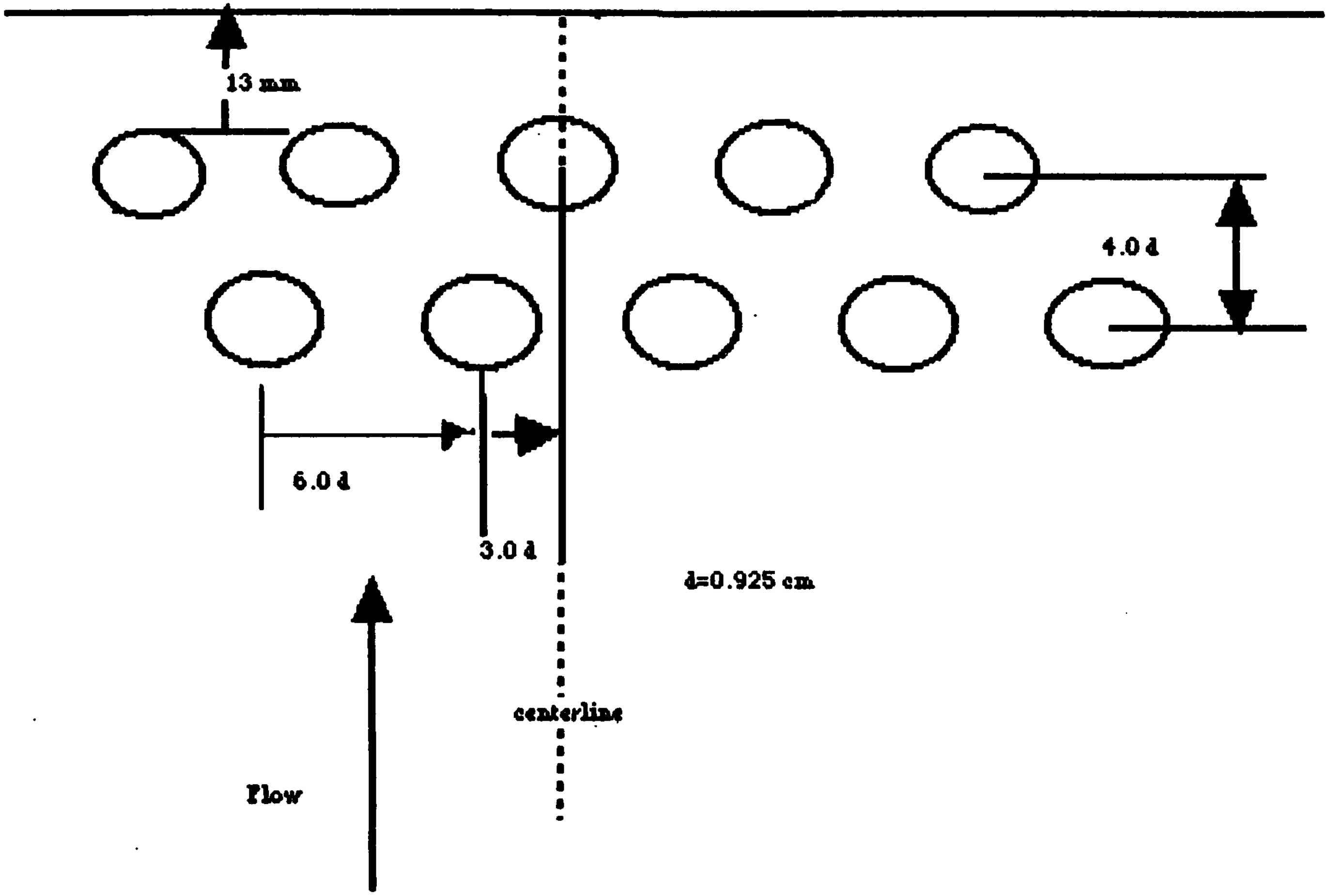

Figure 3. Injection Hole Configuration, Configuration 4, Compound Angle

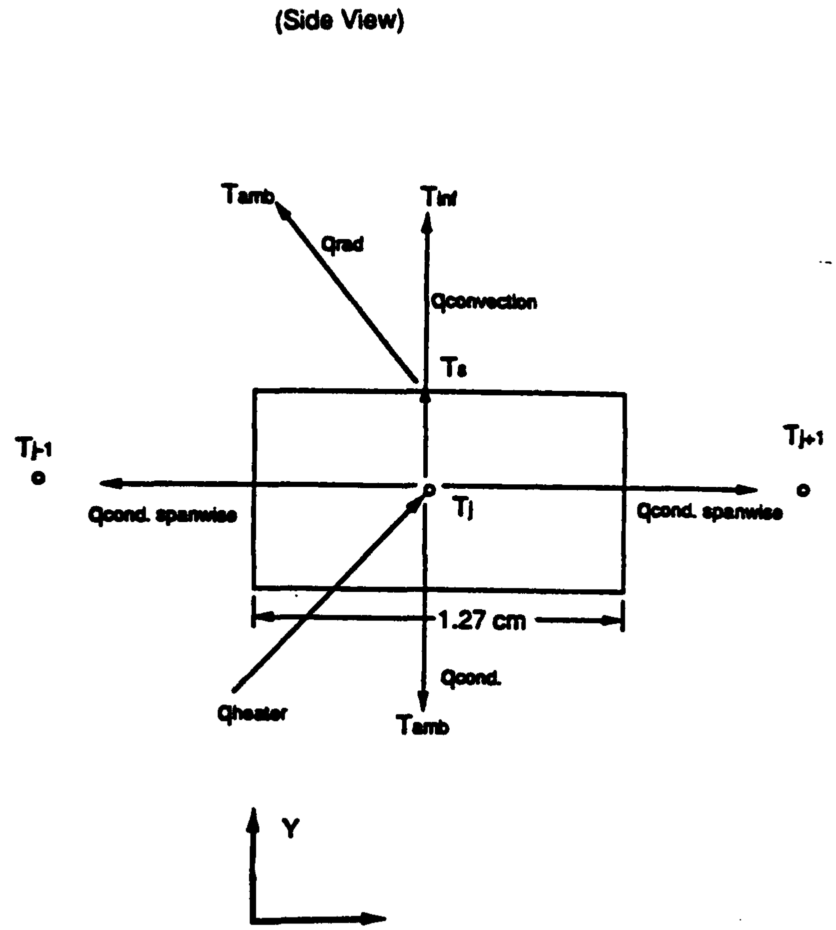

Figure 4. Side View Schematic of Thermocouple Control Volume for Energy Balance Analysis

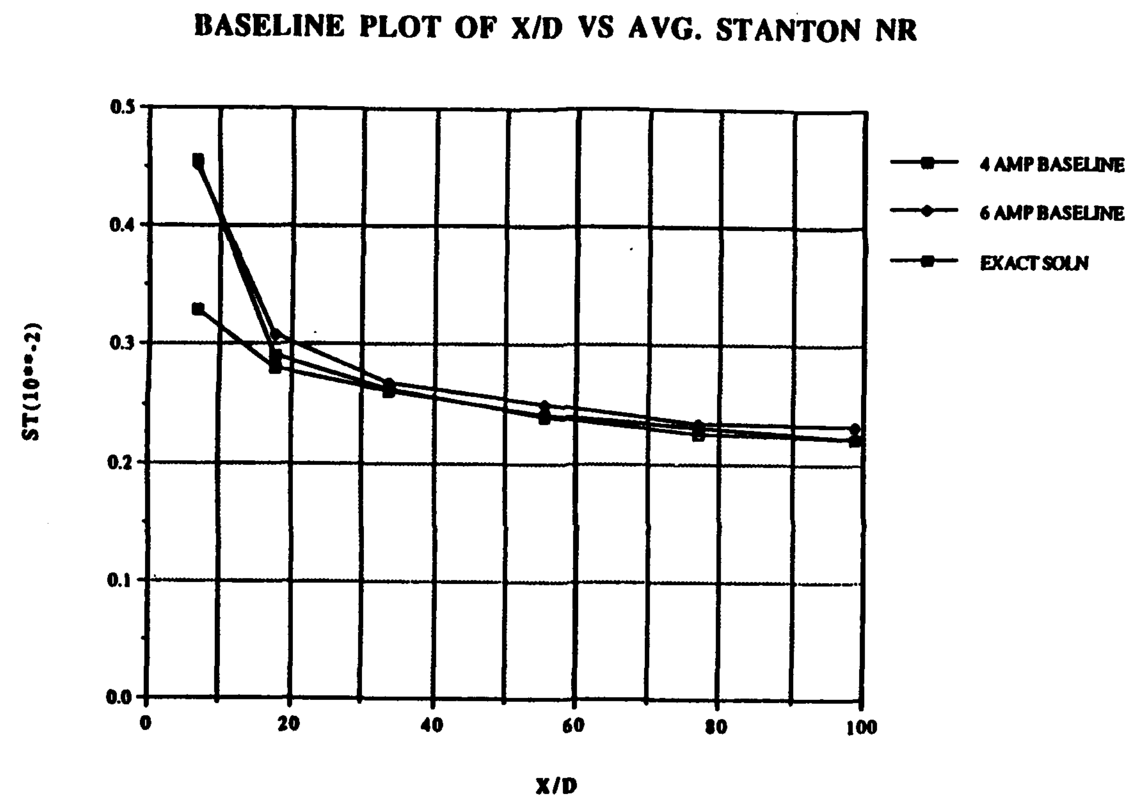

Figure 5. Baseline Stanton number versus x/d, comparison between Correlation and Experimental Measurements

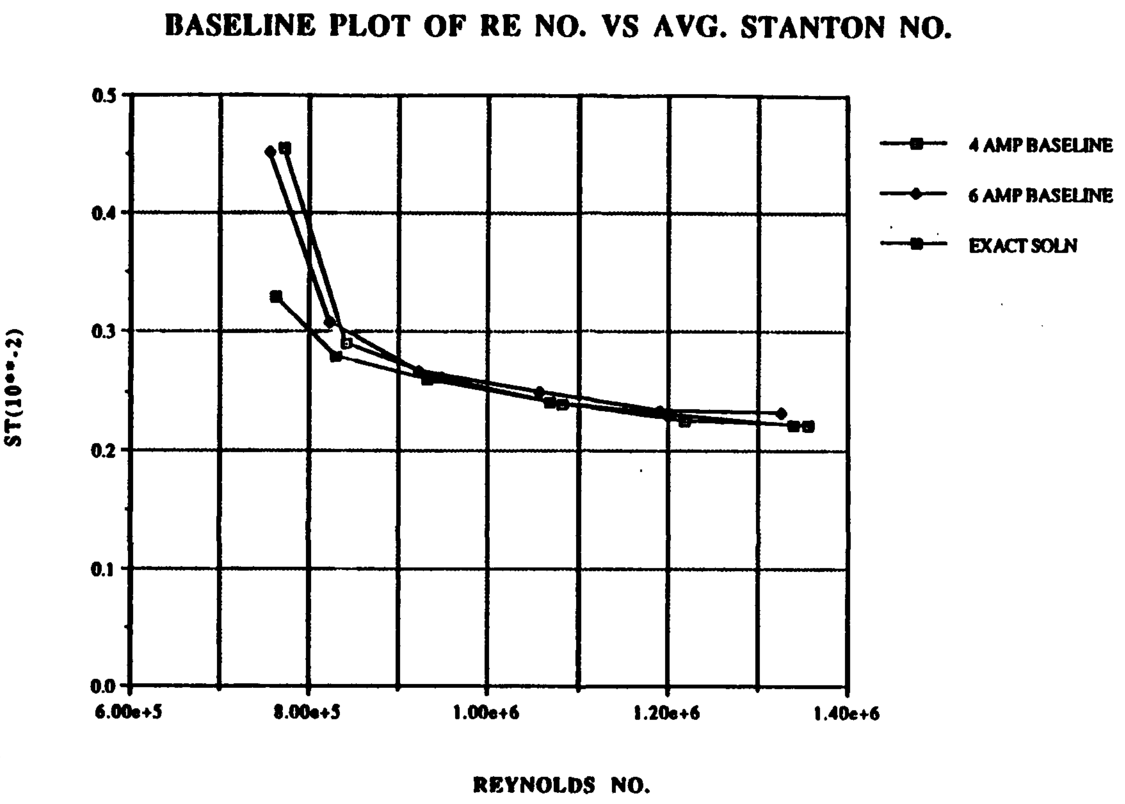

Figure 6. Baseline Stanton number versus Reynolds number, comparison between Correlation and Experimental Measurements

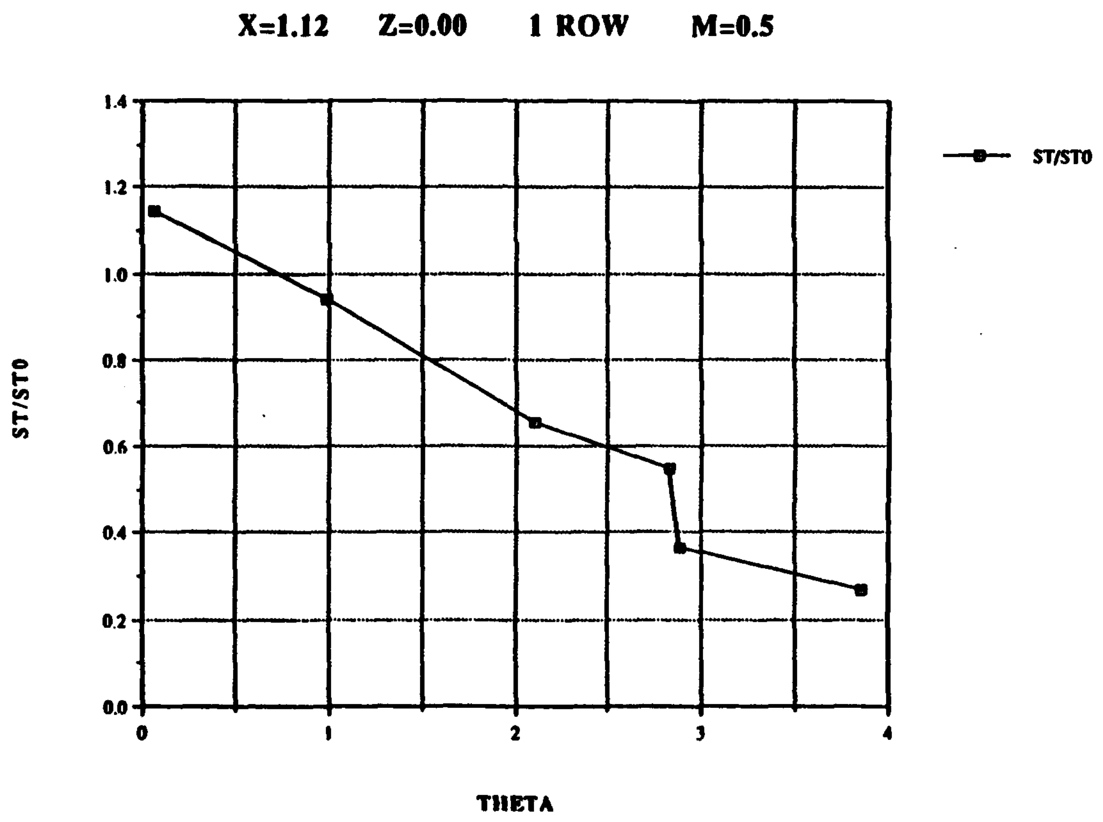

Figure 7. St/St_o vs θ, Compound Angle, 1 row, m=0.5, X=1.12, Z=0.0 m

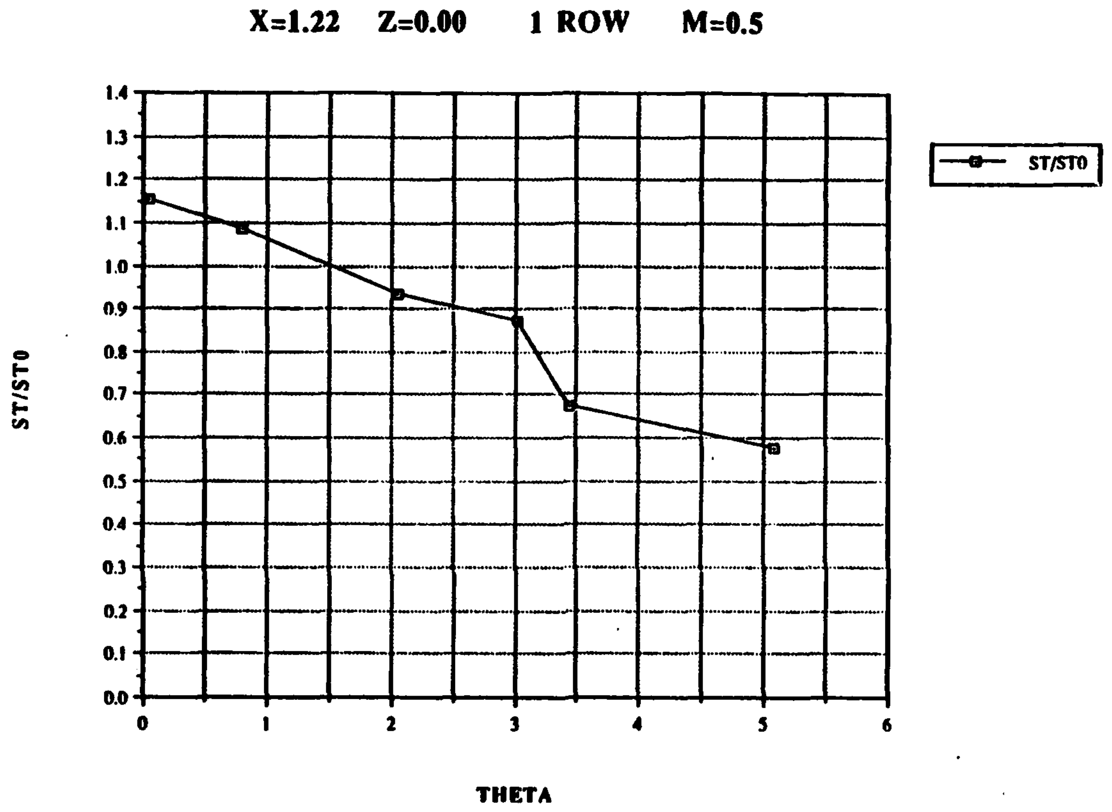

Figure 8. St/St$_0$ vs θ, Compound Angle, 1 row, m=0.5, X=1.22, Z=0.0 m

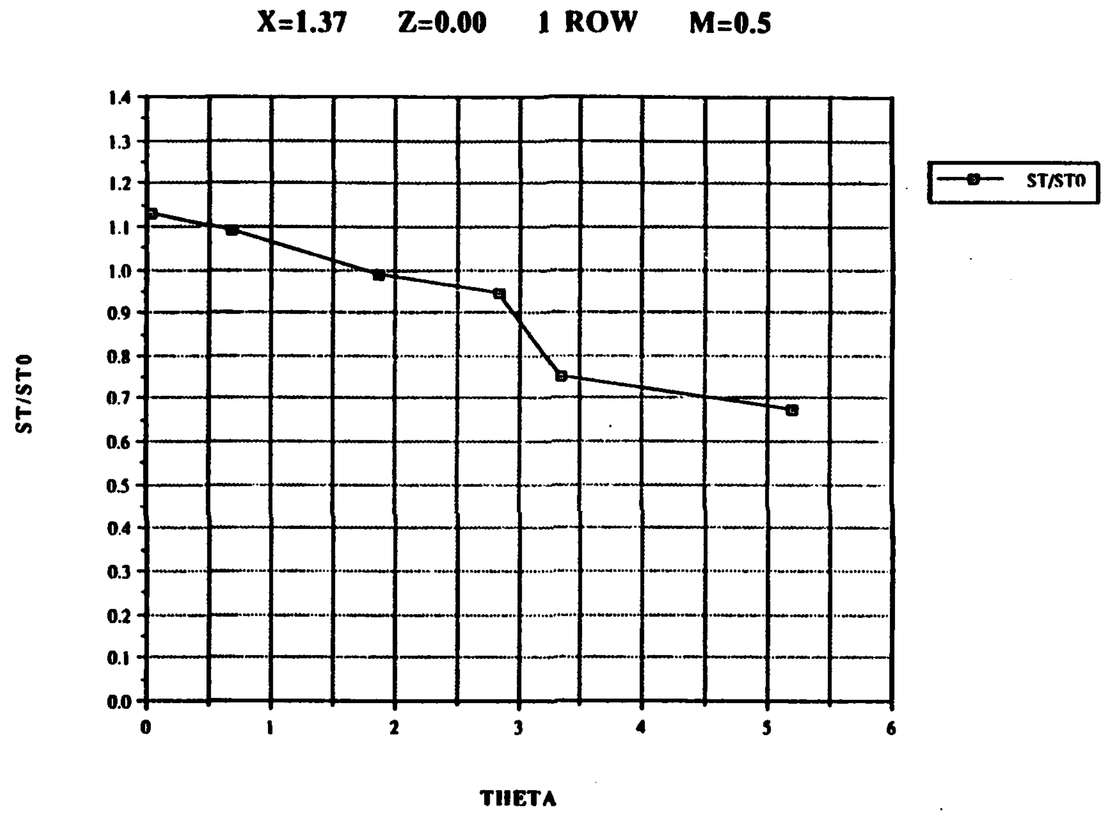

Figure 9. St/St$_0$ vs θ, Compound Angle, 1 row, m=0.5, X=1.37, Z=0.0 m

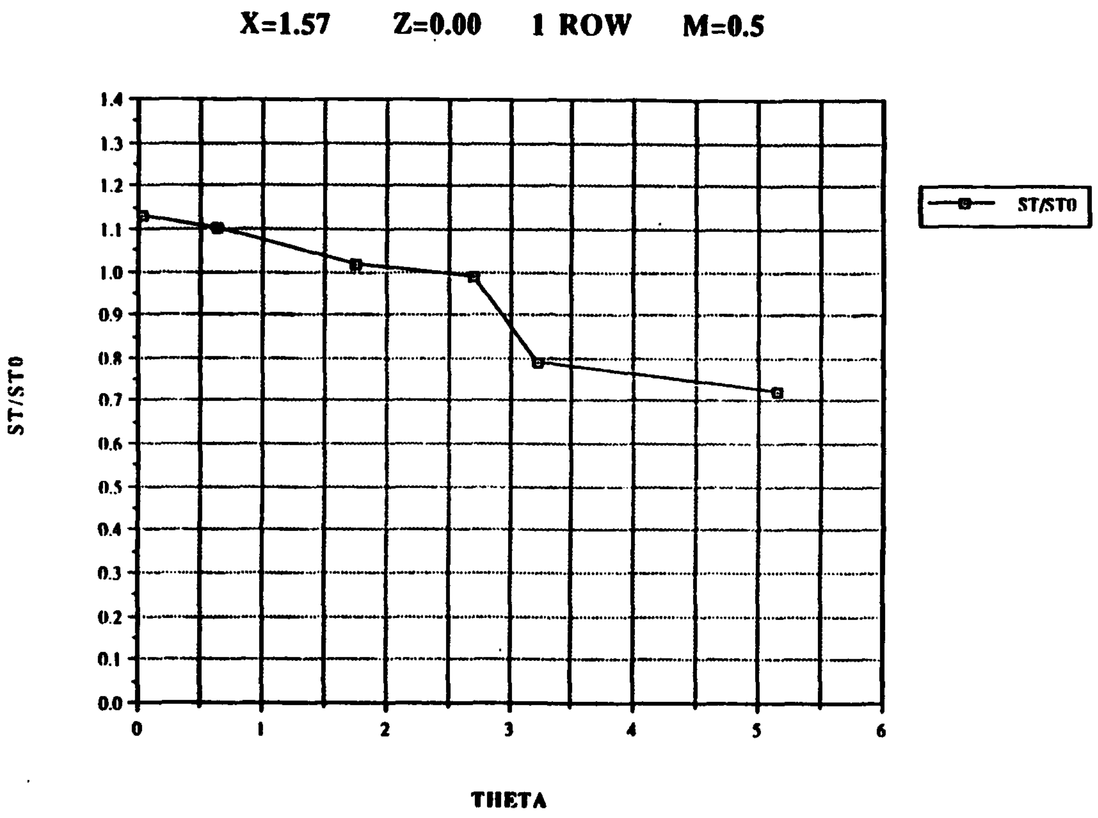

Figure 10. St/St_0 vs θ, Compound Angle, 1 row, m=0.5, X=1.57, Z=0.0 m

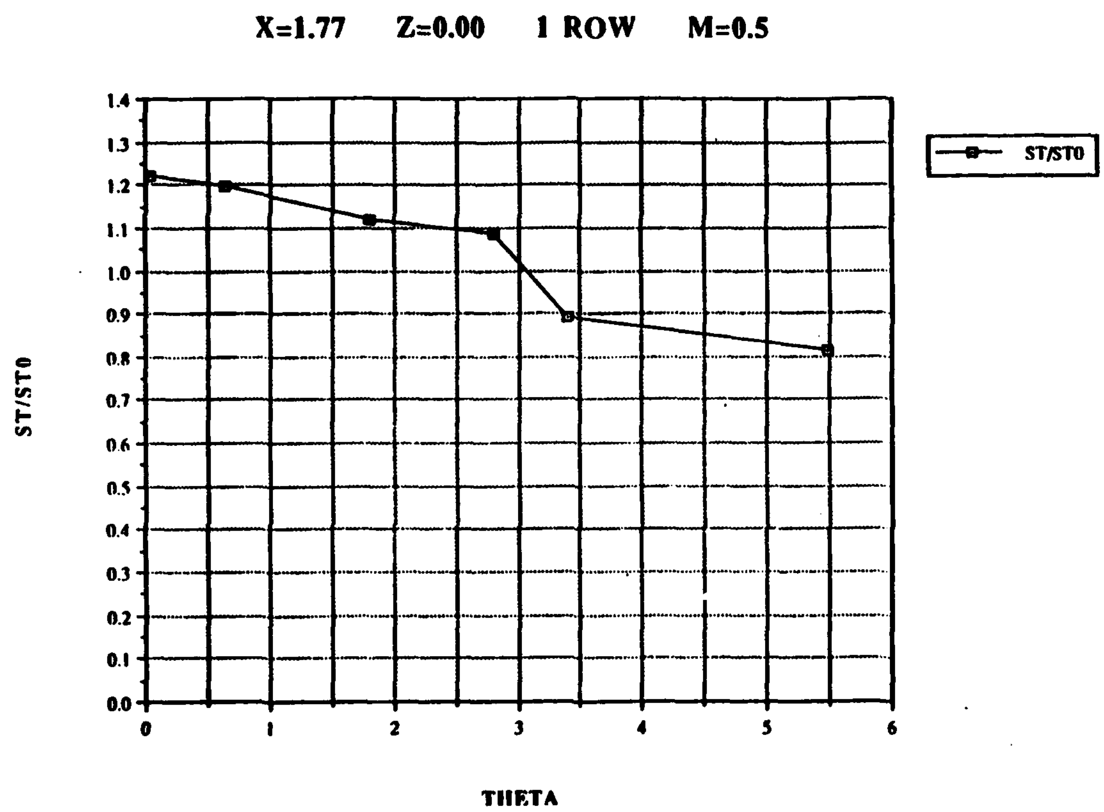

Figure 11. St/St$_0$ vs θ, Compound Angle, 1 row, m=0.5, X=1.77, Z=0.0 m

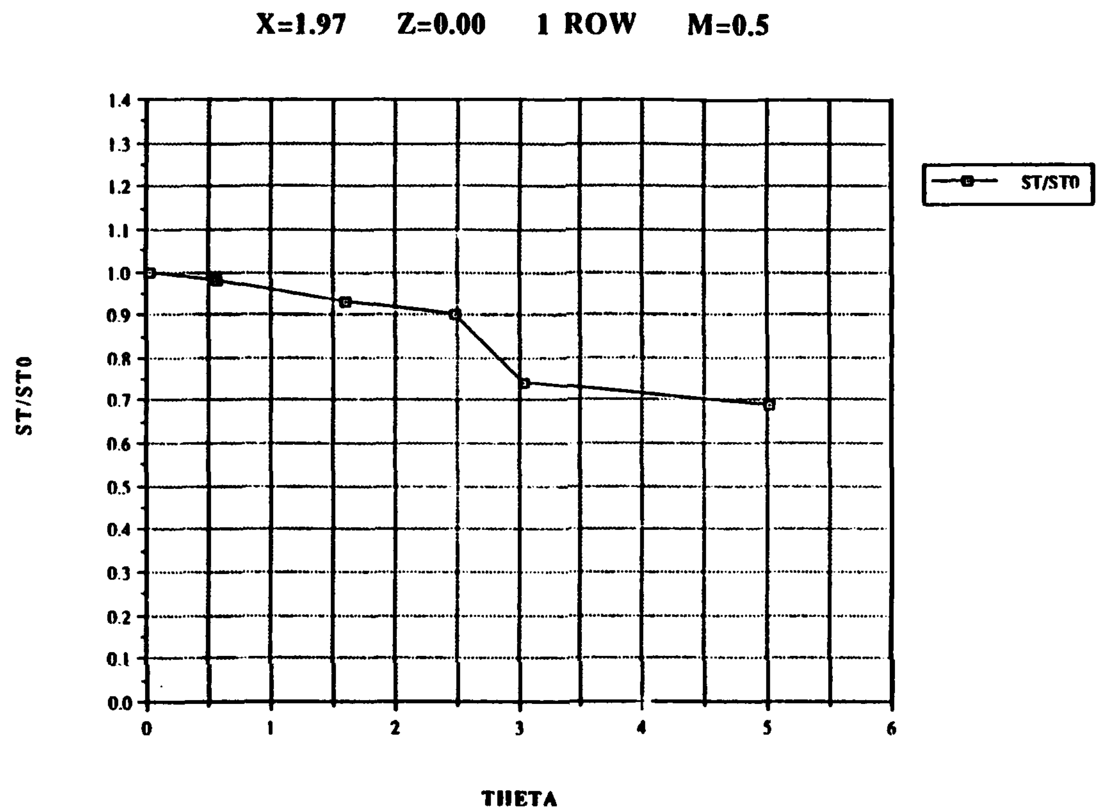

Figure 12. St/St_0 vs θ, Compound Angle, 1 row, m=0.5, X=1.97, Z=0.0 m

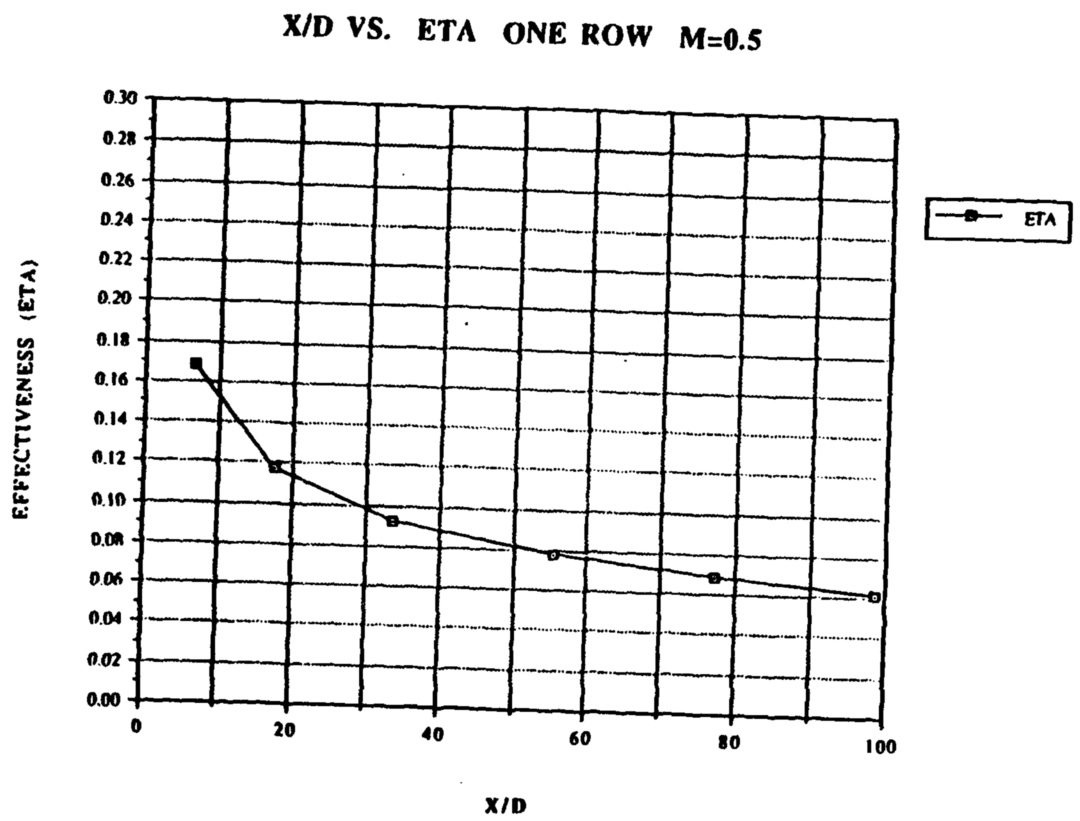

Figure 13. $\overline{\eta}$ vs x/d, Compound Angle, 1 row, m=0.5, Spanwise Averag

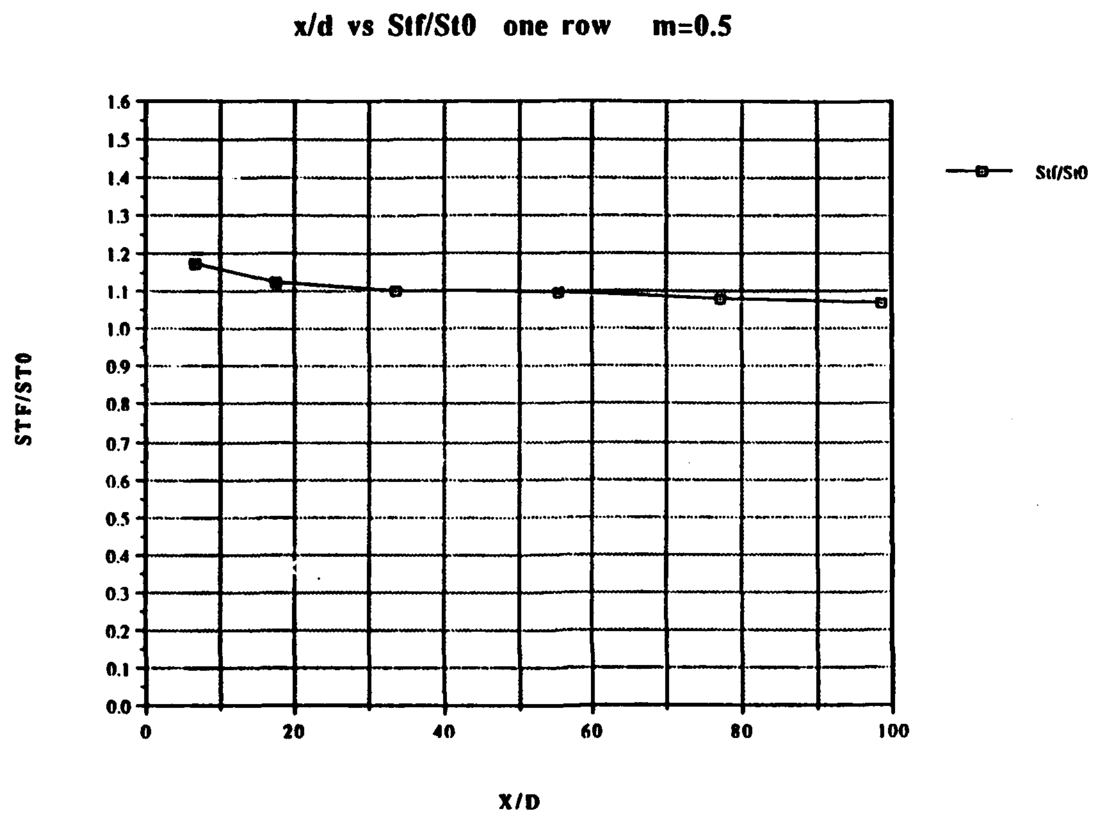

Figure 14. $\overline{St_f / St_o}$ vs x/d, Compound Angle, 1 row, m=0.5, Spanwise Average

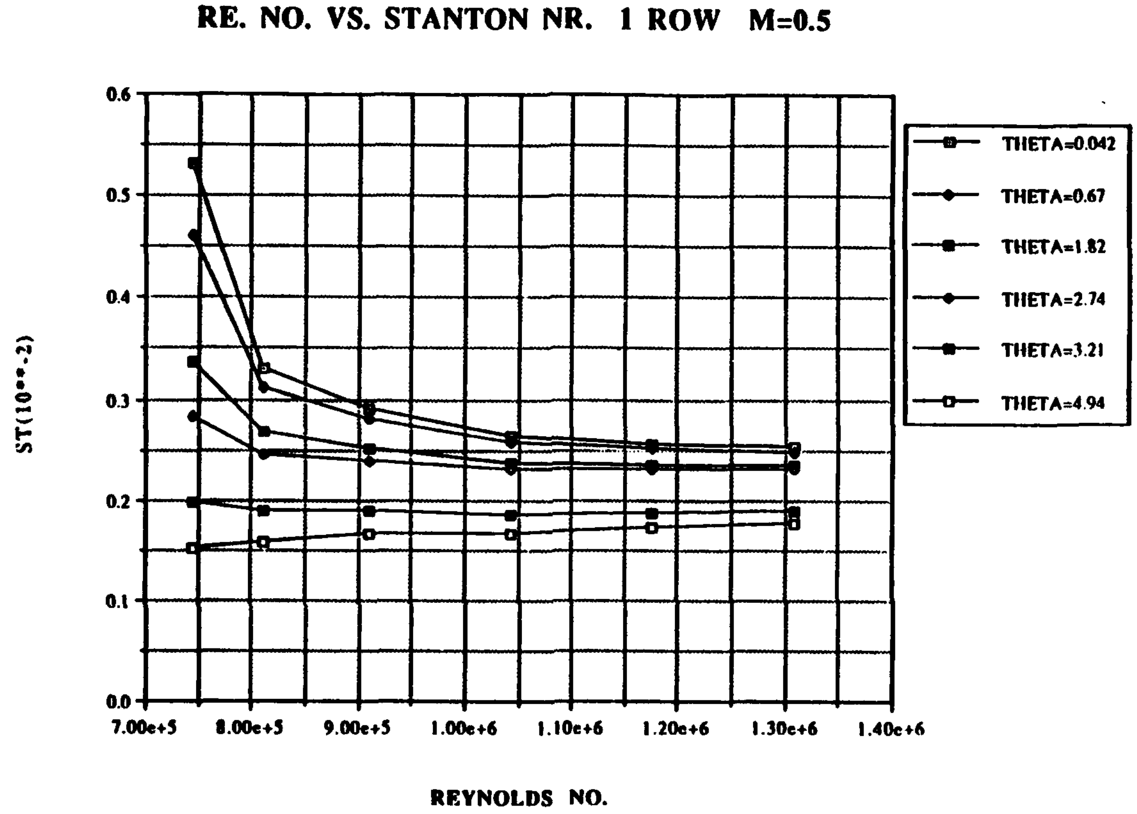

Figure 15. Spanwise averaged Stanton number vs Reynolds number, comparison of different θ values, 1 row, m=0.5

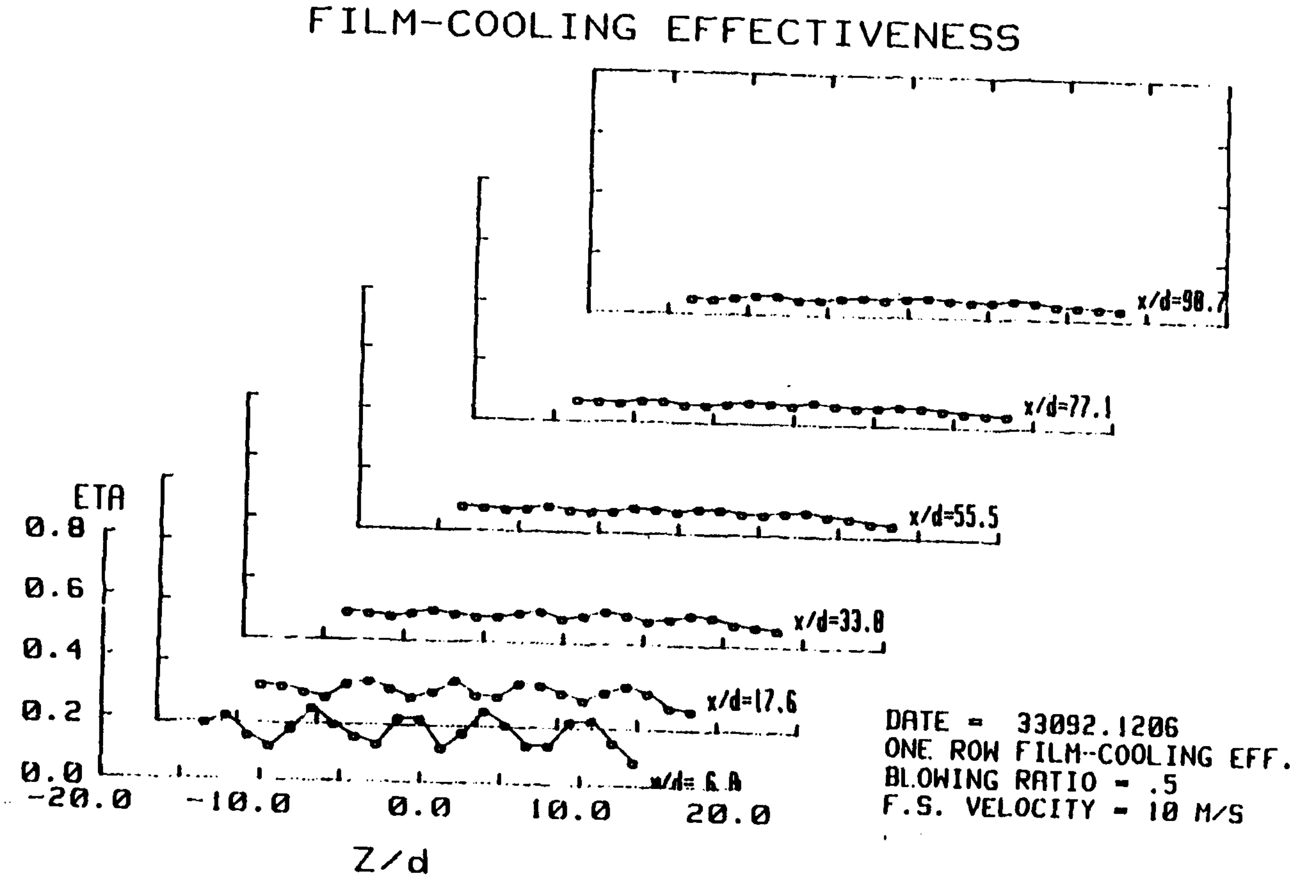

Figure 16. Spanwise Variation of η, Compound Angle, 1 row, m=0.5

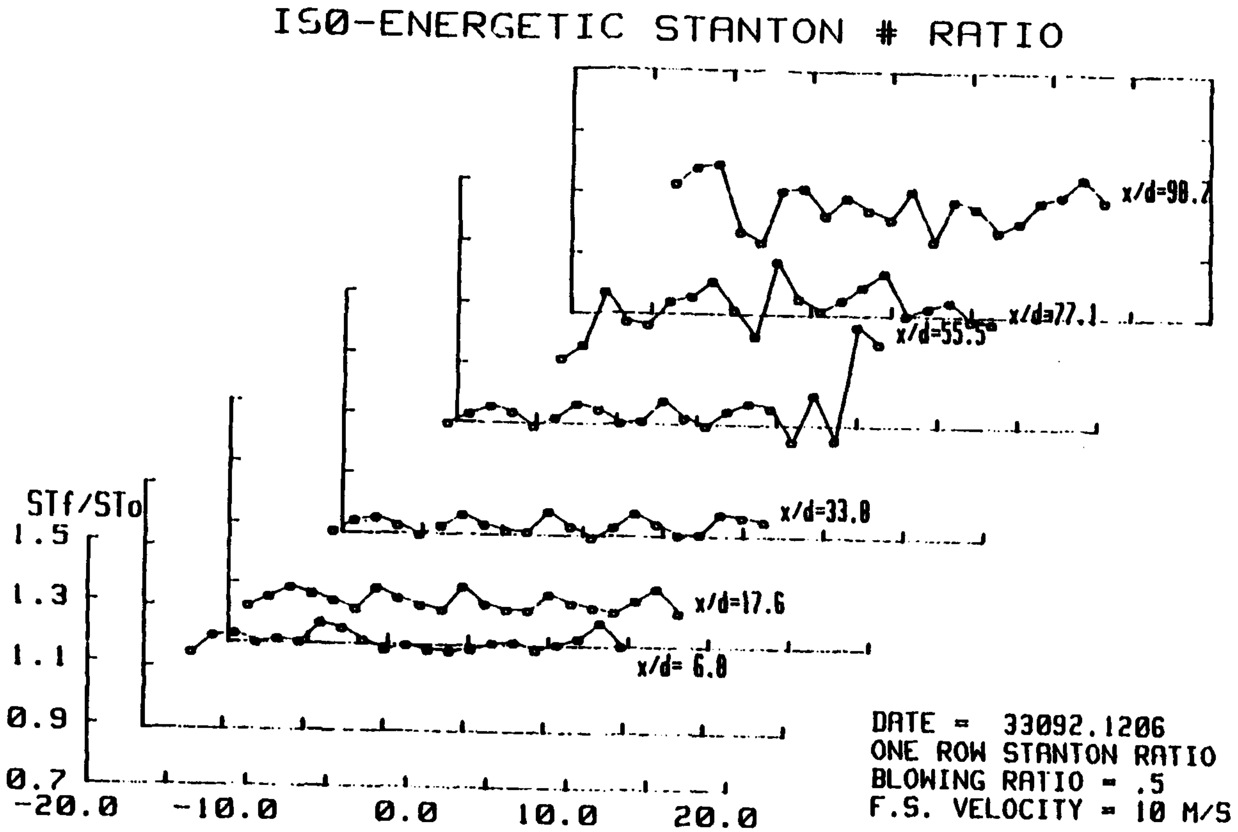

Figure 17. Spanwise Variation of St_f/St_o, Compound Angle, 1 row, m=0.5

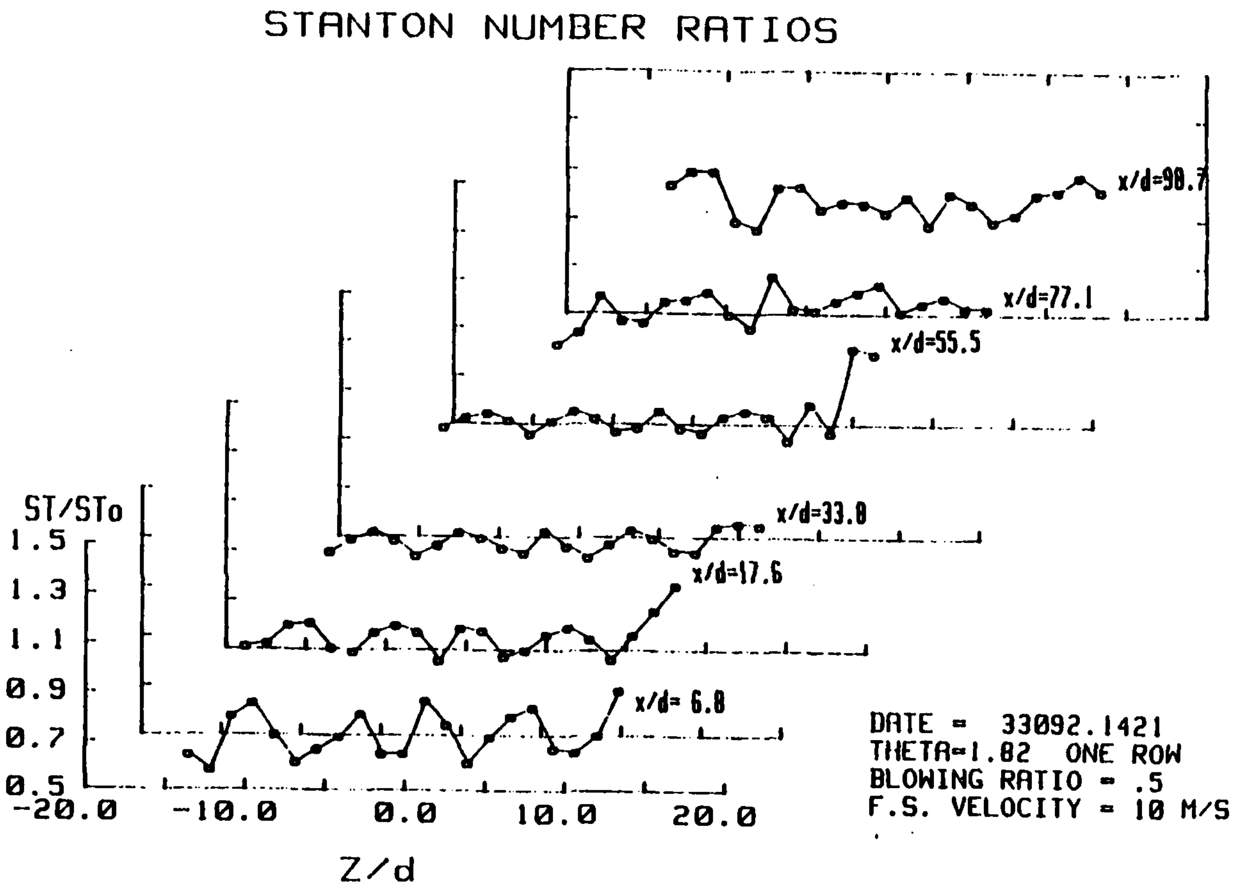

Figure 18. Spanwise Variation of St/St_0, Compound Angle, 1 row, $m=0.5$, $\theta=1.82$

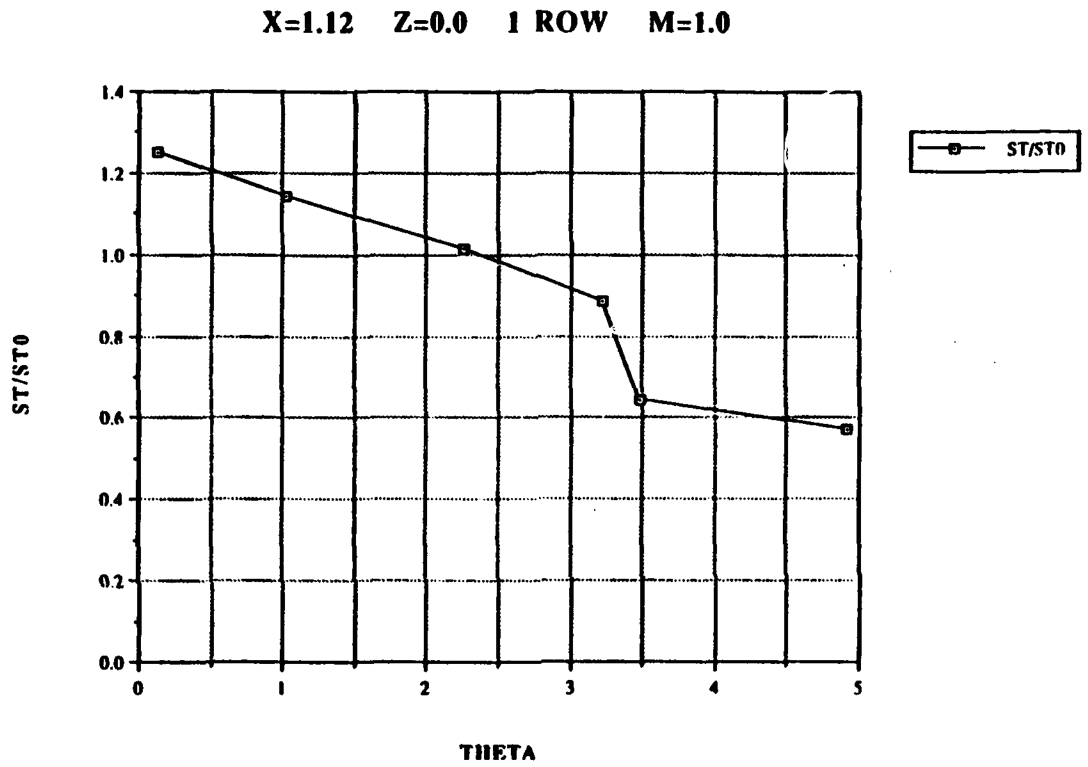

Figure 19. St/St_0 vs θ, Compound Angle, 1 row, m=1.0, X=1.12, Z=0.0 m

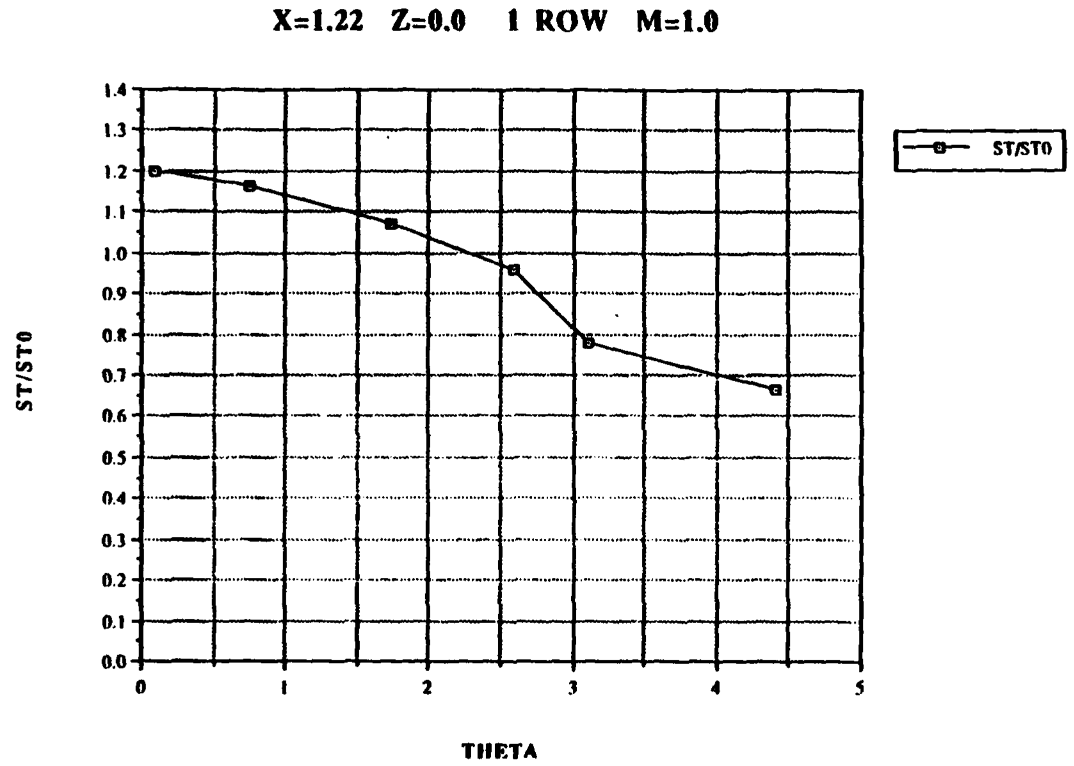

Figure 20. St/Sto vs θ, Compound Angle, 1 row, m=1.0, X=1.22, Z=0.0 m

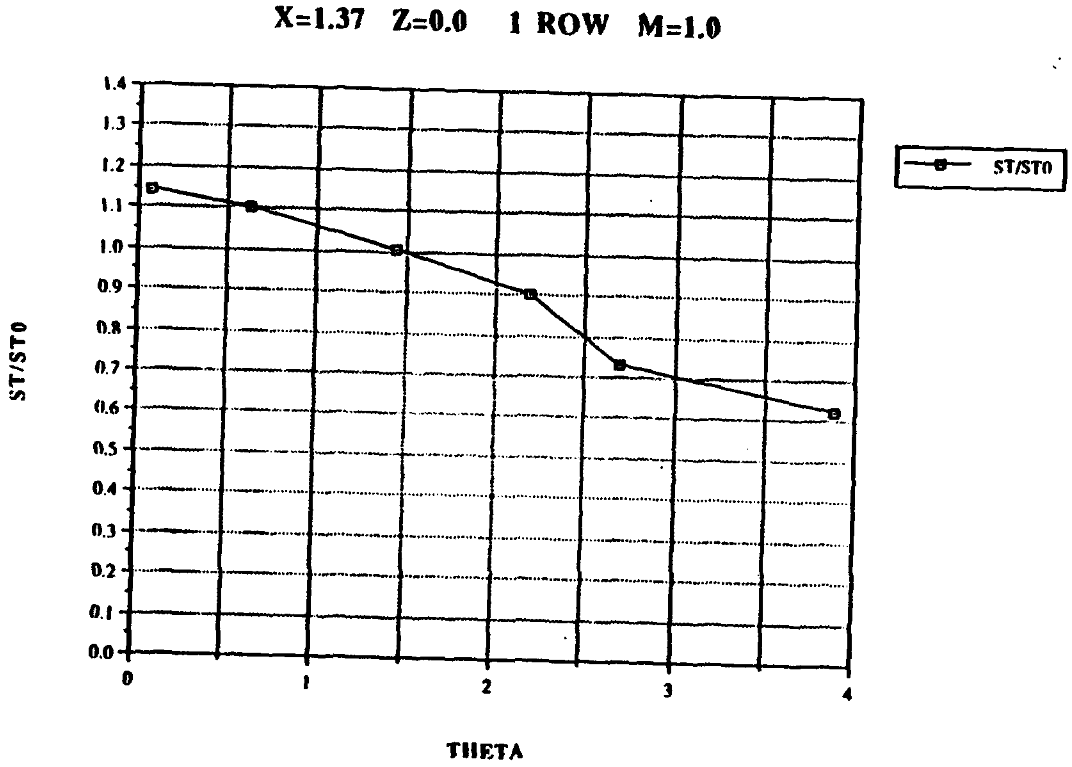

Figure 21. St/St_0 vs θ, Compound Angle, 1 row, m=1.0, X=1.37, Z=0.0 m

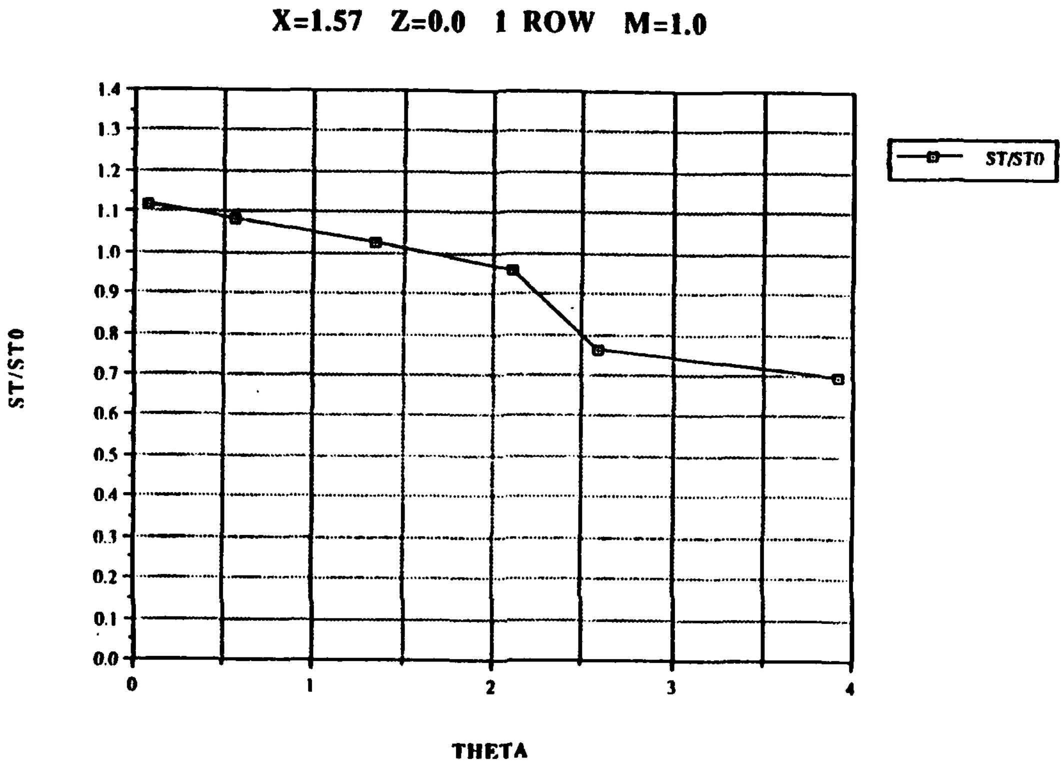

Figure 22. St/St_0 vs θ, Compound Angle, 1 row, m=1.0, X=1.57, Z=0.0 m

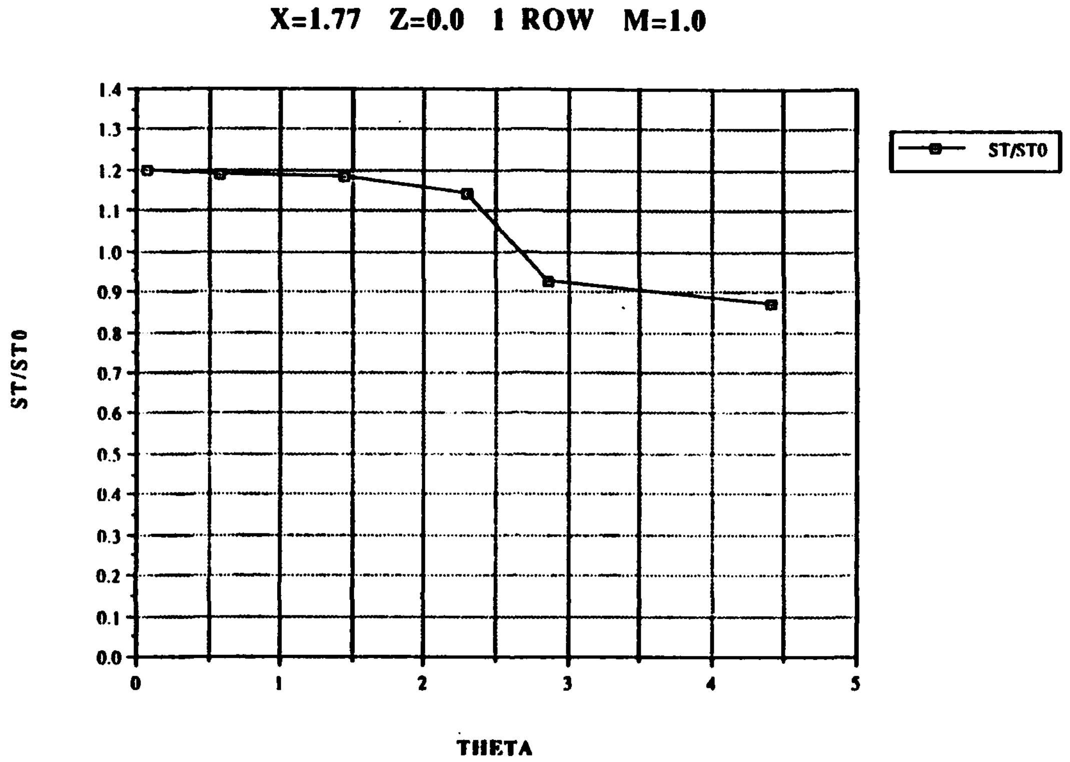

Figure 23. St/St$_0$ vs θ, Compound Angle, 1 row, m=1.0, X=1.77, Z=0.0 m

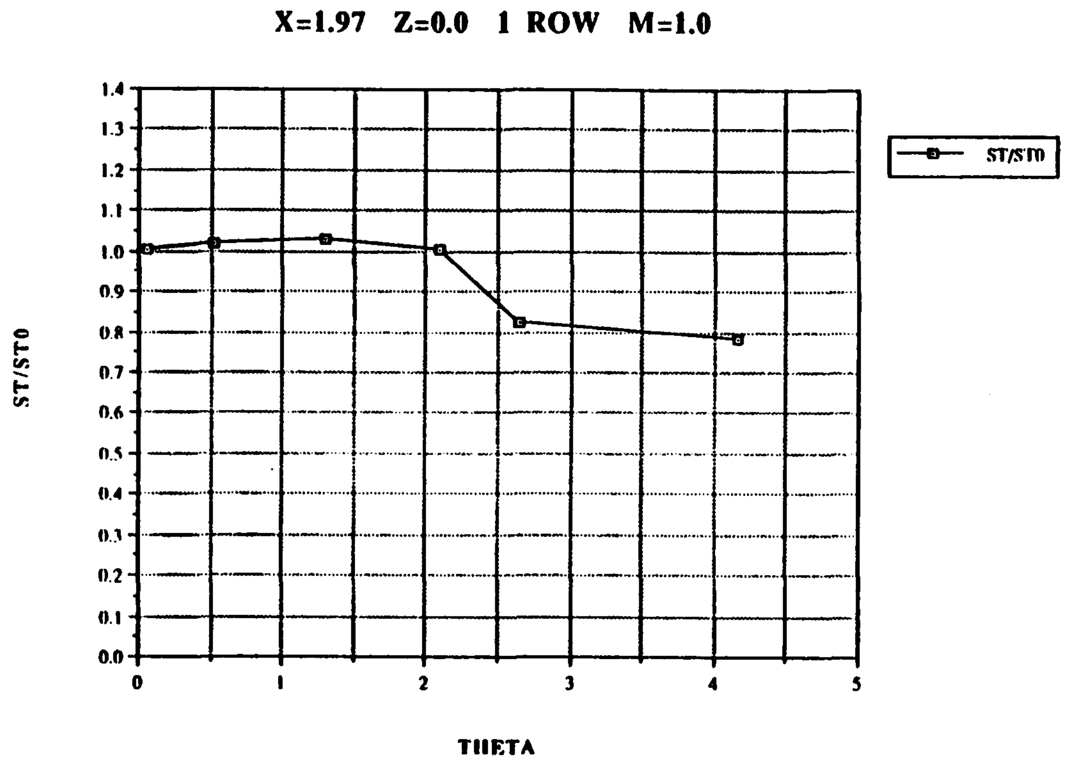

Figure 24. St/St_o vs θ, Compound Angle, 1 row, m=1.0, X=1.97, Z=0.0 m

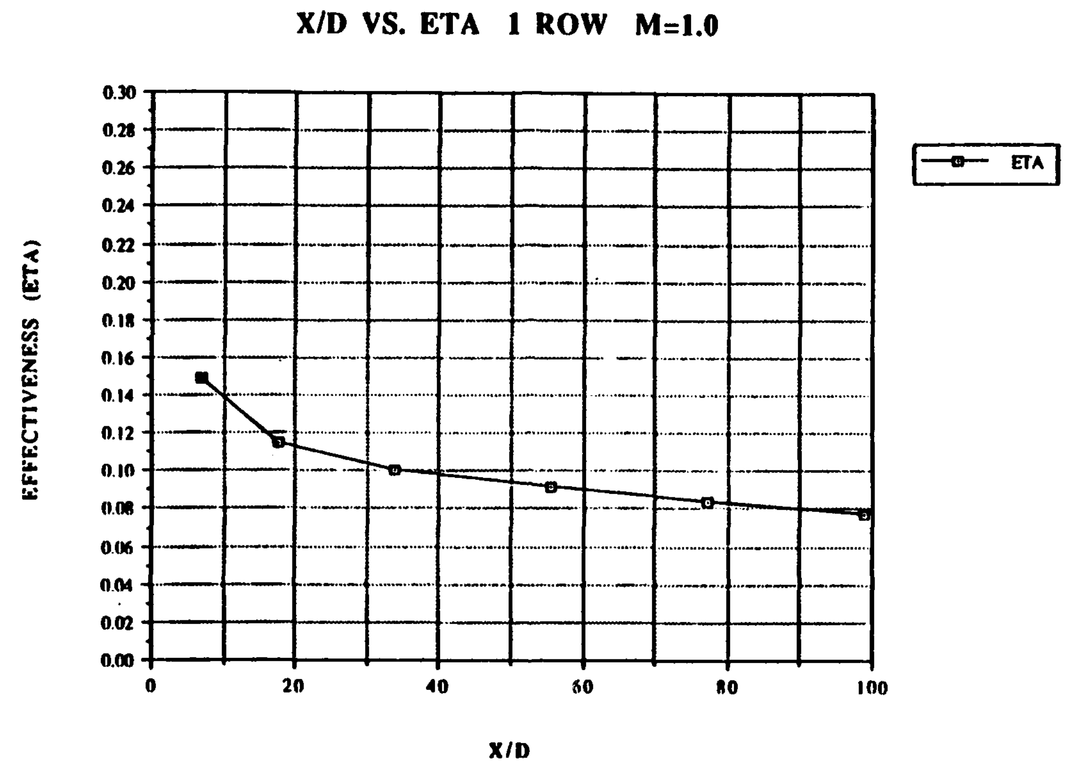

Figure 25. $\overline{\eta}$ vs x/d, Compound Angle, 1 row, m=1.0, Spanwise Average

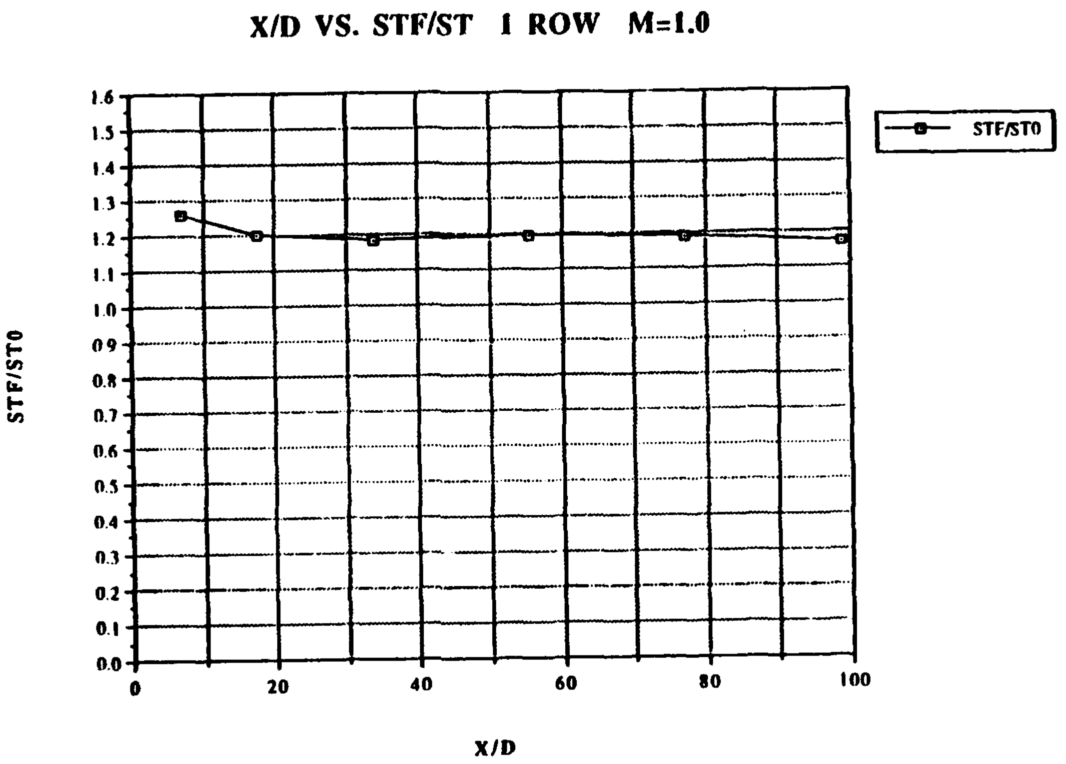

Figure 26. $\overline{St_f / St_o}$ vs x/d, Compound Angle, 1 row, m=1.0, Spanwise Average

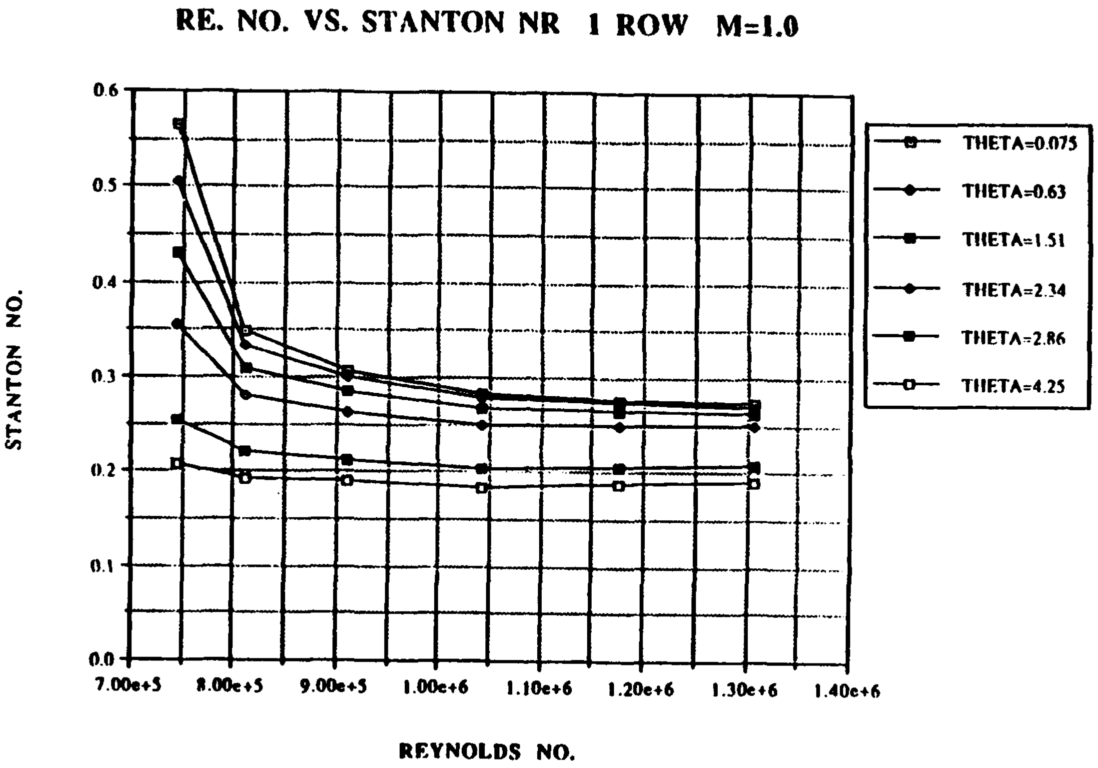

Figure 27. Spanwise averaged Stanton number vs Reynolds number, comparison of different θ values, 1 row, m=1.0

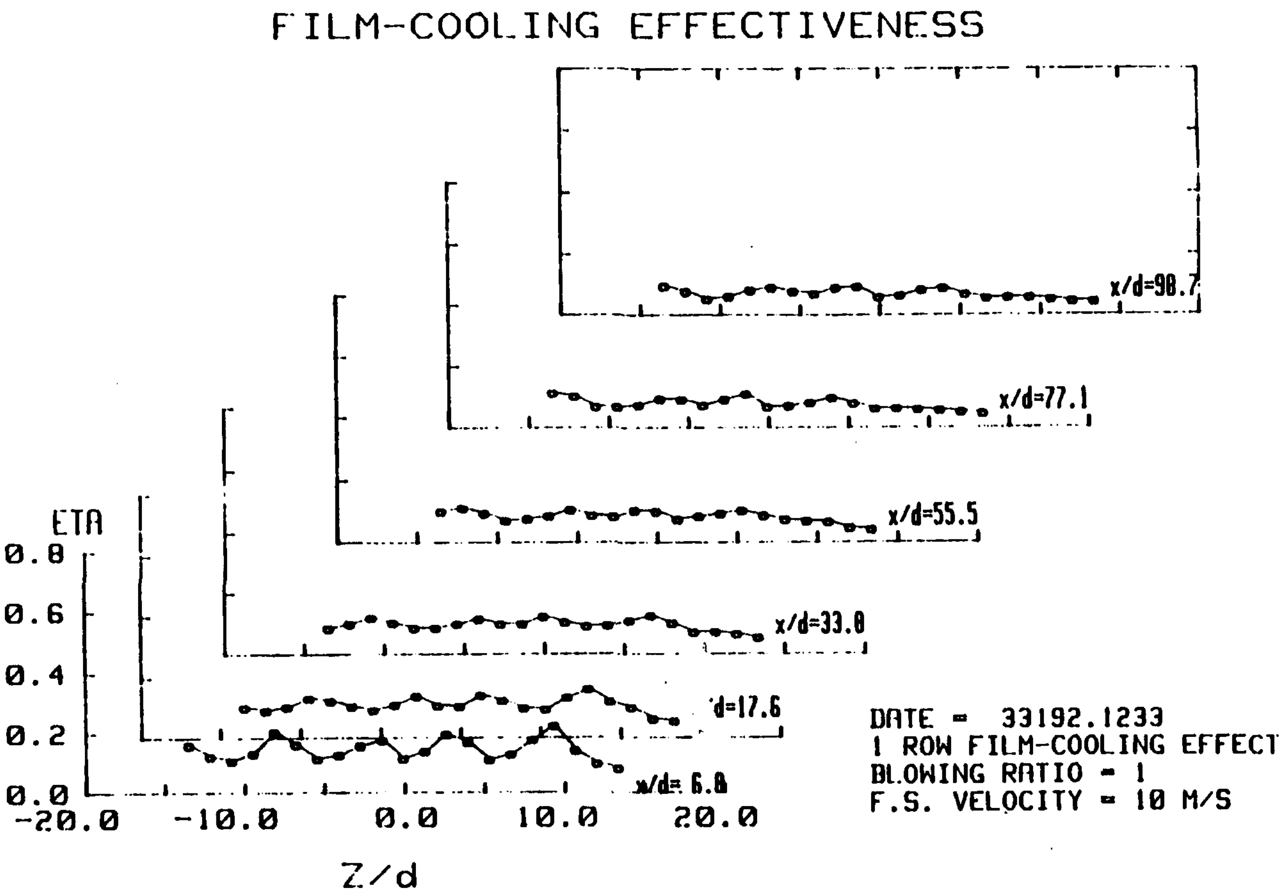

Figure 28. Spanwise Variation of η, Compound Angle, 1 row, m=1.0

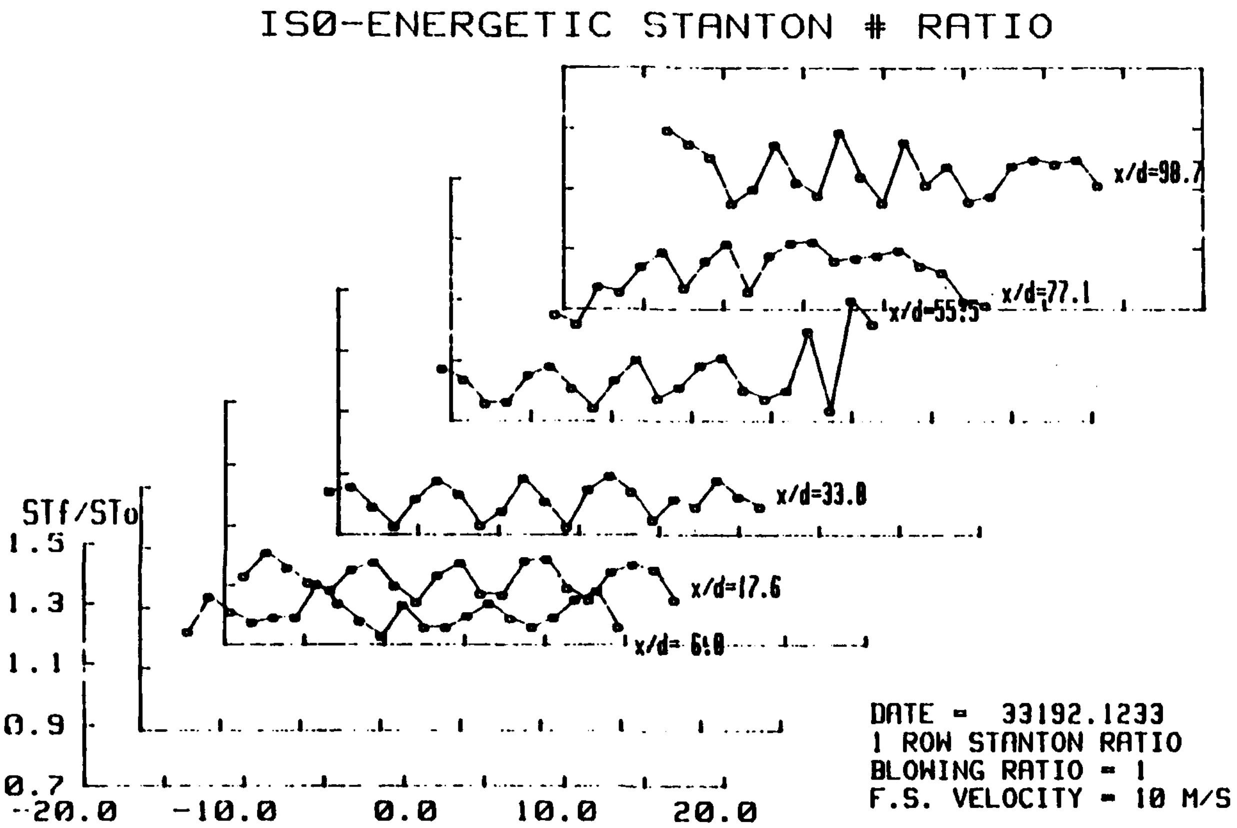

Figure 29. Spanwise Variation of St_f/St_o, Compound Angle, 1 row, m=1.0

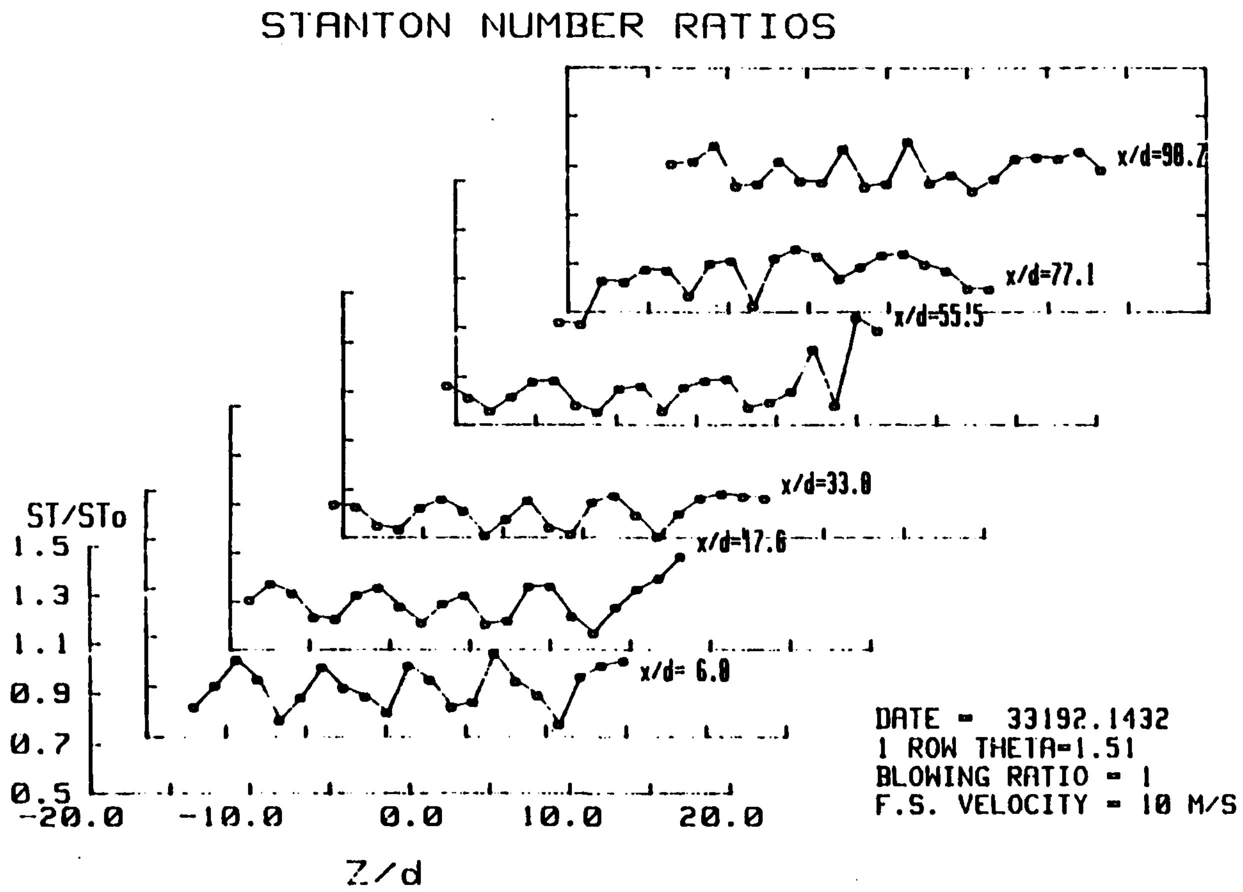

Figure 30. Spanwise Variation of St/St_o, Compound Angle, 1 row, $m=1.0$, $\theta=1.51$

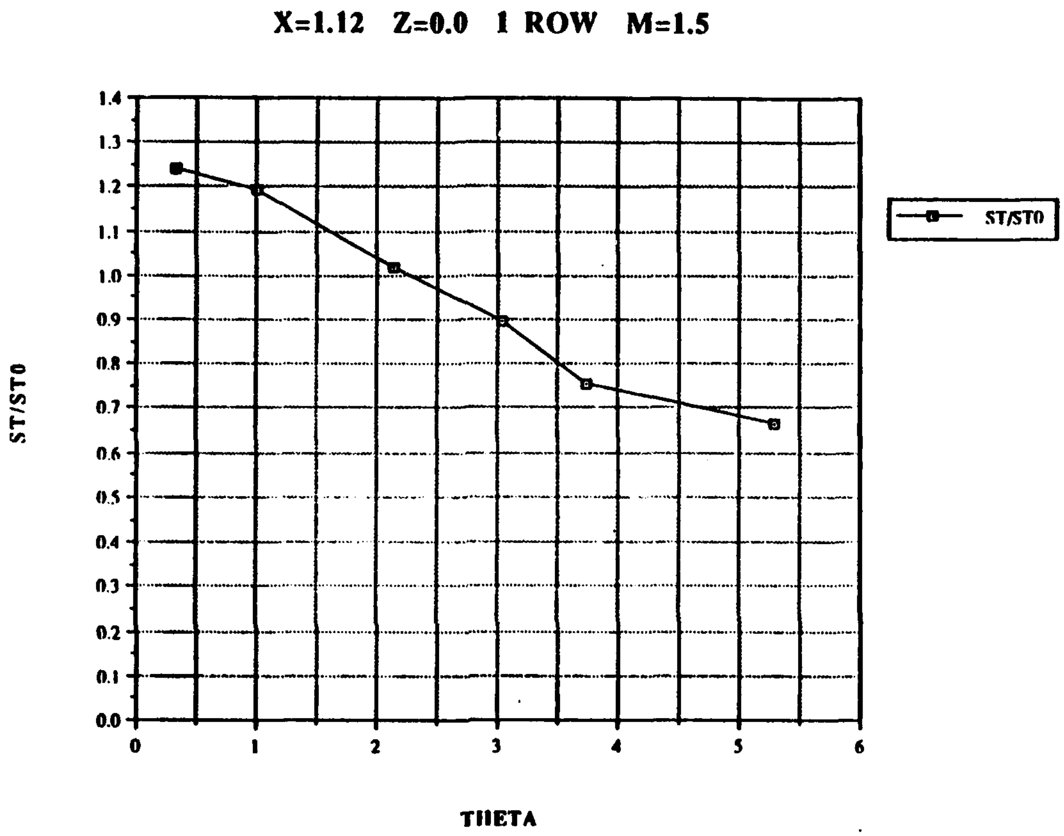

Figure 31. St/St_0 vs θ, Compound Angle, 1 row, m=1.5, X=1.12, Z=0.0 m

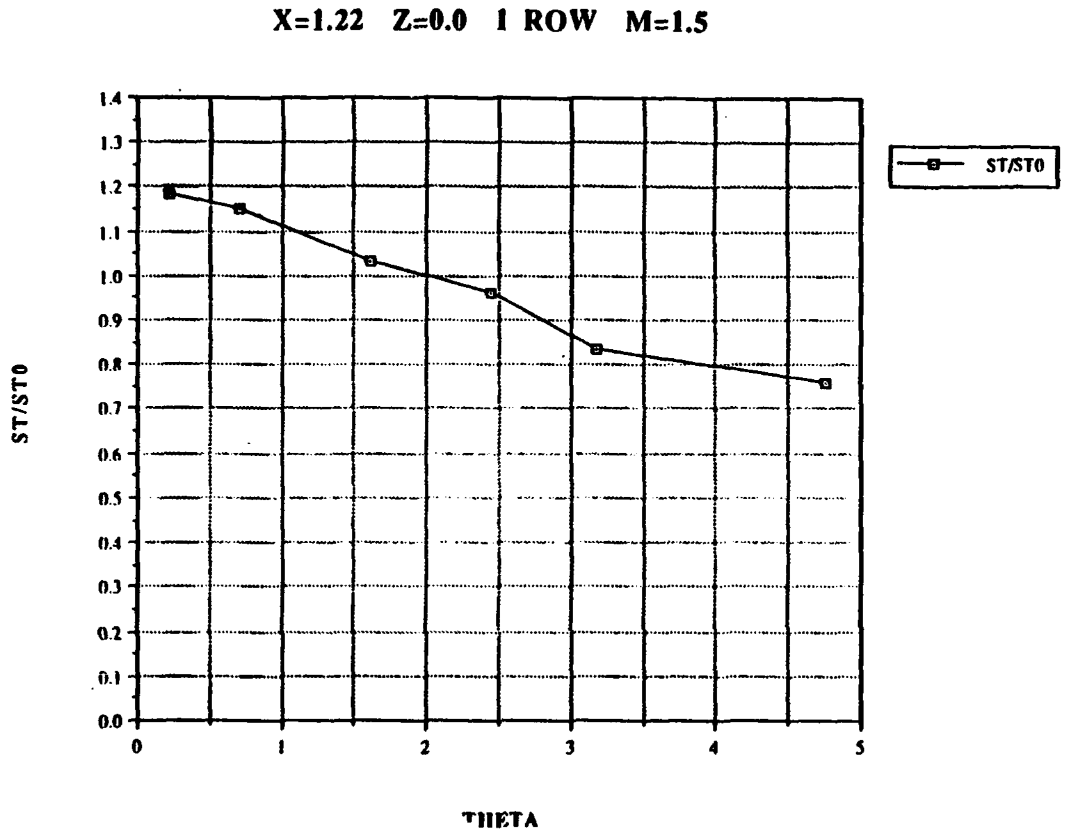

Figure 32. St/St$_0$ vs θ, Compound Angle, 1 row, m=1.5, X=1.22, Z=0.0 m

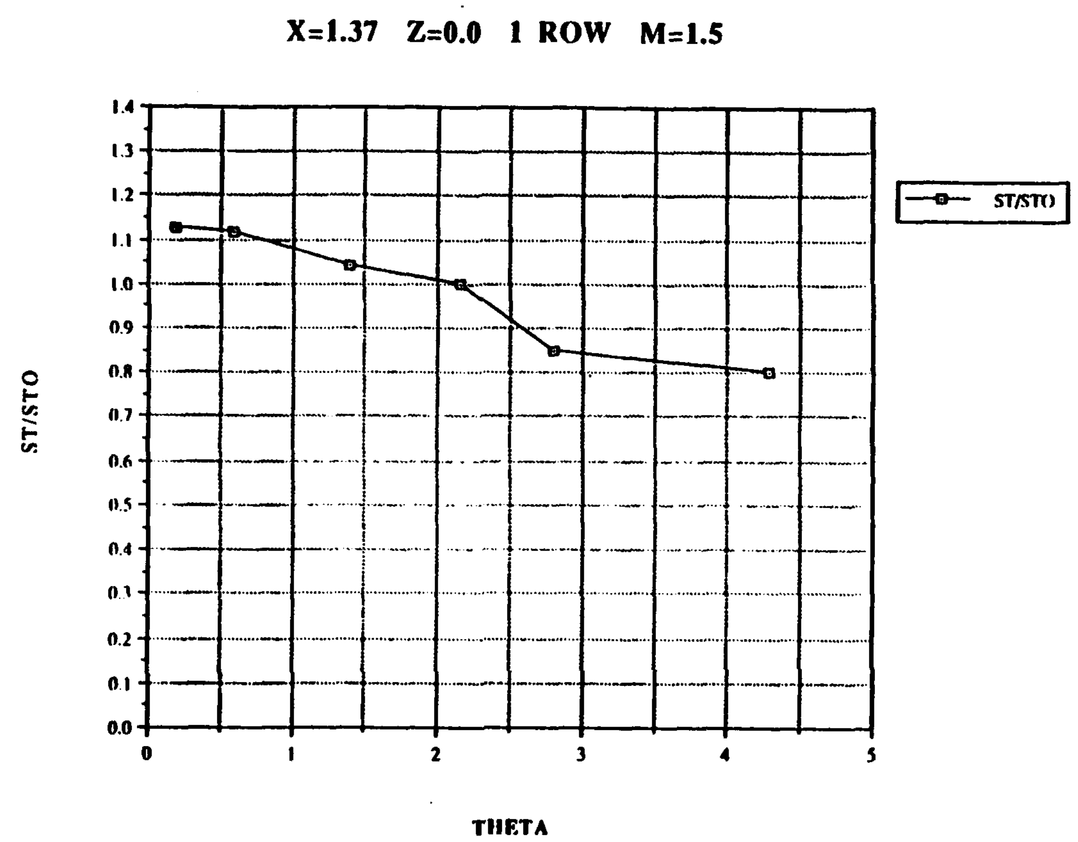

Figure 33. St/St$_0$ vs θ, Compound Angle, 1 row, m=1.5, X=1.37, Z=0.0 m

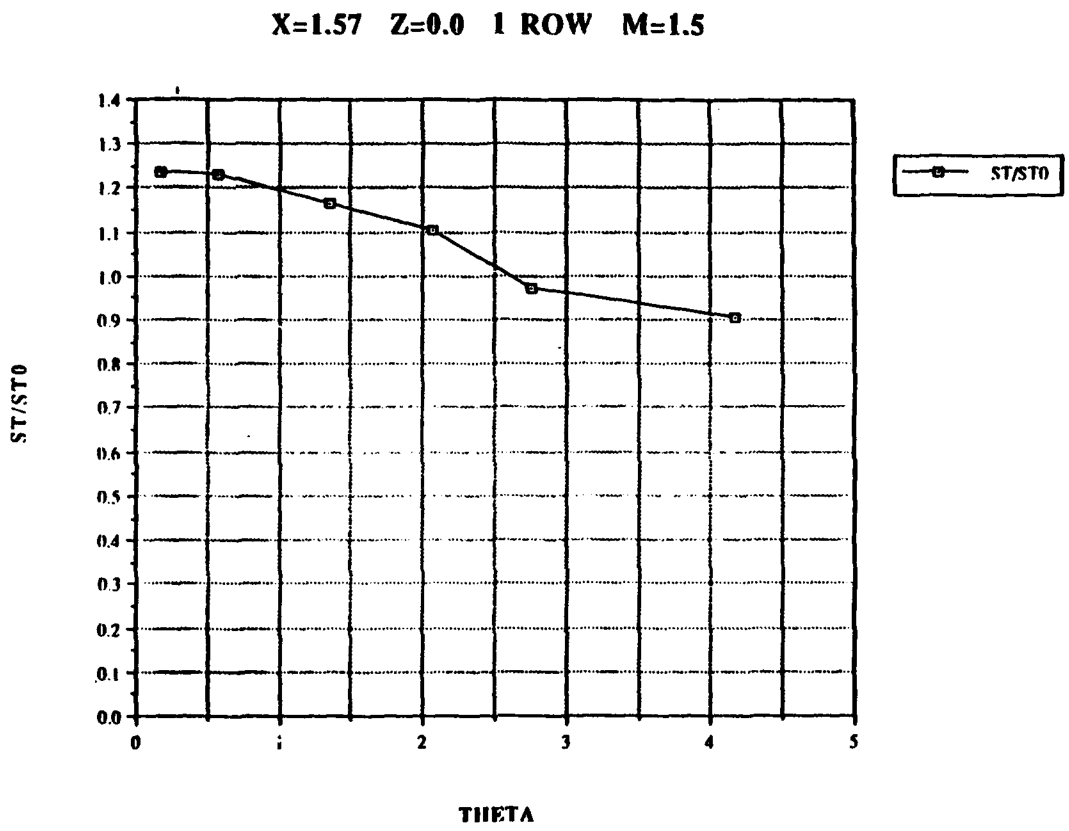

Figure 34. St/Sto vs θ, Compound Angle, 1 row, m=1.5, X=1.57, Z=0.0 m

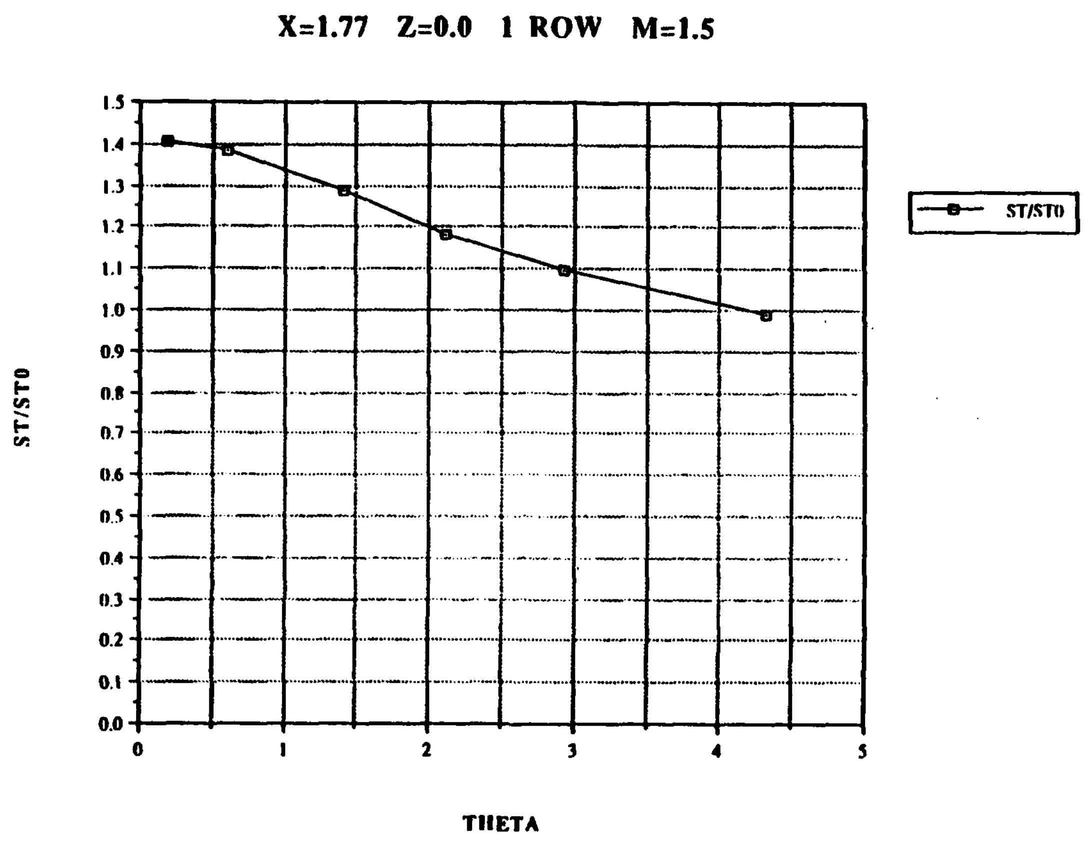

Figure 35. St/St_0 vs θ, Compound Angle, 1 row, m=1.5, X=1.77, Z=0.0 m

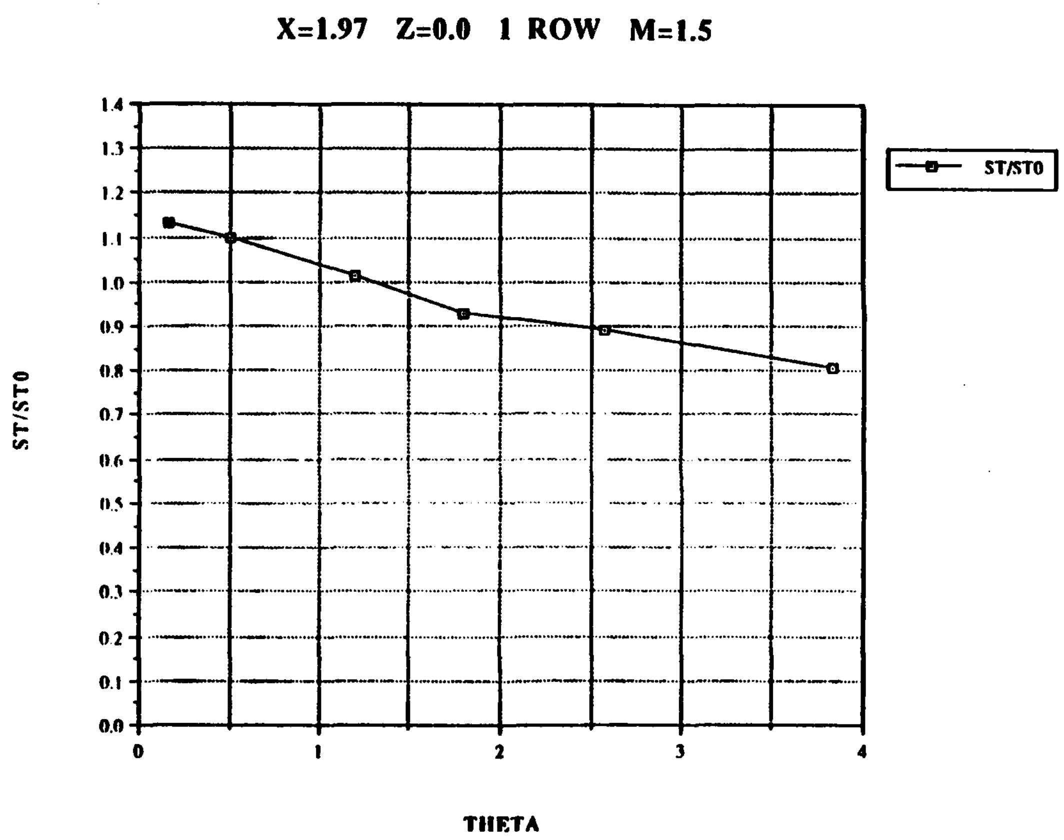

Figure 36. St/St_0 vs θ, Compound Angle, 1 row, m=1.5,X=1.97, Z=0.0 m

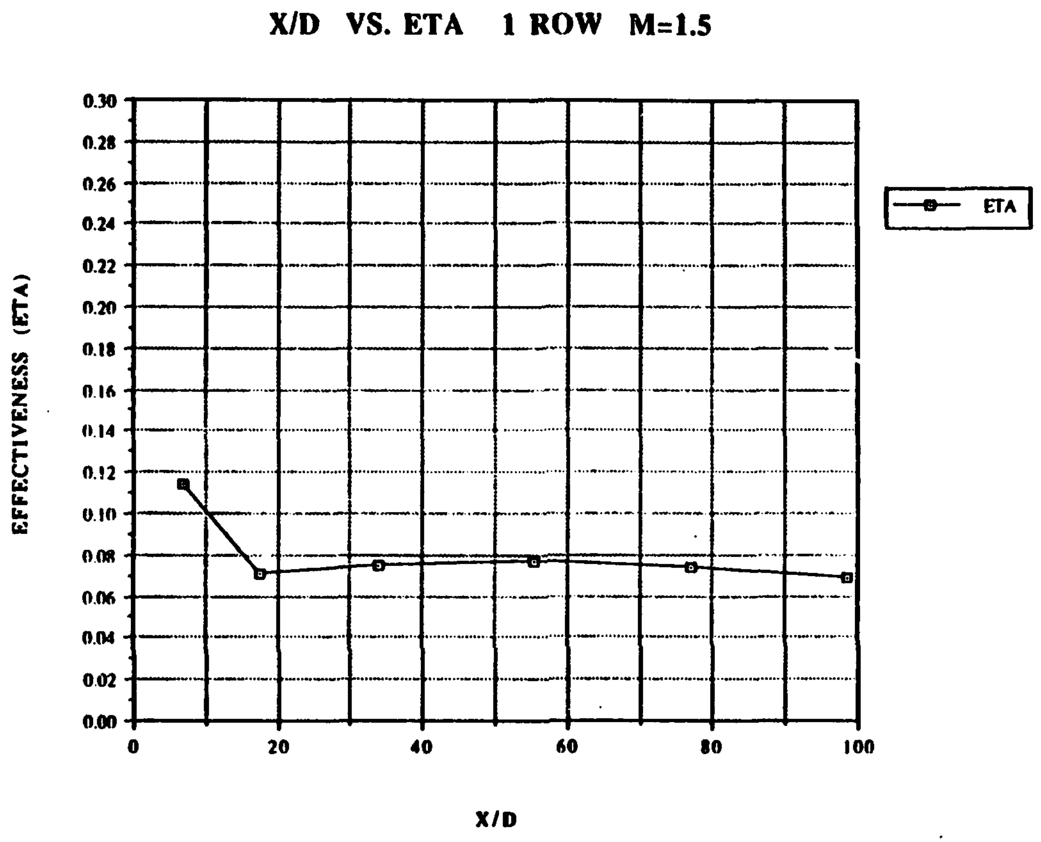

Figure 37. $\bar{\eta}$ vs x/d, Compound Angle, 1 row, m=1.5, Spanwise Average

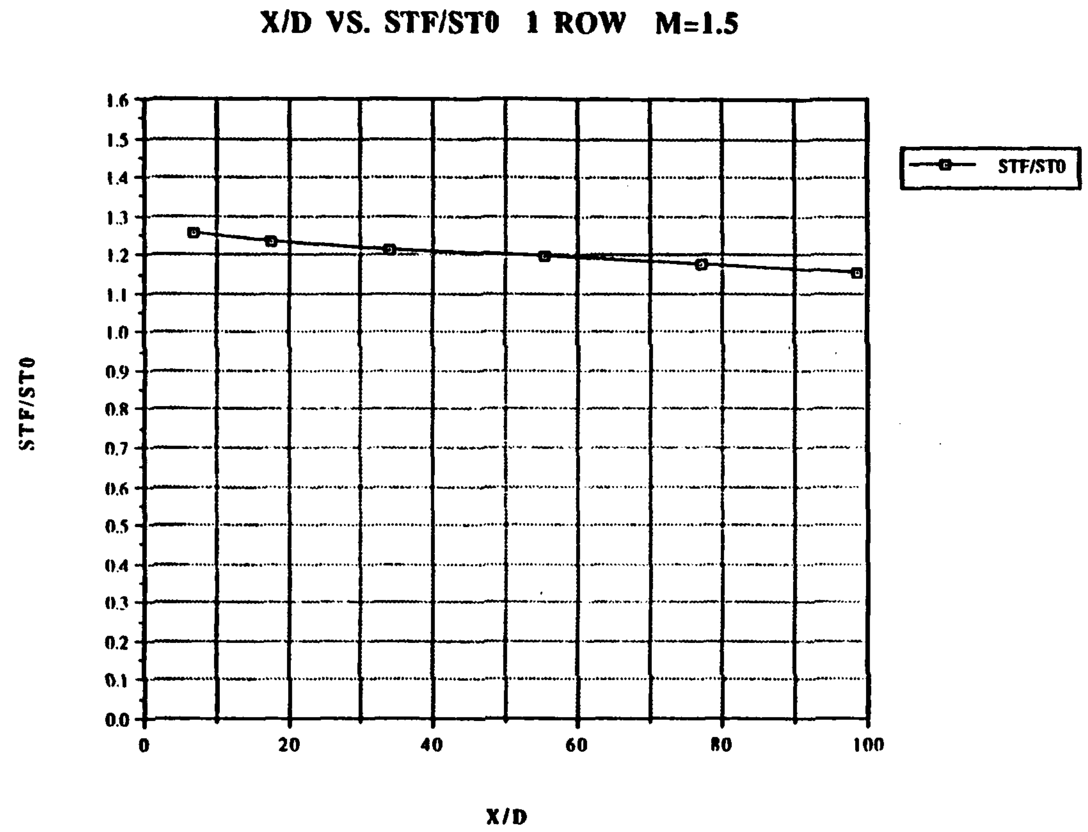

Figure 38. $\overline{St_f / St_o}$ vs x/d, Compound Angle, 1 row, m=1.5, Spanwise Average

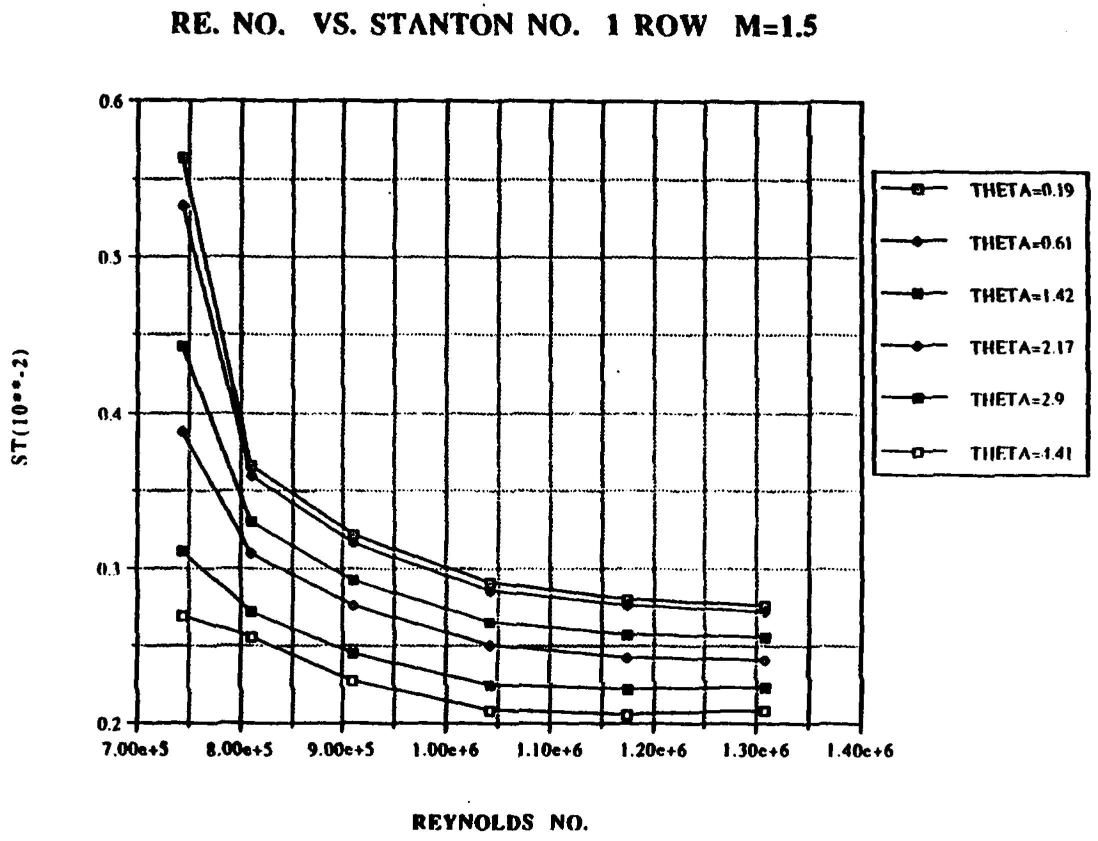

Figure 39. Spanwise averaged Stanton number vs Reynolds number, comparison of different θ values, 1 row, m=1.5

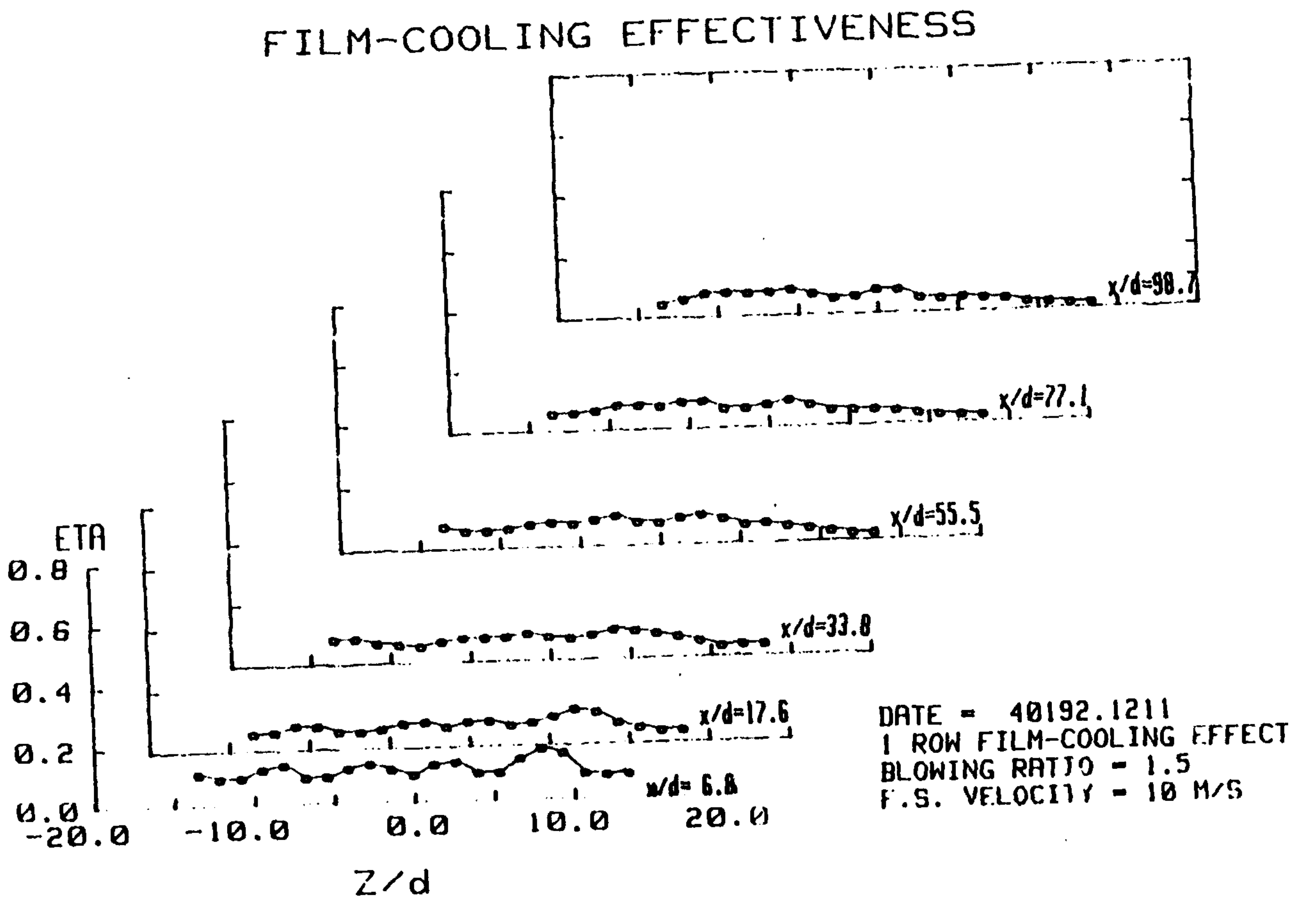

Figure 40. Spanwise Variation of η, Compound Angle, 1 row, m=1.5

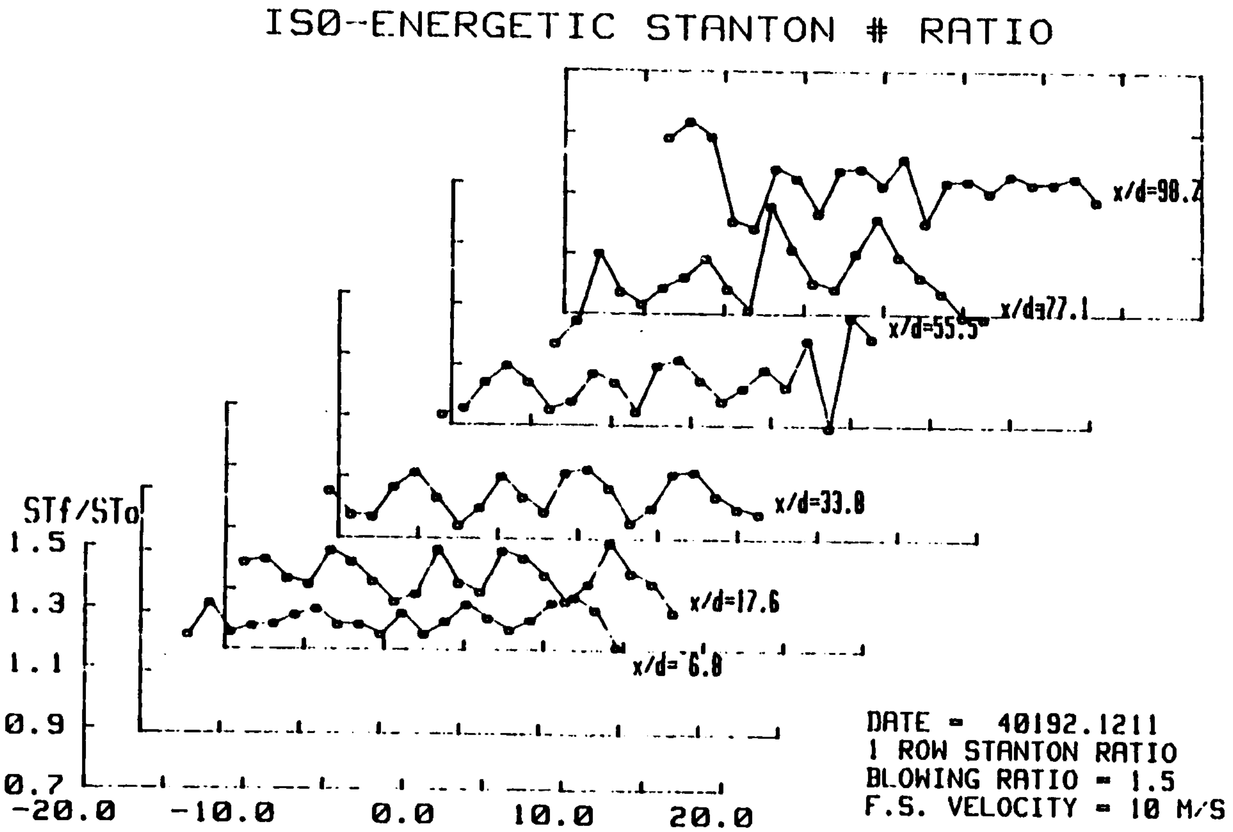

Figure 41. Spanwise Variation of St_f/St_0, Compound Angle, 1 row, m=1.5

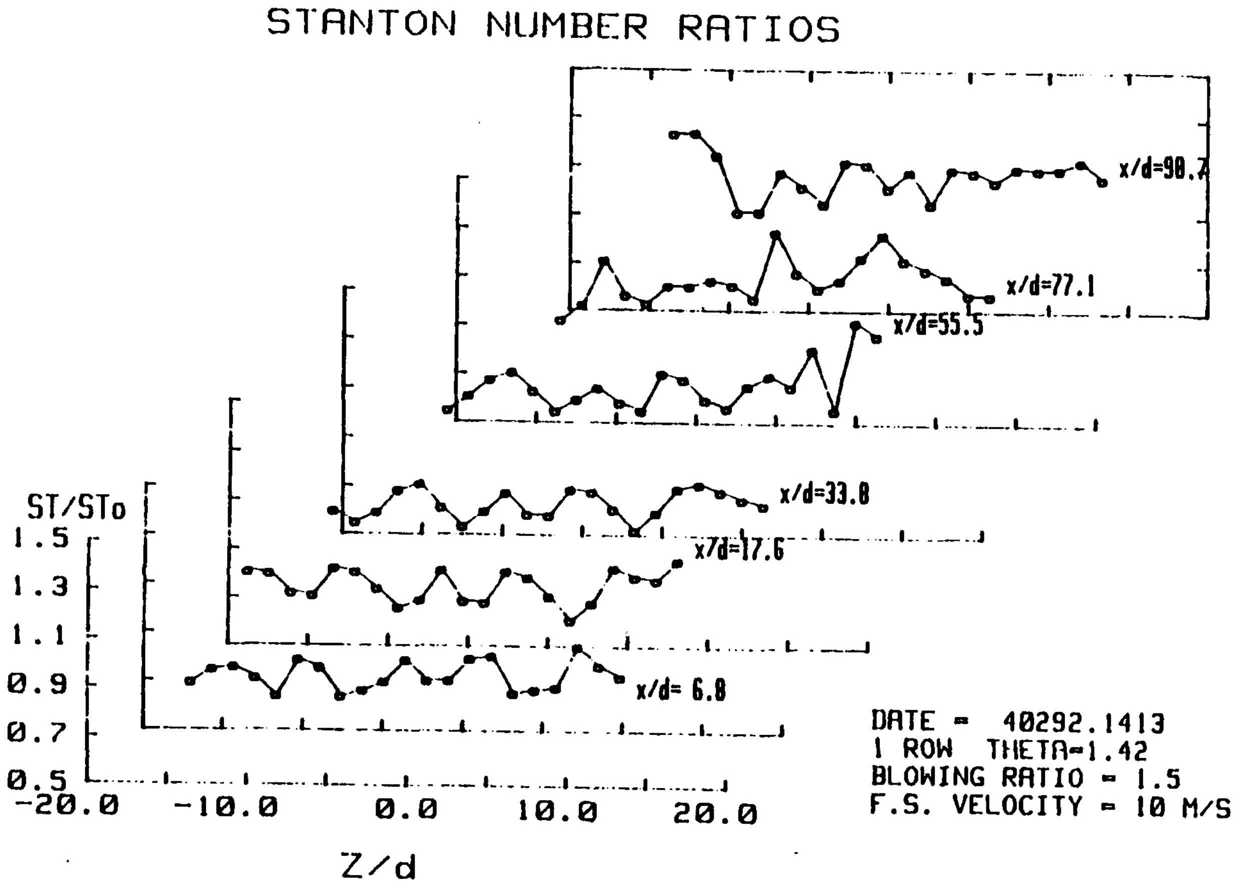

Figure 42. Spanwise Variation of St/St_0, Compound Angle, 1 row, $m=1.5$, $\theta=1.42$

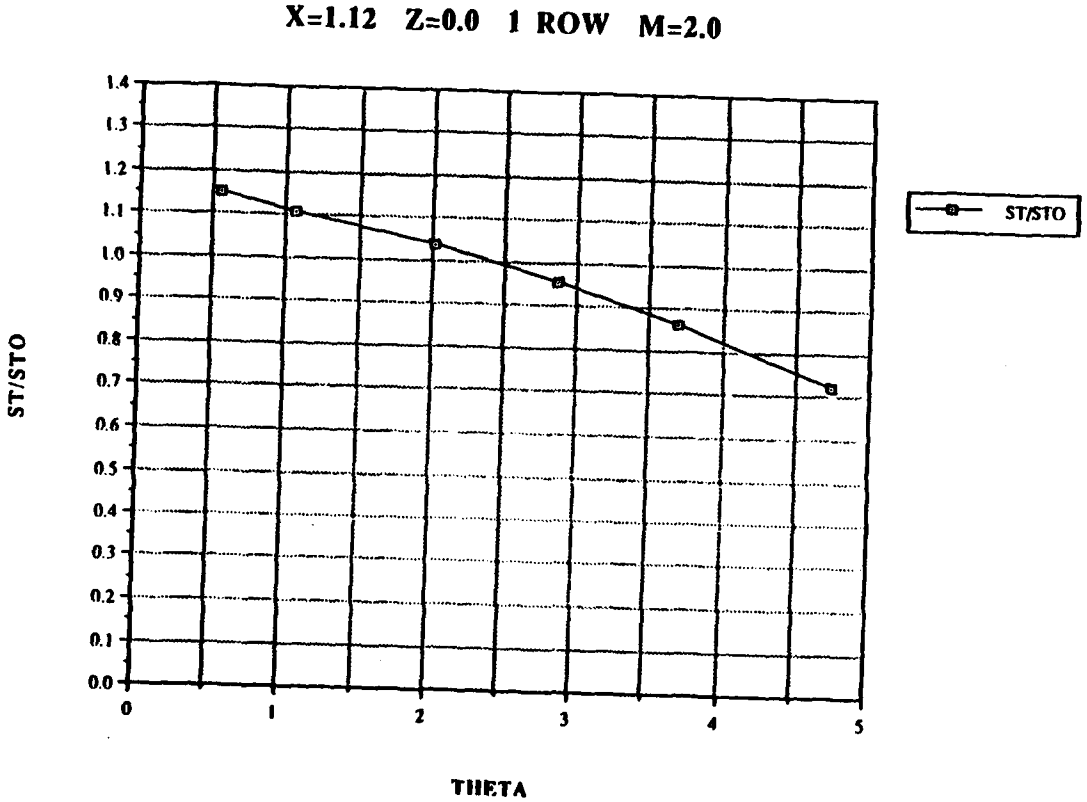

Figure 43. St/Sto vs θ, Compound Angle, 1 row, m=2.0, X=1.12,Z=0.0 m

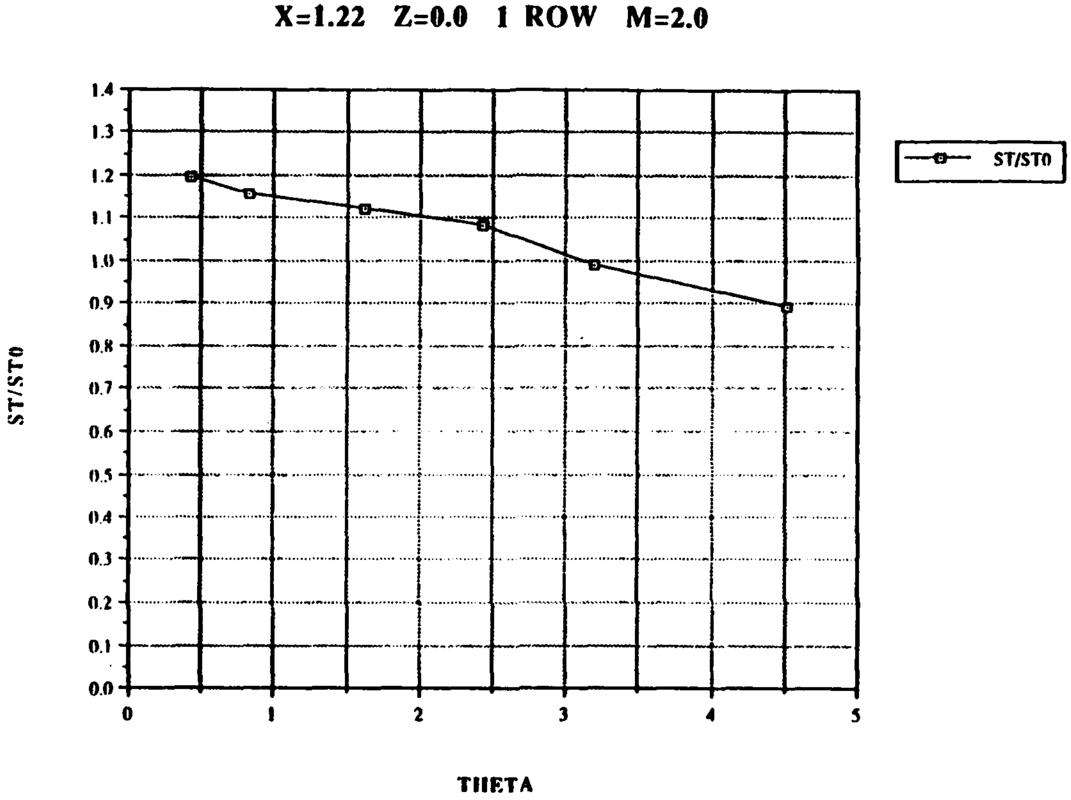
X=1.22 Z=0.0 1 ROW M=2.0

Figure 44. St/St_0 vs θ, Compound Angle, 1 row, m=2.0, X=1.22,Z=0.0 m

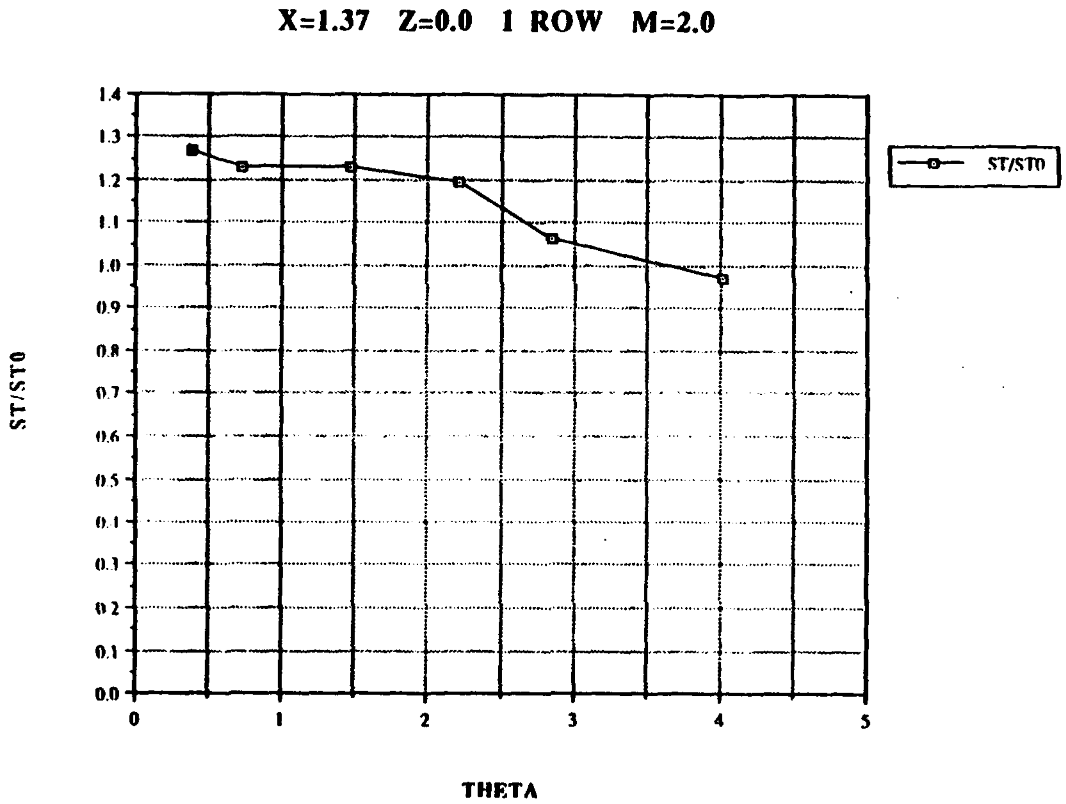
X=1.37 Z=0.0 1 ROW M=2.0

Figure 45. St/St_0 vs θ, Compound Angle, 1 row, m=2.0, X=1.37,Z=0.0 m

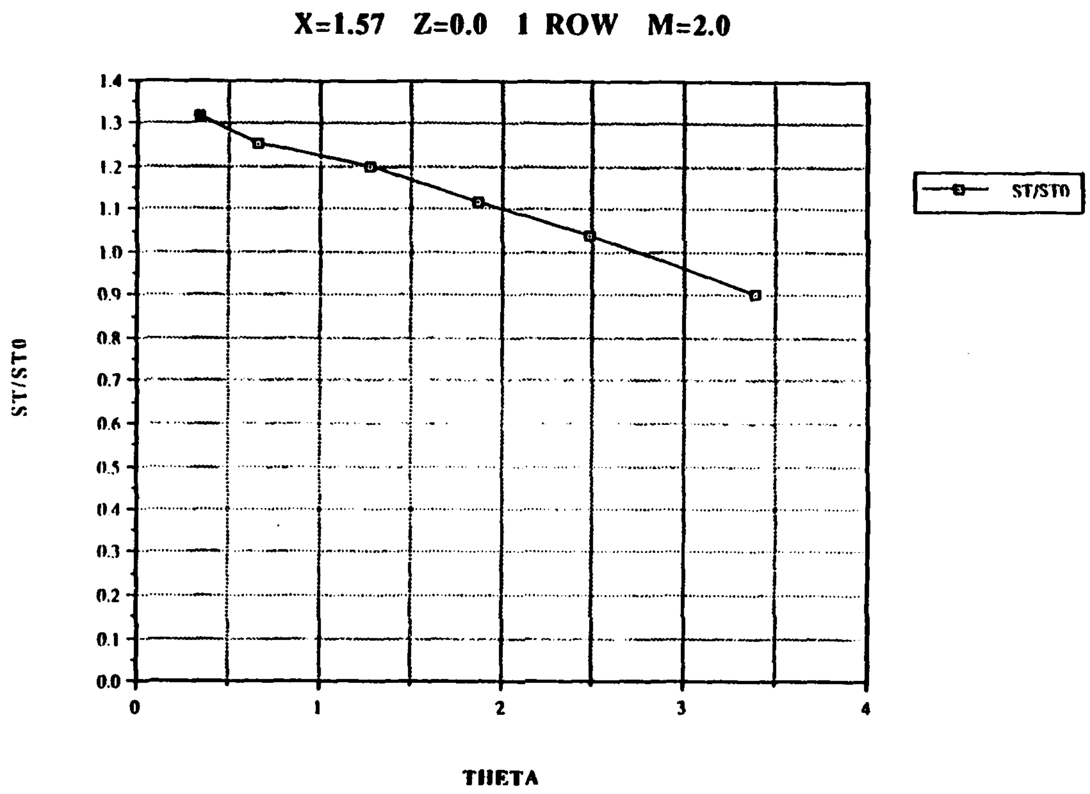

Figure 46. St/St$_0$ vs θ, Compound Angle, 1 row, m=2.0, X=1.57,Z=0.0 m

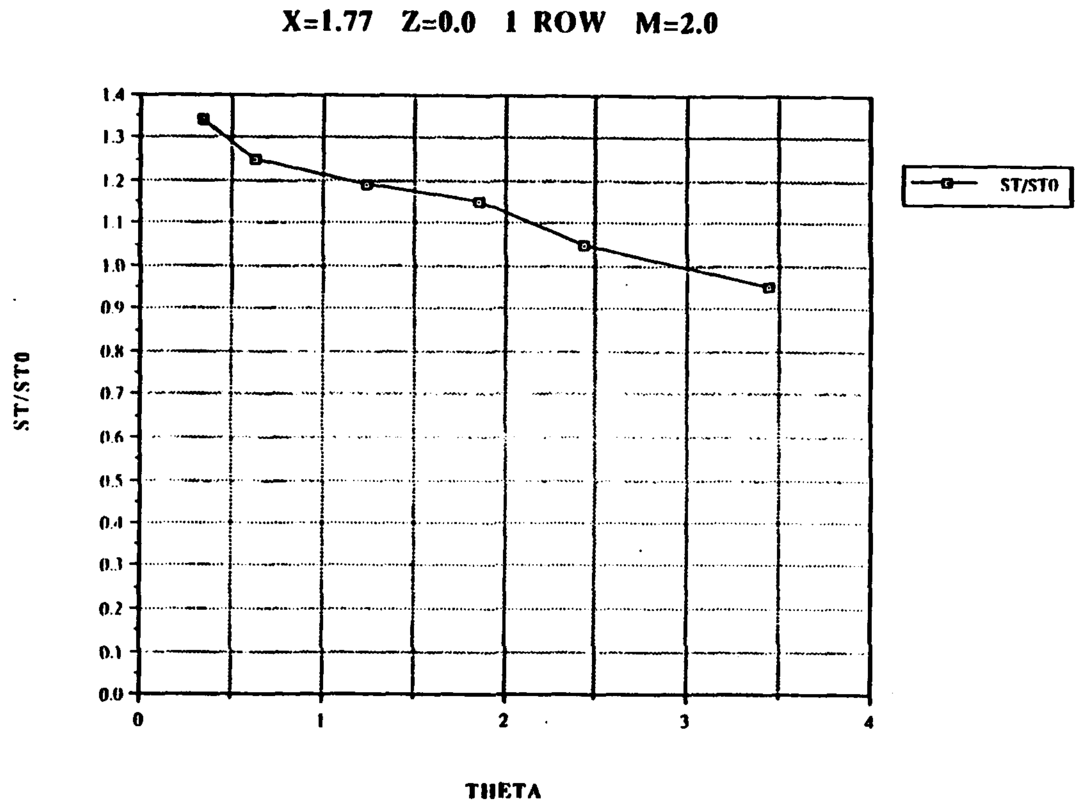

Figure 47. St/St_0 vs θ, Compound Angle, 1 row, m=2.0, X=1.77,Z=0.0 m

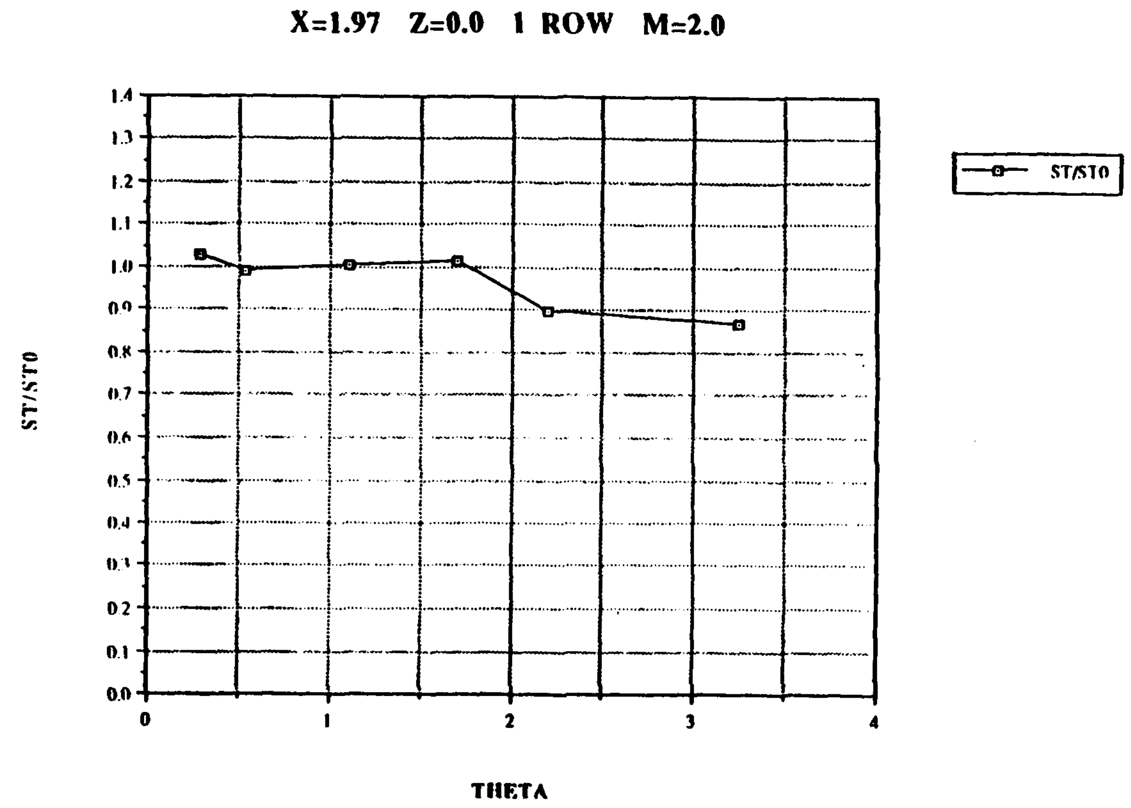

Figure 48. St/St$_0$ vs θ, Compound Angle, 1 row, m=2.0, X=1.97,Z=0.0 m

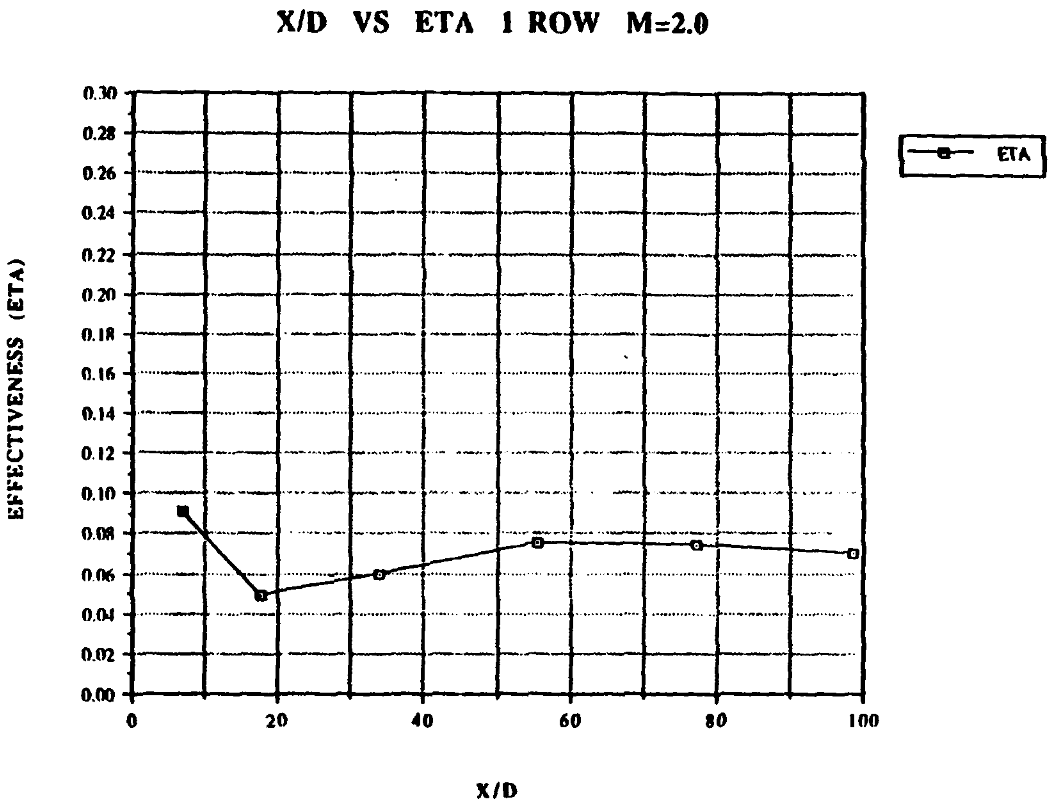

Figure 49. $\overline{\eta}$ vs x/d, Compound Angle, 1 row, m=2.0, Spanwise Average

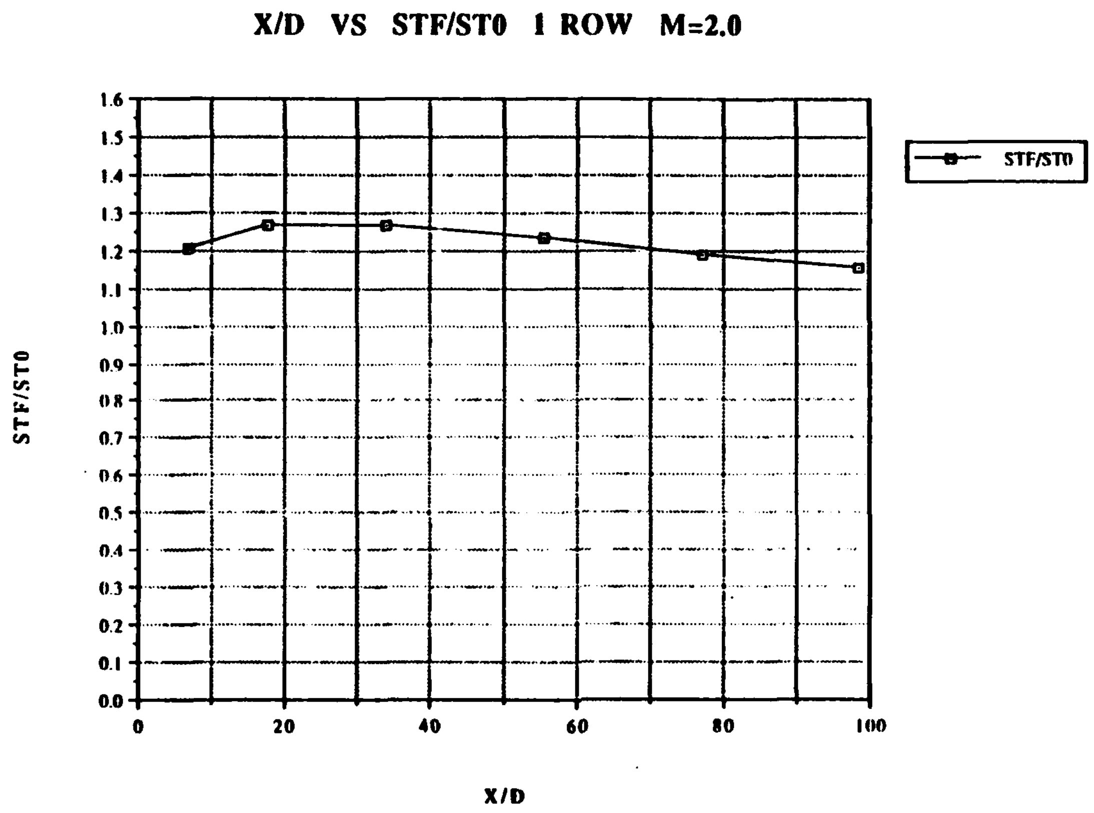

Figure 50. $\overline{St_f / St_o}$ vs x/d, Compound Angle, 1 row, m=2.0, Spanwise Average

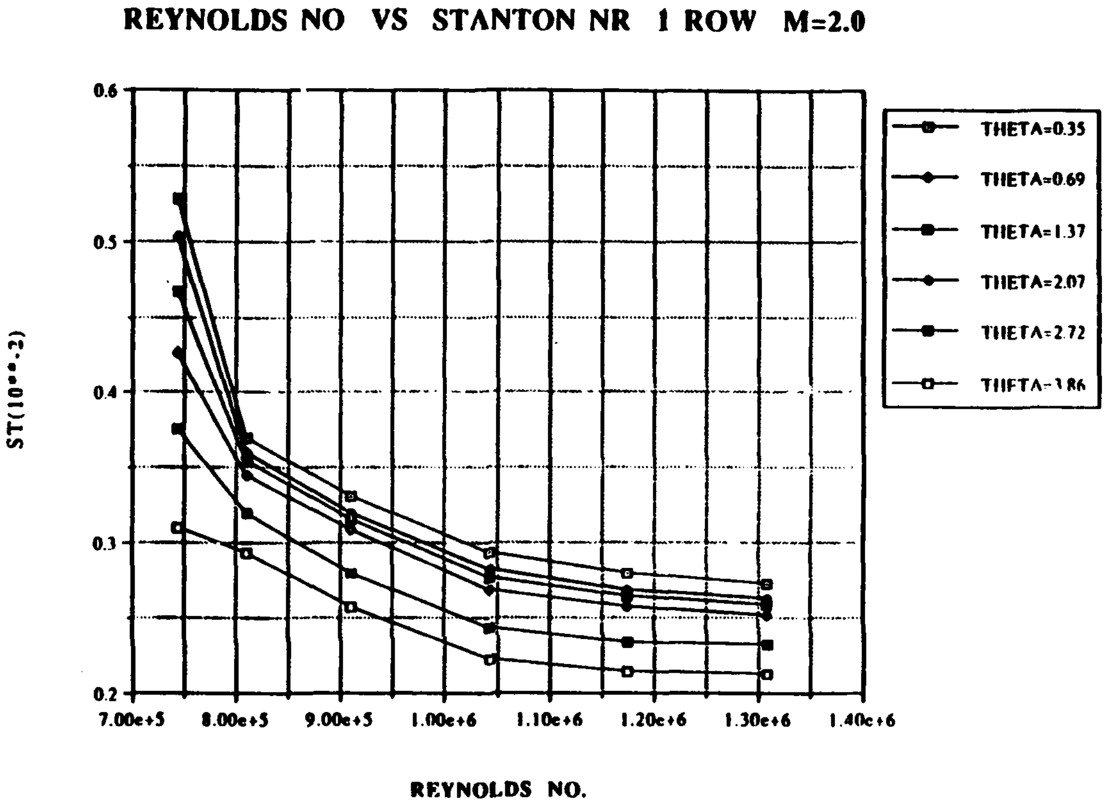

Figure 51. Spanwise averaged Stanton number vs Reynolds number, comparison of different θ values, 1 row, m=2.0

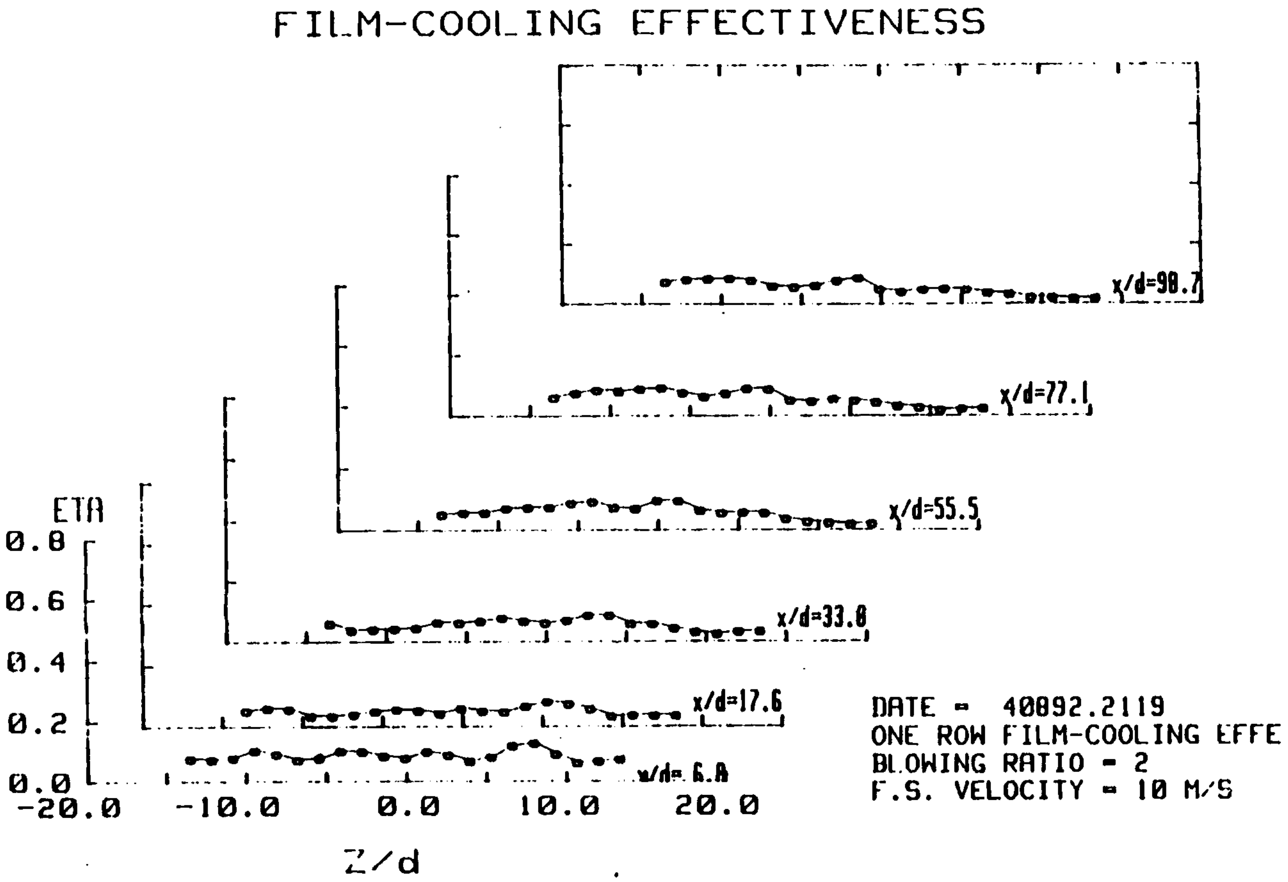

Figure 52. Spanwise Variation of η, Compound Angle, 1 row, m=2.0

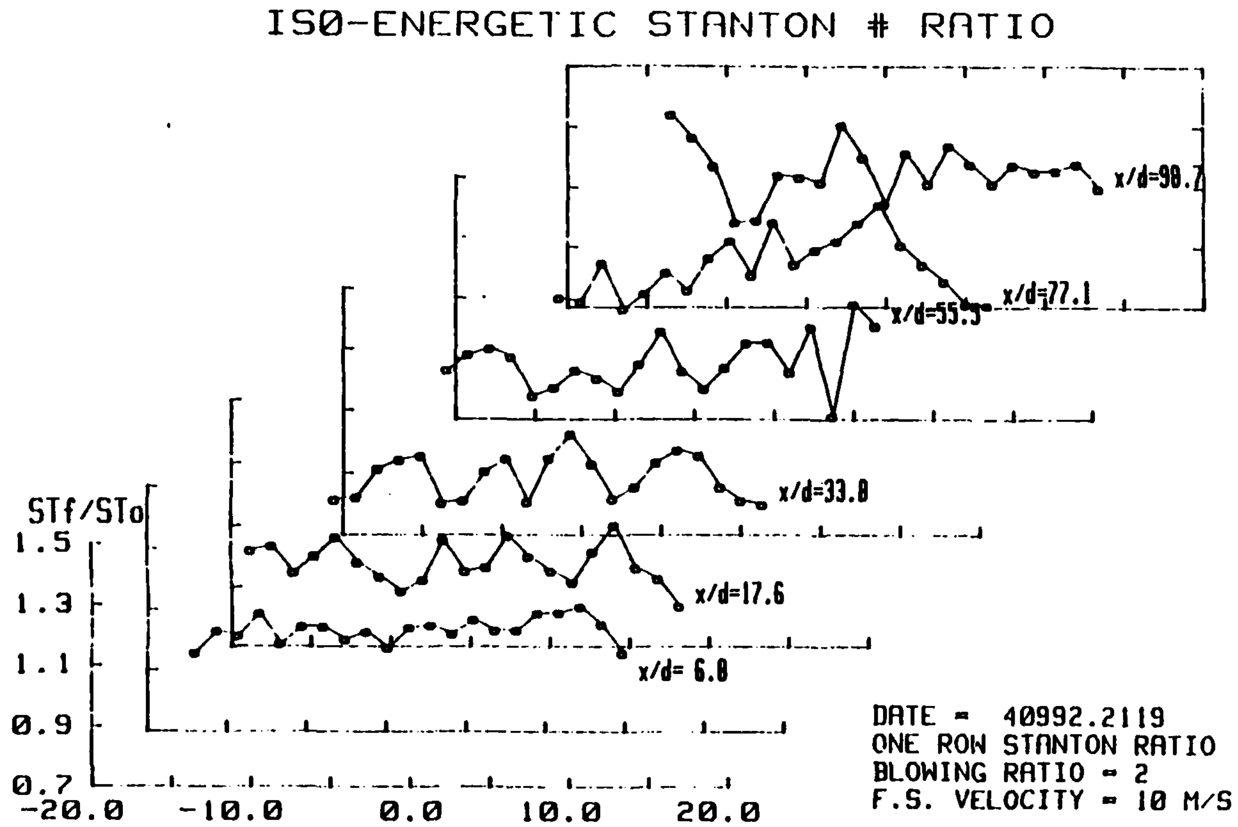

Figure 53. Spanwise Variation of St_f/St_o, Compound Angle, 1 row, m=2.0

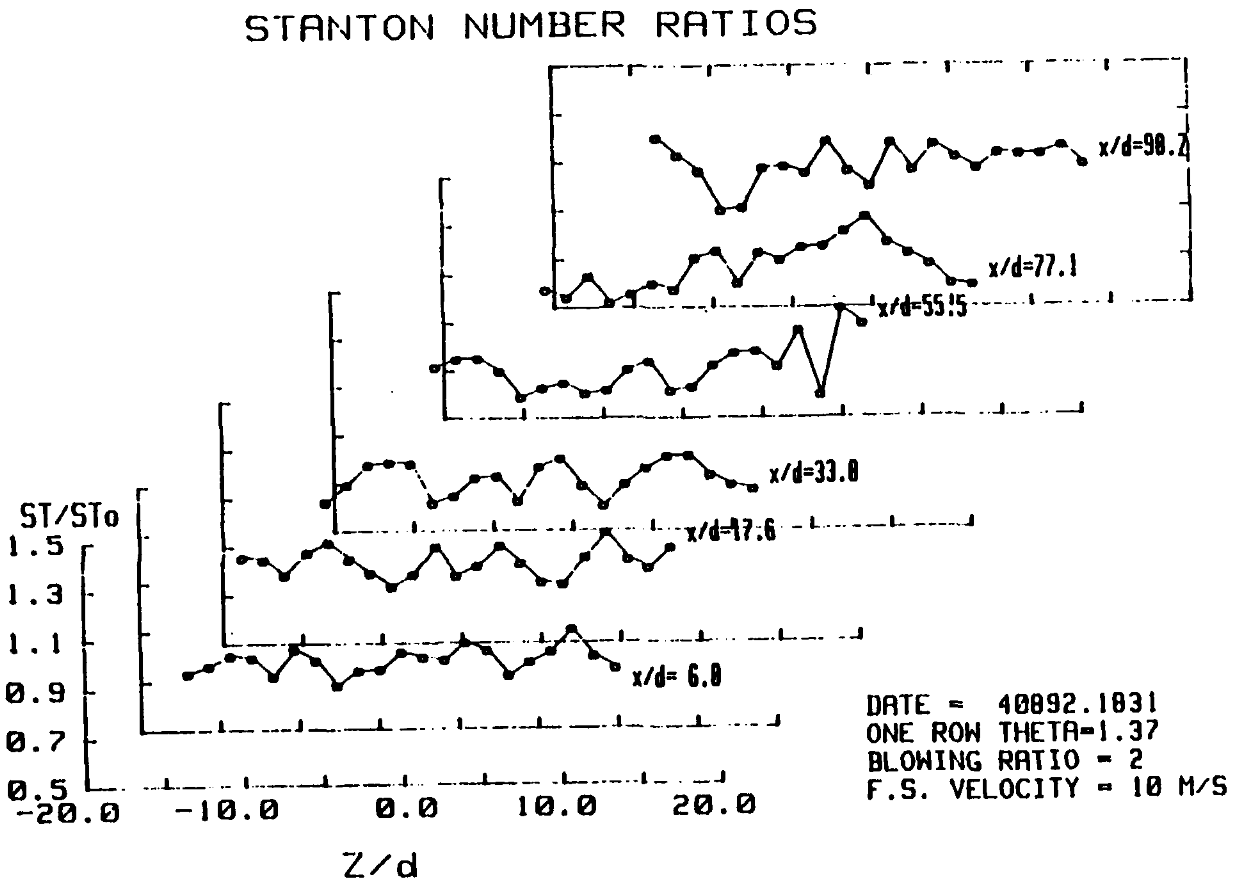

Figure 54. Spanwise Variation of St/St$_0$, Compound Angle, 1 row, m=2.0, θ =1.37

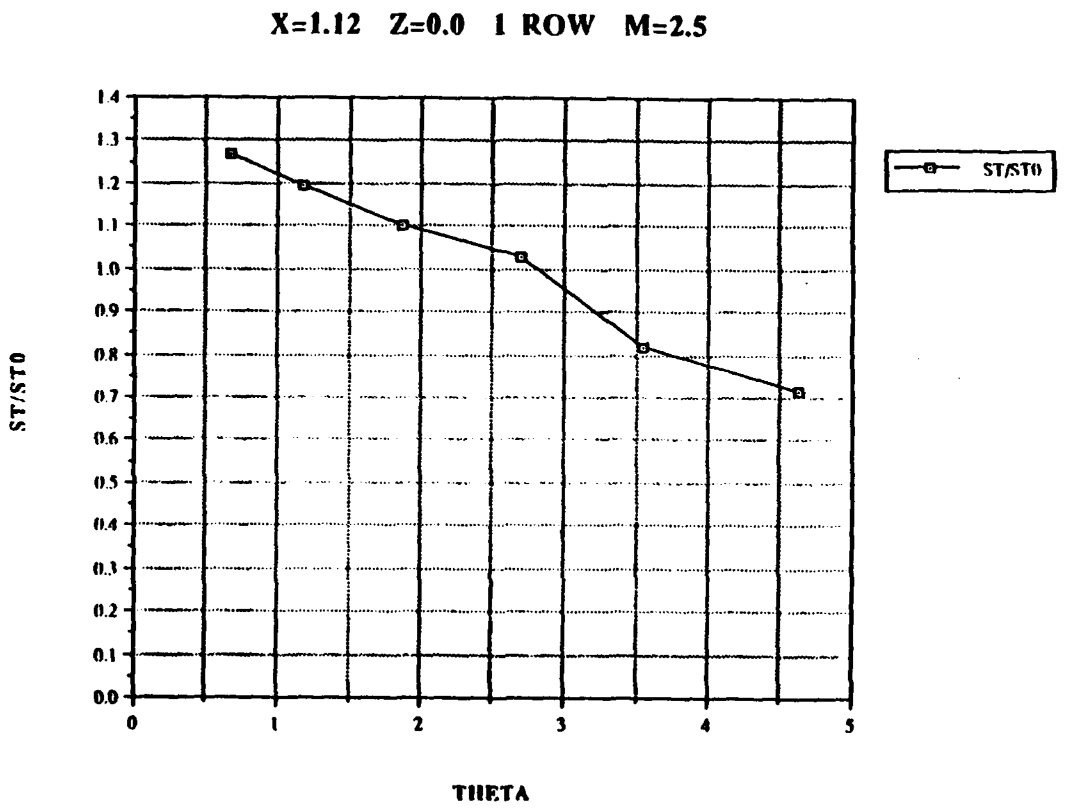

Figure 55. St/Sto vs θ, Compound Angle, 1 row, m=2.5, X=1.12,Z=0.0 m

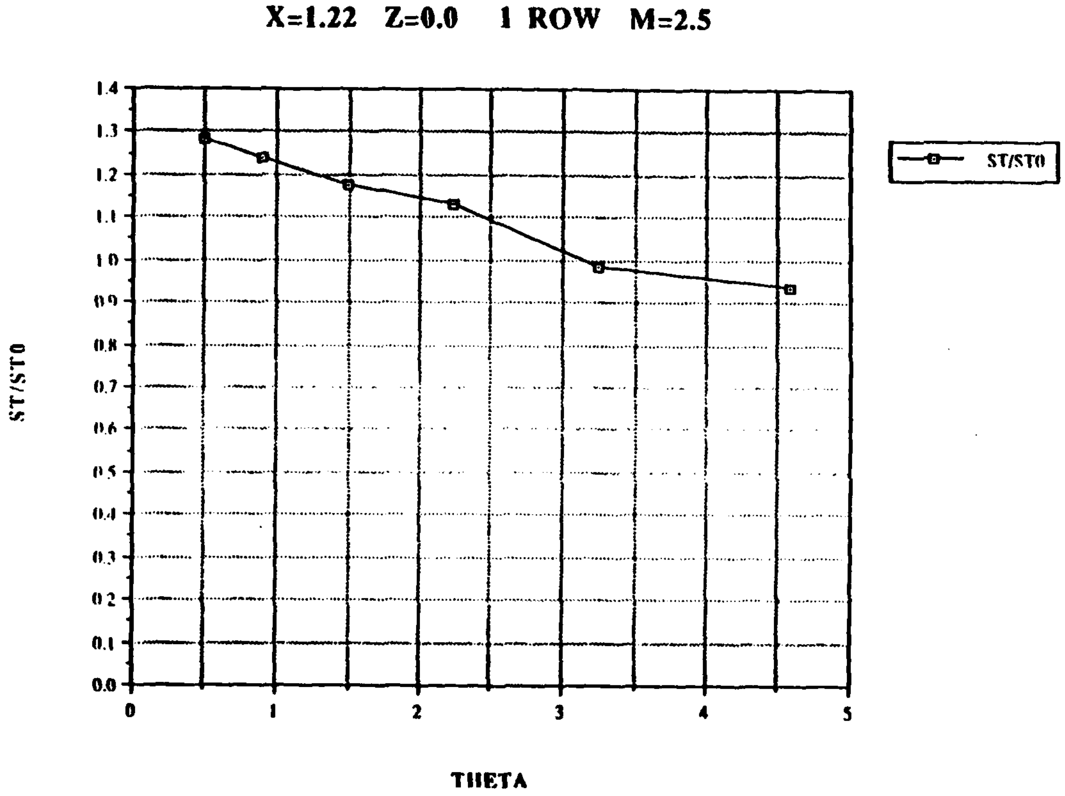

Figure 56. St/St_0 vs θ, Compound Angle, 1 row, m=2.5, X=1.22,Z=0.0 m

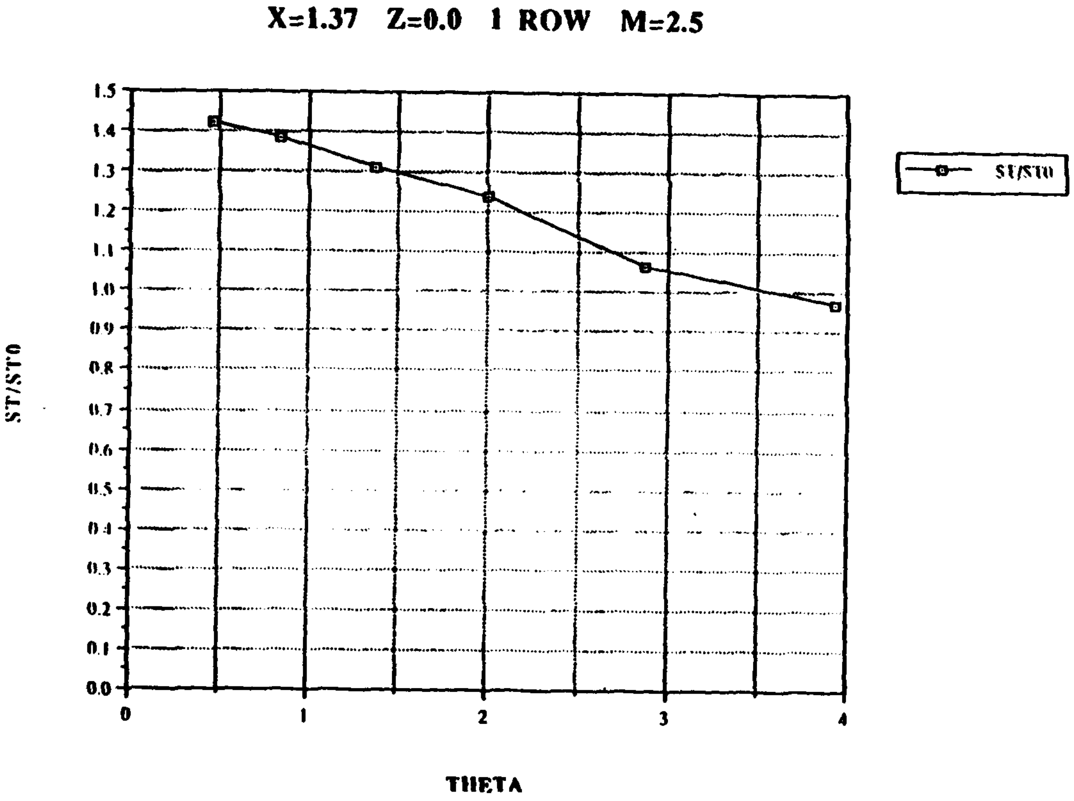

Figure 57. St/Sto vs θ, Compound Angle, 1 row, m=2.5, X=1.37,Z=0.0 m

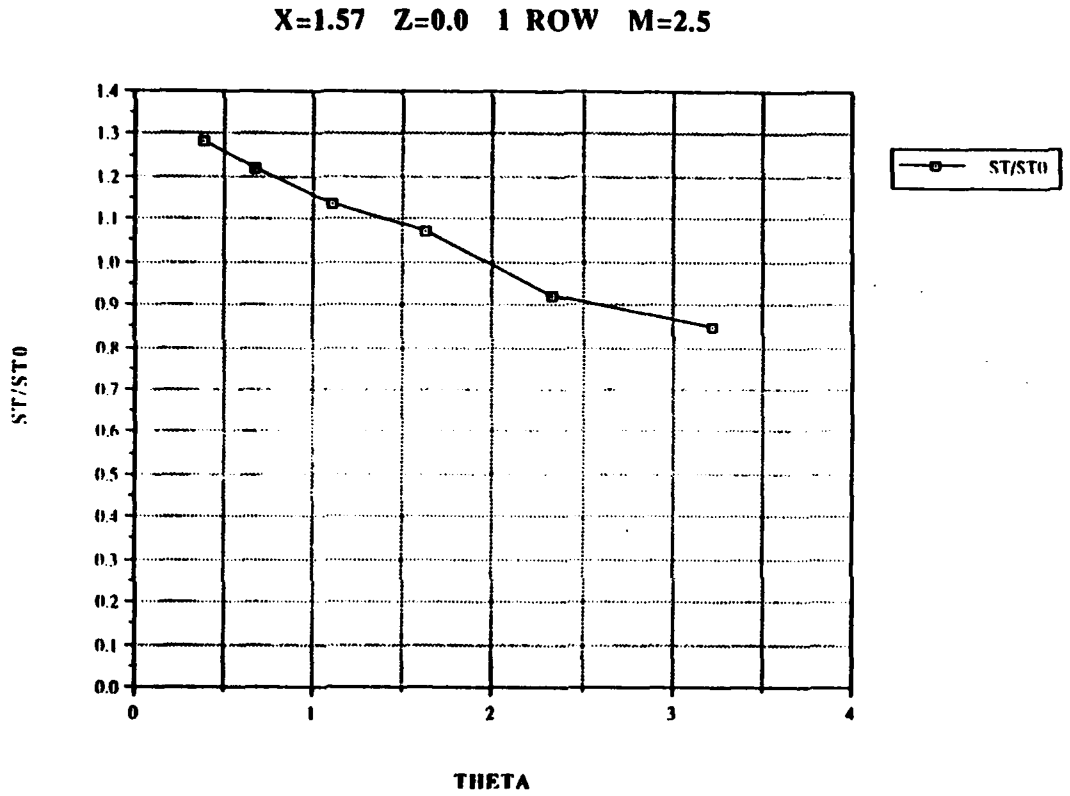

Figure 58. St/St$_0$ vs θ, Compound Angle, 1 row, m=2.5, X=1.57,Z=0.0 m

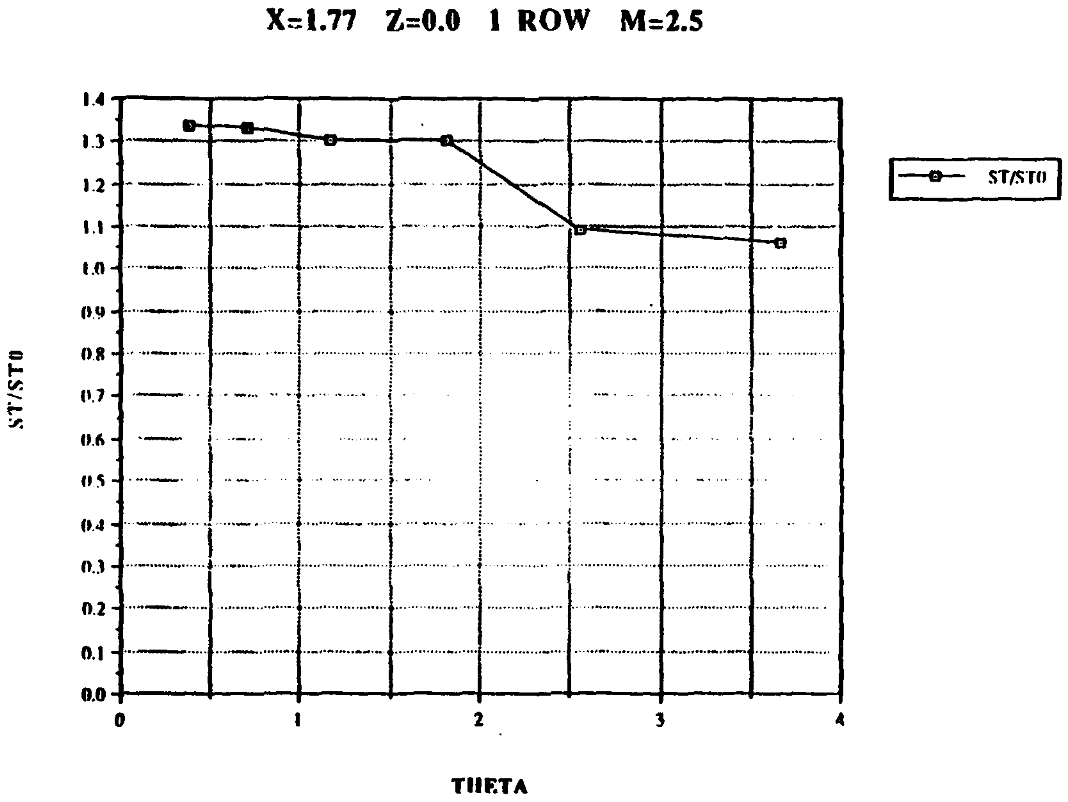

Figure 59. St/St$_0$ vs θ, Compound Angle, 1 row, m=2.5, X=1.77,Z=0.0 m

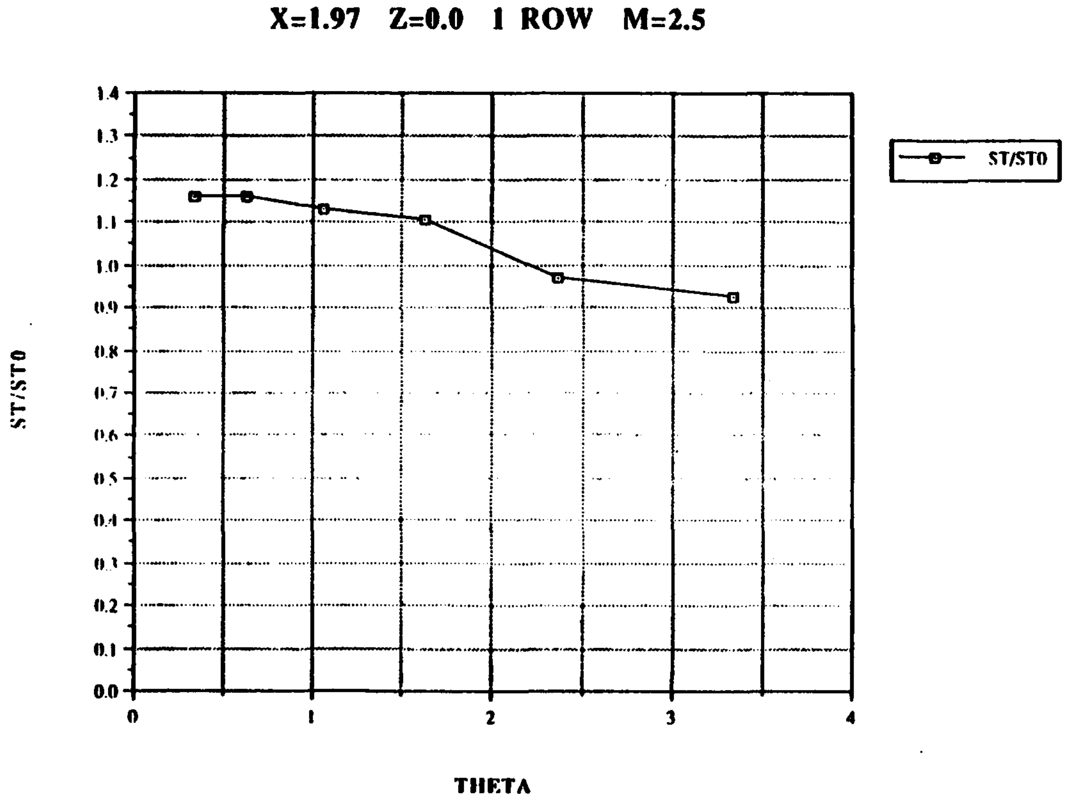

Figure 60. St/St$_0$ vs θ, Compound Angle, 1 row, m=2.5,X=1.97, Z=0.0 m

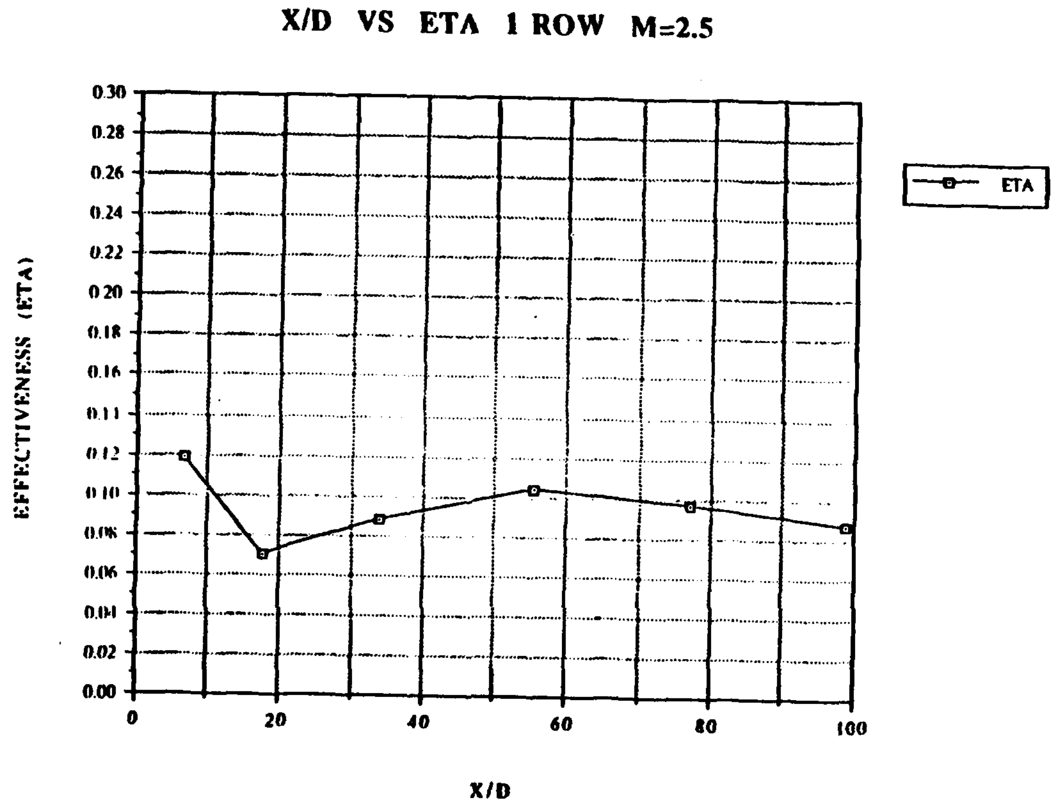

Figure 61. $\overline{\eta}$ vs x/d, Compound Angle, 1 row, m=2.5, Spanwise Average

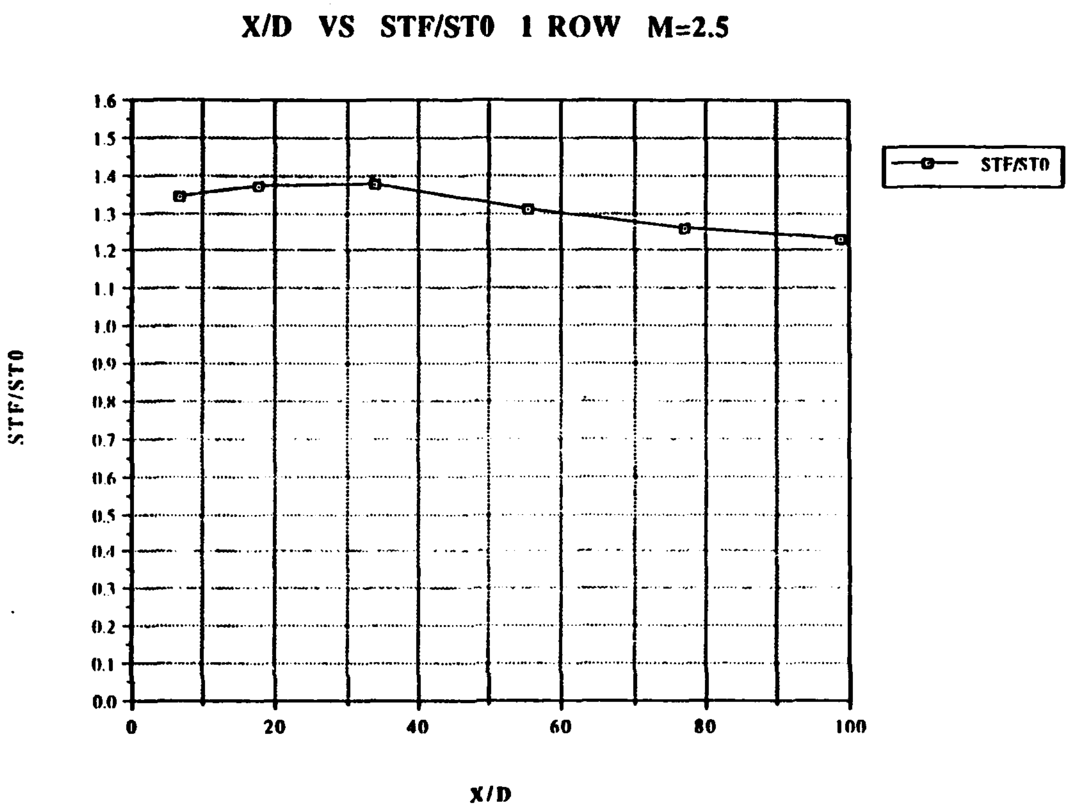

Figure 62. $\overline{St_f / St_o}$ vs x/d, Compound Angle, 1 row, m=2.5, Spanwise Average

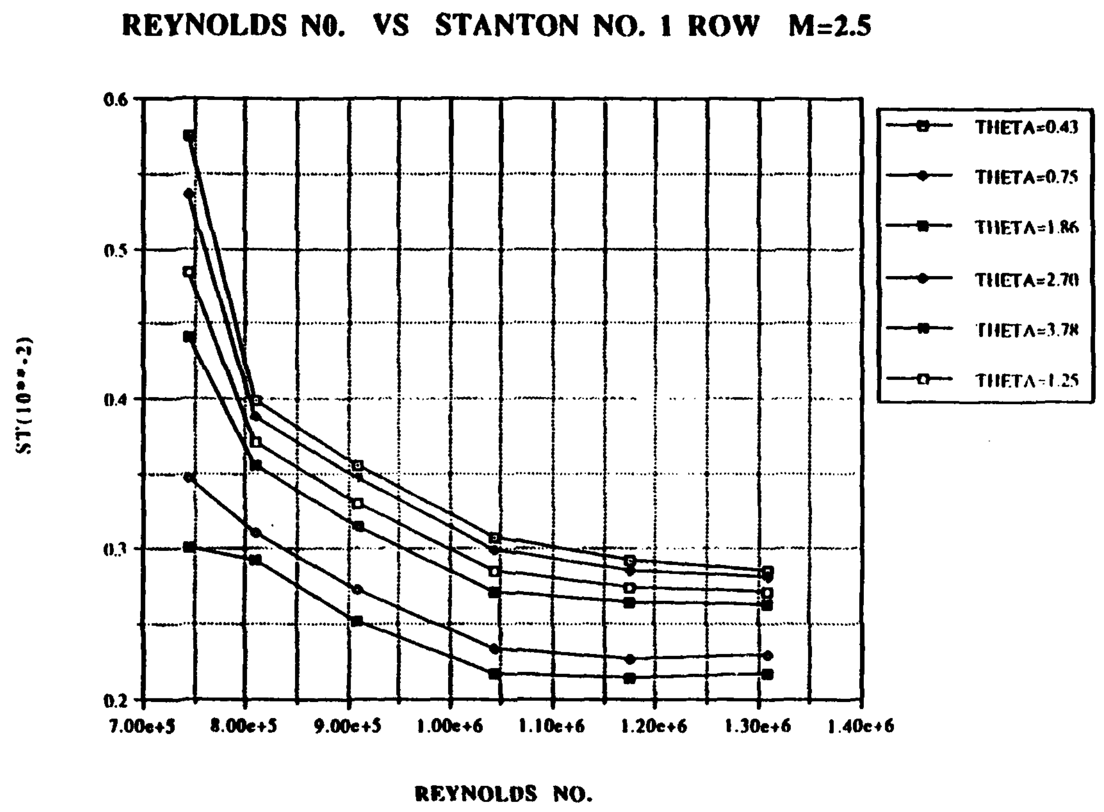

Figure 63. Spanwise averaged Stanton number vs Reynolds number, comparison of different θ values, 1 row, m=2.5

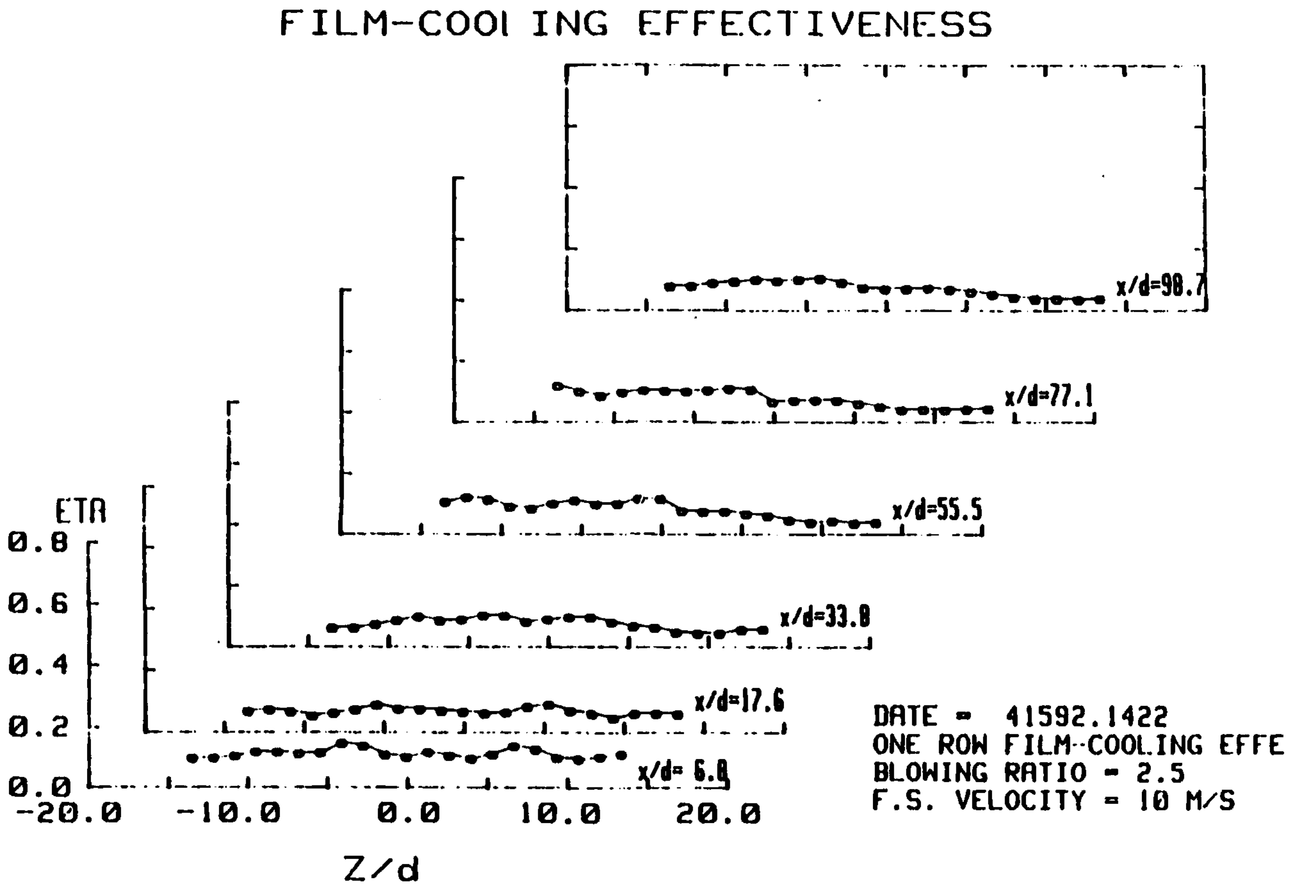

Figure 64. Spanwise Variation of η, Compound Angle, 1 row, m=2.5

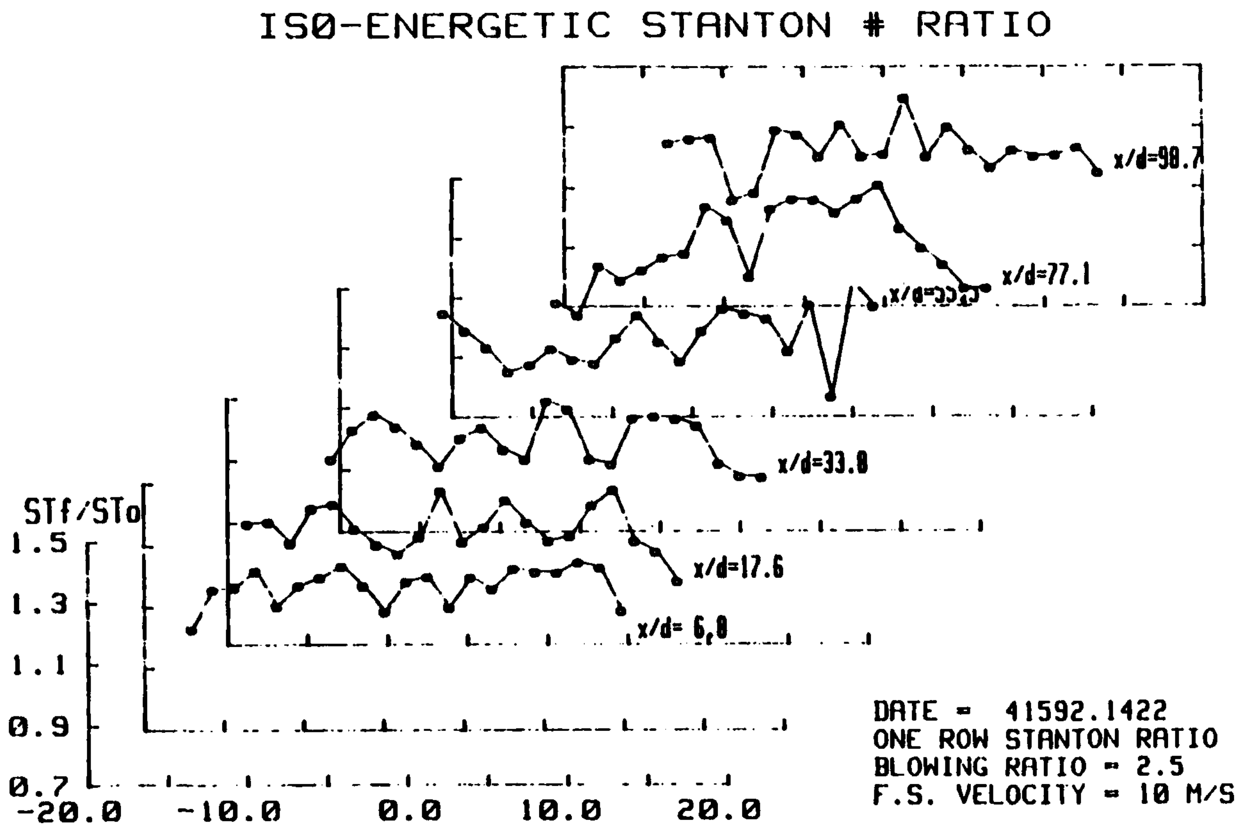

Figure 65. Spanwise Variation of St_f/St_o, Compound Angle, 1 row, m=2.5

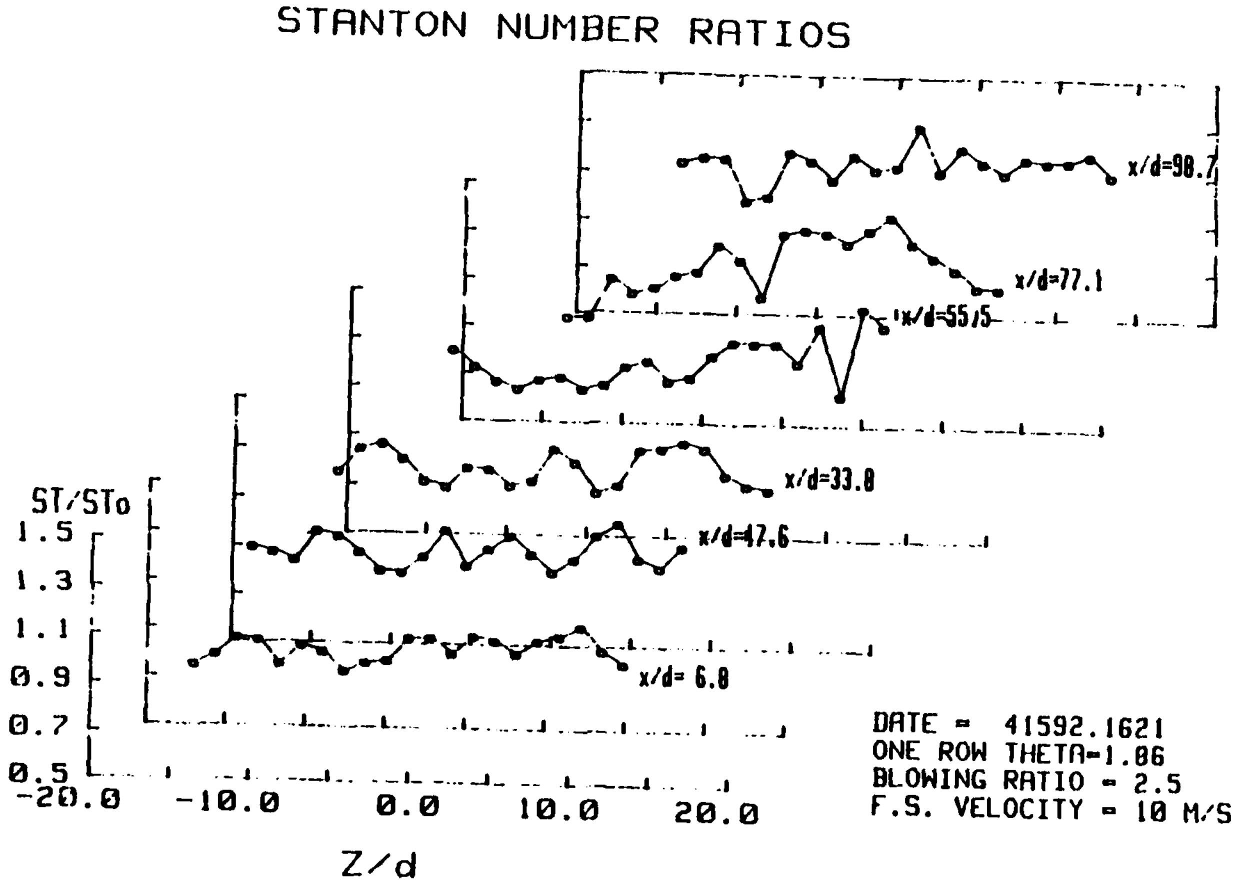

Figure 66. Spanwise Variation of St/St$_0$, Compound Angle, 1 row, m=2.5, θ =1.86

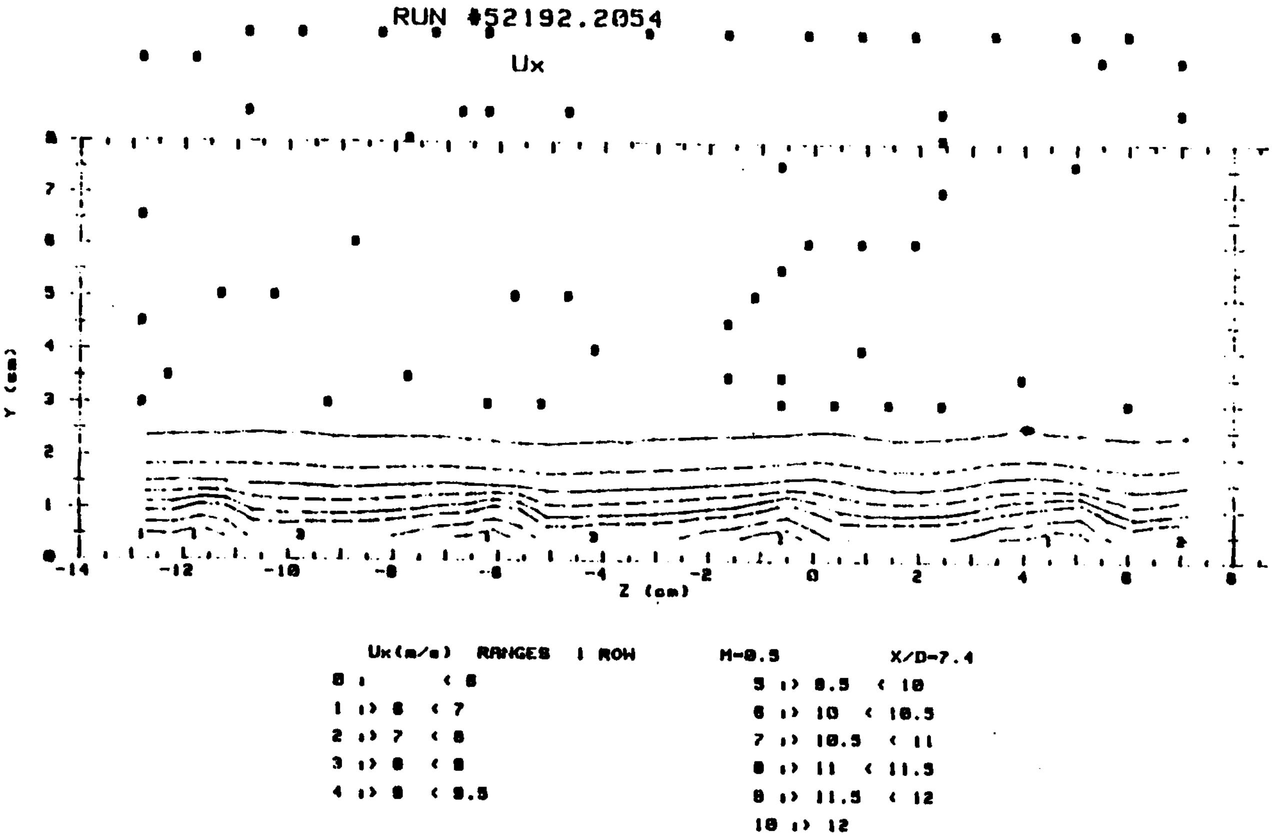

Figure 67. Streamwise Velocity Field, Compound Angle, 1 row, m=0.5, x/d=7.4

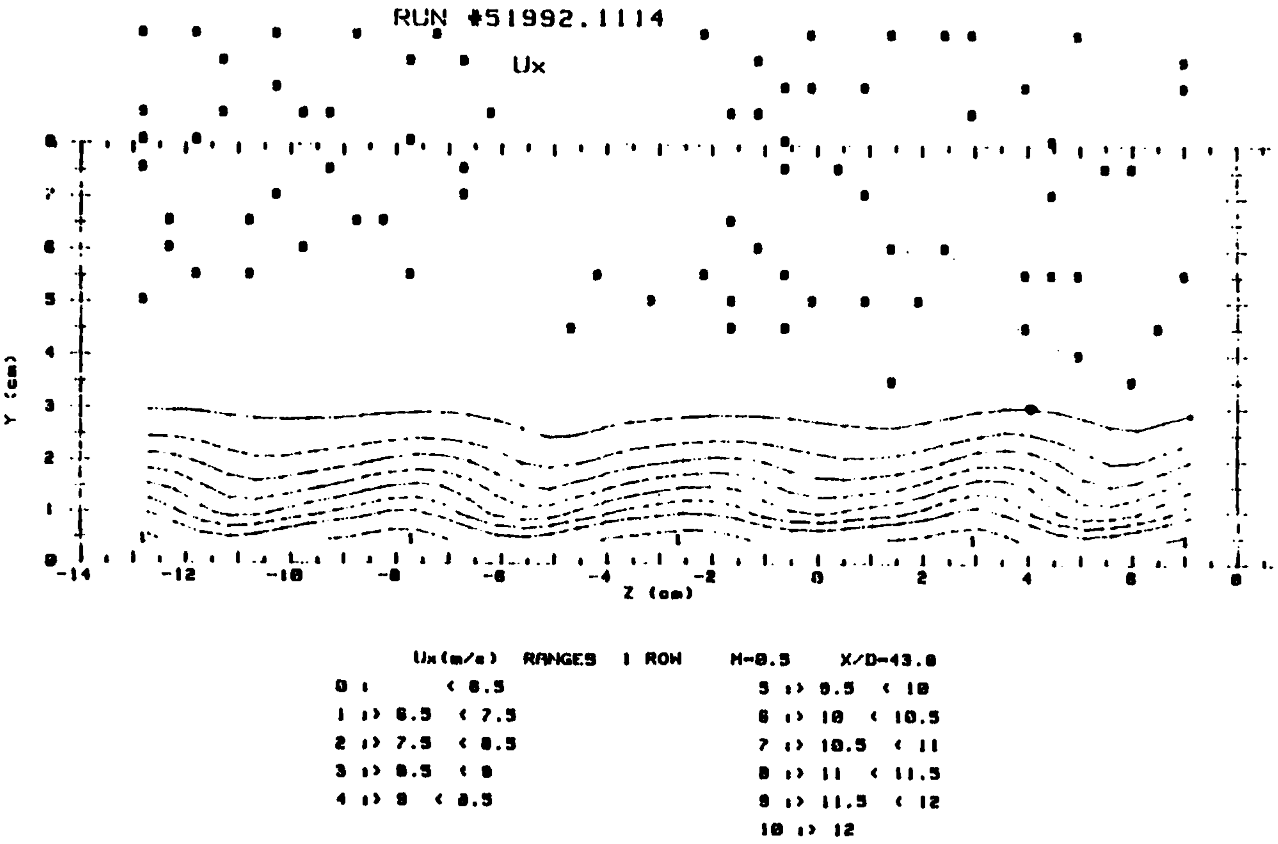

Figure 68. Streamwise Velocity Field, Compound Angle, 1 row, m=0.5, x/d=43.8

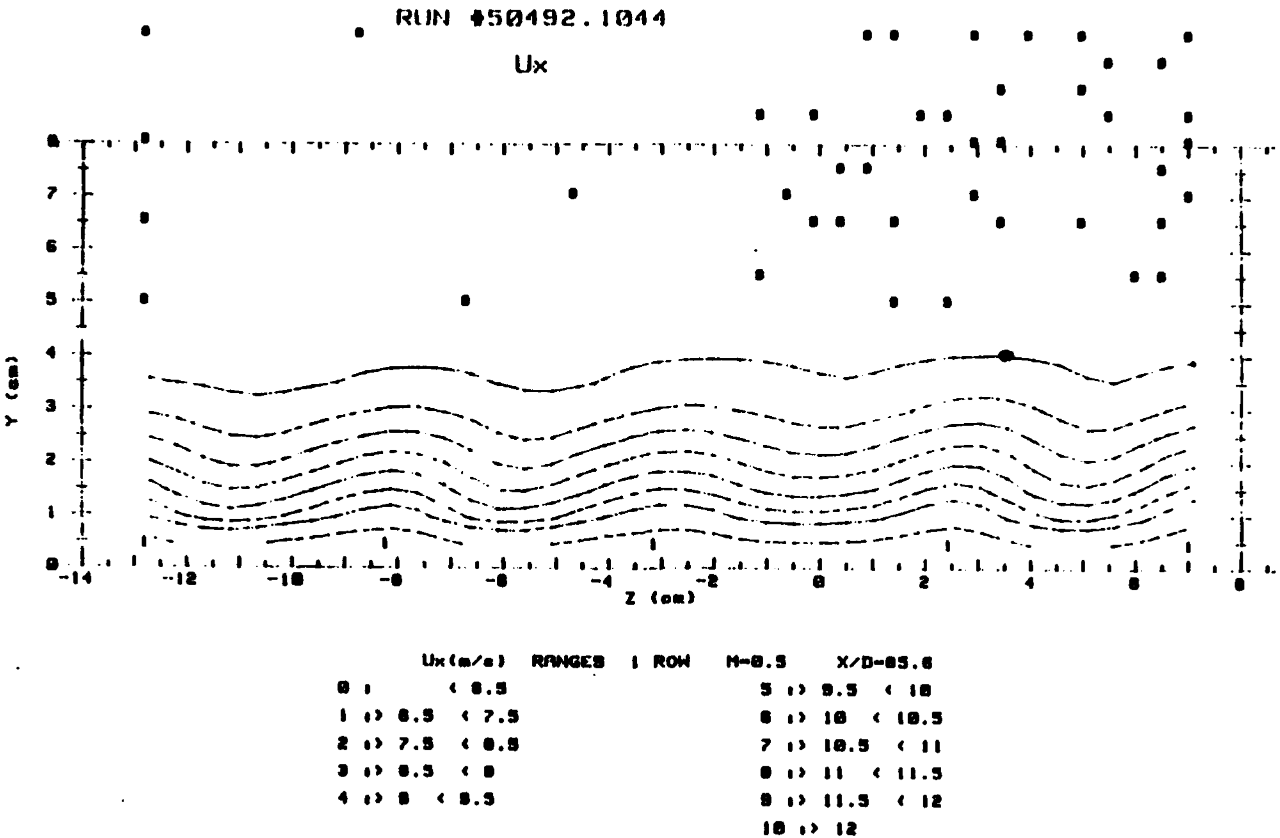

Figure 69. Streamwise Velocity Field, Compound Angle, 1 row, m=0.5, x/d=85.6

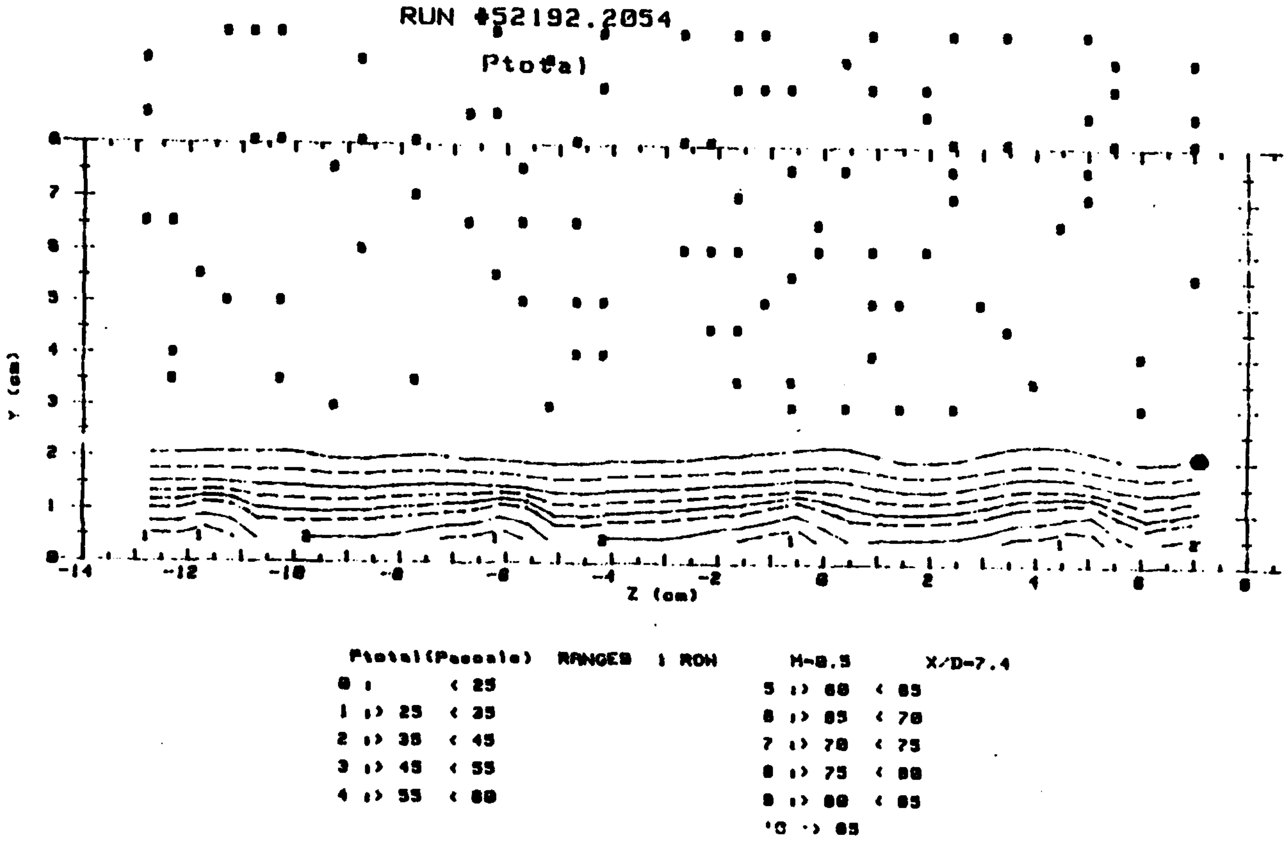

Figure 70. Streamwise Pressure Field, Compound Angle, 1 row, m=0.5, x/d=7.4

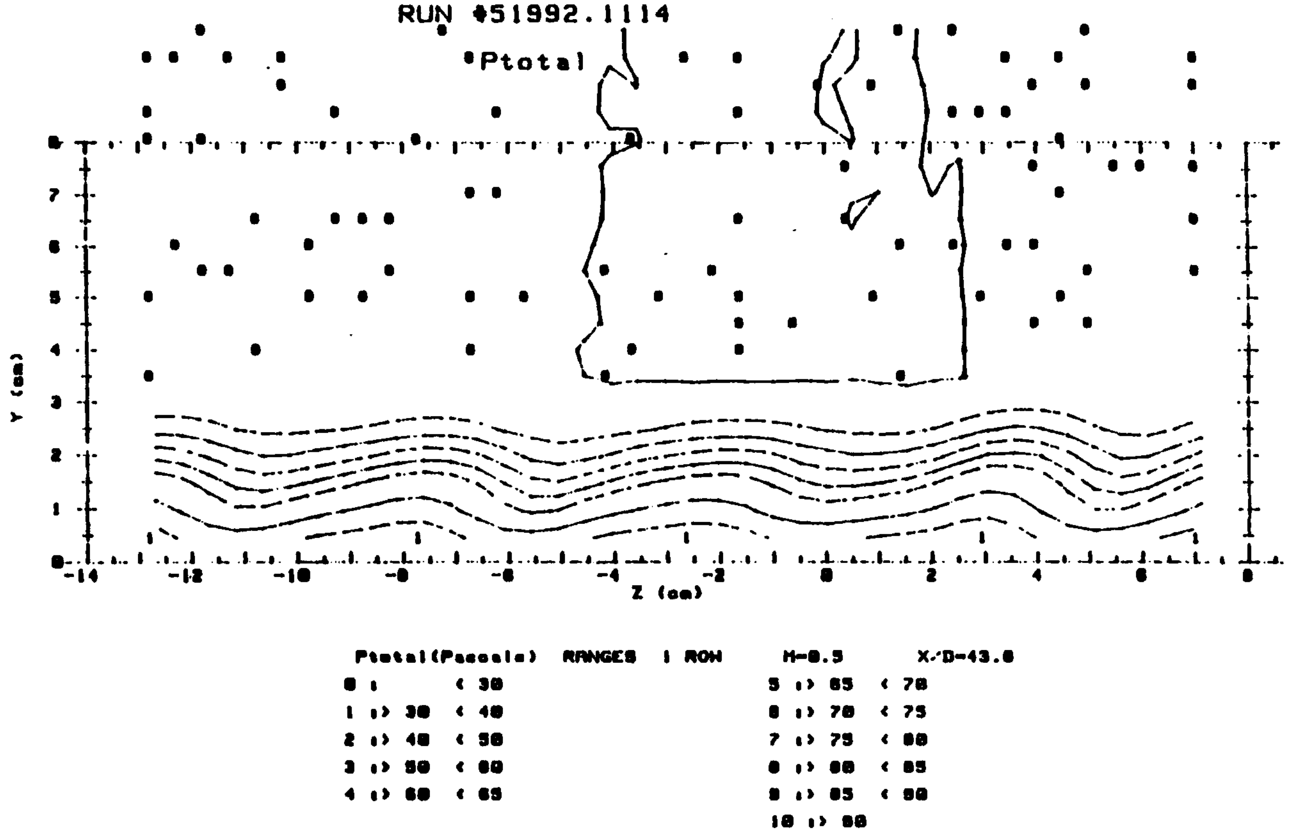

Figure 71. Streamwise Pressure Field, Compound Angle, 1 row, m=0.5, x/d=43.8

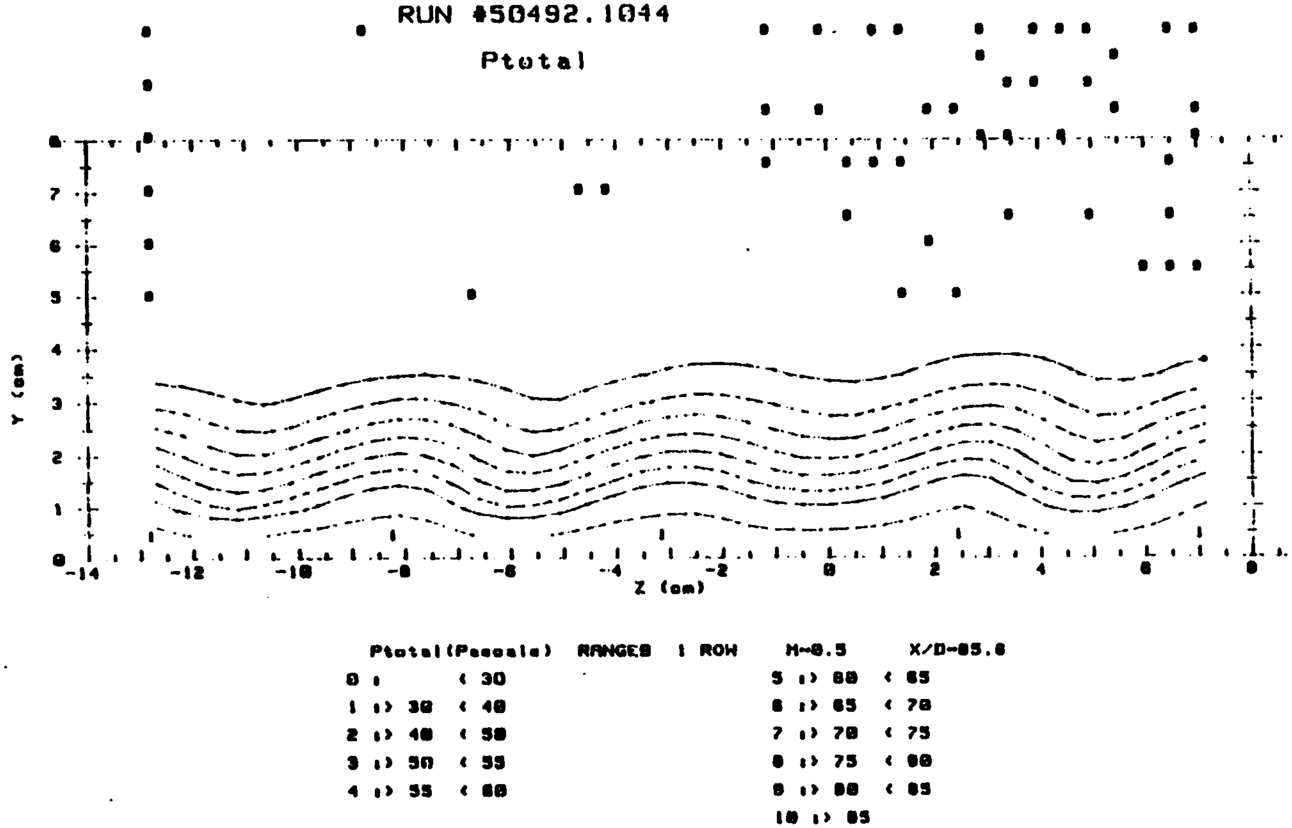

Figure 72. Streamwise Pressure Field, Compound Angle, 1 row, m=0.5, x/d=85.6

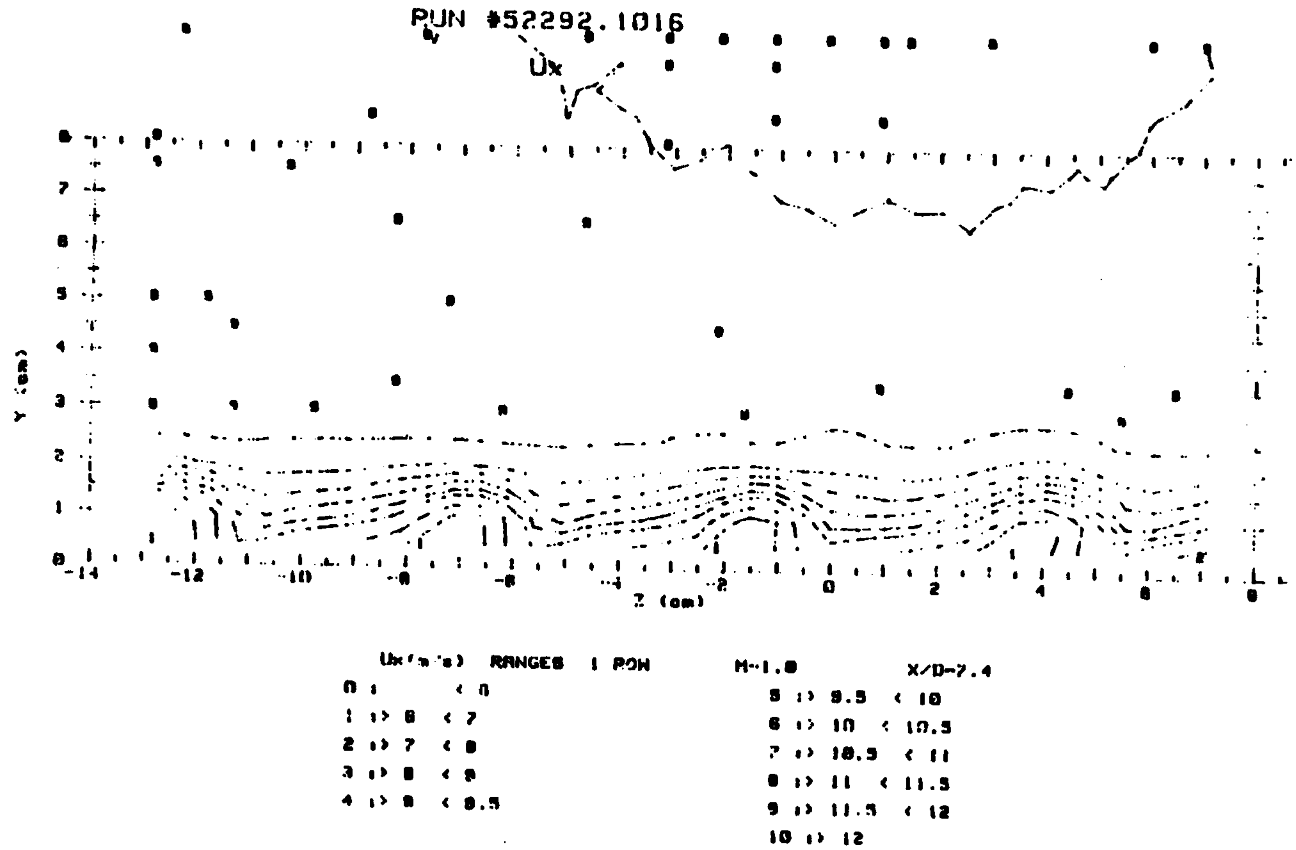

Figure 73. Streamwise Velocity Field, Compound Angle, 1 row, m=1.0, x/d=7.4

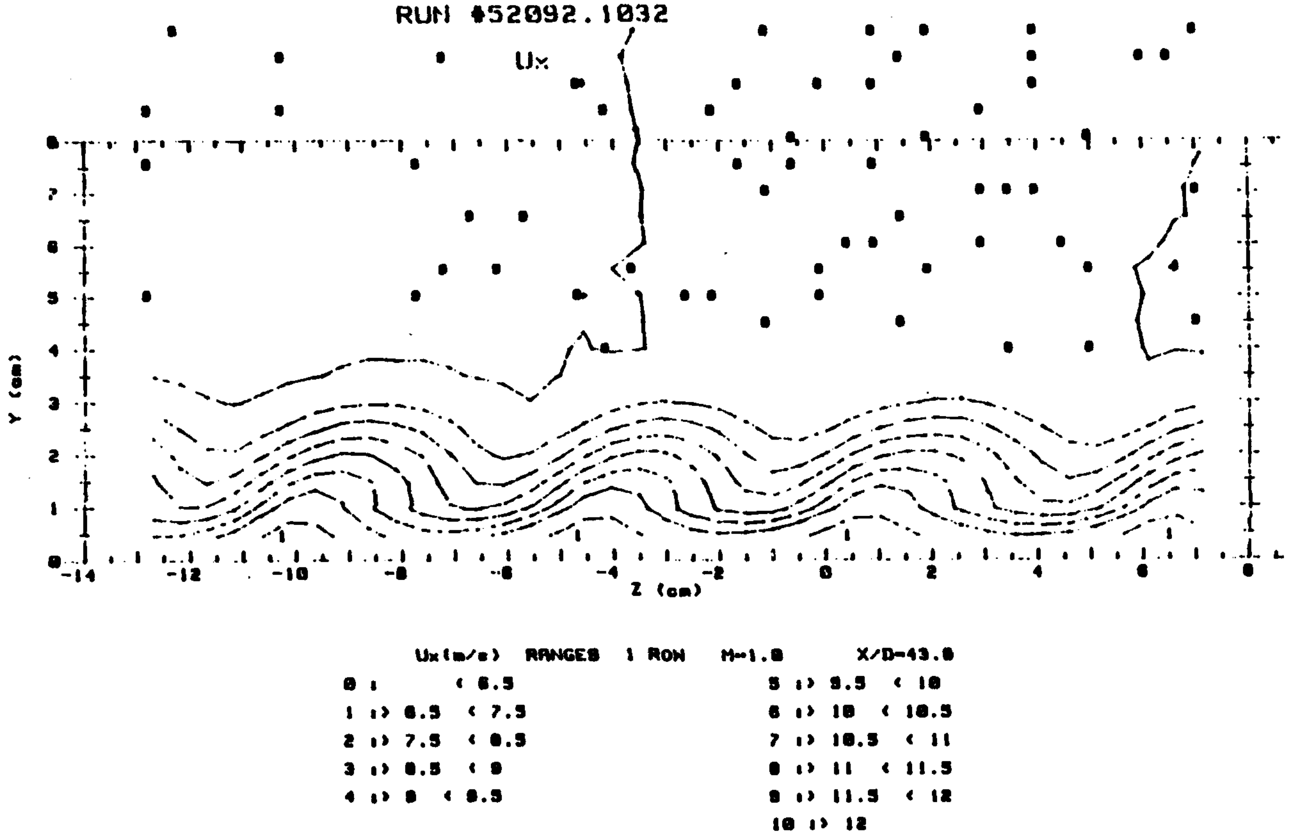

Figure 74. Streamwise Velocity Field, Compound Angle, 1 row, m=1.0, x/d=43.8

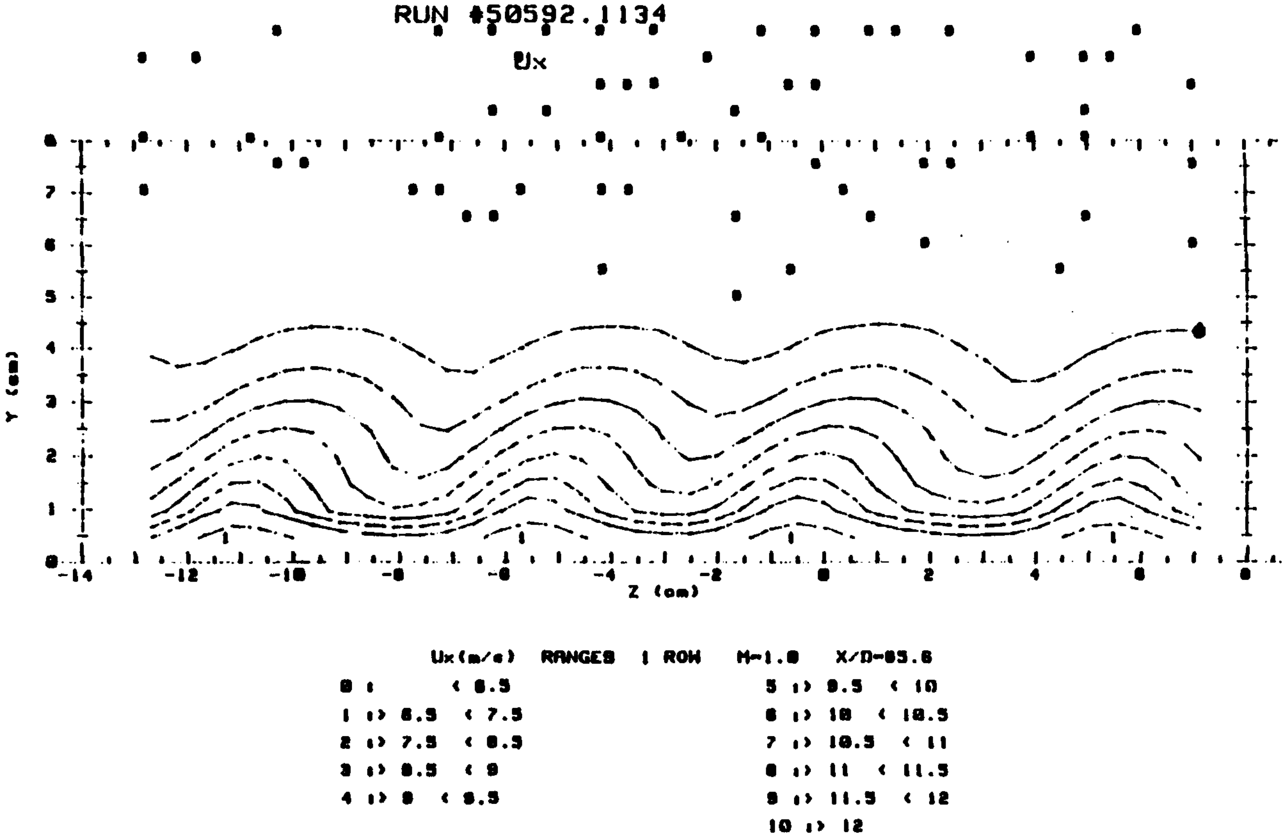

Figure 75. Streamwise Velocity Field, Compound Angle, 1 row, m=1.0, x/d=85.6

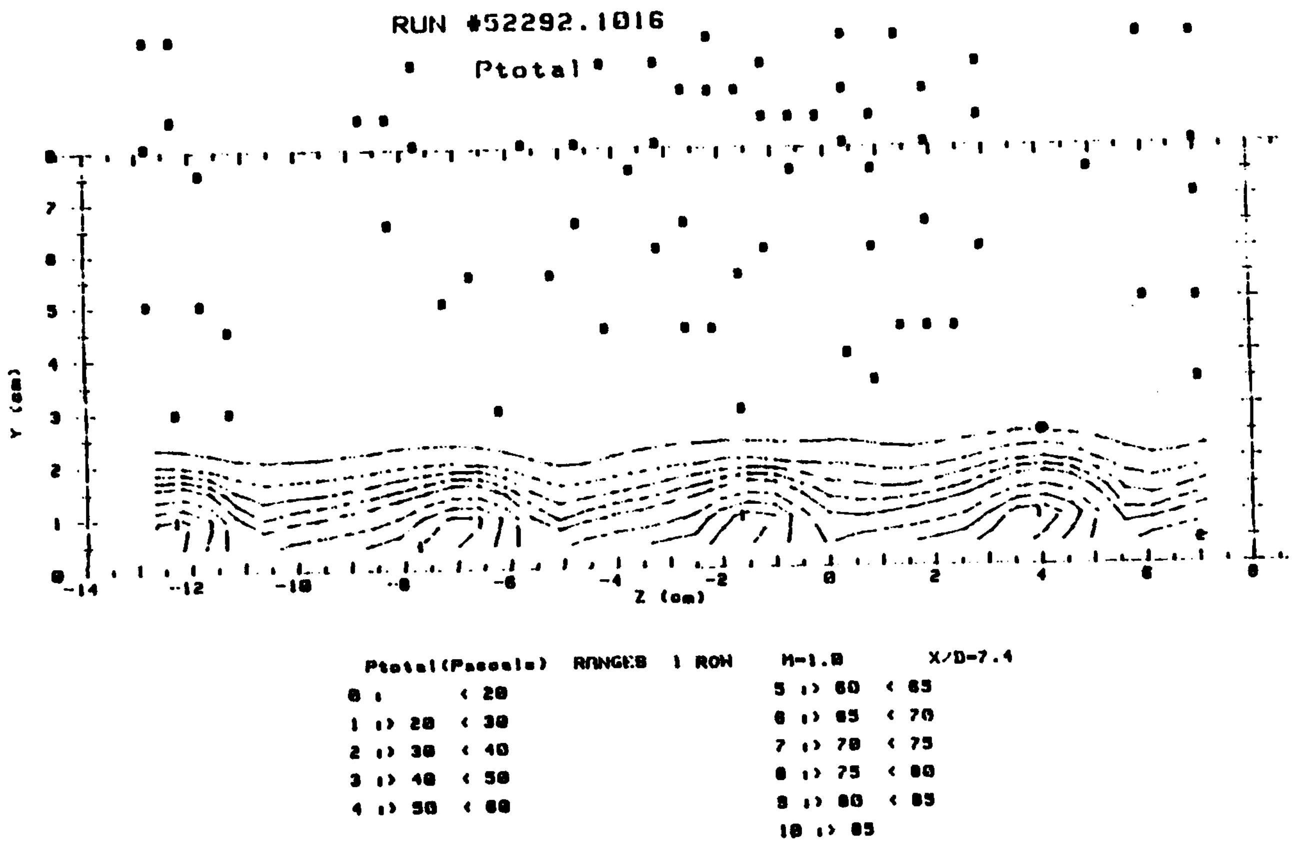

Figure 76. Streamwise Pressure Field, Compound Angle, 1 row, m=1.0, x/d=7.4

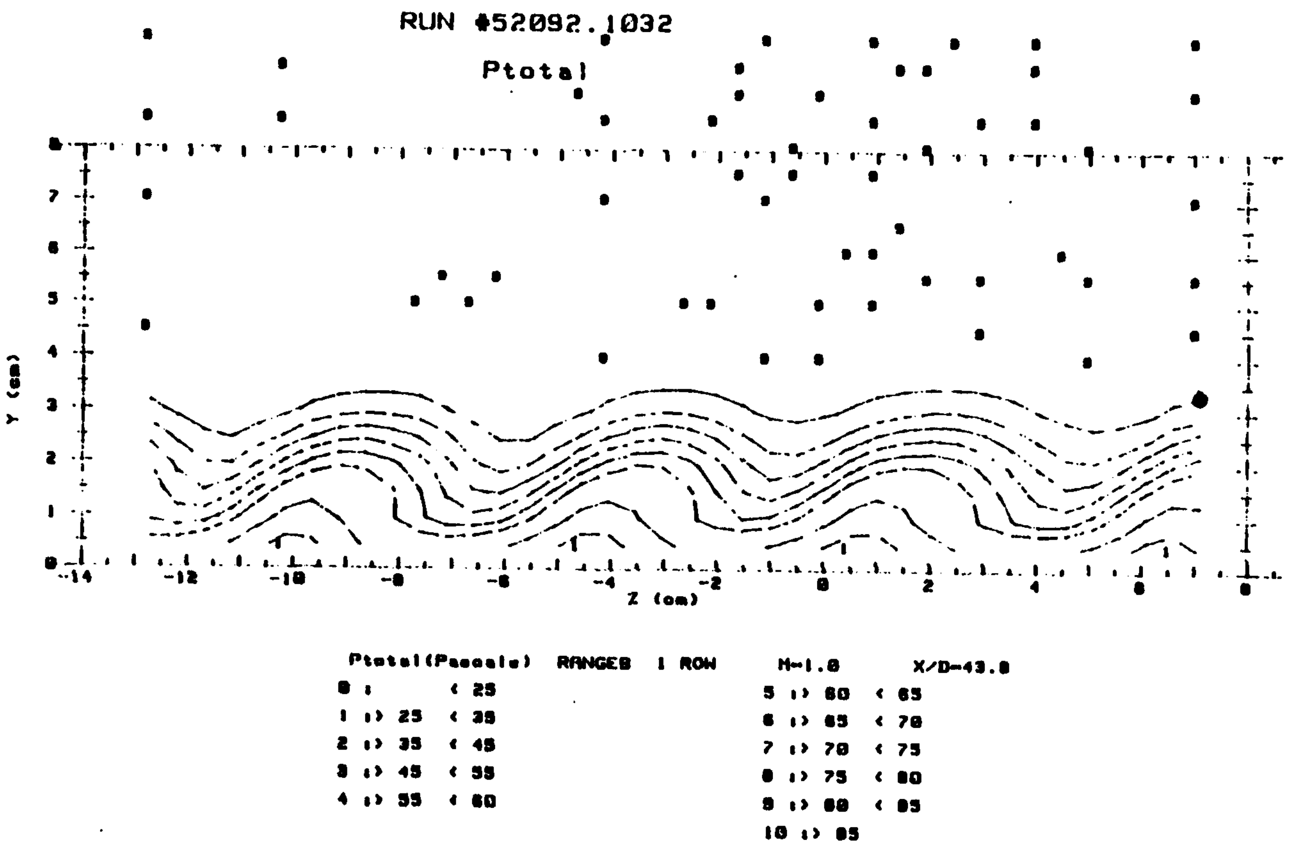

Figure 77. Streamwise Pressure Field, Compound Angle, 1 row, m=1.0, x/d=43.8

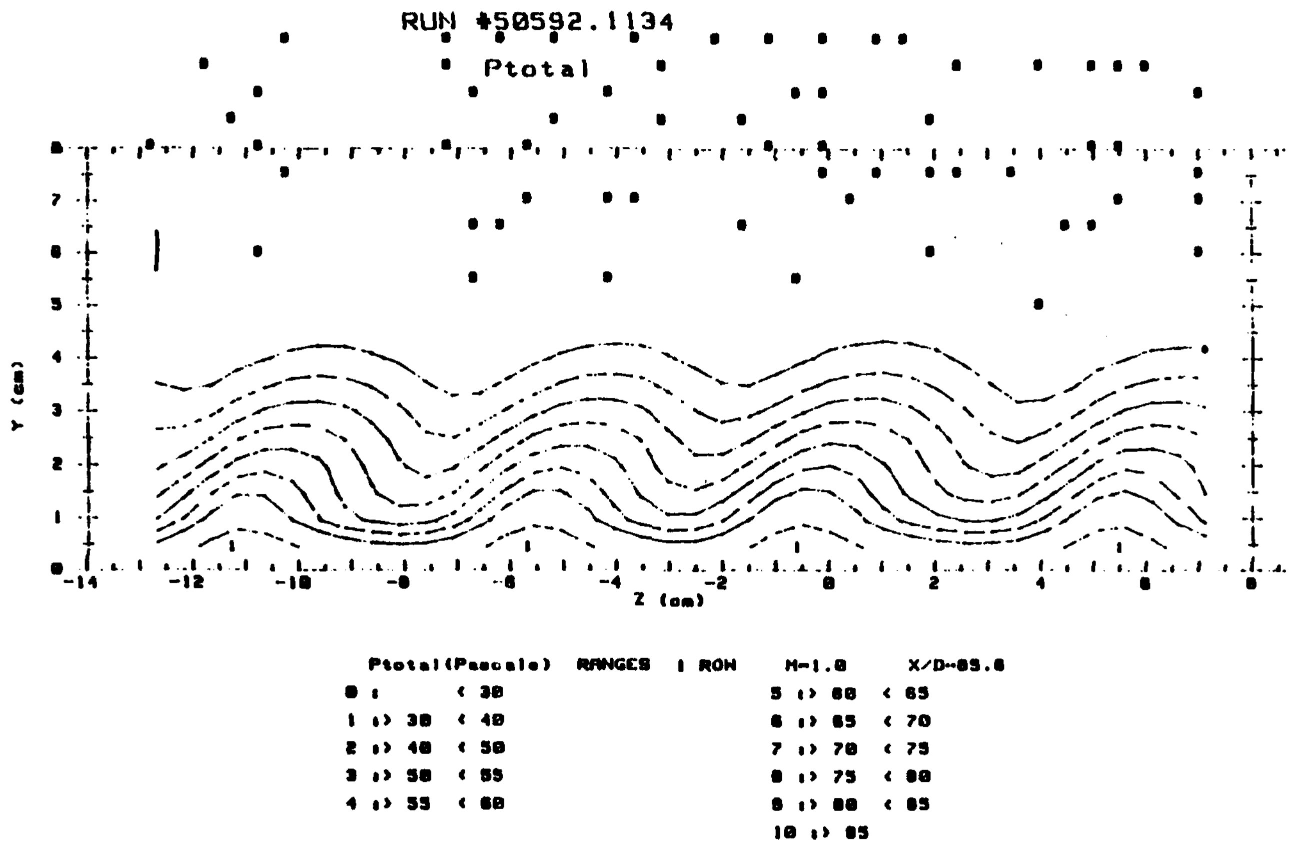

Figure 78. Streamwise Pressure Field, Compound Angle, 1 row, m=1.0, x/d=85.6

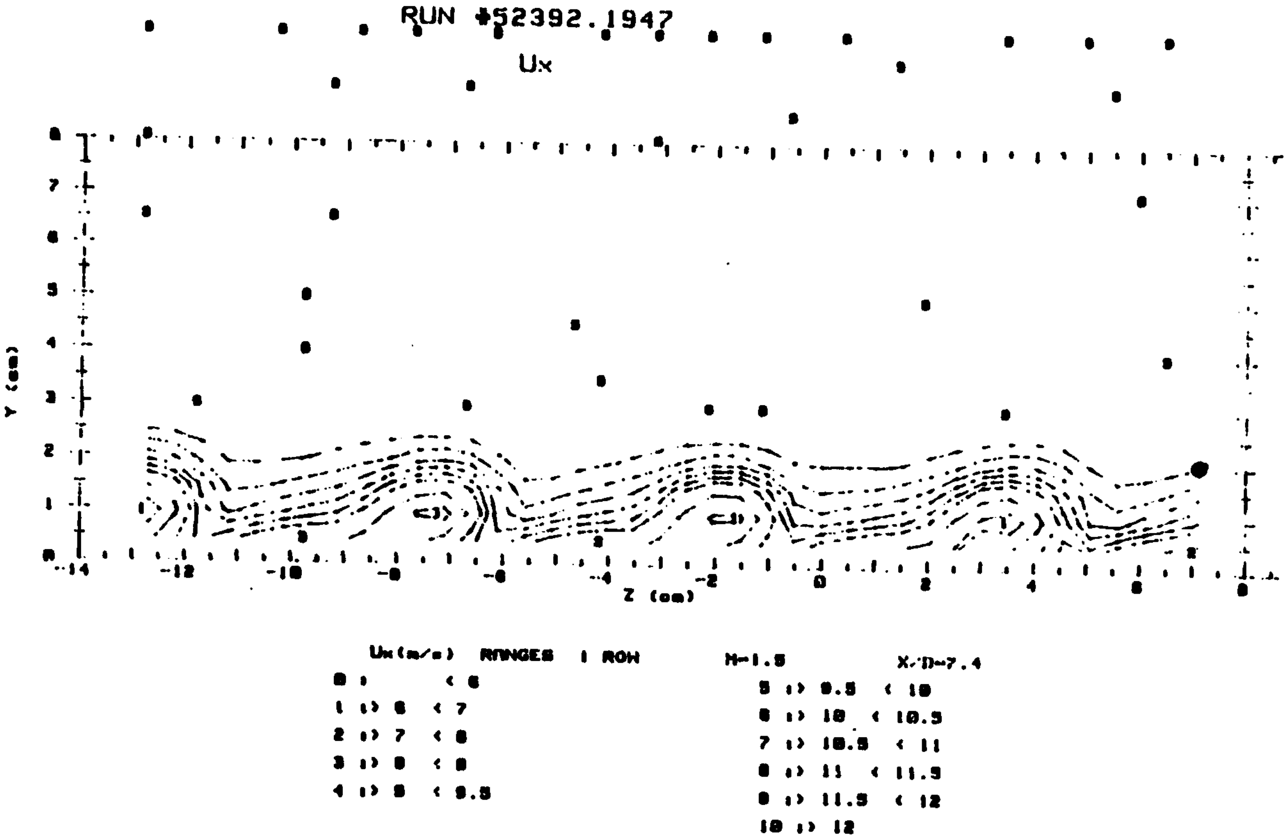

Figure 79. Streamwise Velocity Field, Compound Angle, 1 row, m=1.5, x/d=7.4

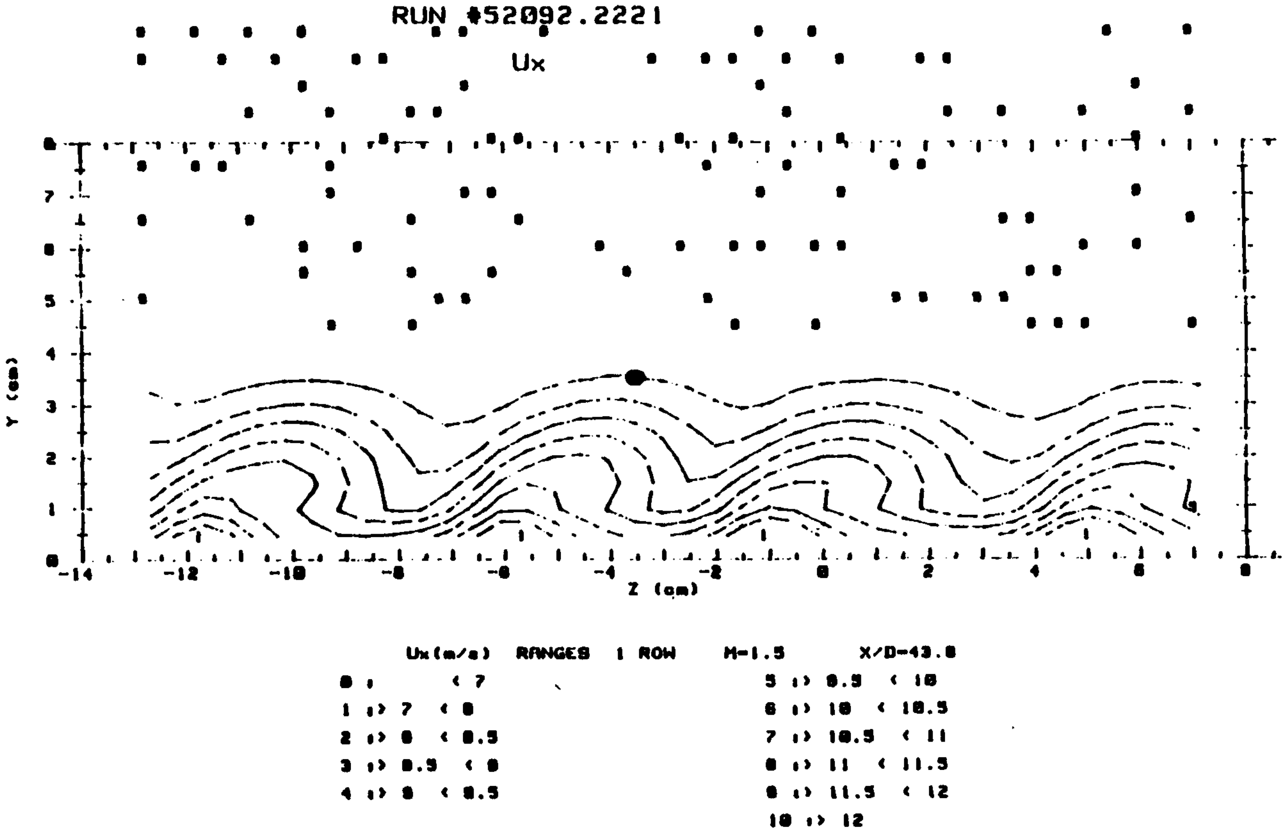

Figure 80. Streamwise Velocity Field, Compound Angle, 1 row, m=1.5, x/d=43.8

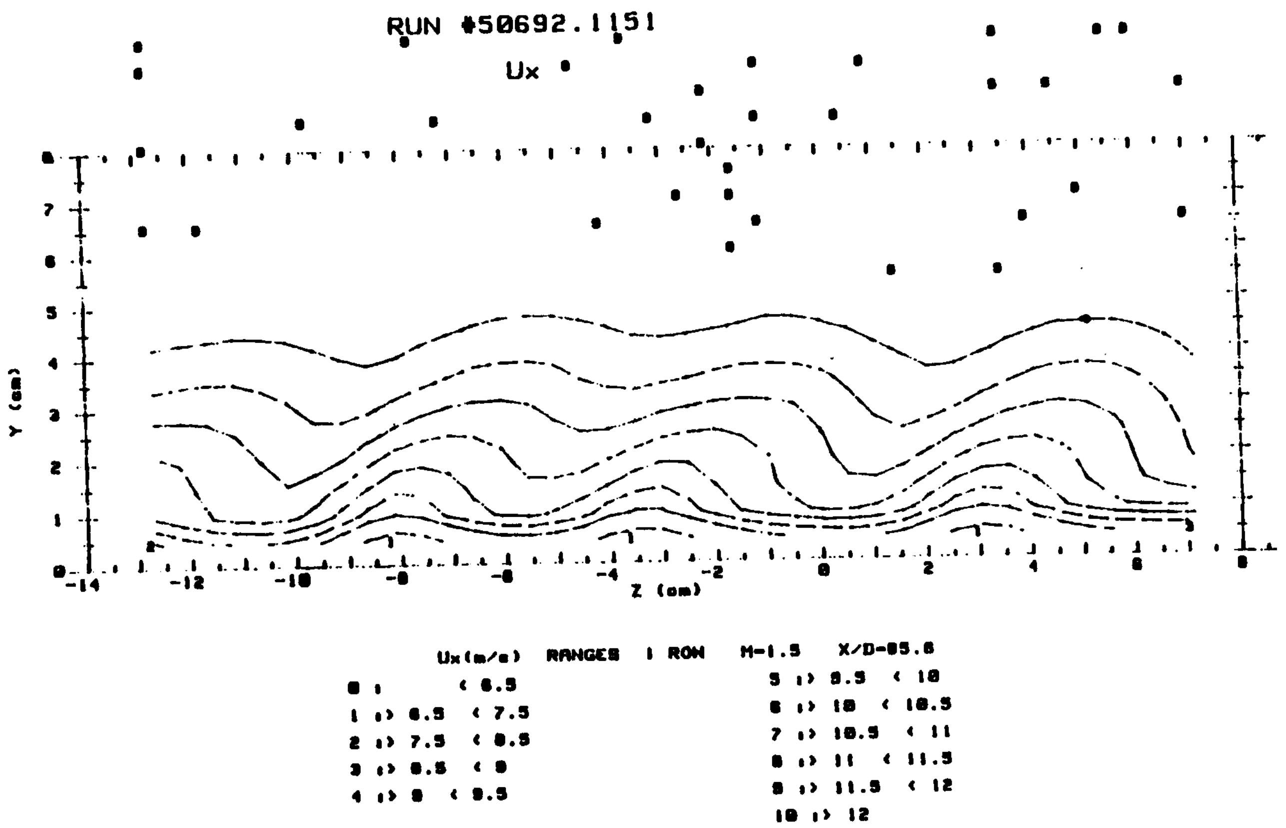

Figure 81. Streamwise Velocity Field, Compound Angle, 1 row, m=1.5, x/d=85.6

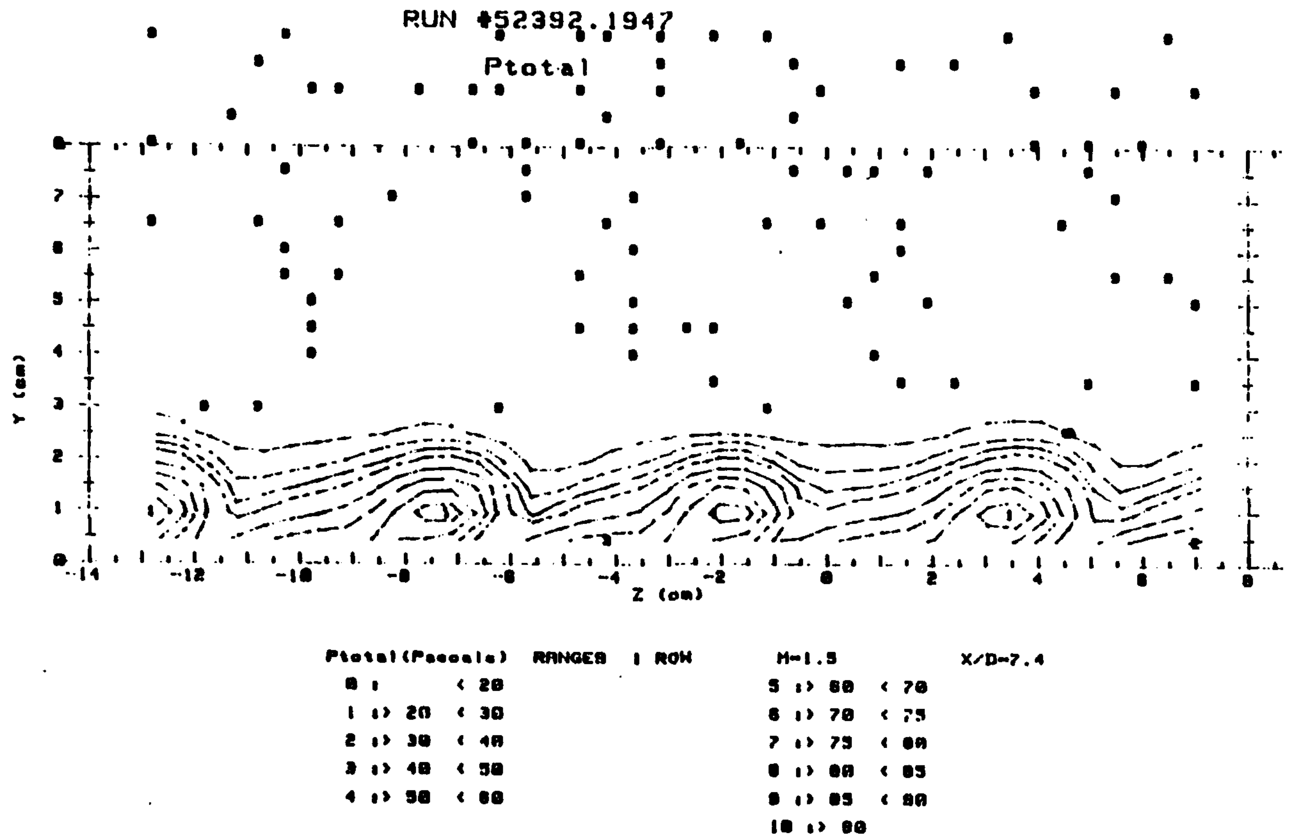

Figure 82. Streamwise Pressure Field, Compound Angle, 1 row, m=1.5, x/d=7.4

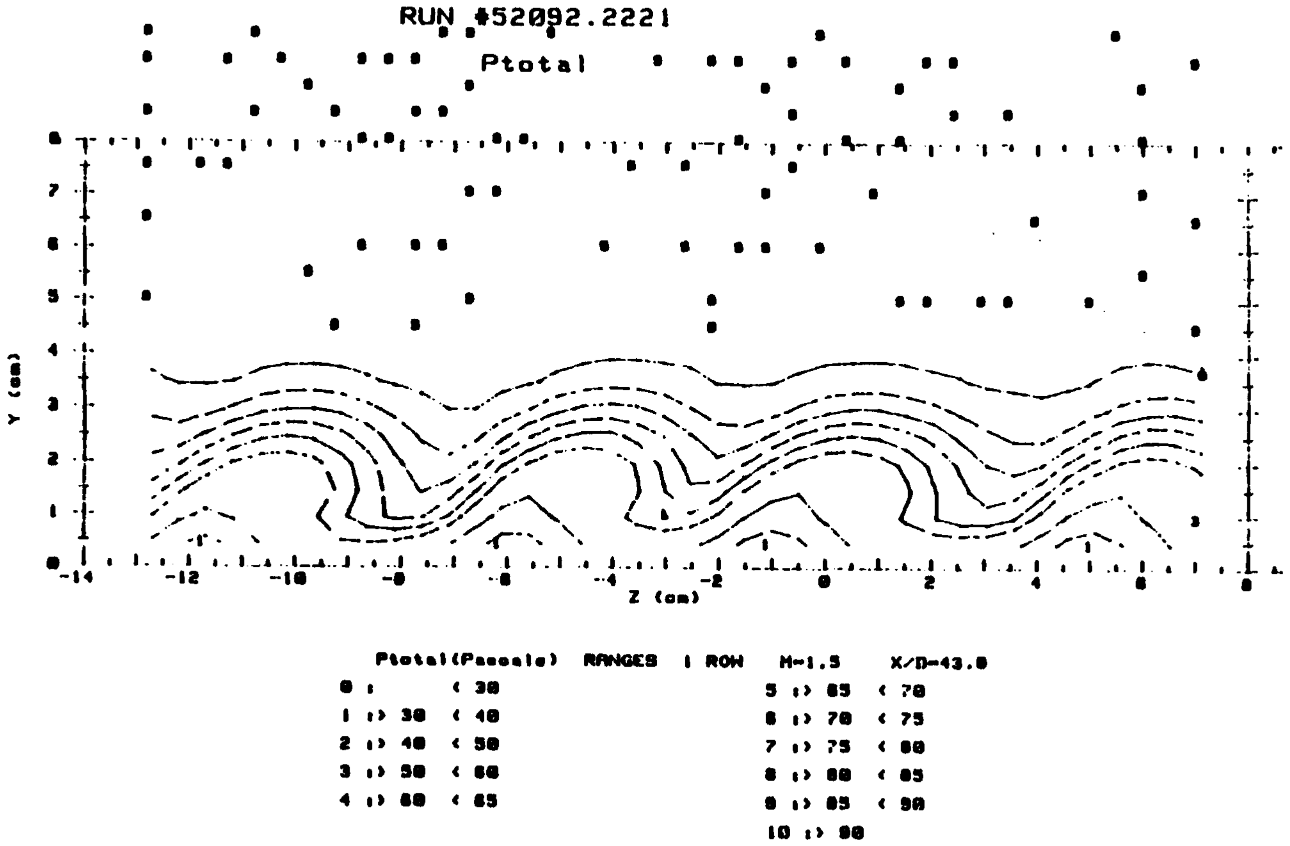

Figure 83. Streamwise Pressure Field, Compound Angle, 1 row, m=1.5, x/d=43.8

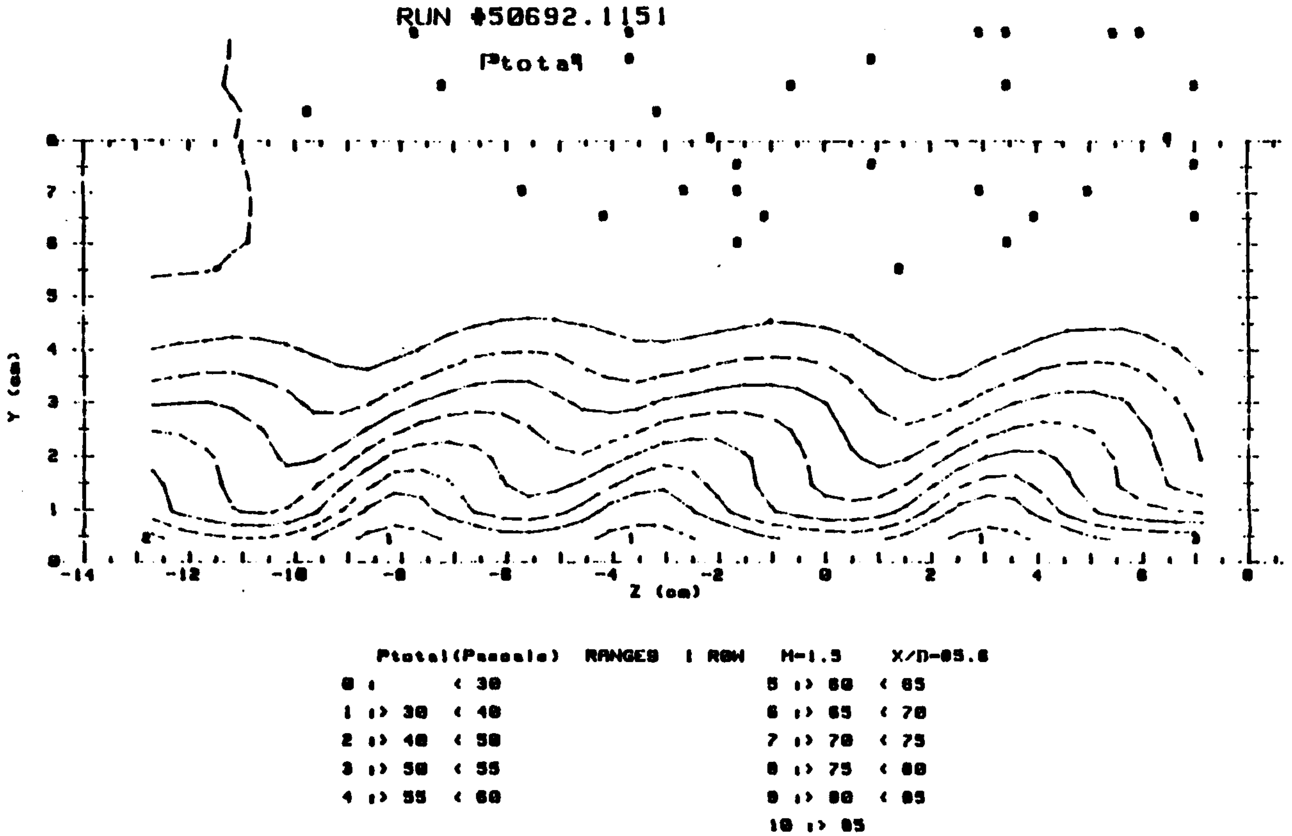

Figure 84. Streamwise Pressure Field, Compound Angle, 1 row, m=1.5, x/d=85.6

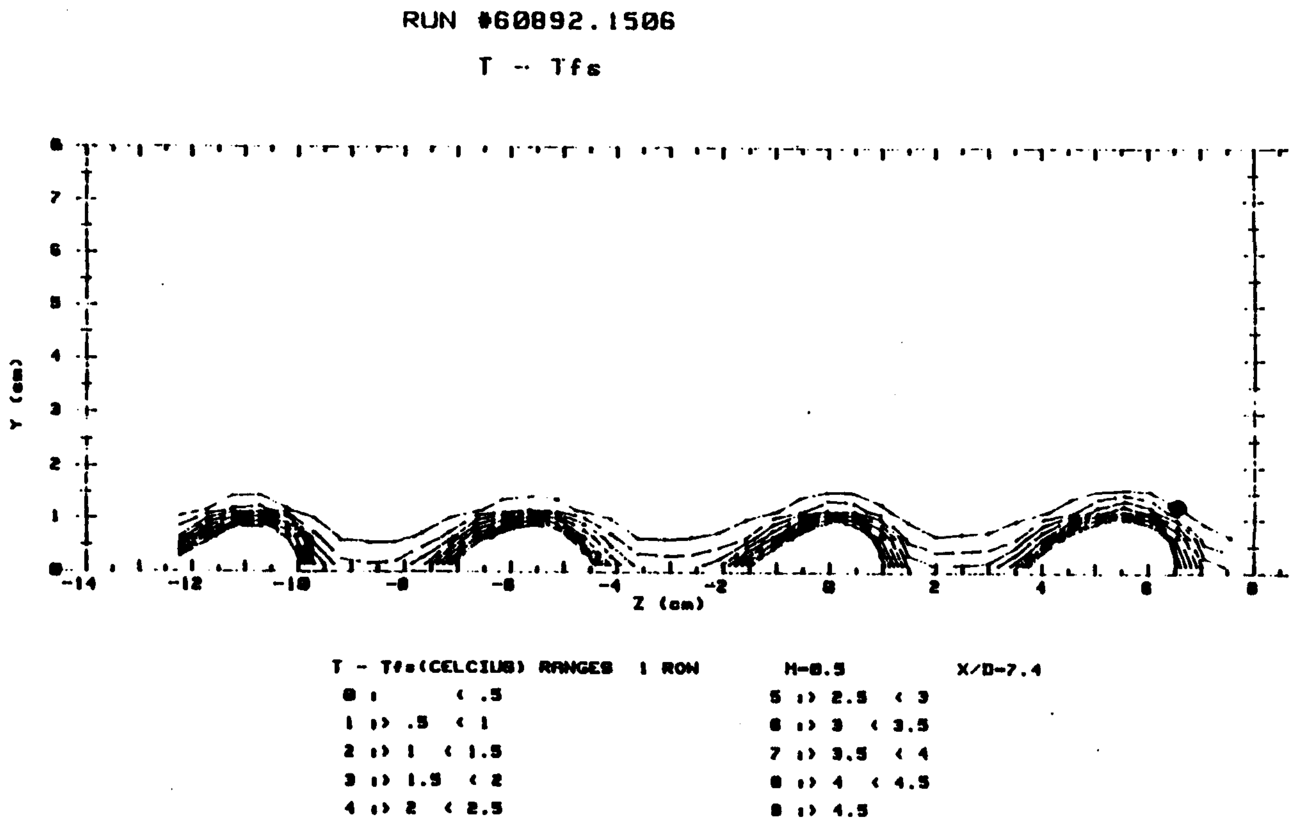

Figure 85. Streamwise Injectant Distribution, Compound Angle, 1 row, m=0.5, x/d=7.4

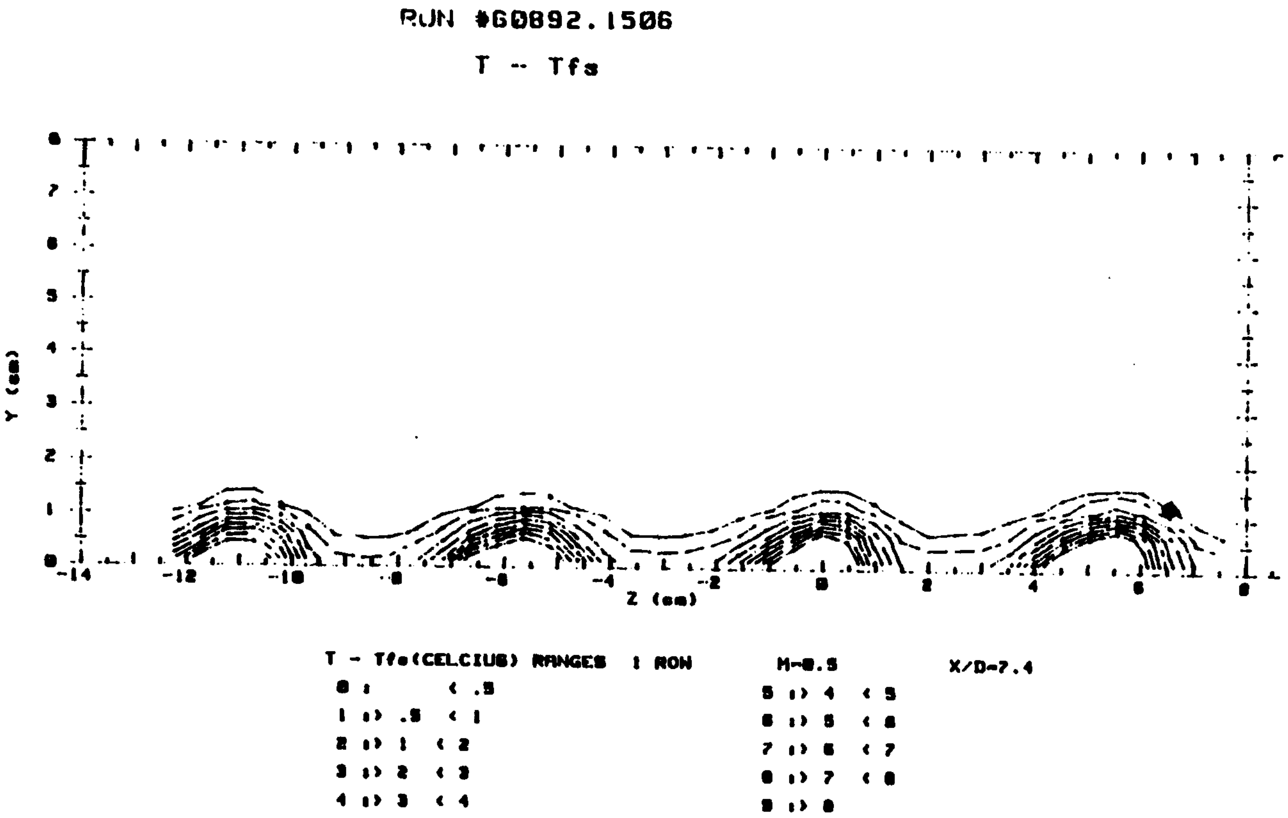

Figure 86. Streamwise Injectant Distribution, Compound Angle, 1 row (larger range), m=0.5, x/d=7.4

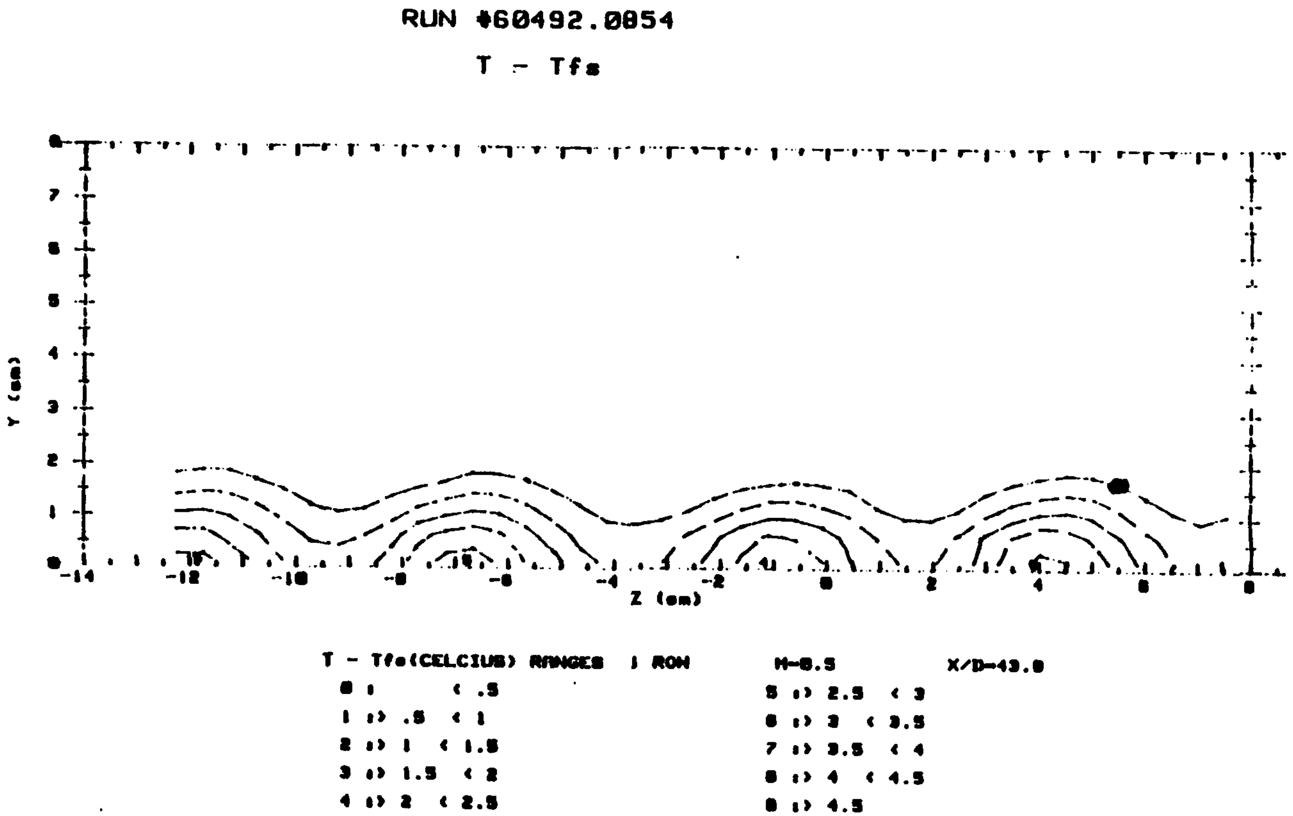

Figure 87. Streamwise Injectant Distribution, Compound Angle, 1 row, m=0.5, x/d=43.8

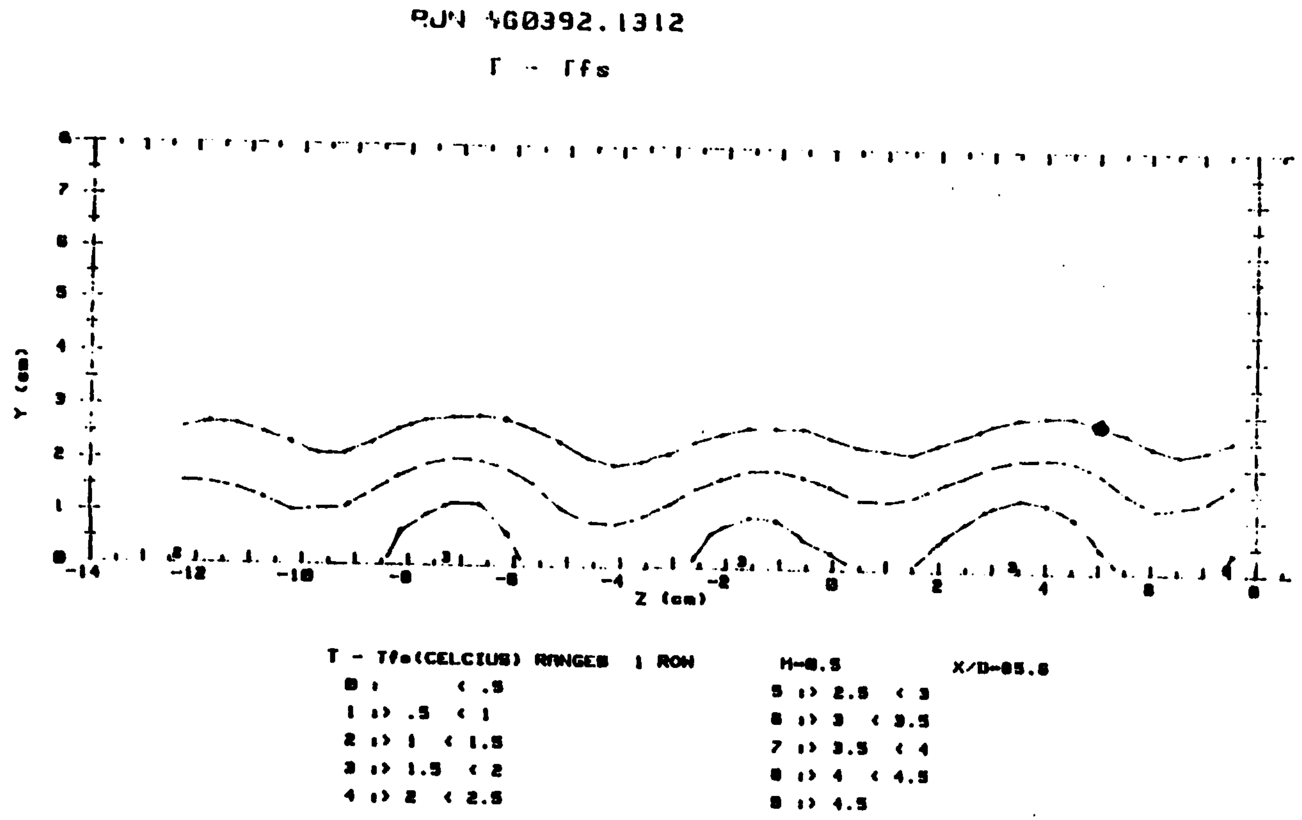

Figure 88. Streamwise Injectant Distribution, Compound Angle, 1 row, m=0.5, x/d=85.6

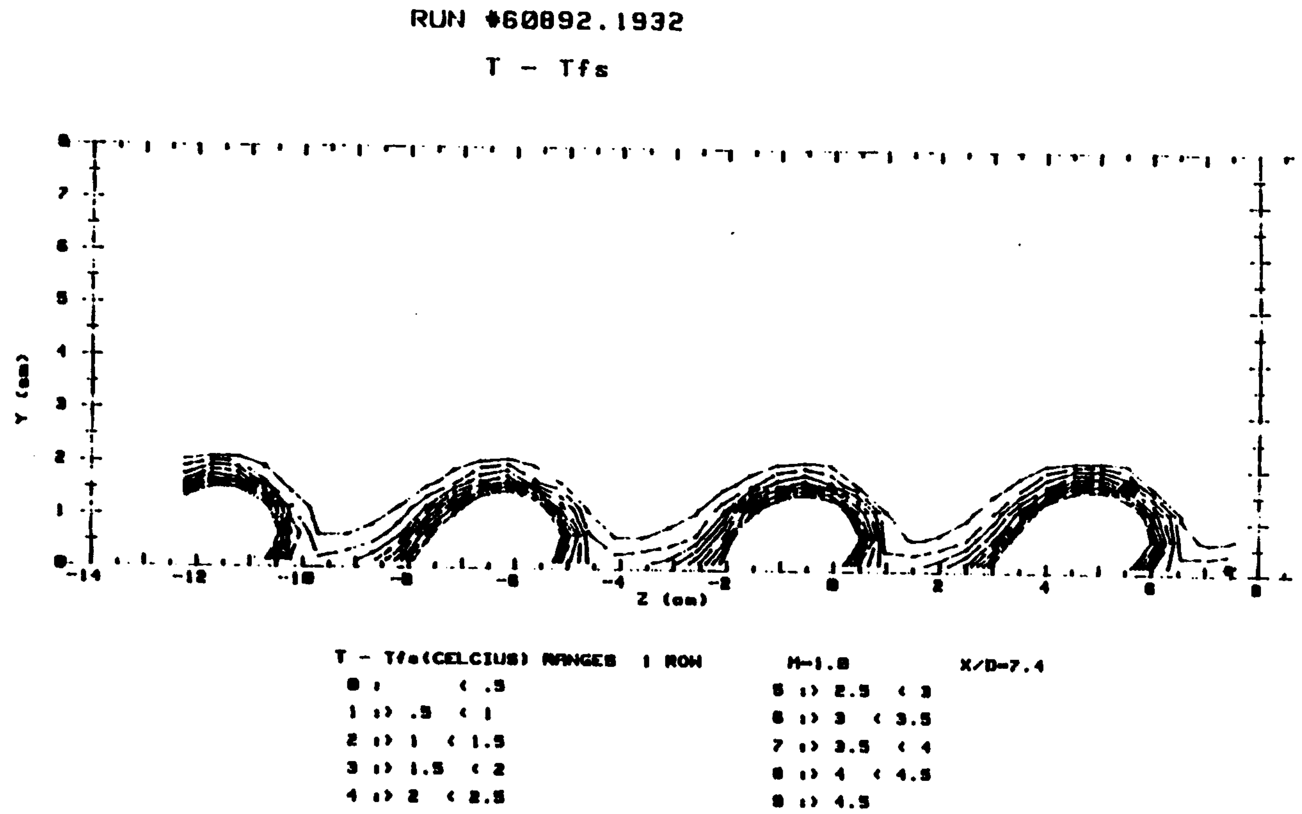

Figure 89. Streamwise Injectant Distribution, Compound Angle, 1 row, m=1.0, x/d=7.4

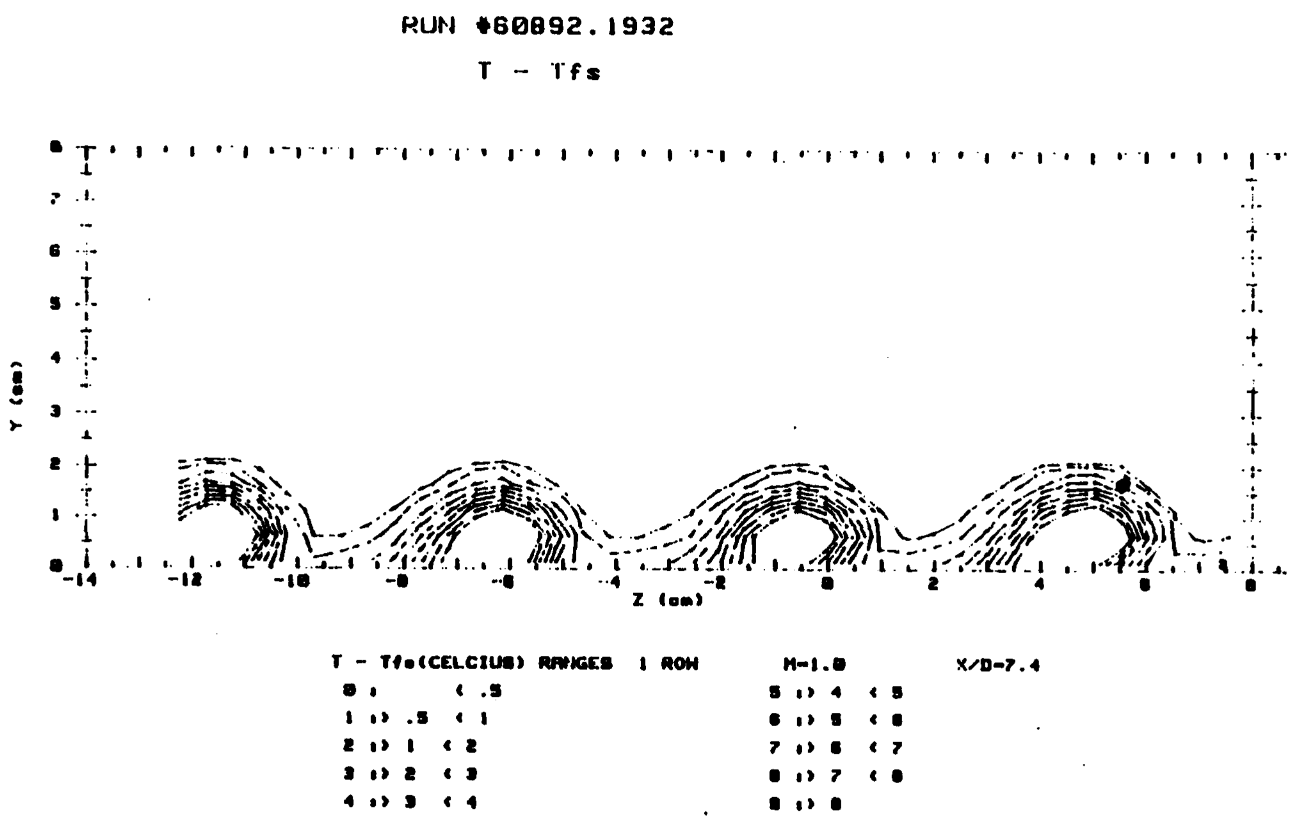

Figure 90. Streamwise Injectant Distribution, Compound Angle, 1 row (larger range), m=1.0, x/d=7.4

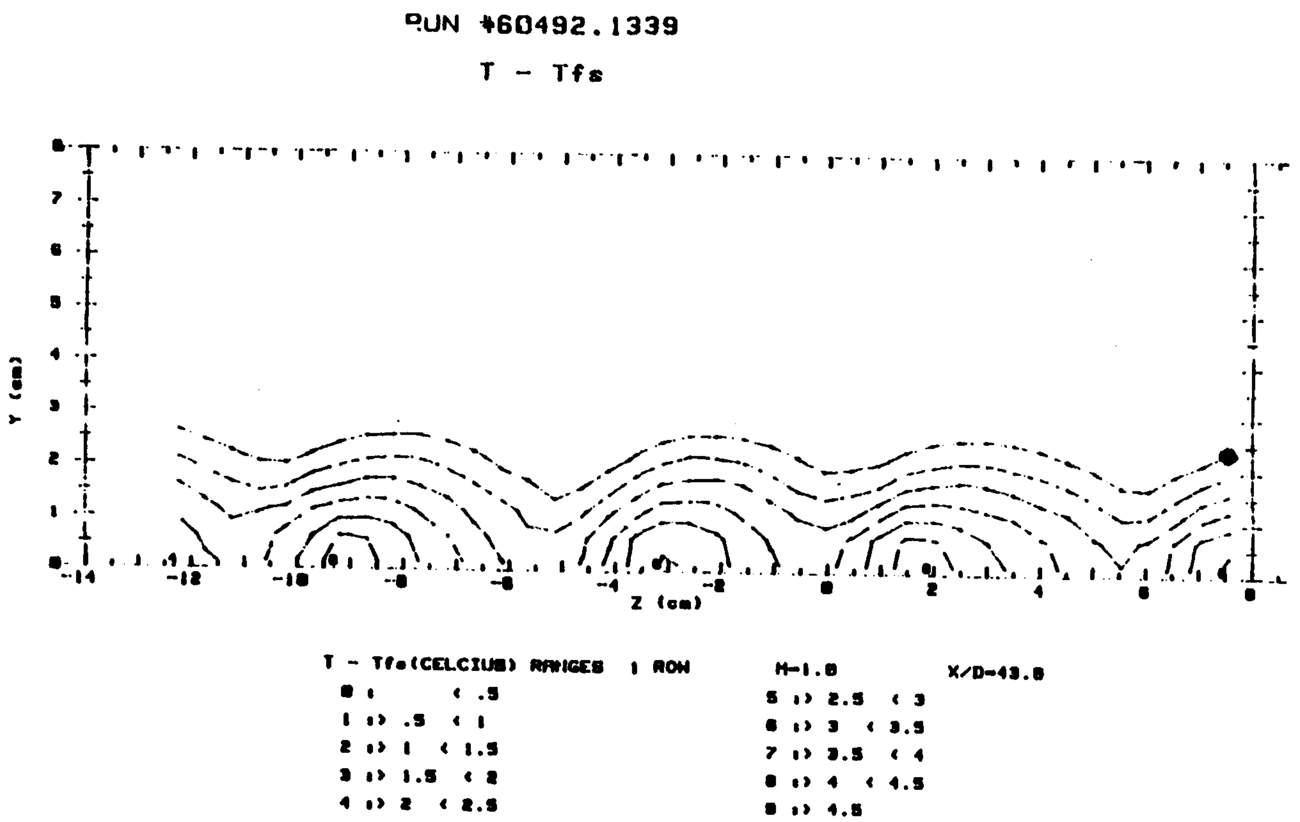

Figure 91. Streamwise Injectant Distribution, Compound Angle, 1 row, m=1.0, x/d=43.8

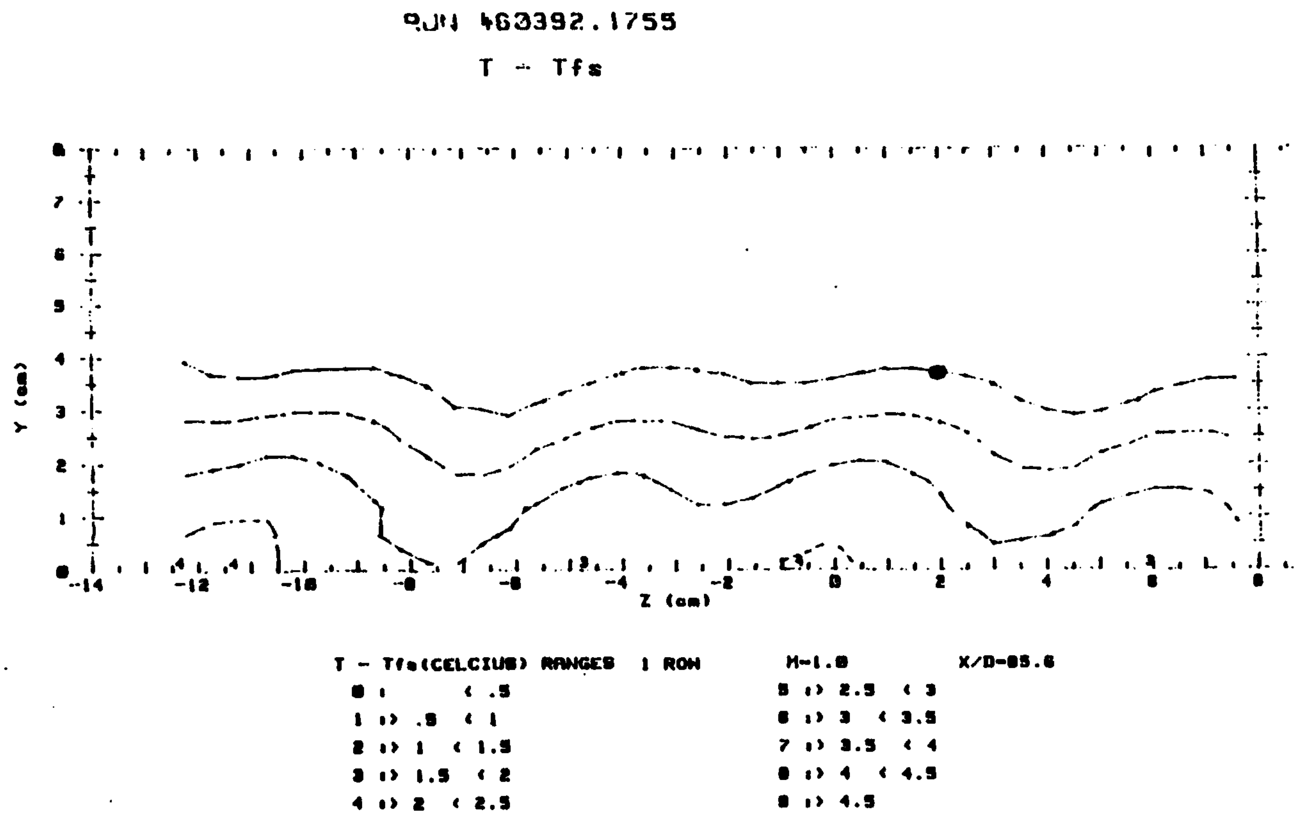

Figure 92. Streamwise Injectant Distribution, Compound Angle, 1 row, m=1.0, x/d=85.6

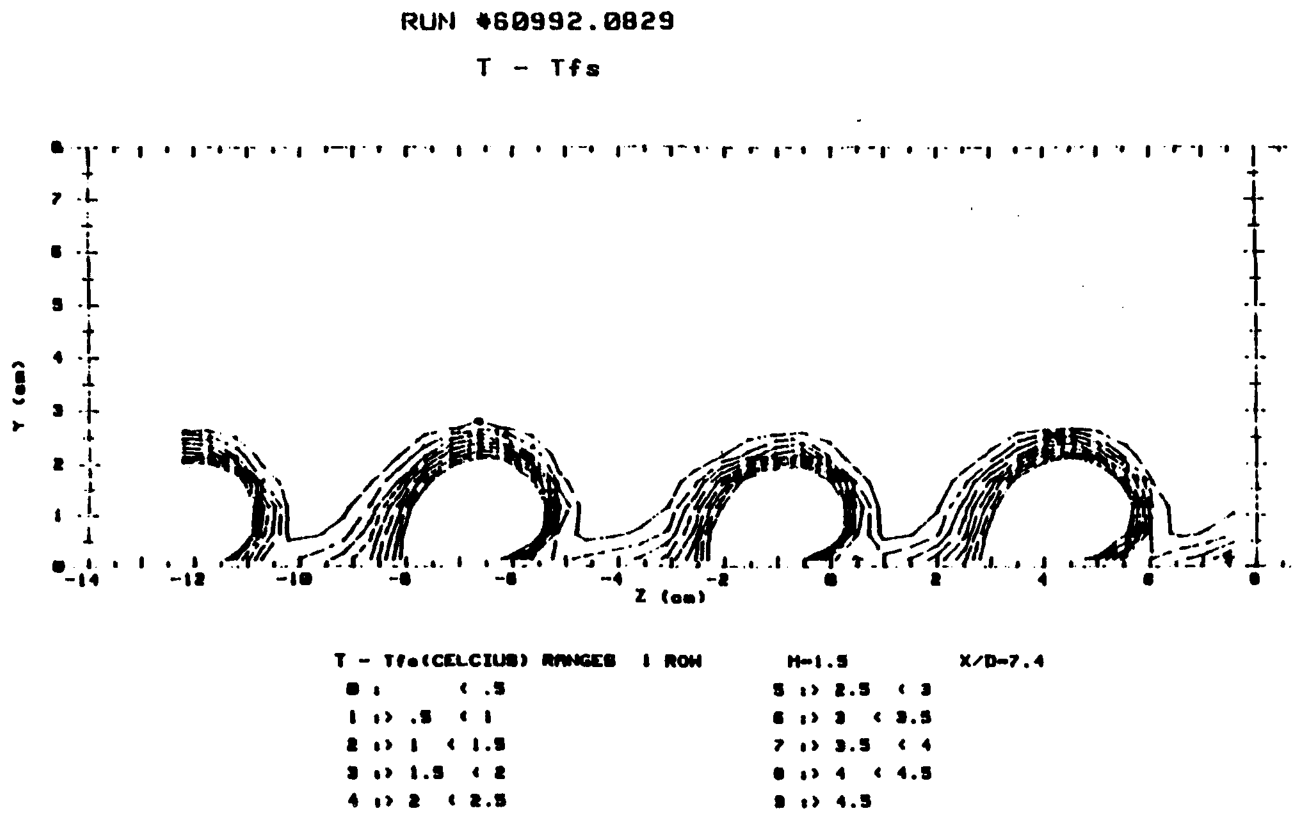

Figure 93. Streamwise Injectant Distribution, Compound Angle, 1 row, m=1.5, x/d=7.4

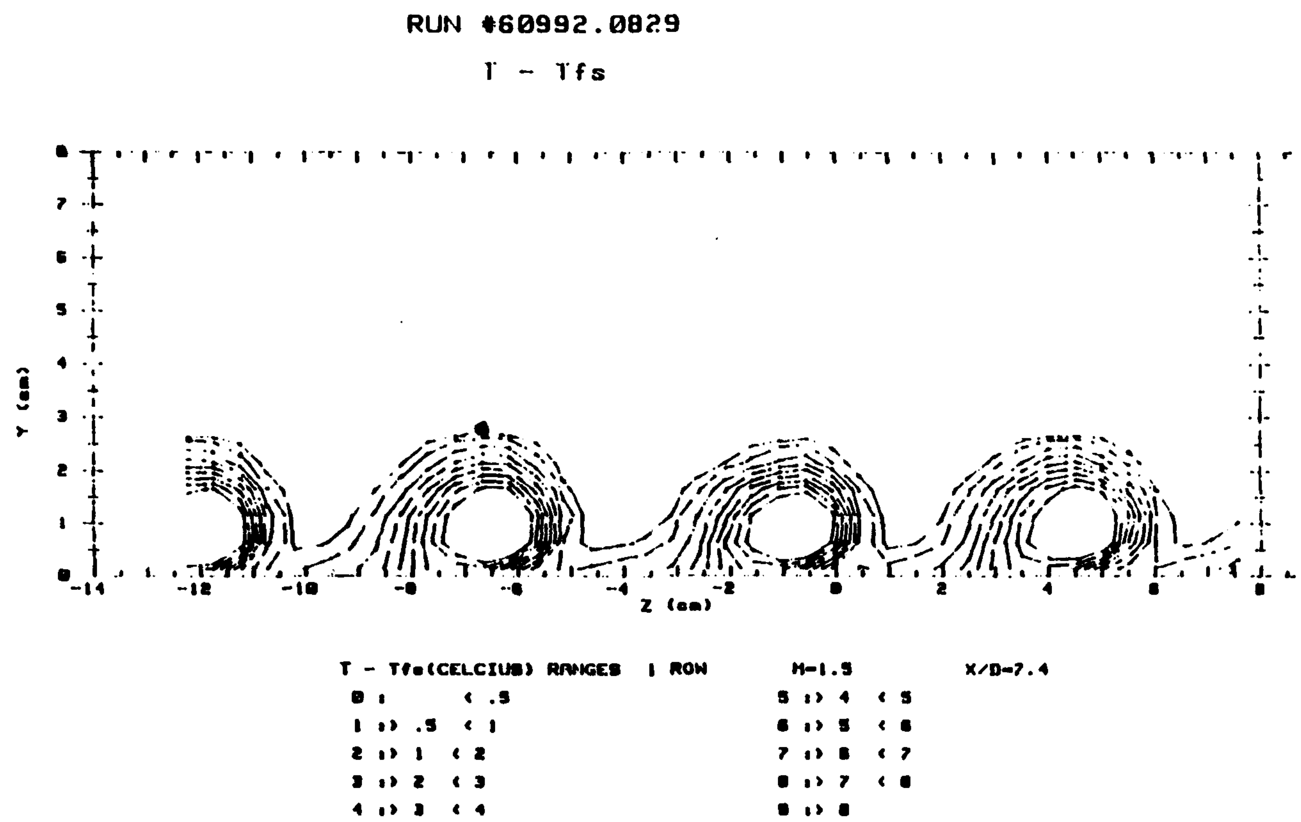

Figure 94. Streamwise Injectant Distribution, Compound Angle, 1 row (larger range), m=1.5, x/d=7.4

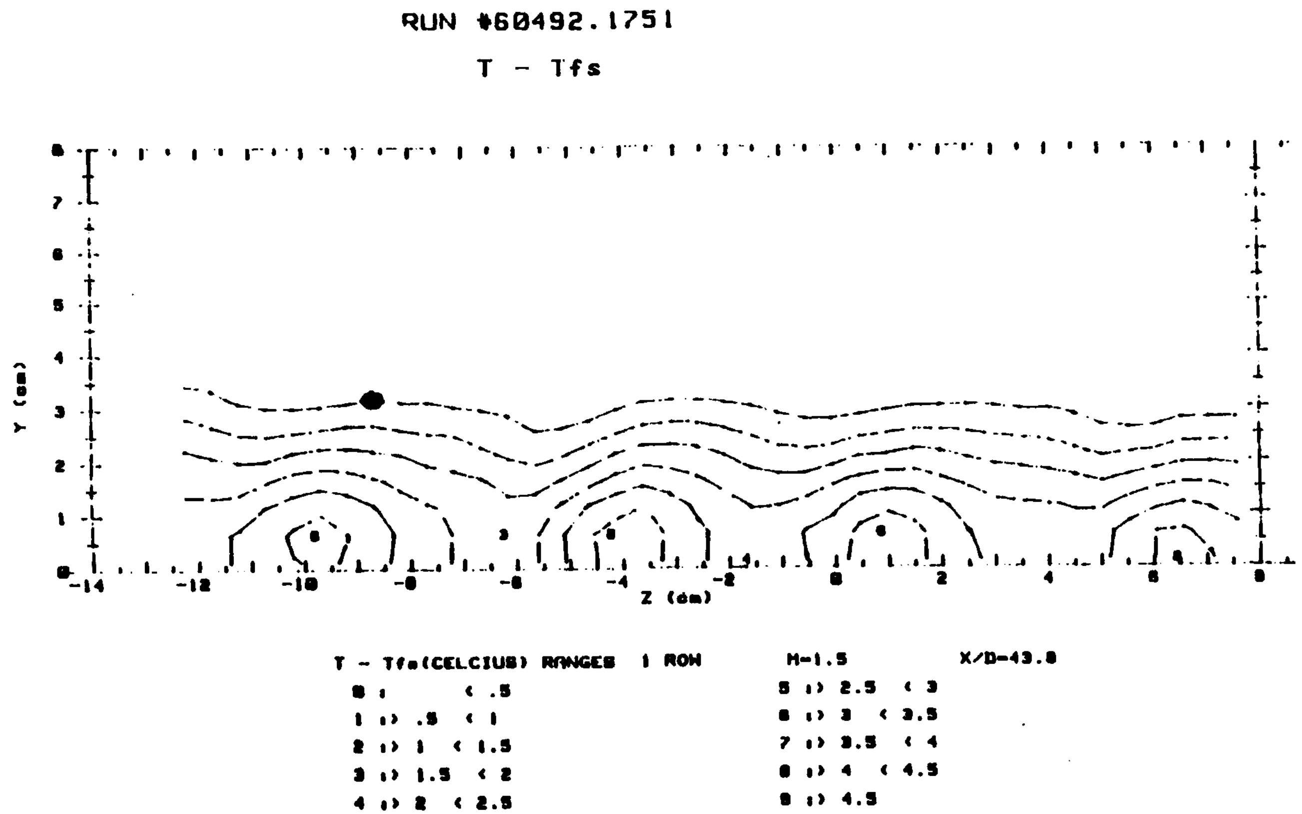

Figure 95. Streamwise Injectant Distribution, Compound Angle, 1 row, m=1.5, x/d=43.8

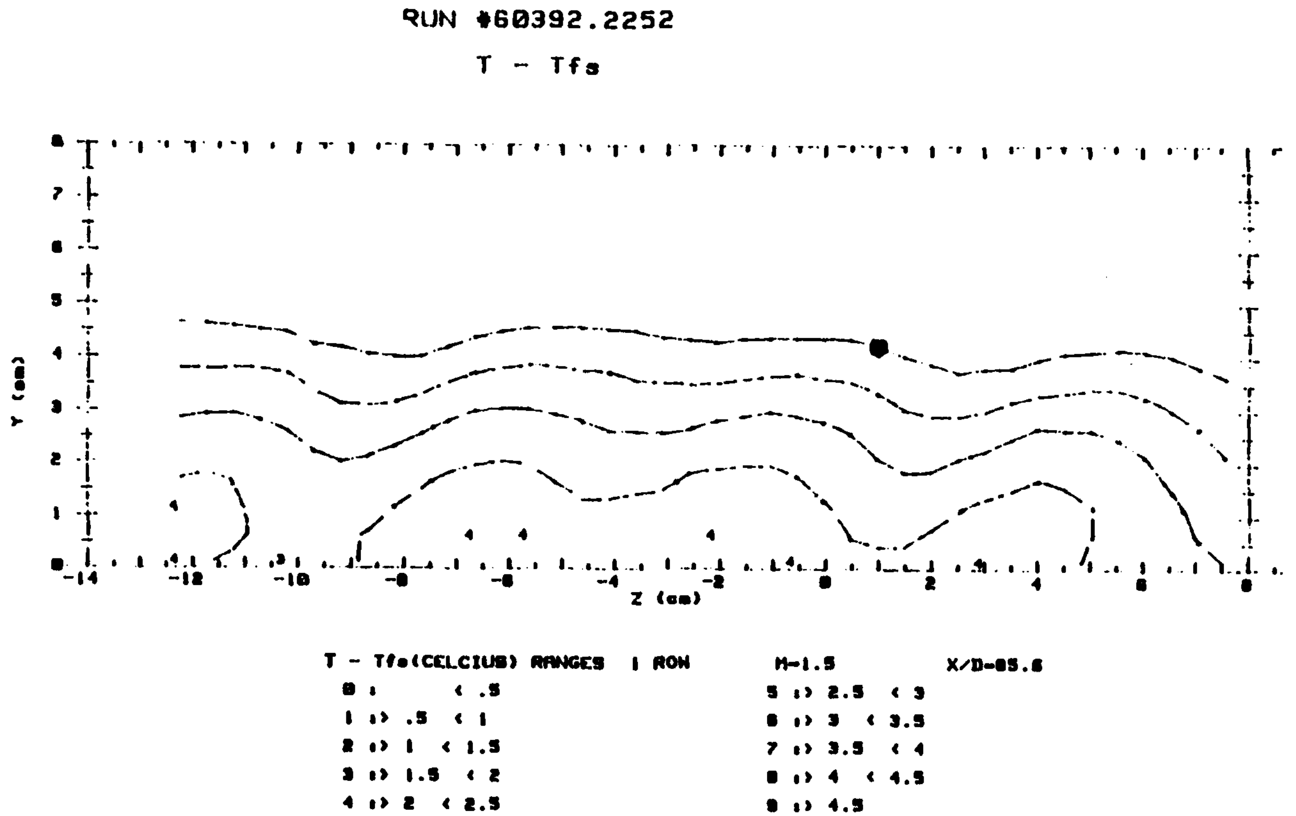

Figure 96. Streamwise Injectant Distribution, Compound Angle, 1 row, m=1.5, x/d=85.6

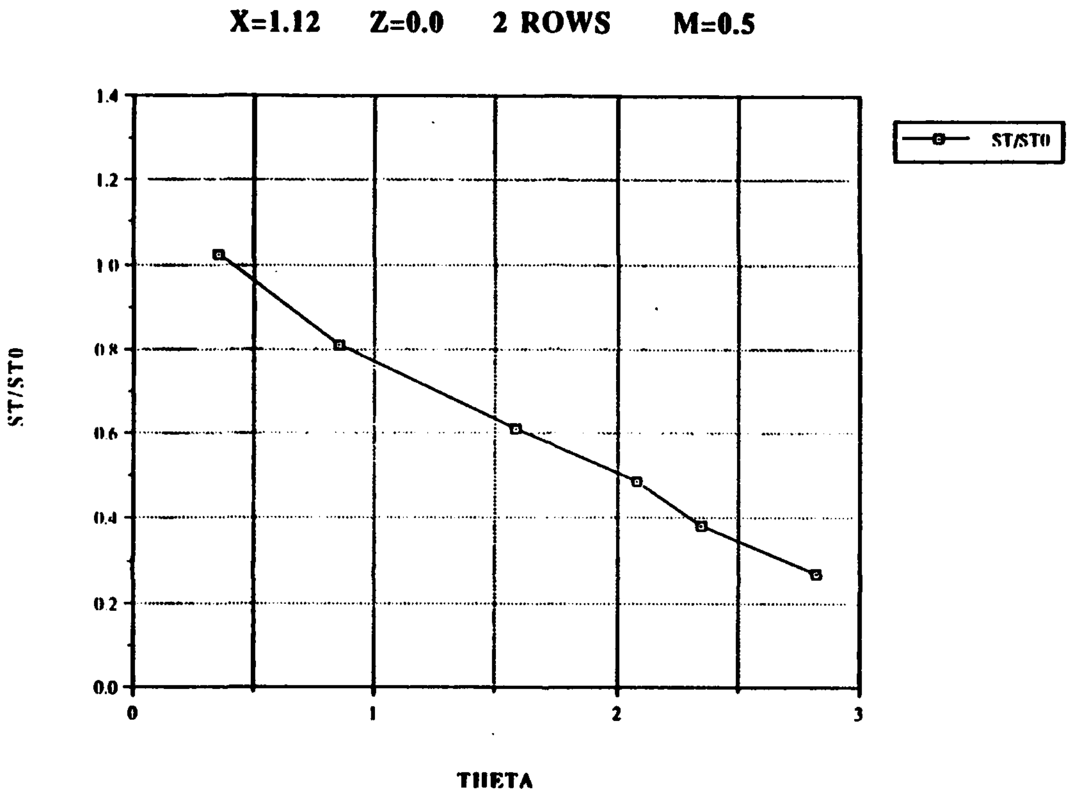

Figure 97. St/St$_0$ vs θ, Compound Angle,2 rows,m=0.5, X=1.12,Z=0.0 m

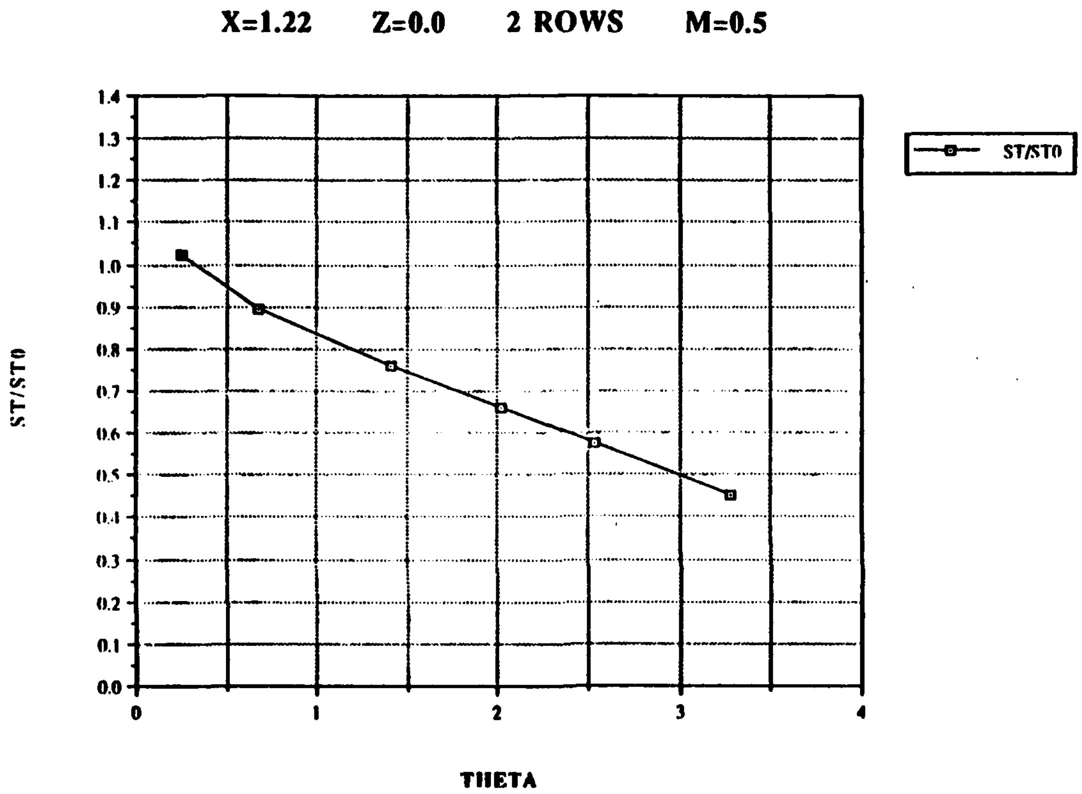

Figure 98. St/St_o vs θ, Compound Angle,2 rows, m=0.5,X=1.22,Z=0.0 m

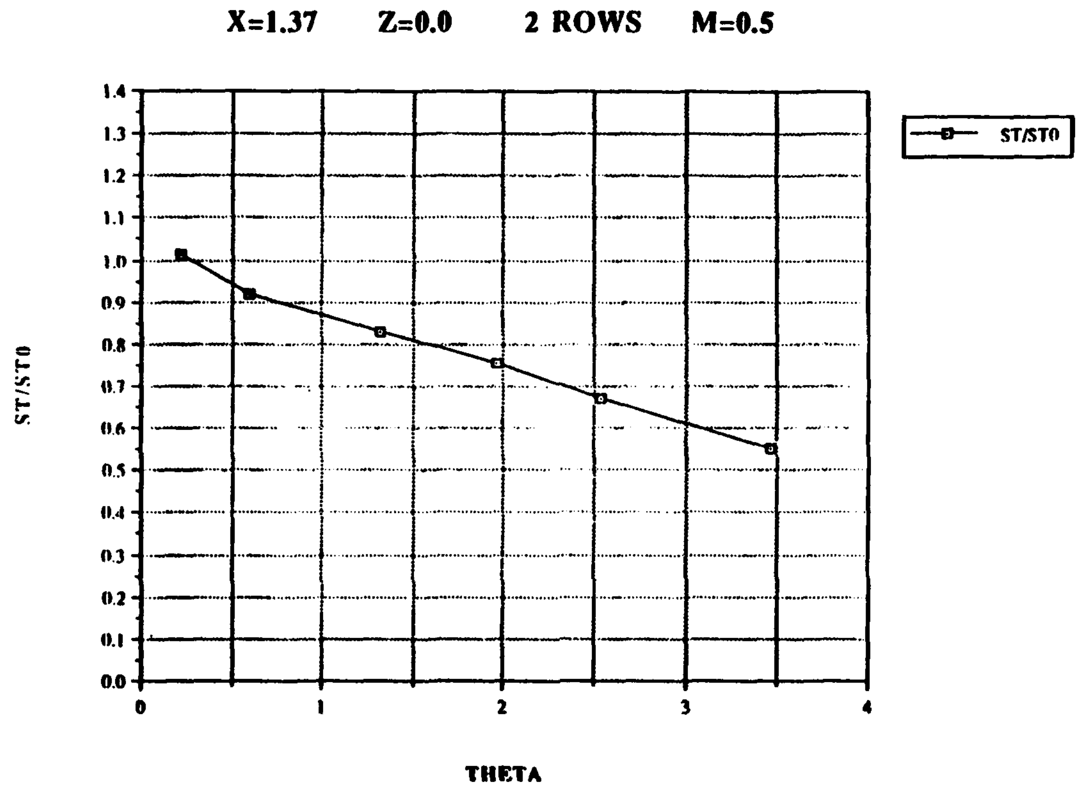

Figure 99. St/St_0 vs θ, Compound Angle,2 rows,m=0.5,X=1.37, Z=0.0 m

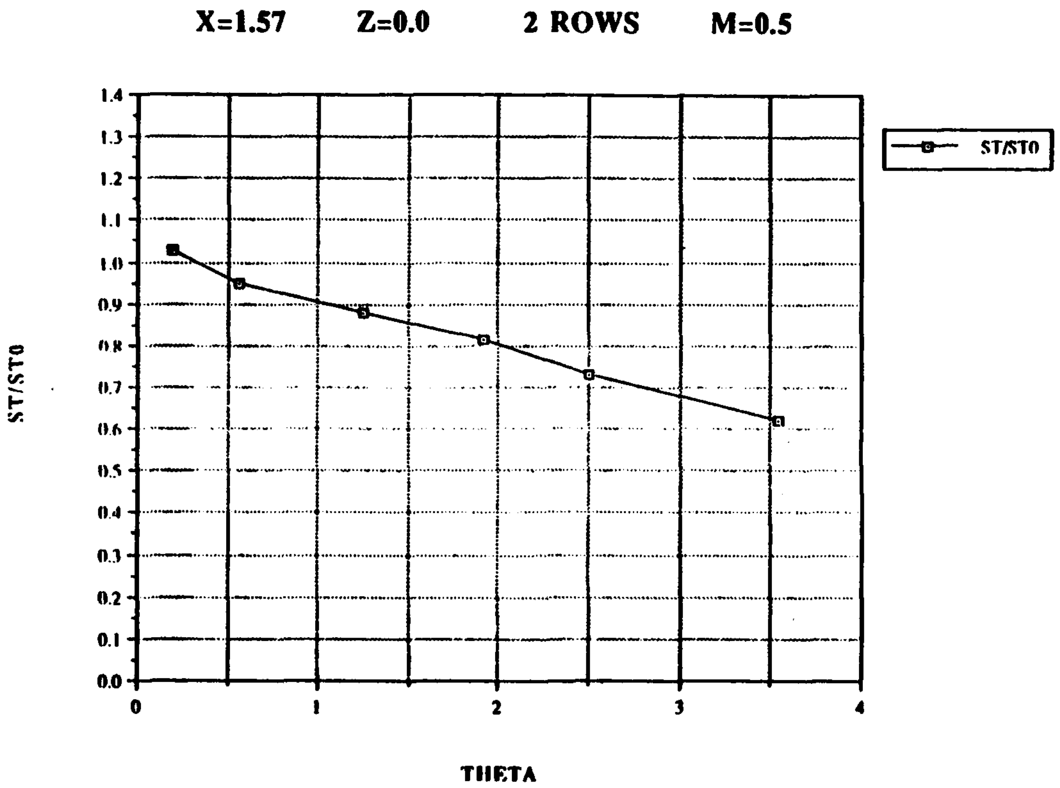

Figure 100. St/St_0 vs θ, Compound Angle,2 rows,m=0.5,X=1.57,Z=0.0 m

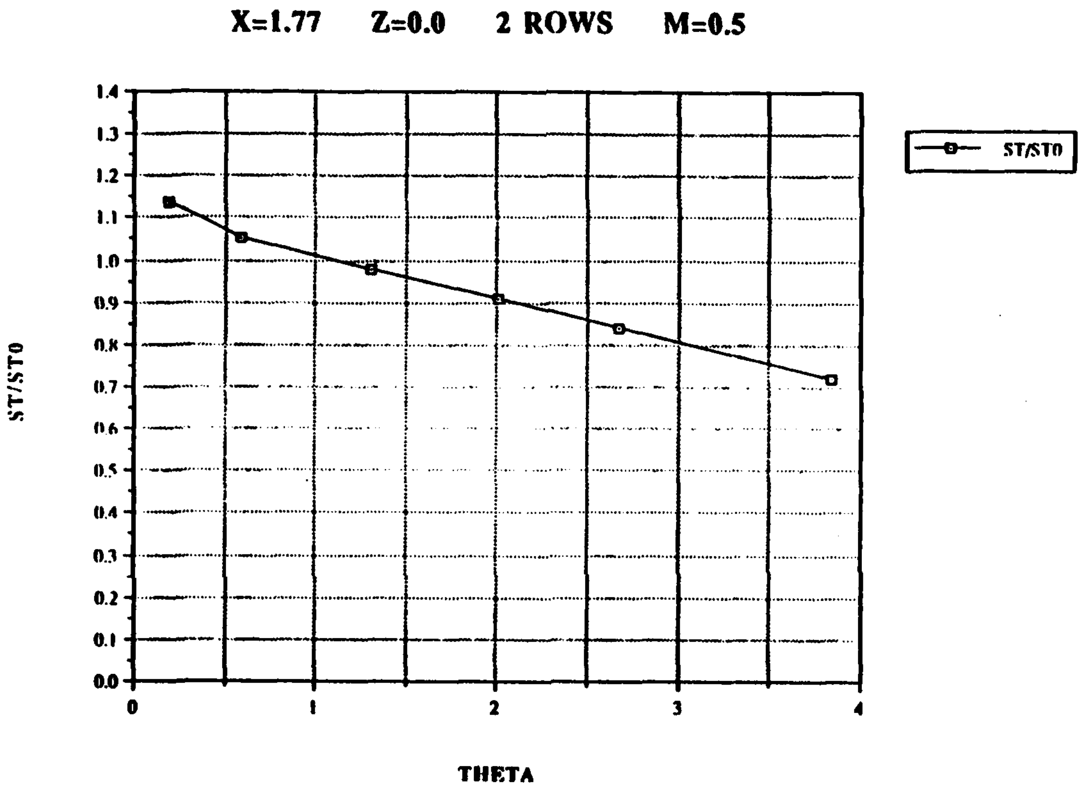

Figure 101. St/St_0 vs θ, Compound Angle,2 rows,m=0.5,X=1.77,Z=0.0 m

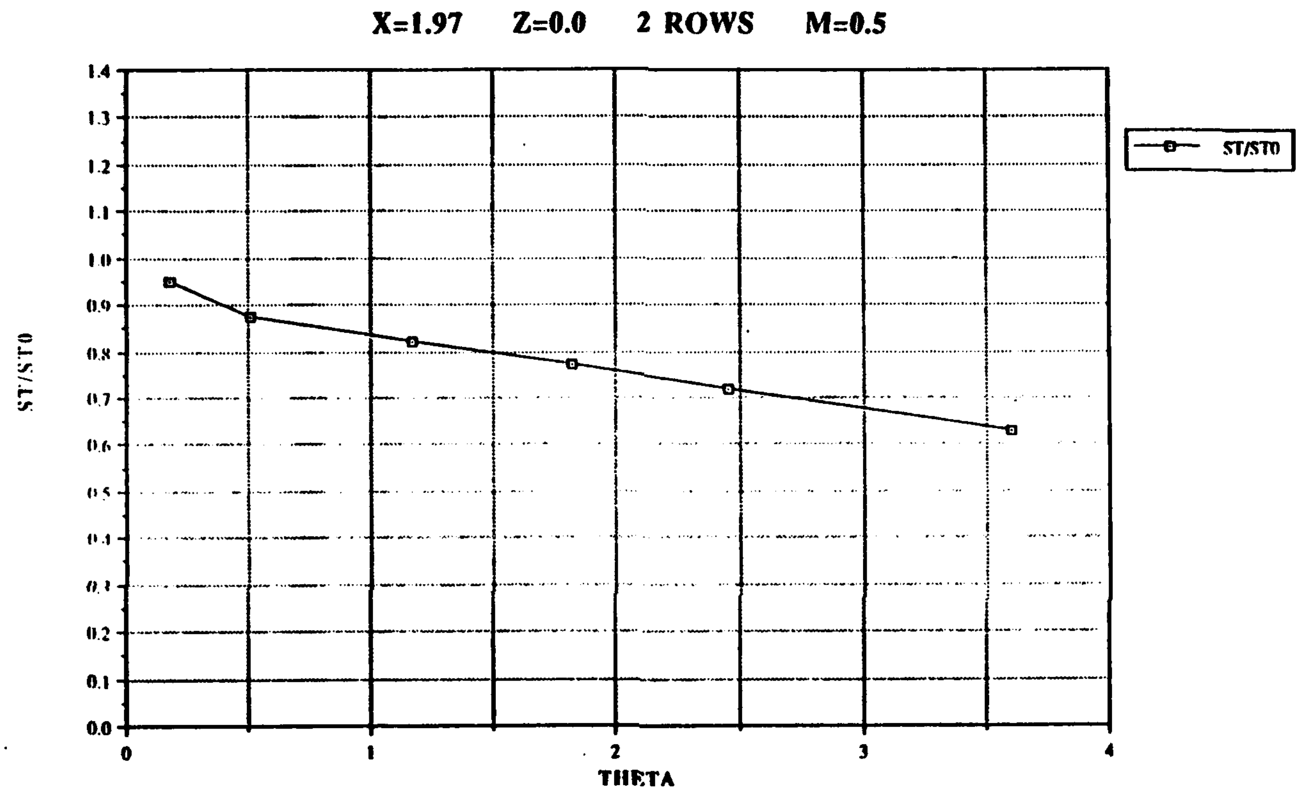

Figure 102. St/St_o vs θ, Compound Angle,2 rows,m=0.5,X=1.97,Z=0.0 m

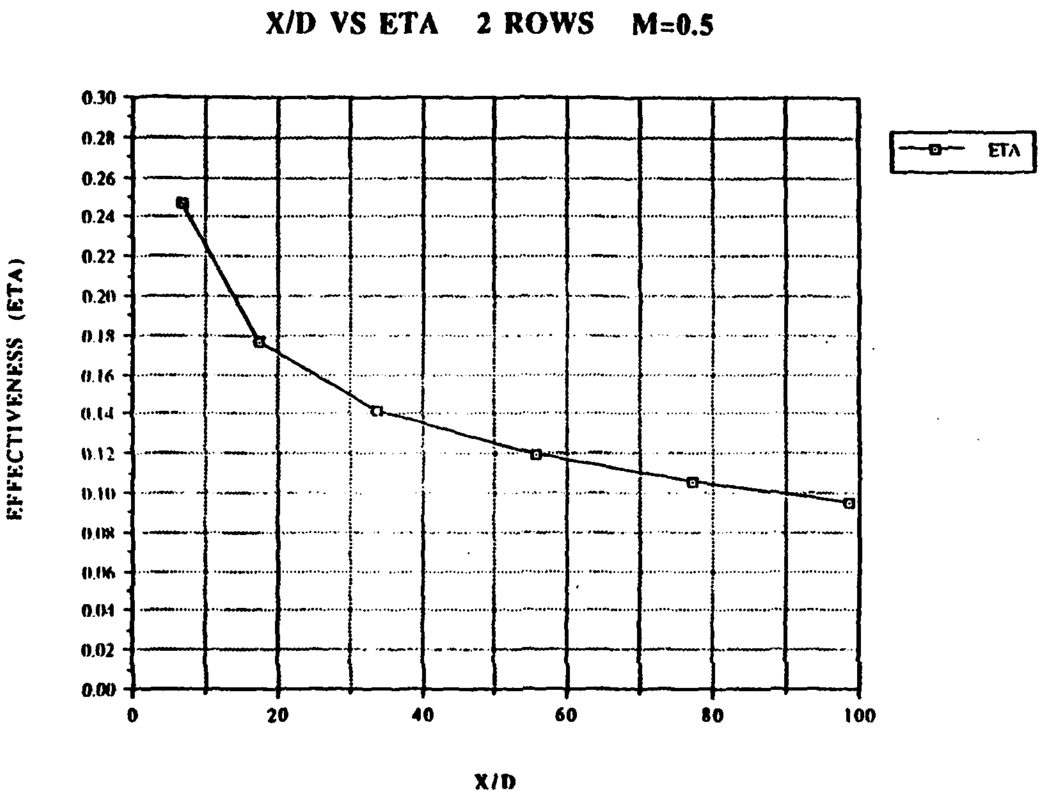

Figure 103. $\overline{\eta}$ vs x/d, Compound Angle, 2 rows, m=0.5, Spanwise Average

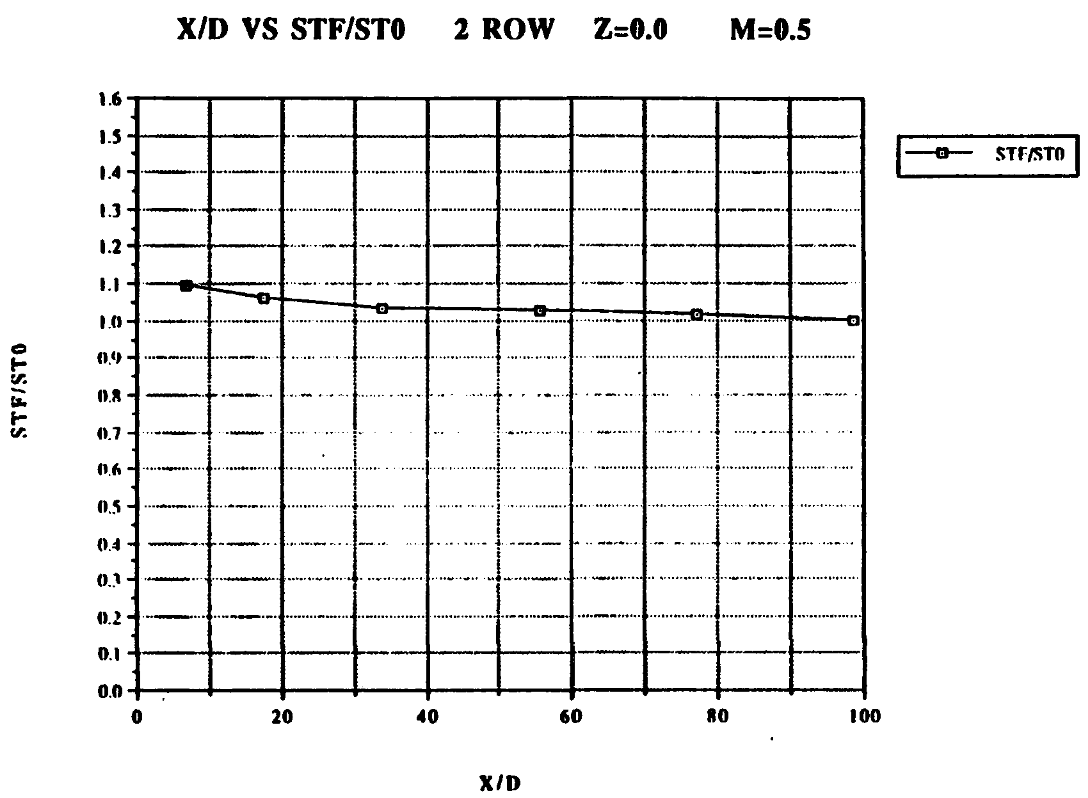

Figure 104. $\overline{St_f / St_o}$ vs x/d, Compound Angle, 2 rows, m=0.5, Spanwise Average

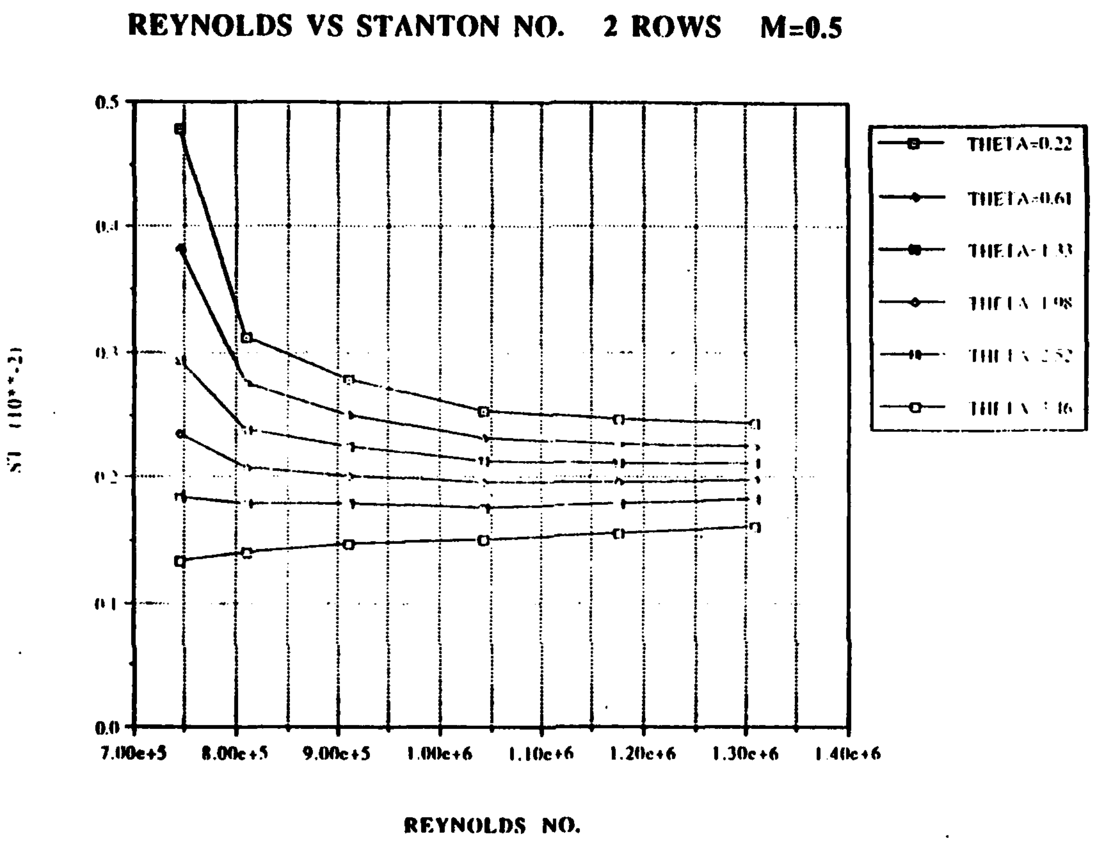

Figure 105. Spanwise averaged Stanton number vs Reynolds number, comparison of different θ values, 2 rows, m=0.5

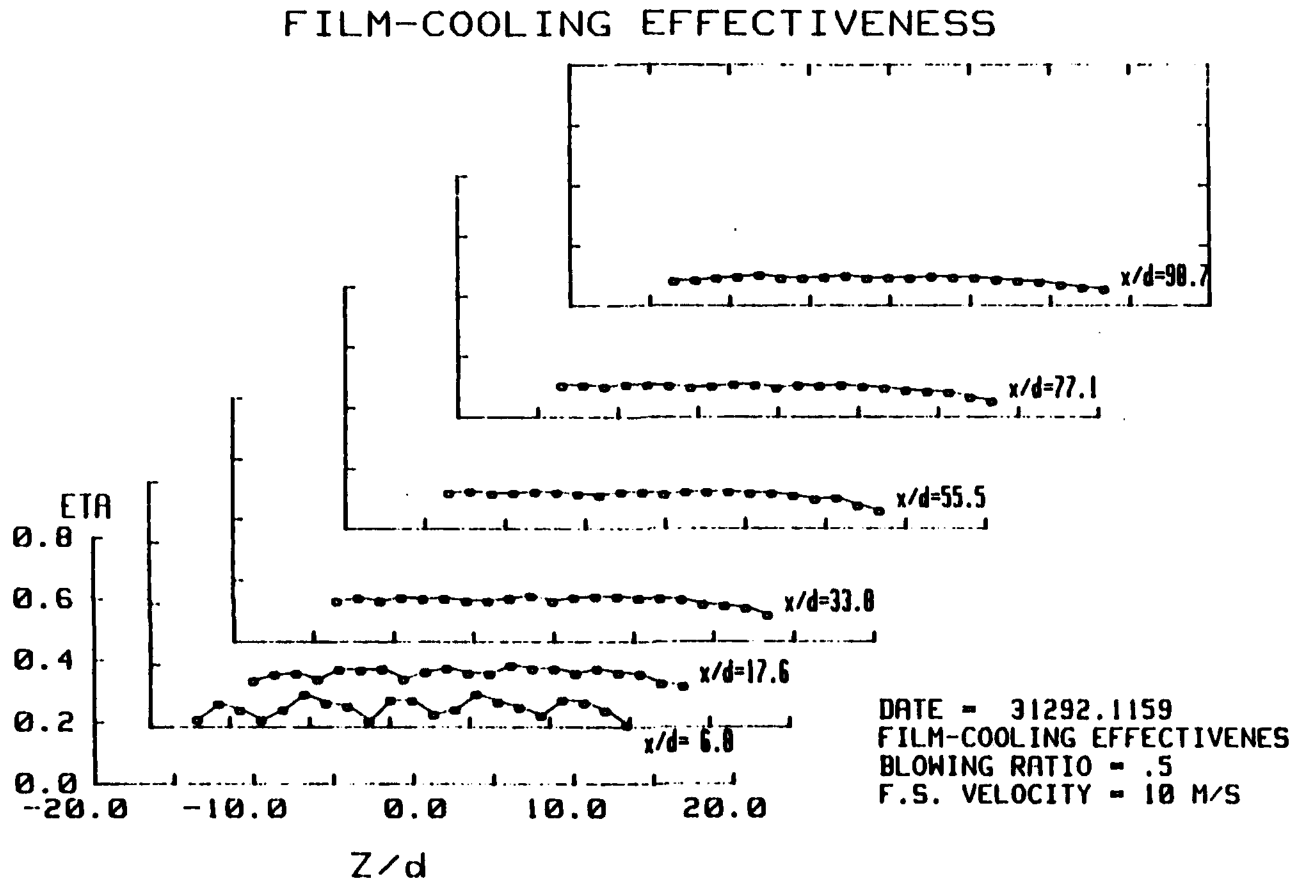

Figure 106. Spanwise Variation of η, Compound Angle, 2 rows, m=0.5

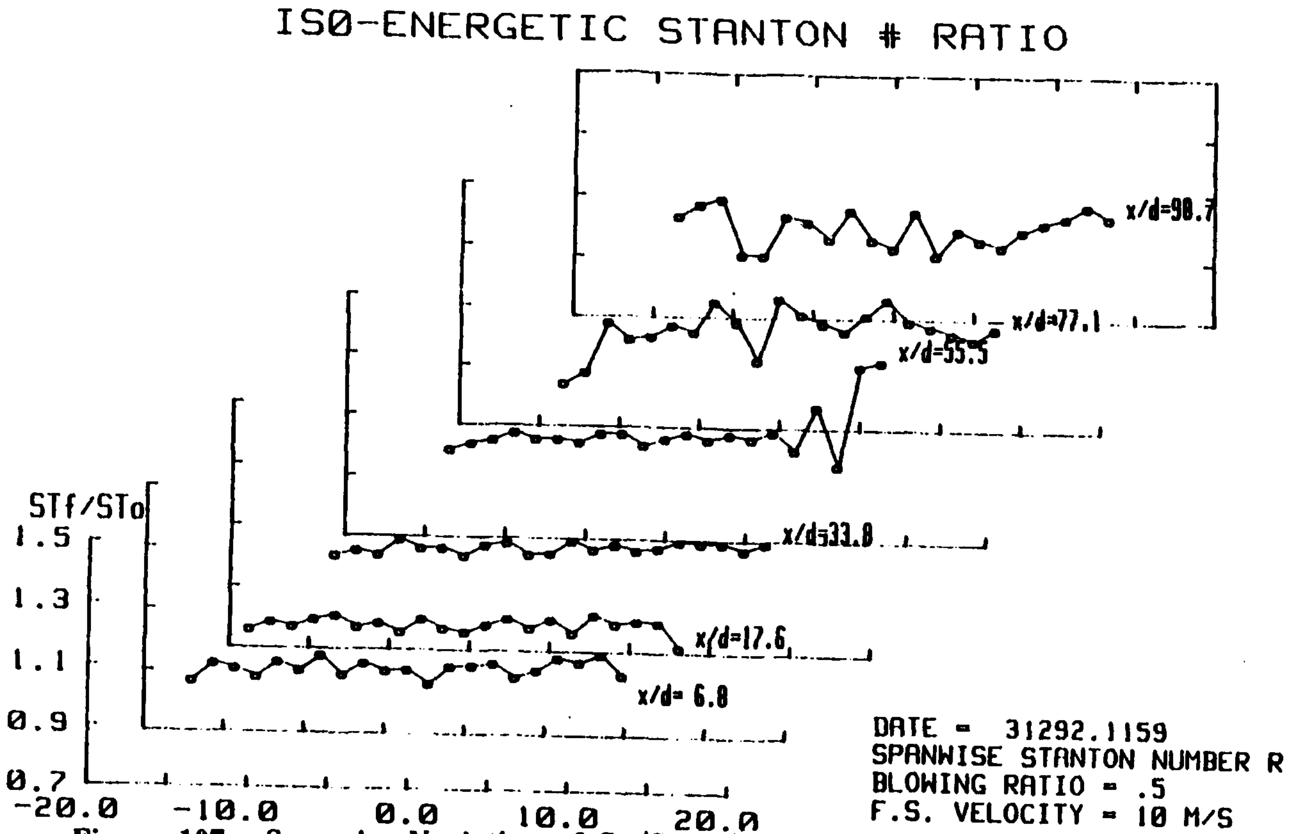

Figure 107. Spanwise Variation of St_f/St_o, Compound Angle, 2 rows, m=0.5

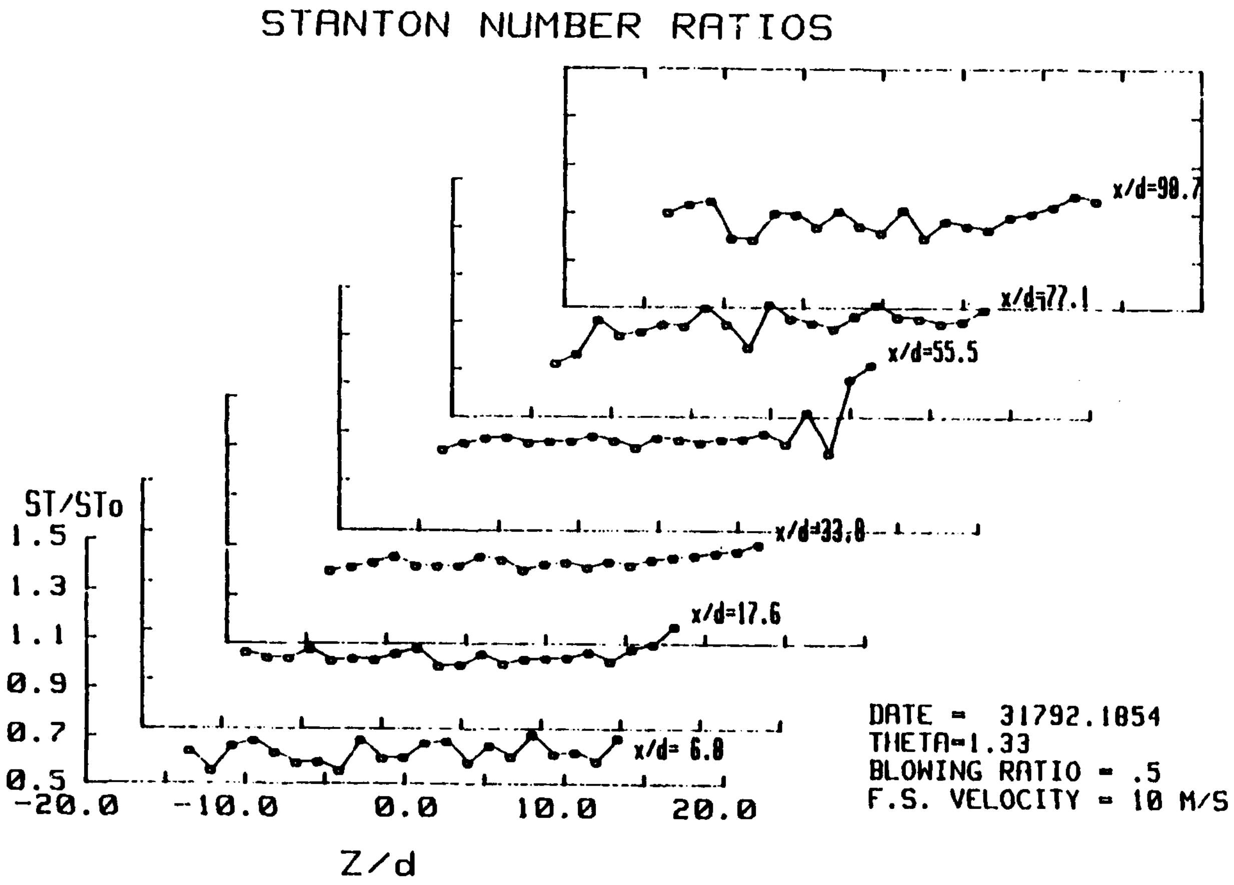

Figure 108. Spanwise Variation of St/St_0, Compound Angle, 2 rows, $m=0.5$, $\theta=1.33$

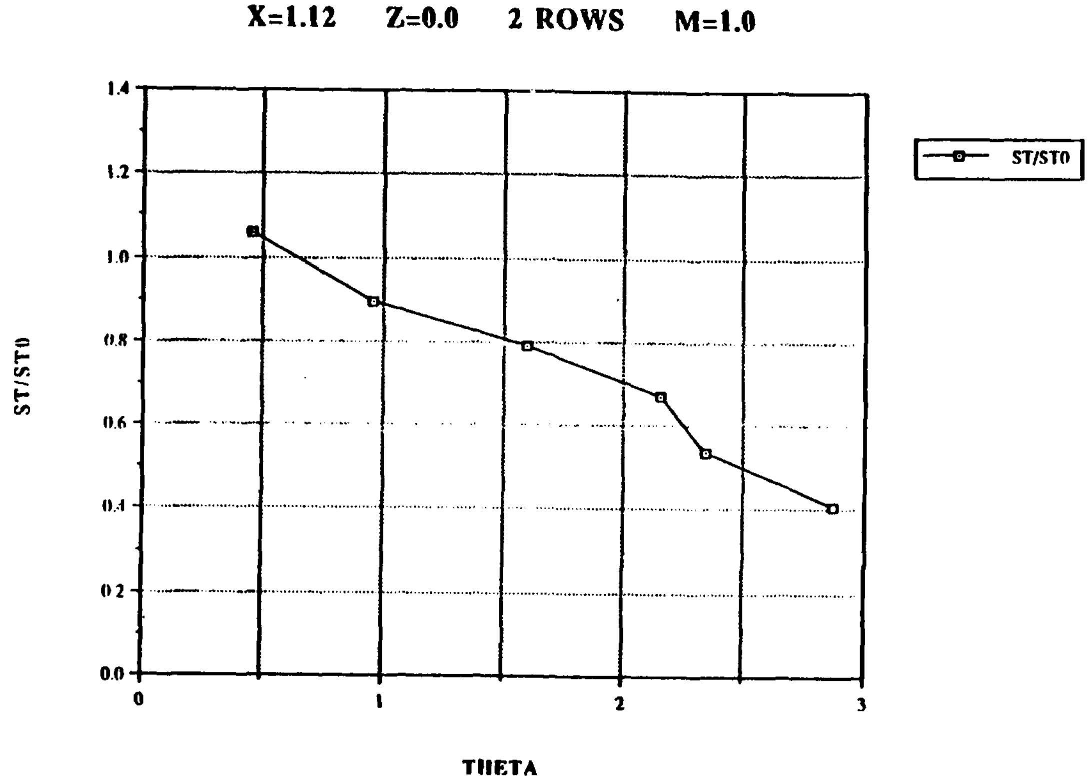

Figure 109. St/St$_0$ vs θ, Compound Angle,2 rows,m=1.0,X=1.12,Z=0.0 m

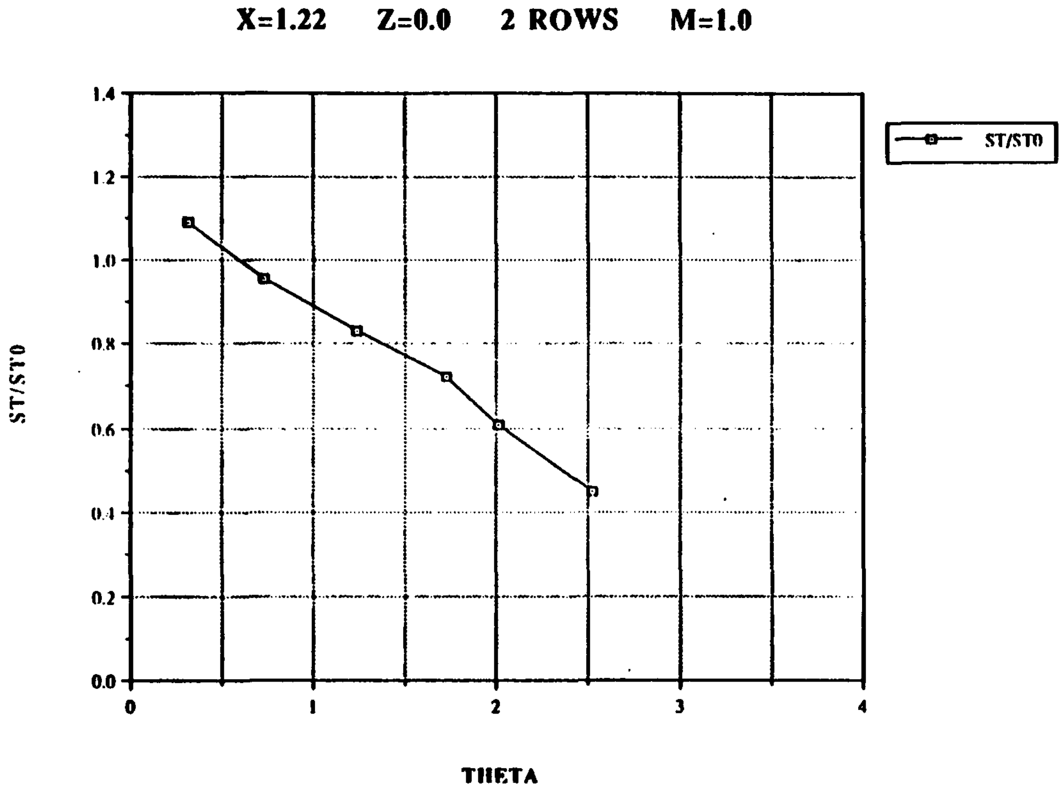

Figure 110. St/St_0 vs θ, Compound Angle,2 rows,m=1.0,X=1.22,Z=0.0 m

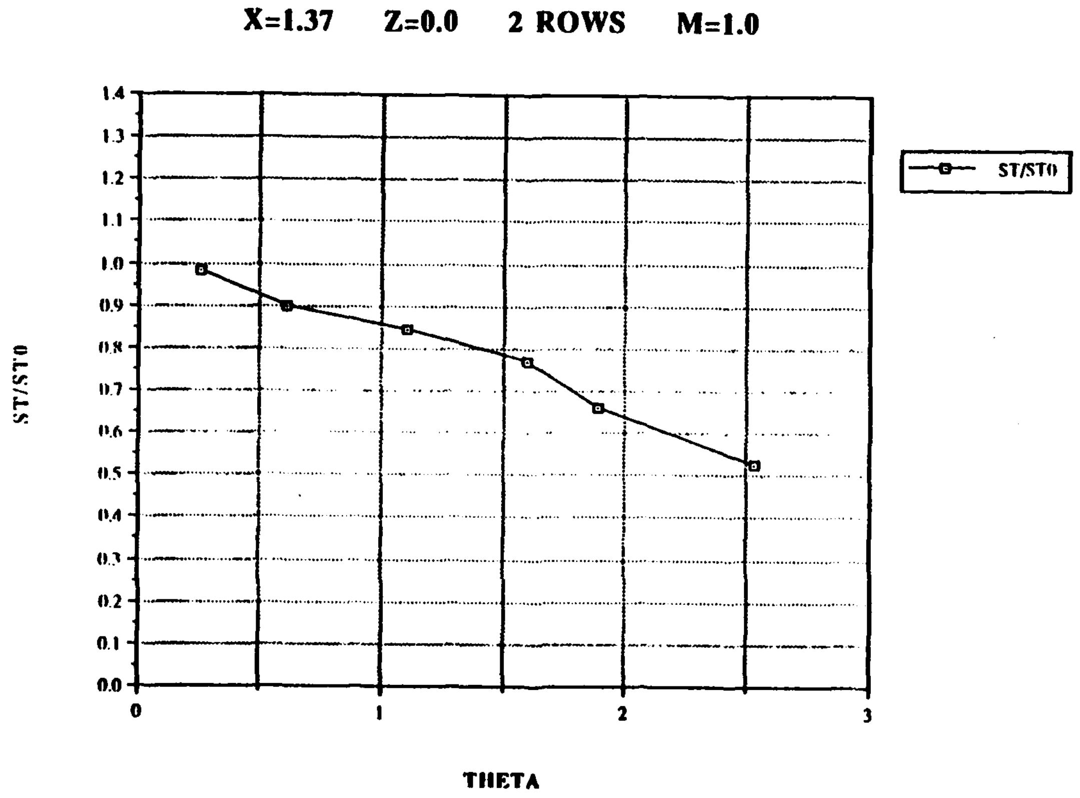

Figure 111. St/St$_0$ vs θ, Compound Angle,2 rows,m=1.0,X=1.37,Z=0.0 m

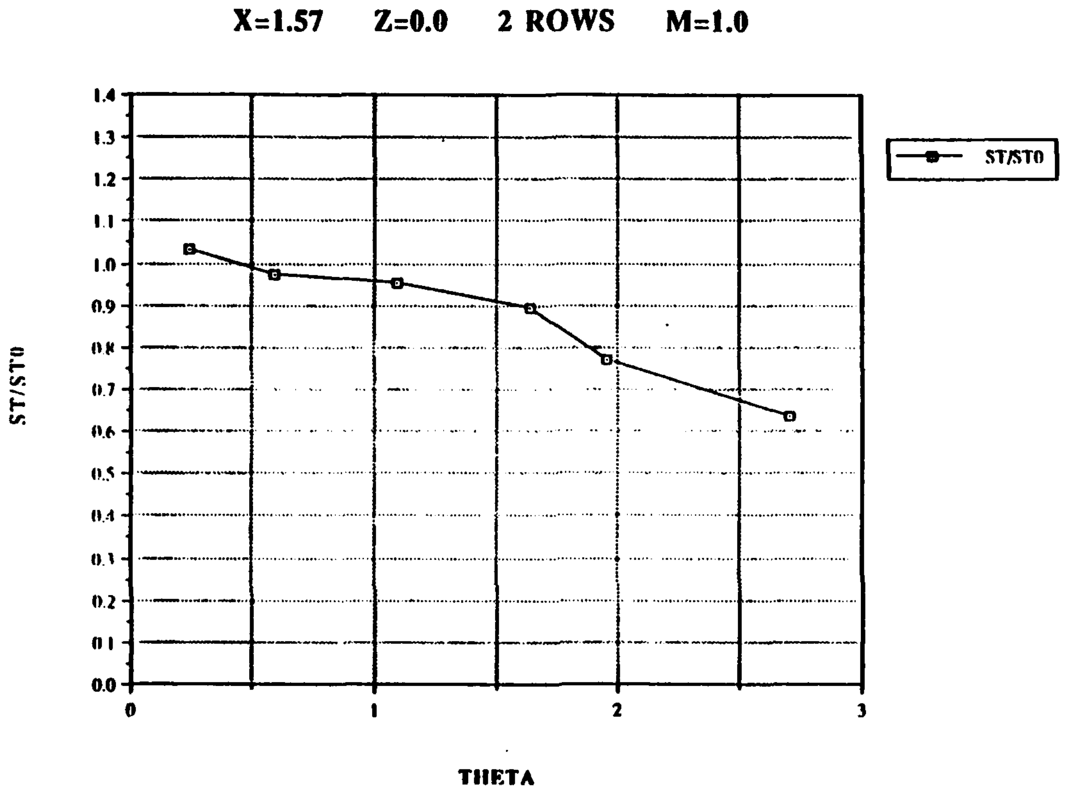

Figure 112. St/St_0 vs θ, Compound Angle,2 rows,m=1.0,X=1.57,Z=0.0 m

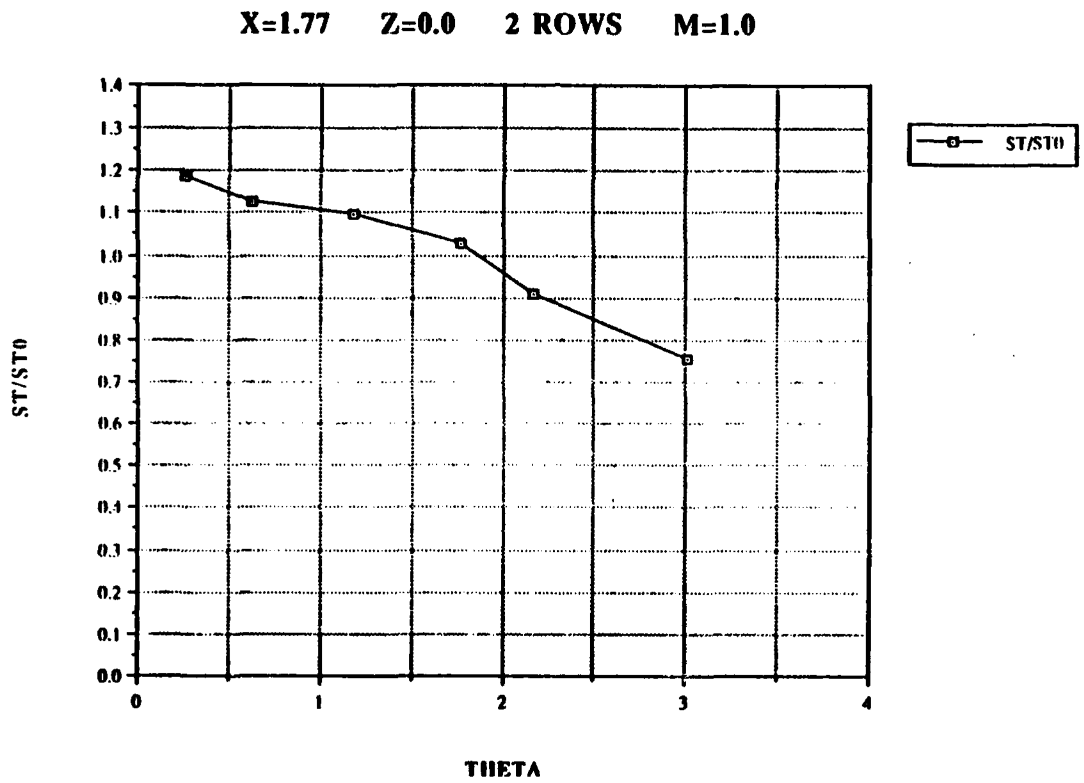

Figure 113. St/St_o vs θ, Compound Angle,2 rows,m=1.0,X=1.77,Z=0.0 m

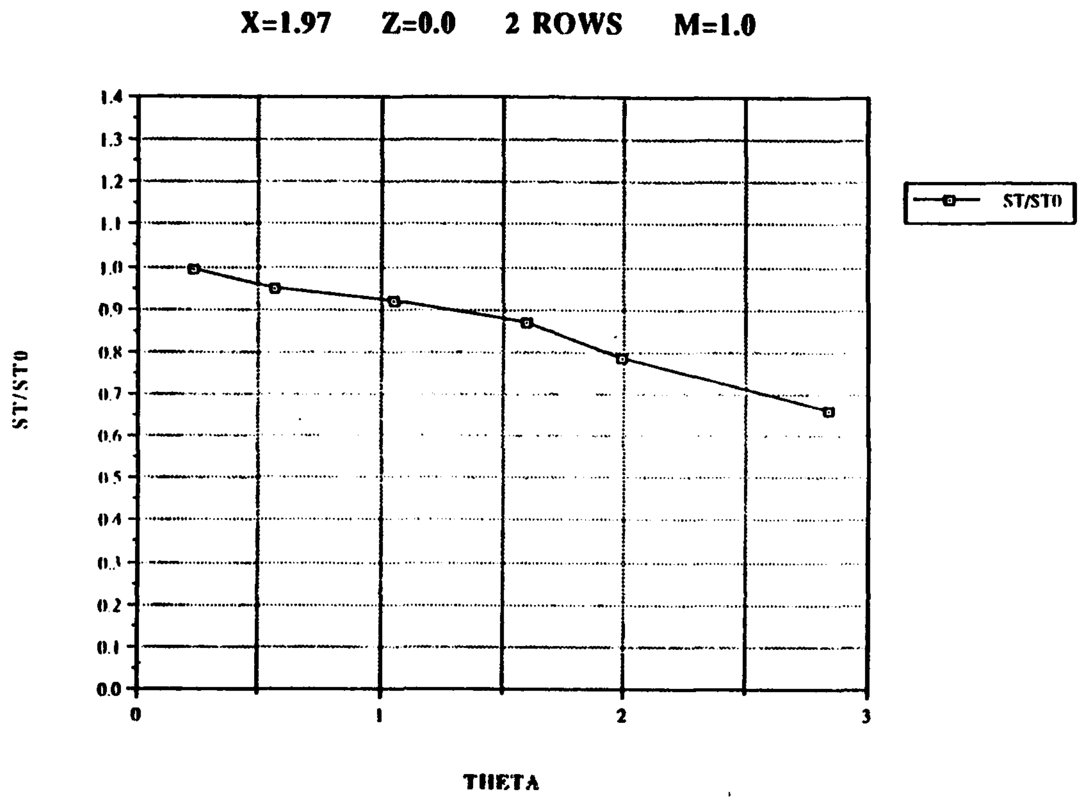

Figure 114. St/St$_0$ vs θ, Compound Angle,2 rows,m=1.0,X=1.97,Z=0.0 m

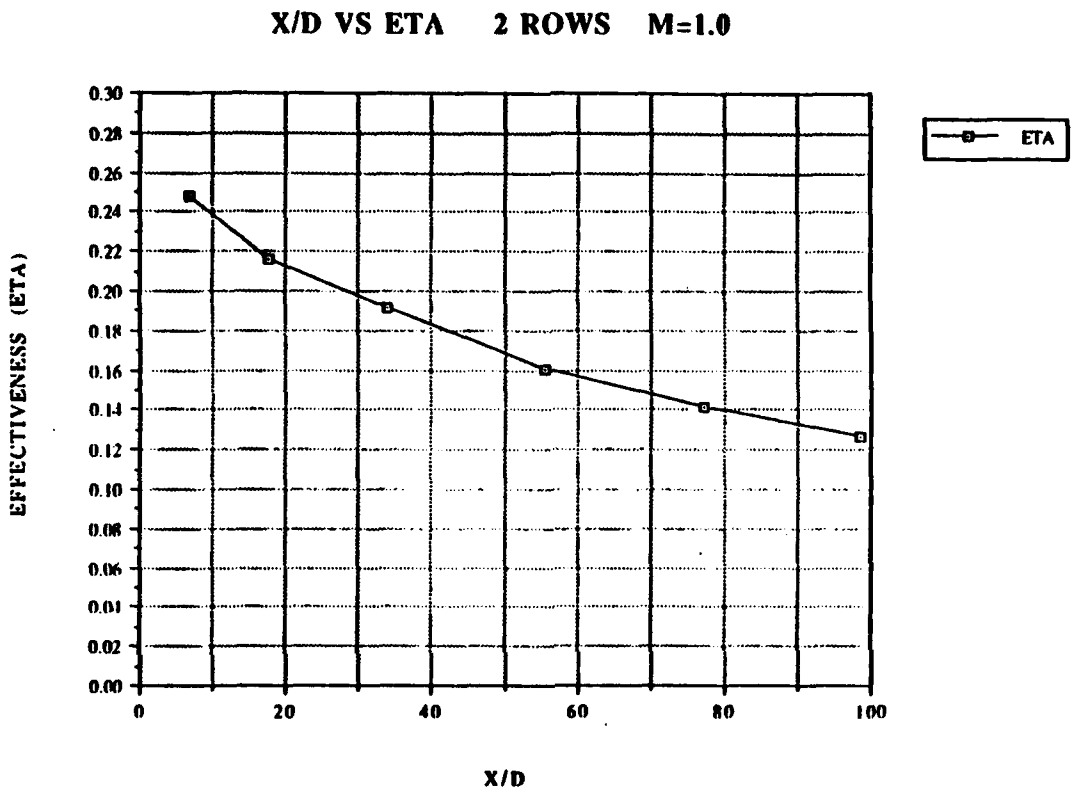

Figure 115. $\overline{\eta}$ vs x/d, Compound Angle, 2 rows, m=1.0, Spanwise Average

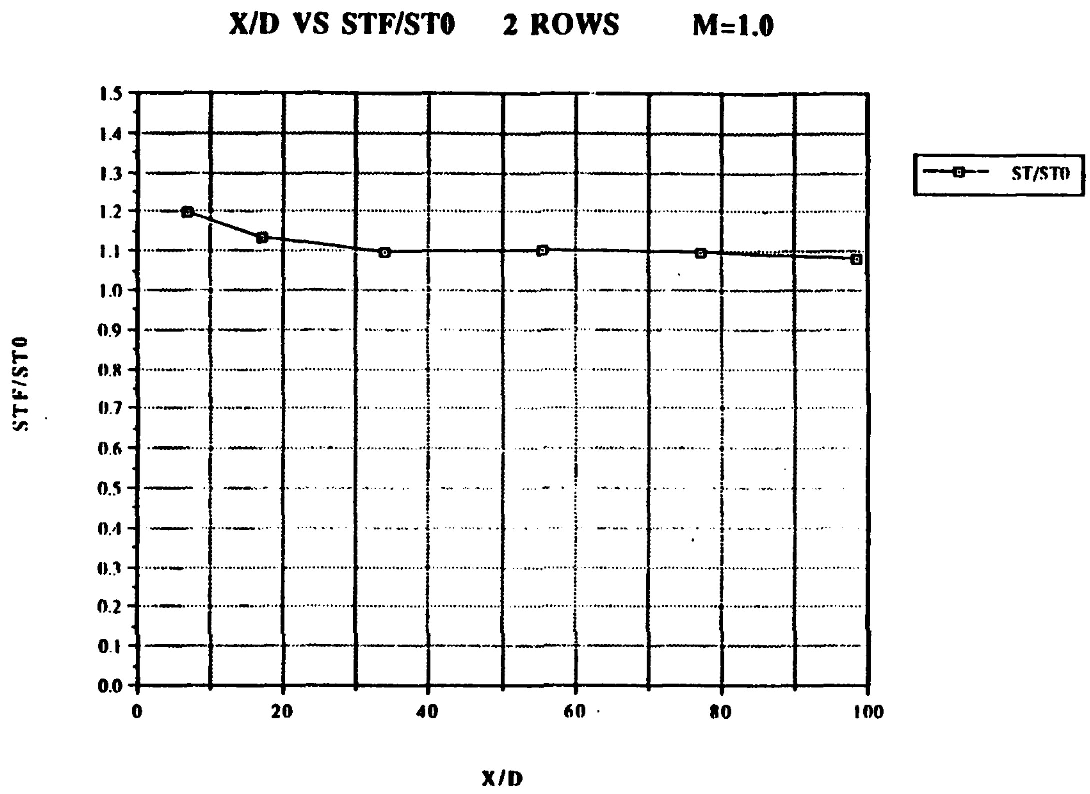

Figure 116. $\overline{St_f / St_o}$ vs x/d, Compound Angle, 2 rows, m=1.0, Spanwise Average

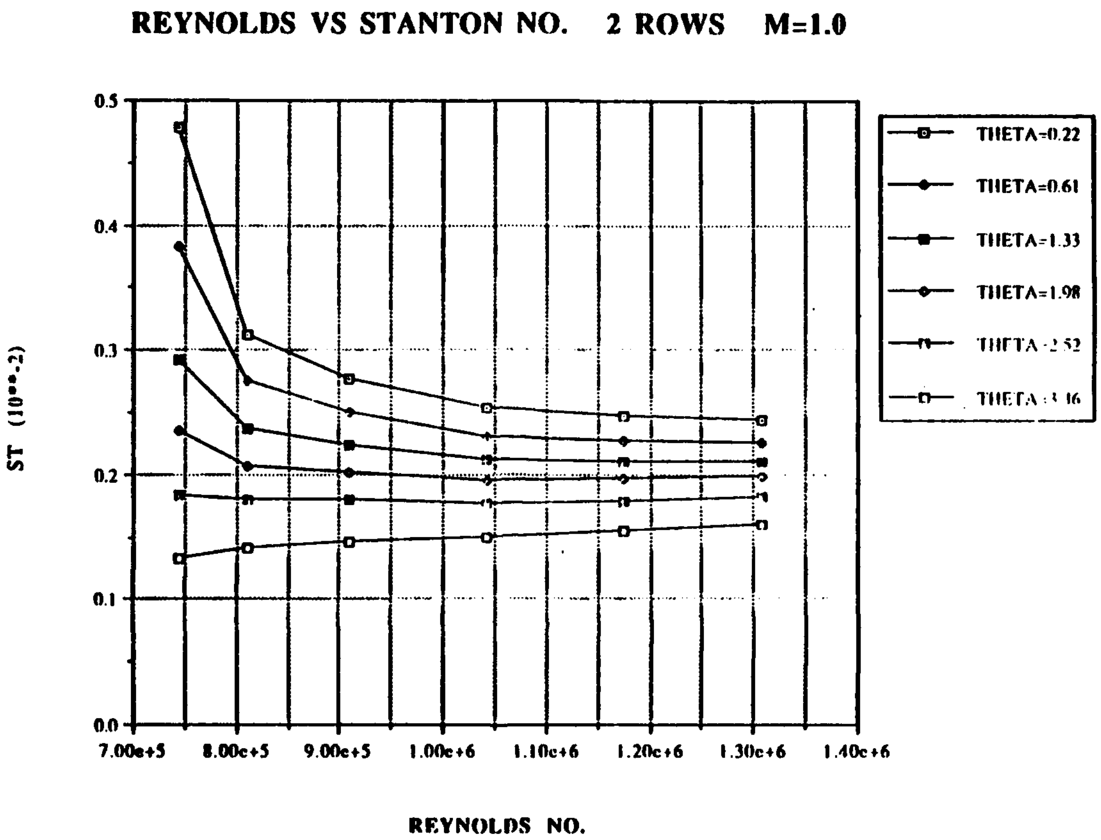

Figure 117. Spanwise averaged Stanton number vs Reynolds number, comparison of different θ values, 2 rows, m=1.0

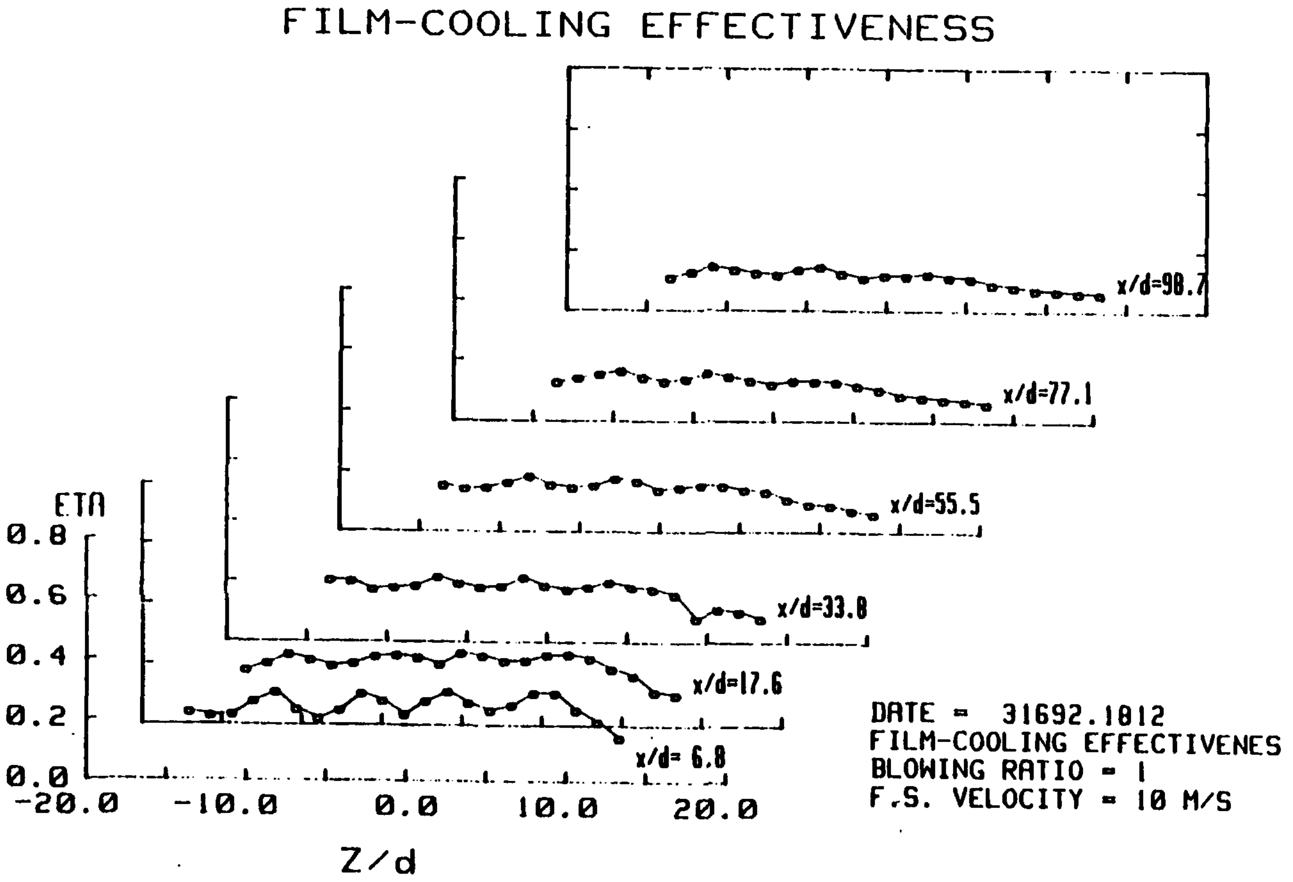

Figure 118. Spanwise Variation of η, Compound Angle, 2 rows, m=1.0

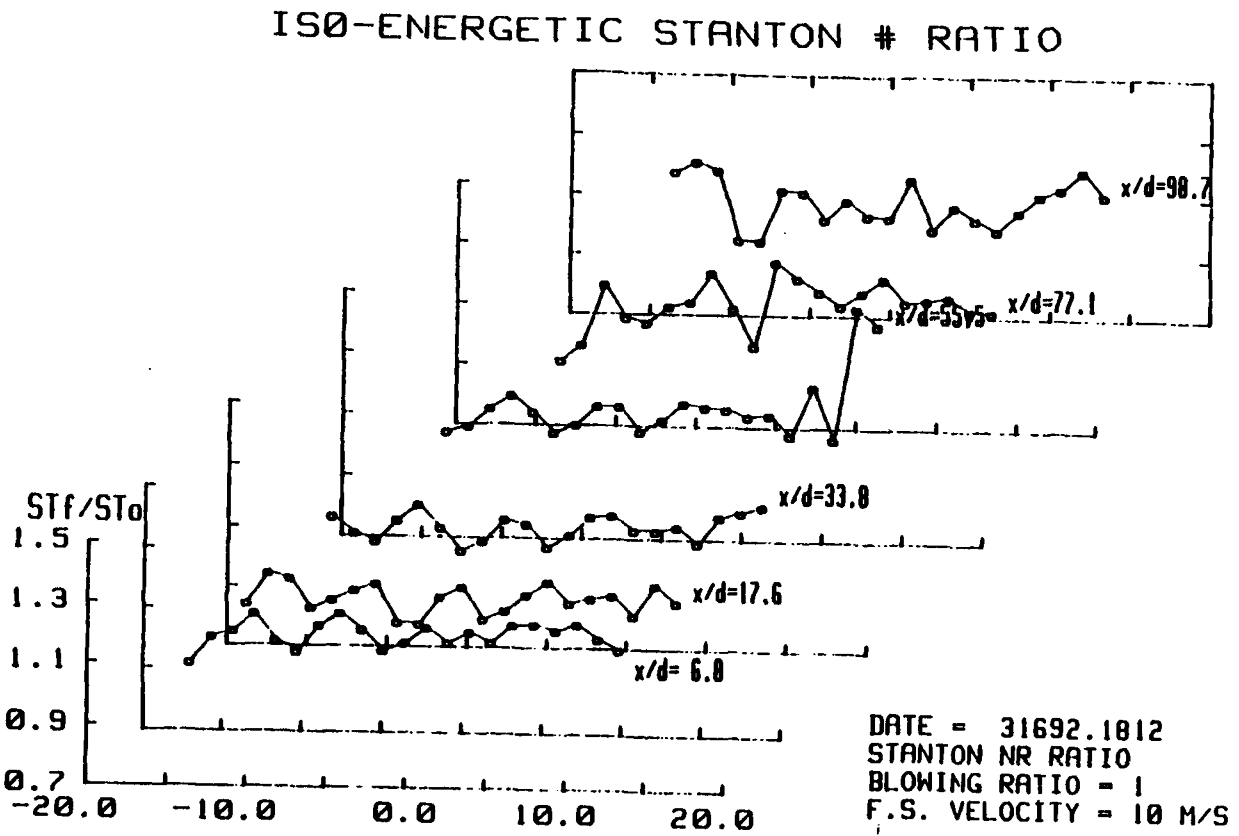

Figure 119. Spanwise Variation of St_f/St_o, Compound Angle, 2 rows, m=1.0

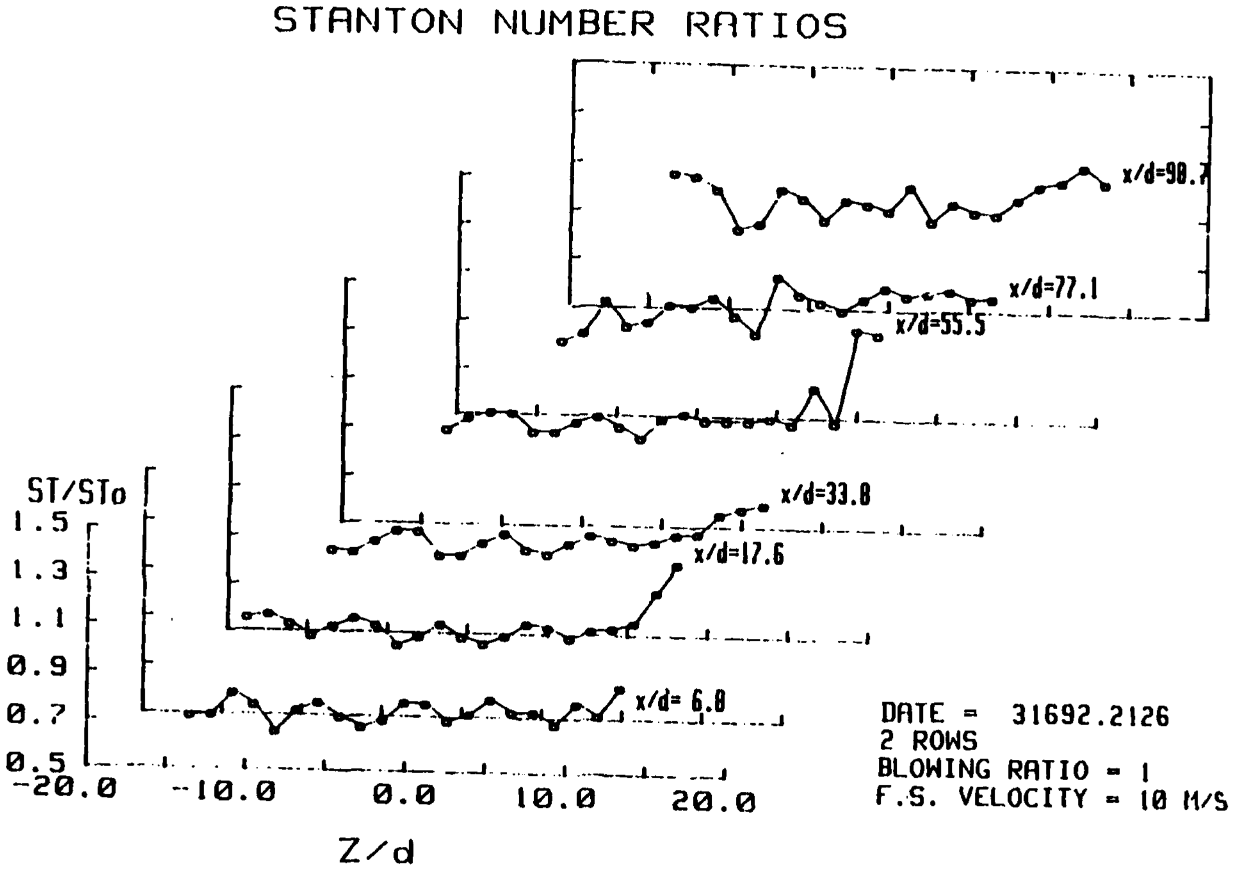

Figure 120. Spanwise Variation of St/St$_0$, Compound Angle, 2 rows, m=1.0, θ =1.18

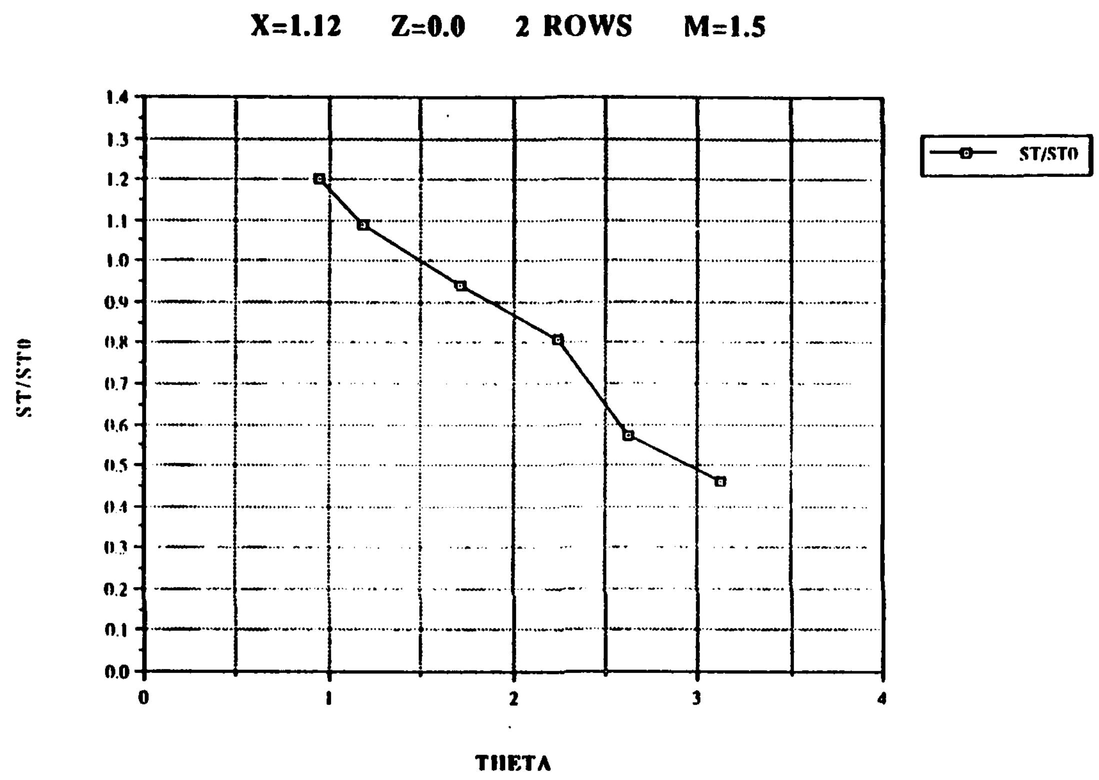

Figure 121. St/St$_0$ vs θ, Compound Angle,2 rows,m=1.5,X=1.12,Z=0.0 m

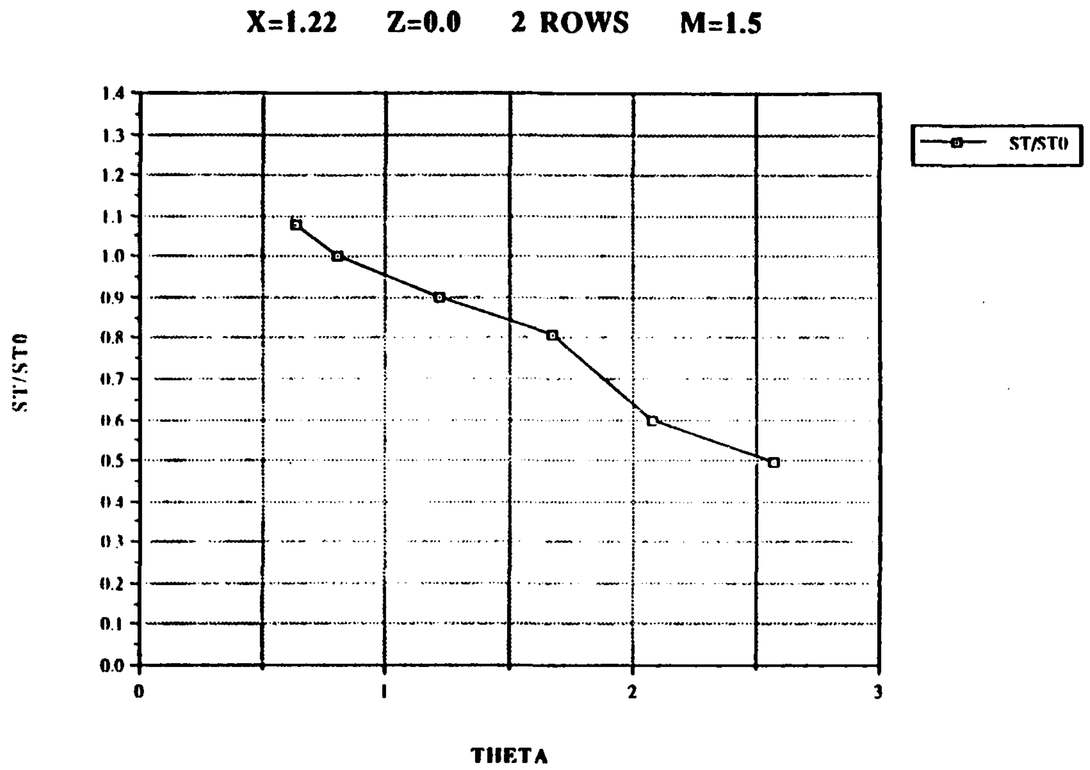

Figure 122. St/St$_0$ vs θ, Compound Angle,2 rows,m=1.5,X=1.22,Z=0.0 m

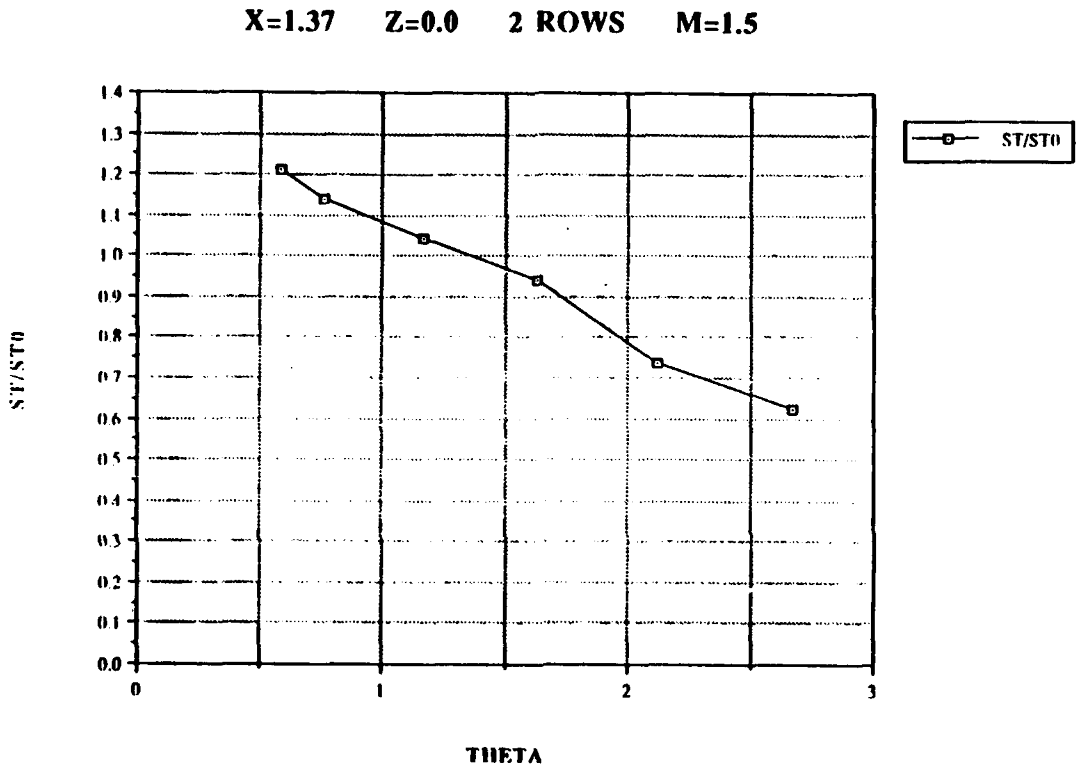

Figure 123. St/St$_0$ vs θ, Compound Angle,2 rows,m=1.5,X=1.37,Z=0.0 m

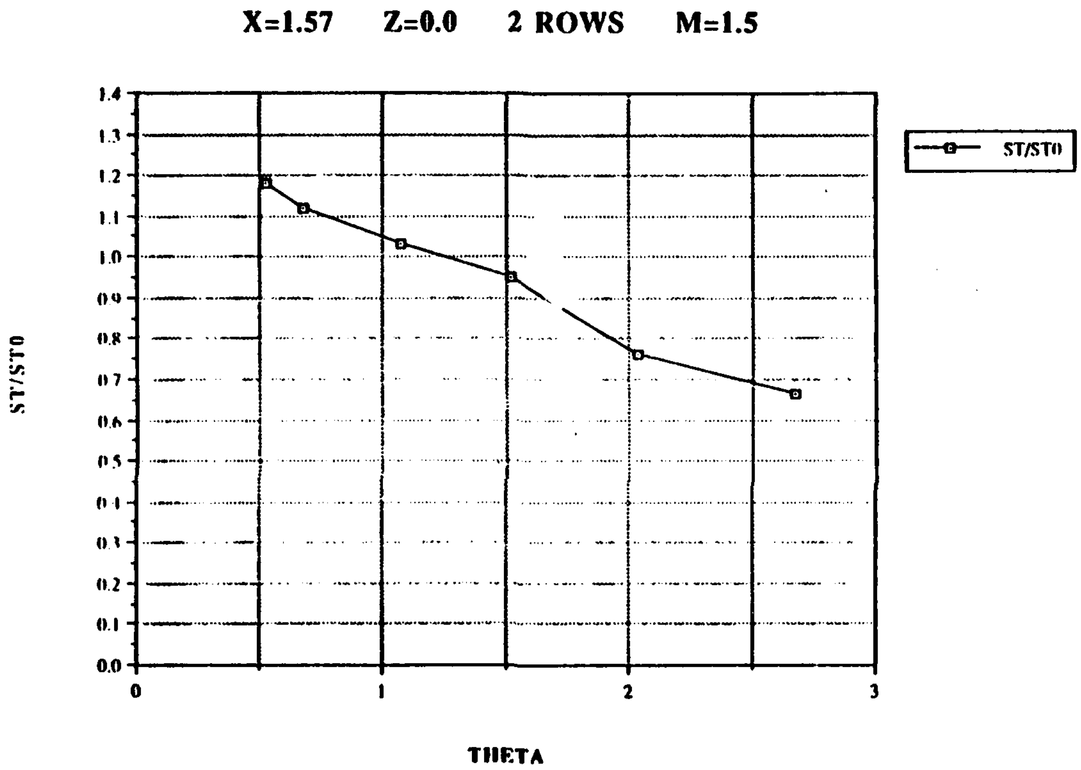

Figure 124. St/St$_0$ vs θ, Compound Angle,2 rows,m=1.5,X=1.57,Z=0.0 m

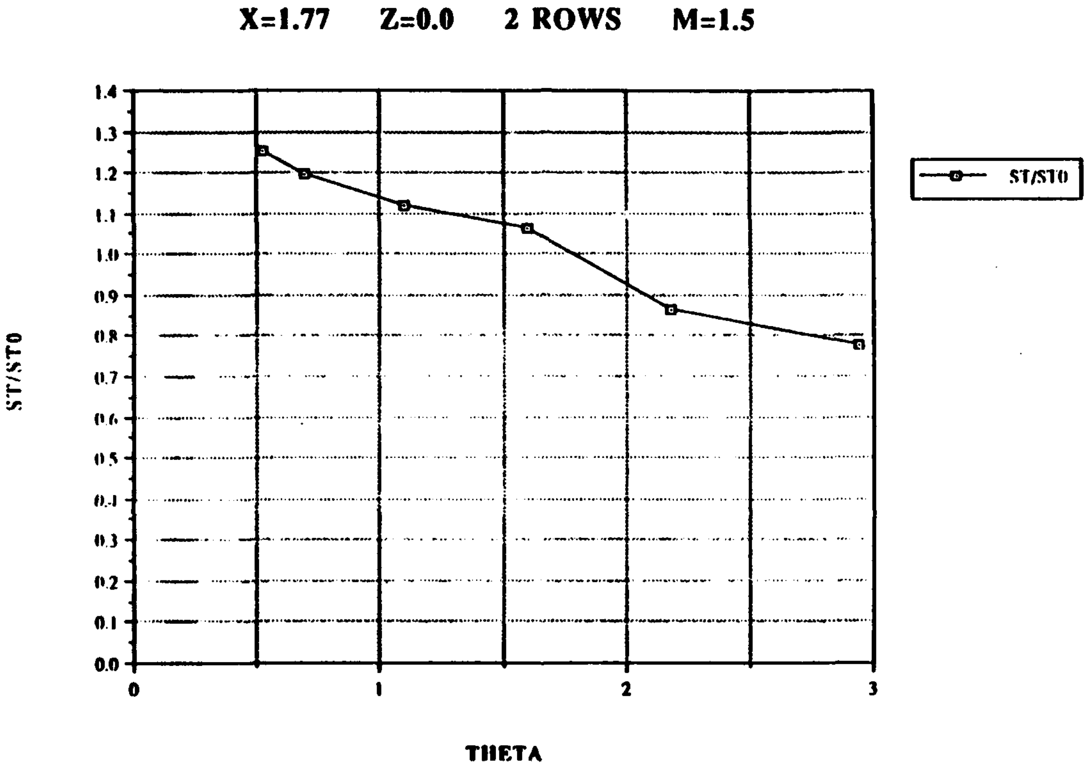

Figure 125. St/St$_0$ vs θ, Compound Angle,2 rows,m=1.5,X=1.77,Z=0.0 m

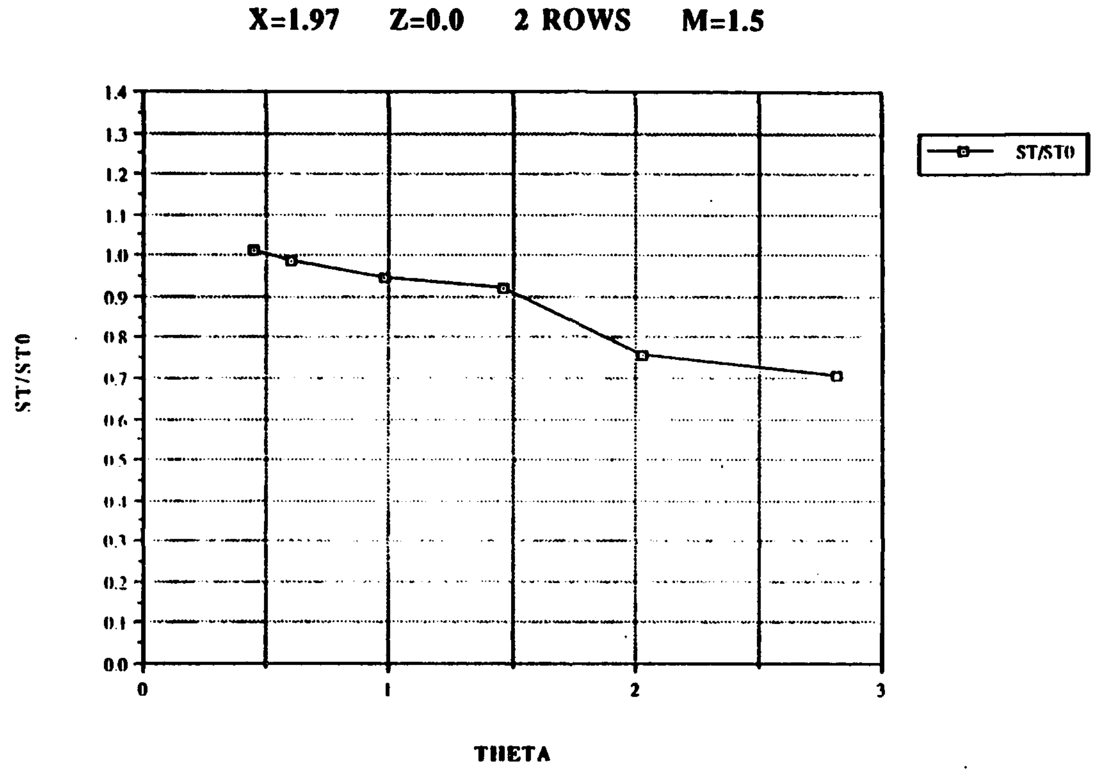

Figure 126. St/St_0 vs θ, Compound Angle,2 rows,m=1.5,X=1.97,Z=0.0 m

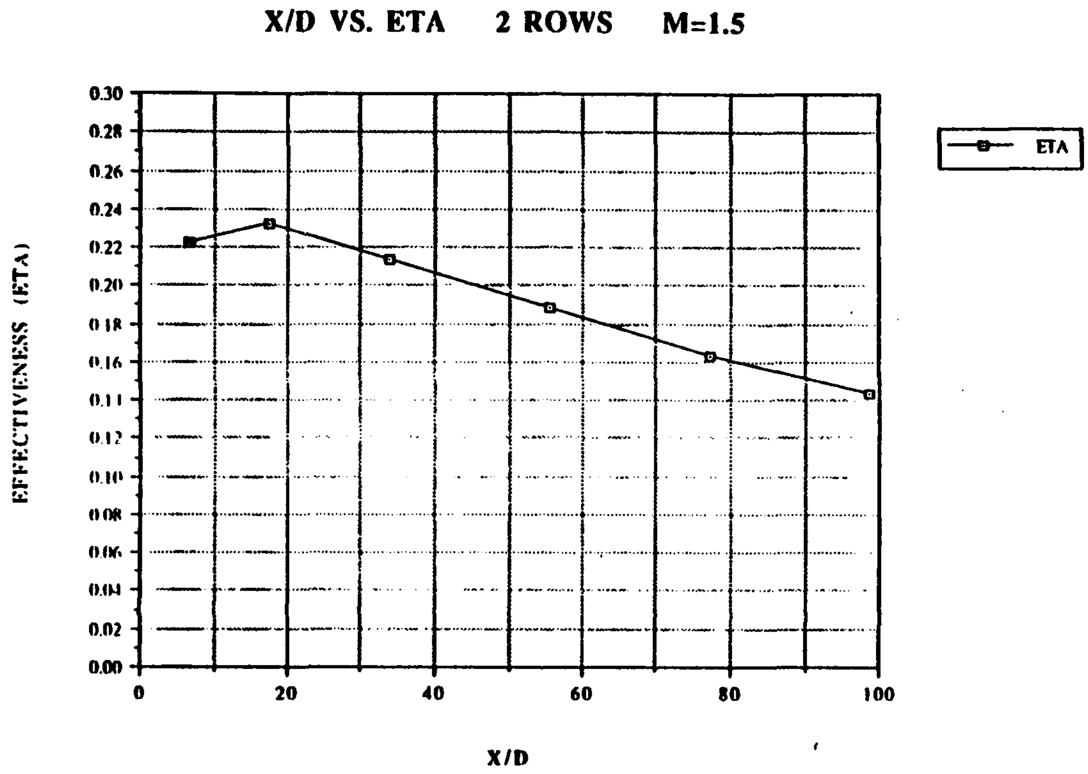

Figure 127. $\overline{\eta}$ vs x/d, Compound Angle, 2 rows, m=1.5, Spanwise Average

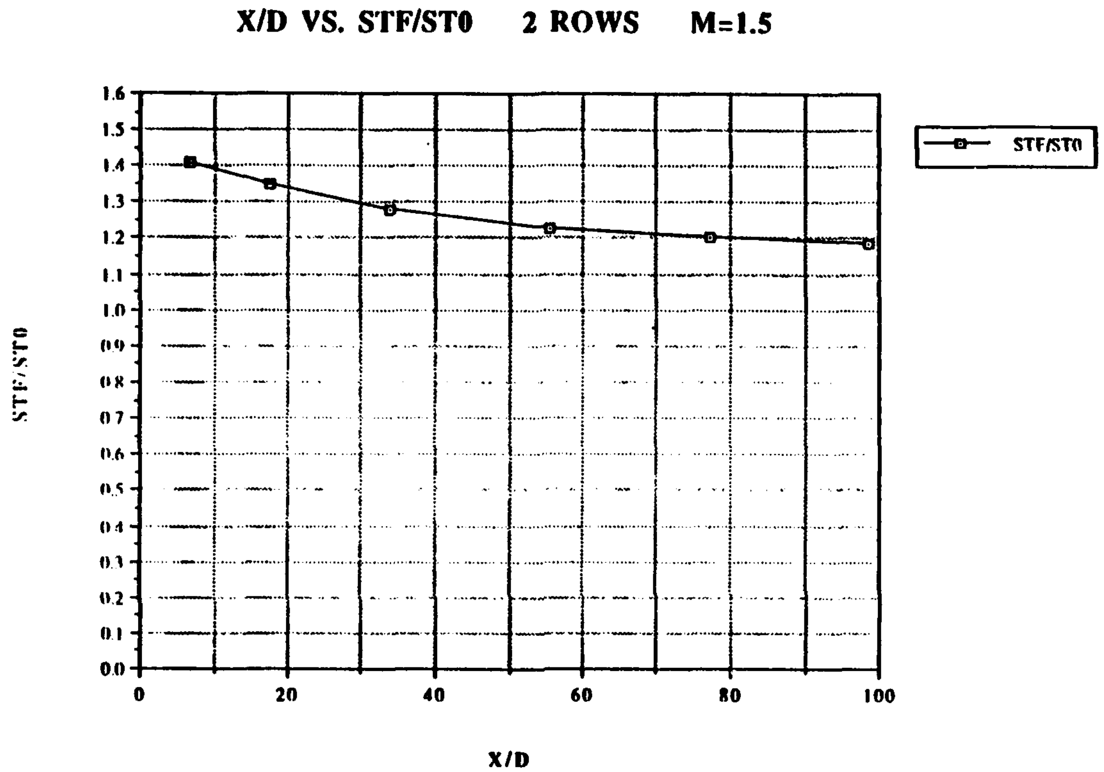

Figure 128. $\overline{St_f / St_o}$ vs x/d, Compound Angle, 2 rows, m=1.5, Spanwise Average

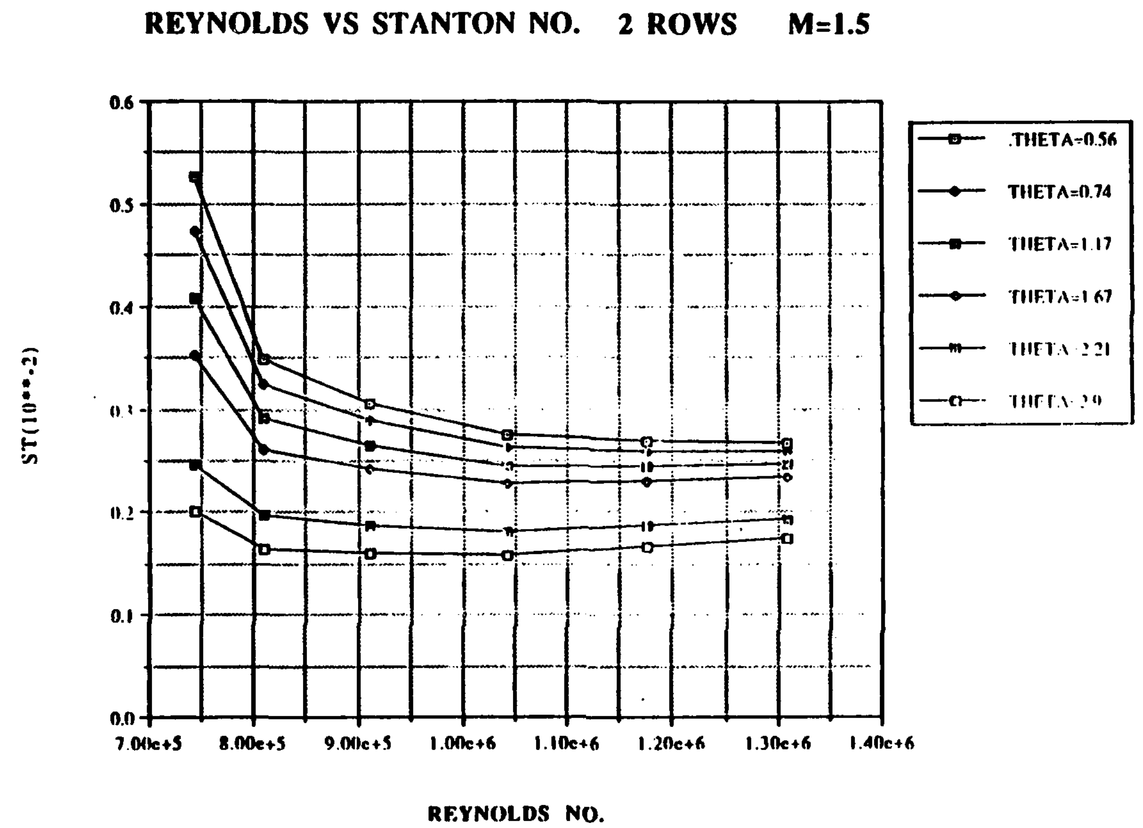

Figure 129. Spanwise averaged Stanton number vs Reynolds number, comparison of different θ values, 2 rows, m=1.5

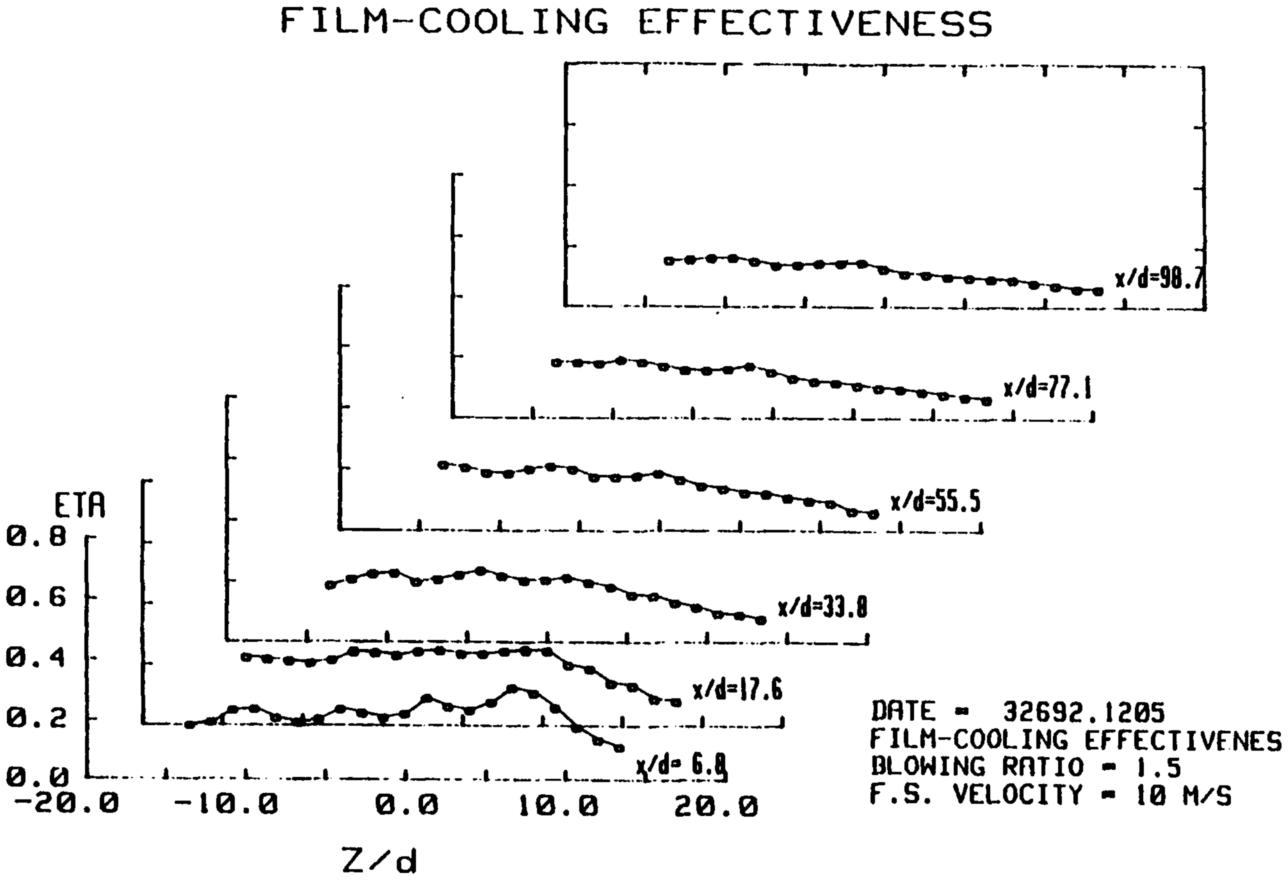

Figure 130. Spanwise Variation of η, Compound Angle, 2 rows, m=1.5

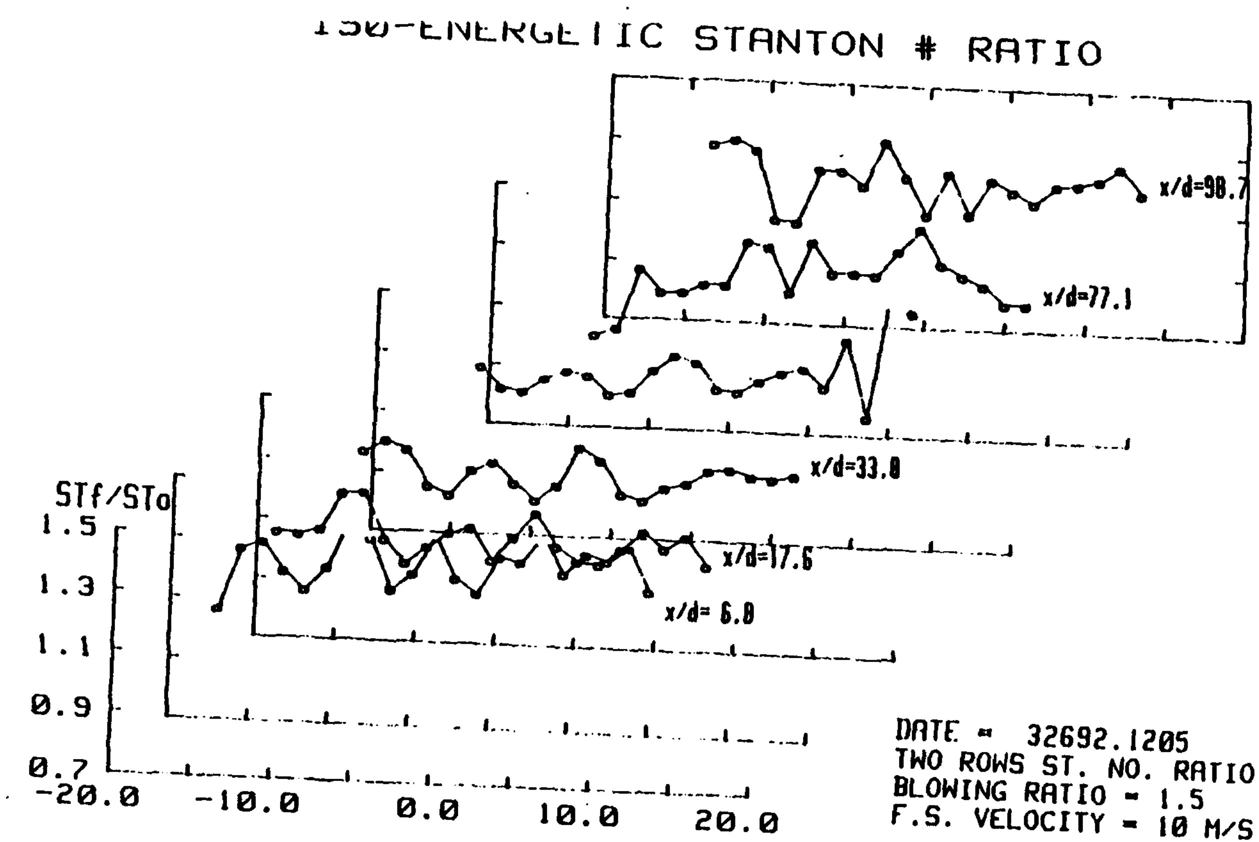

Figure 131. Spanwise Variation of St_f/St_o, Compound Angle, 2 rows, m=1.5

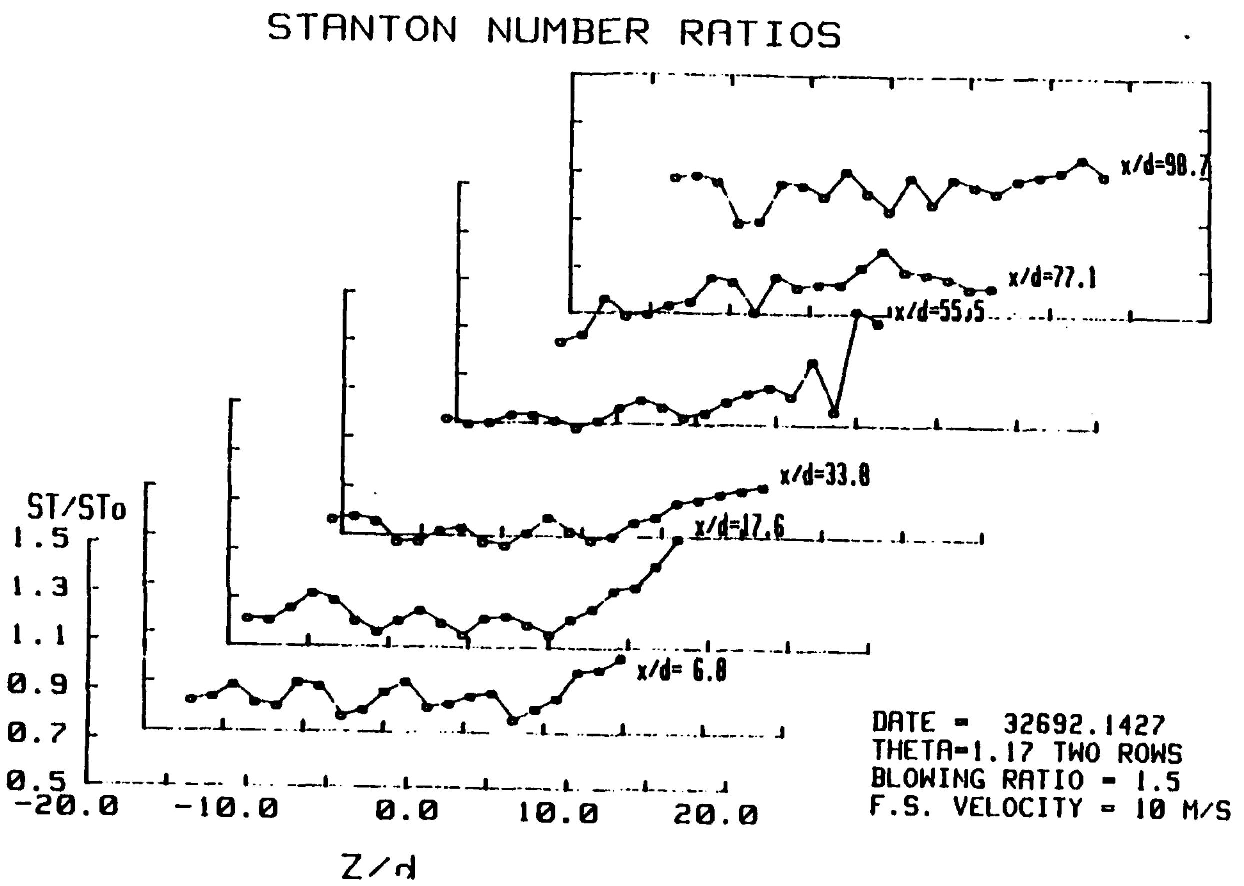

Figure 132. Spanwise Variation of St/St_0, Compound Angle, 2 rows, m=1.0, θ =1.17

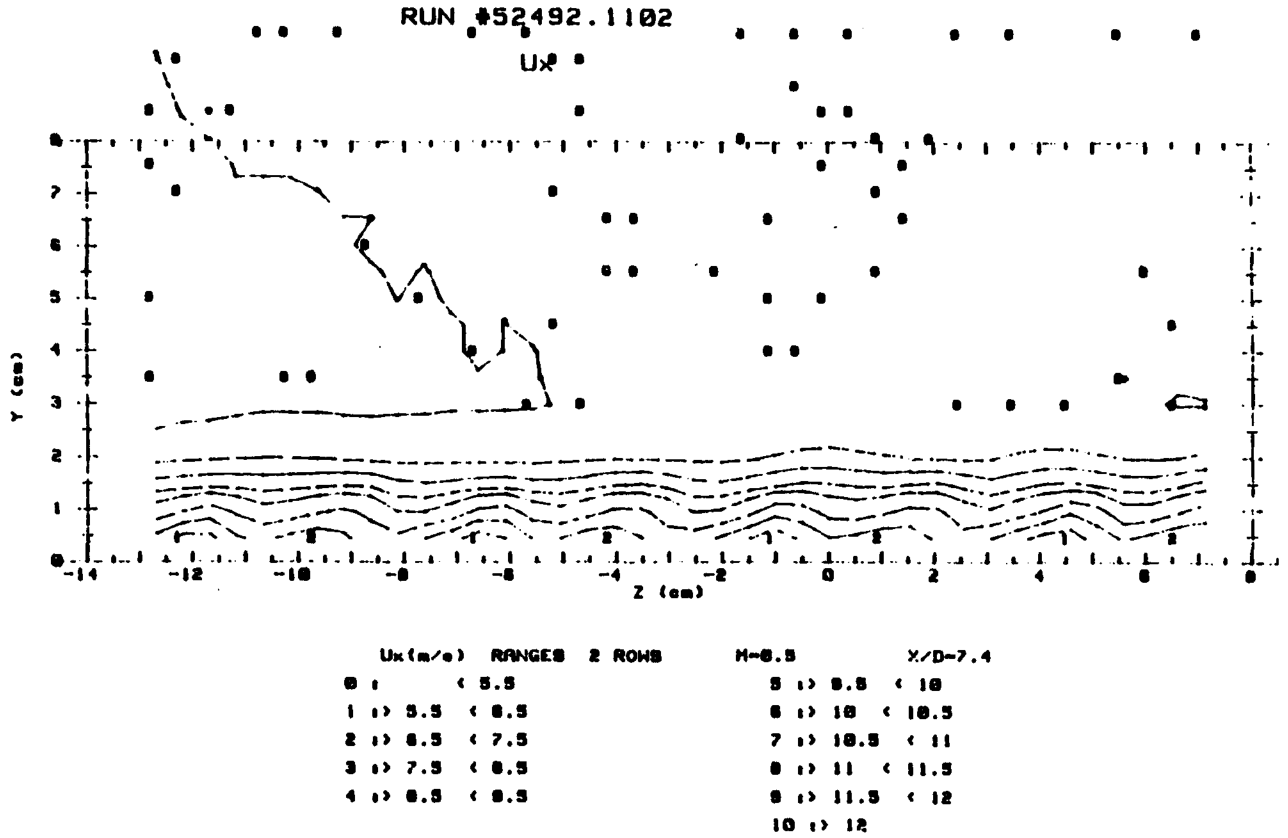

Figure 133. Streamwise Velocity Field, Compound Angle, 2 rows, m=0.5, x/d=7.4

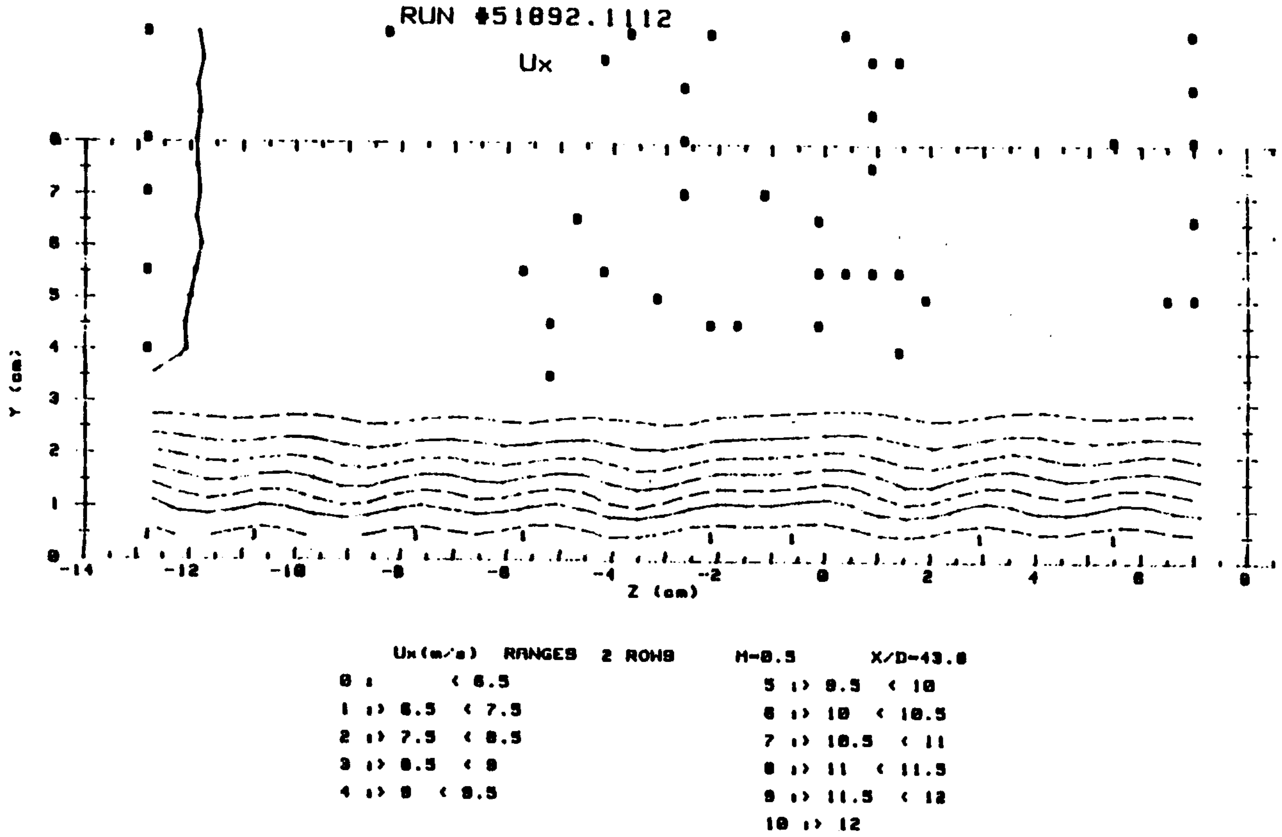

Figure 134. Streamwise Velocity Field, Compound Angle, 2 rows, m=0.5, x/d=43.8

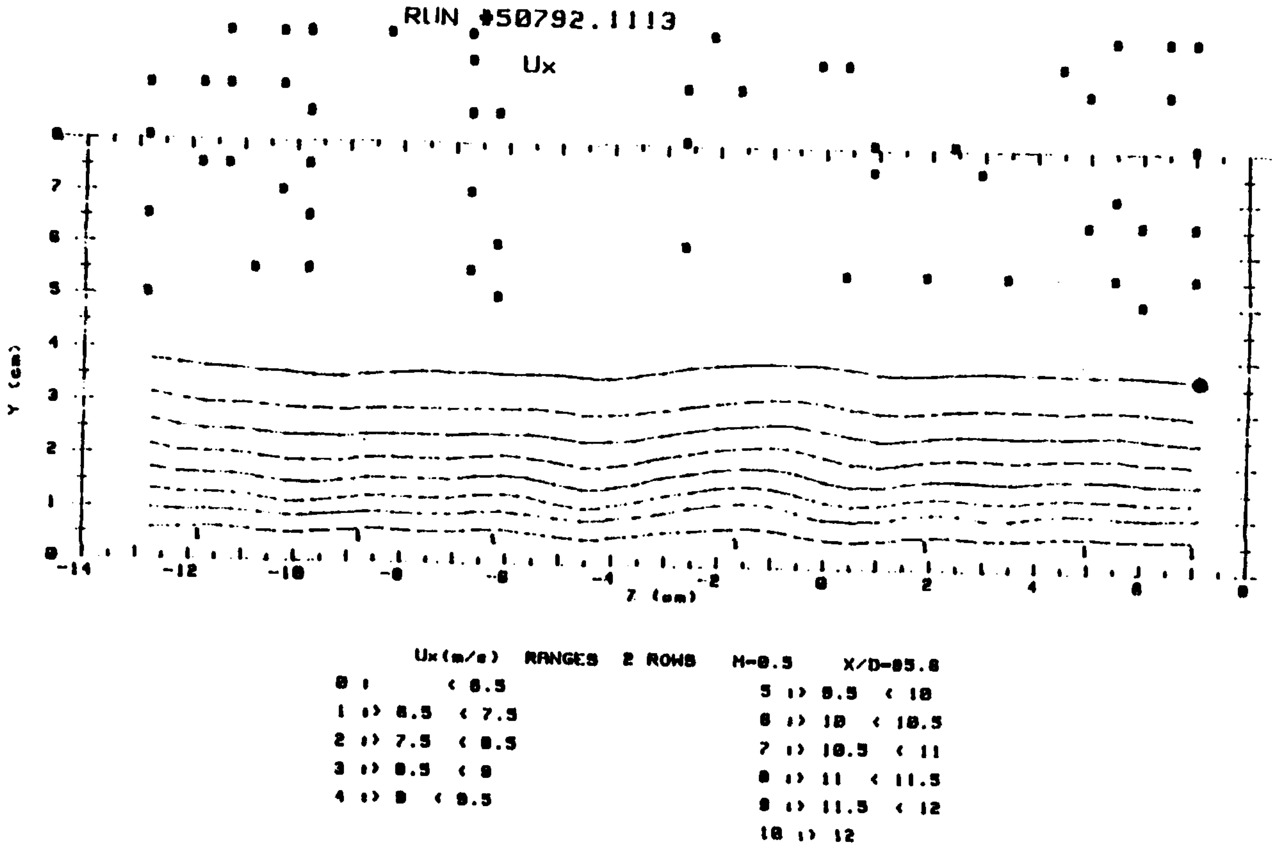

Figure 135. Streamwise Velocity Field, Compound Angle, 2 rows, m=0.5, x/d=85.6

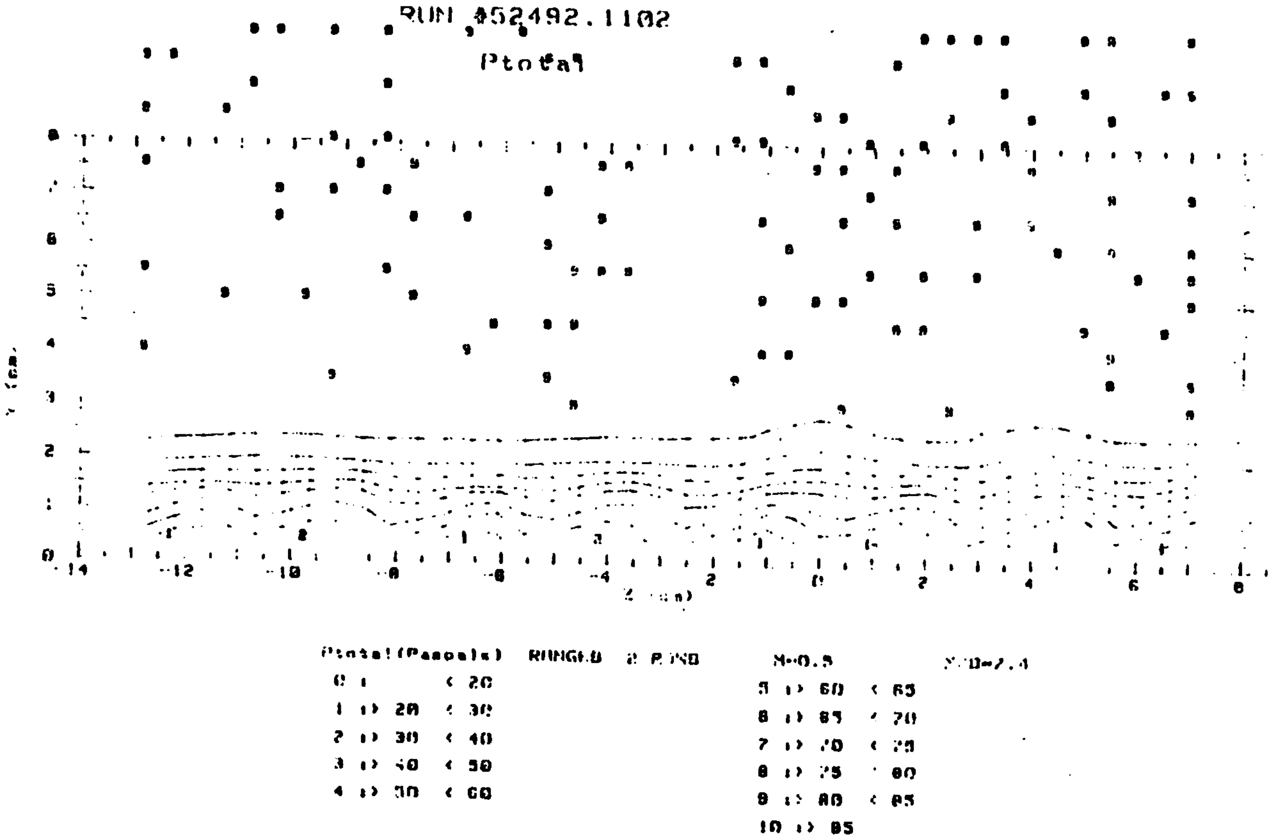

Figure 136. Streamwise Pressure Field, Compound Angle, 2 rows, m=0.5, x/d=7.4

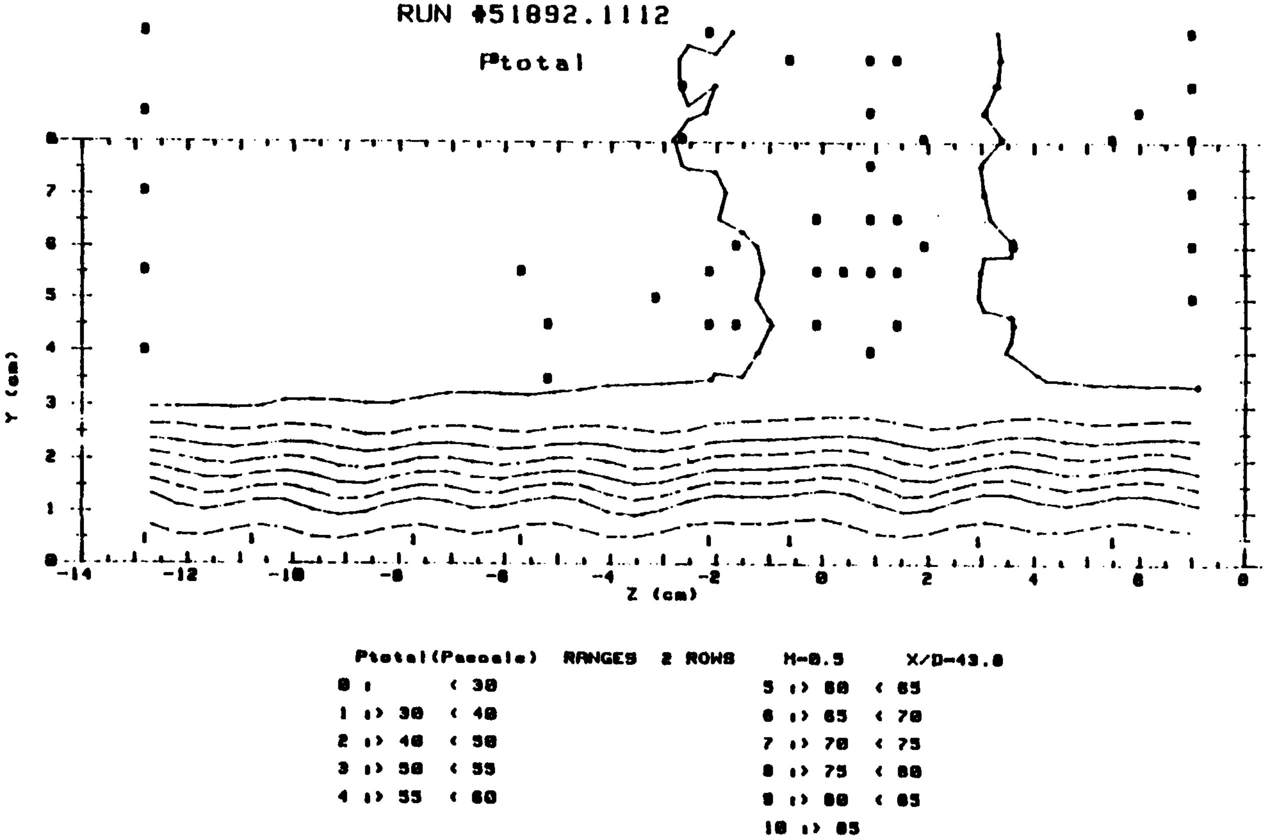

Figure 137. Streamwise Pressure Field, Compound Angle, 2 rows, m=0.5, x/d=43.8

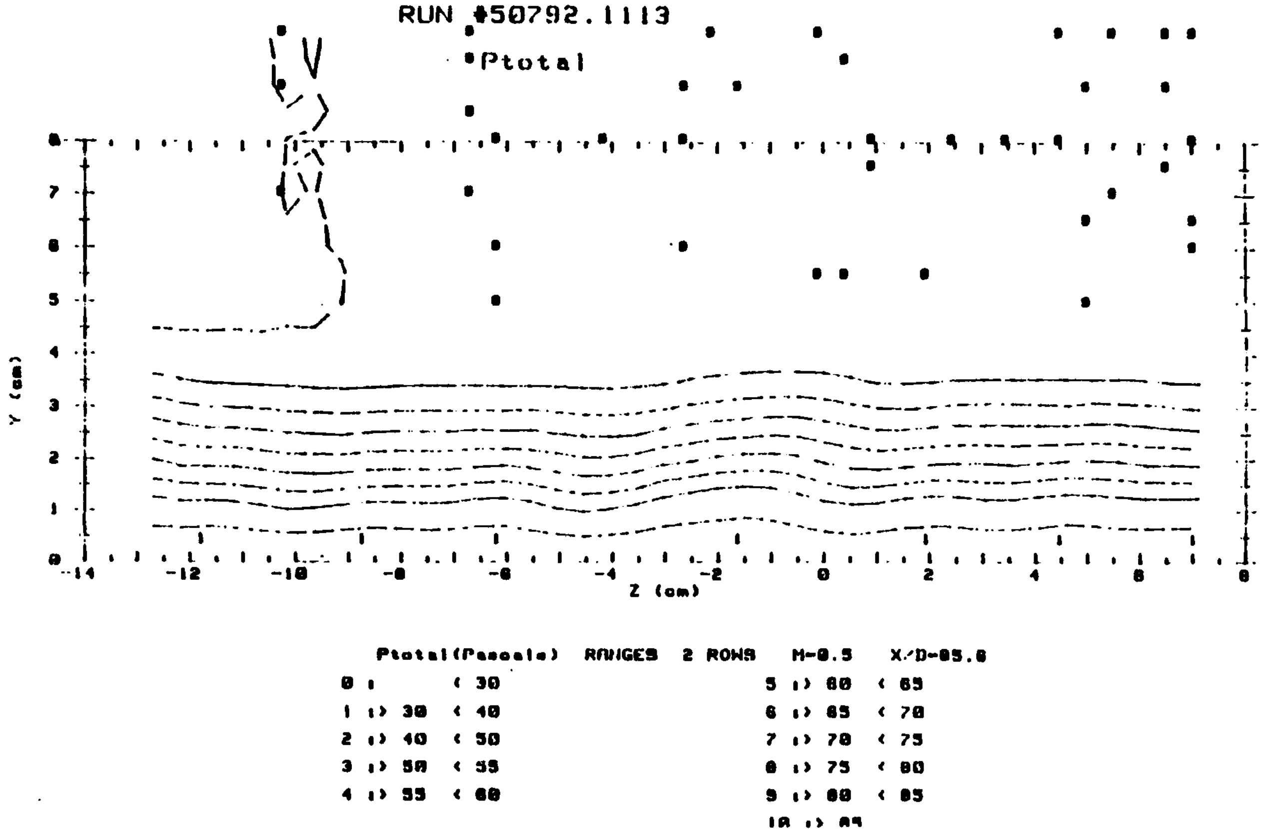

Figure 138. Streamwise Pressure Field, Compound Angle, 2 rows, m=0.5, x/d=85.6

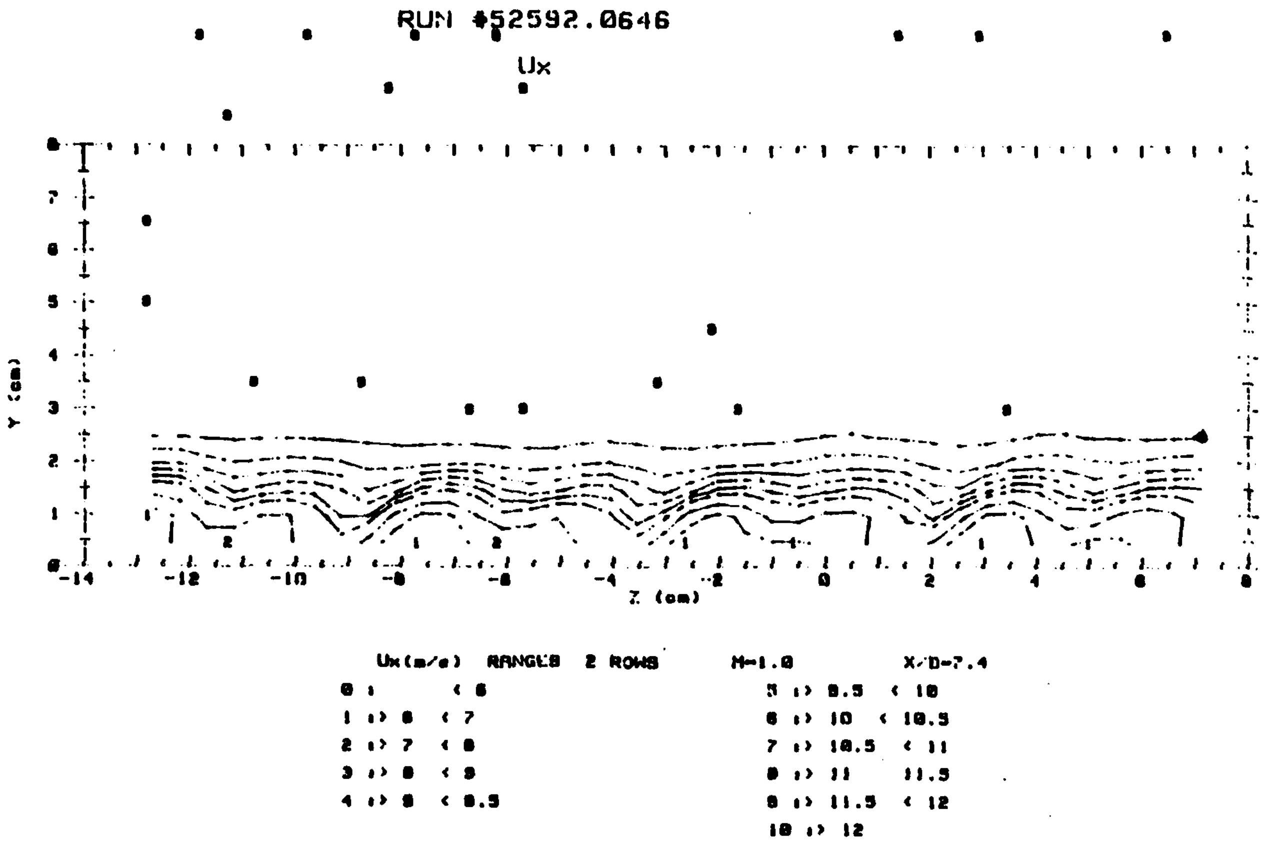

Figure 139. Streamwise Velocity Field, Compound Angle, 2 rows, m=1.0, x/d=7.4

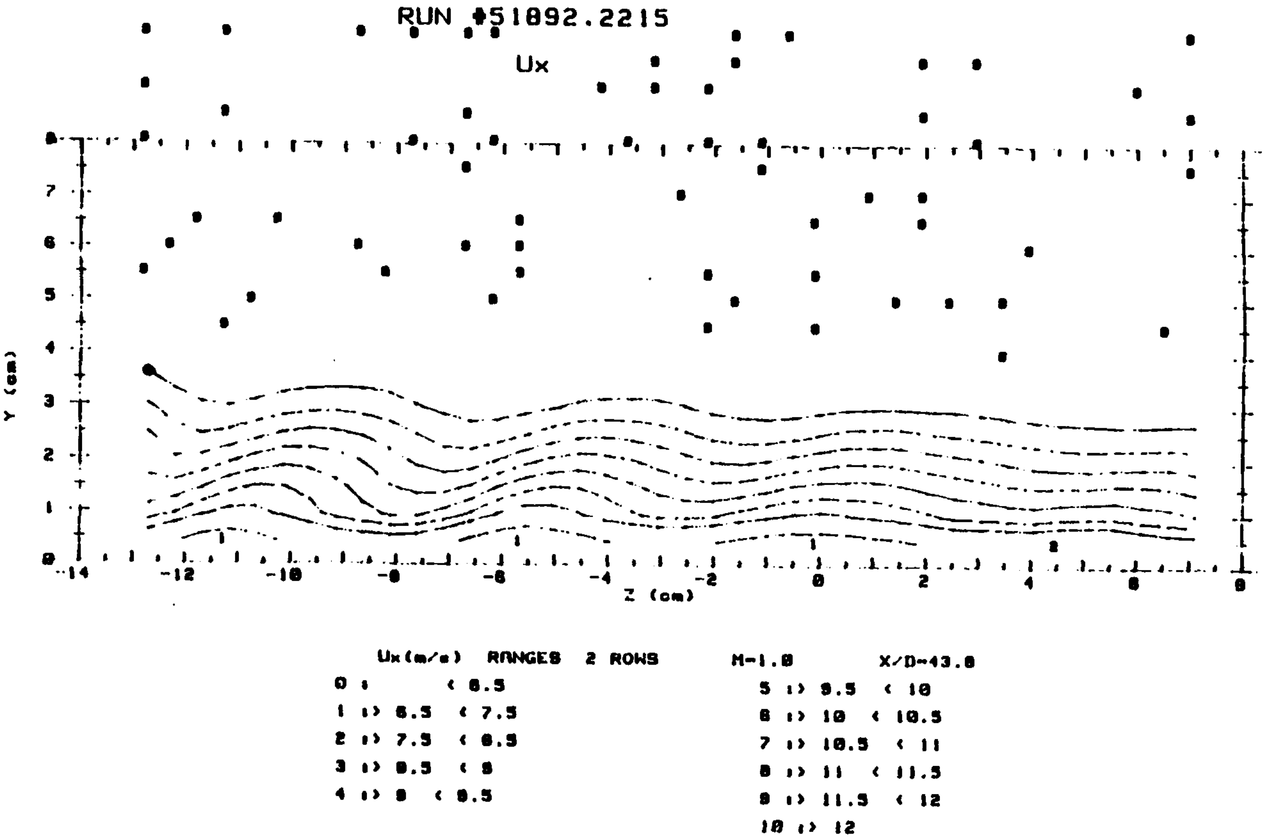

Figure 140. Streamwise Velocity Field, Compound Angle, 2 rows, m=1.0, x/d=43.8

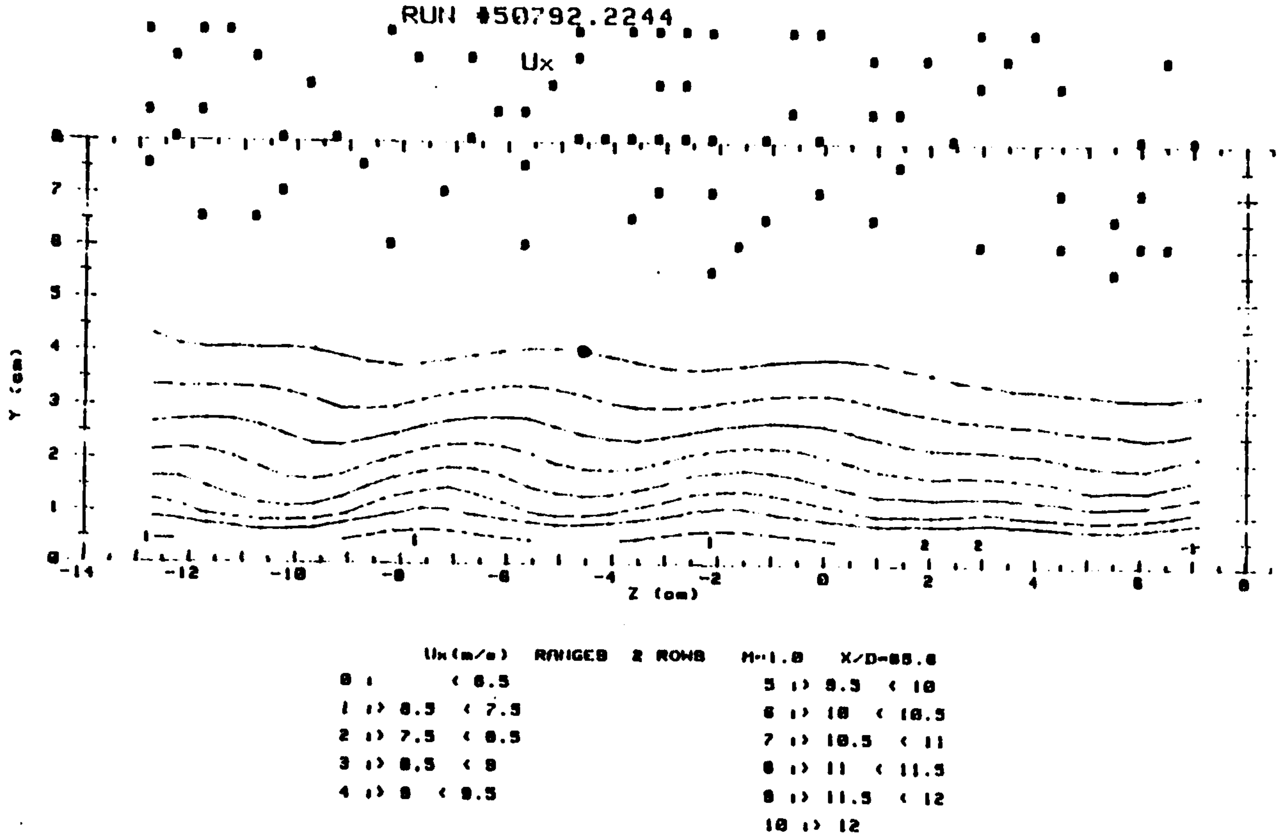

Figure 141. Streamwise Velocity Field, Compound Angle, 2 rows, m=1.0, x/d=85.6

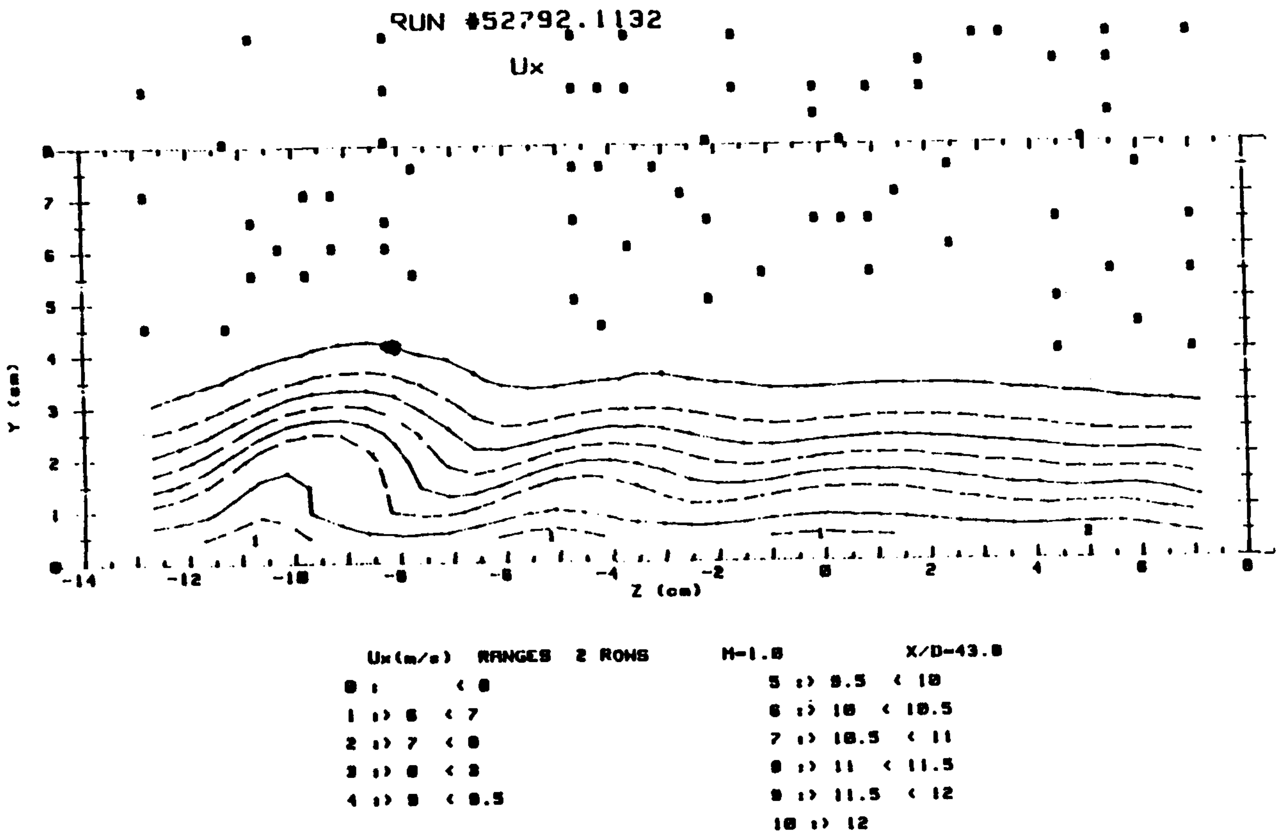

Figure 142. Streamwise Velocity Field, Compound Angle, 2 rows (8 holes), m=1.0, x/d=43.8

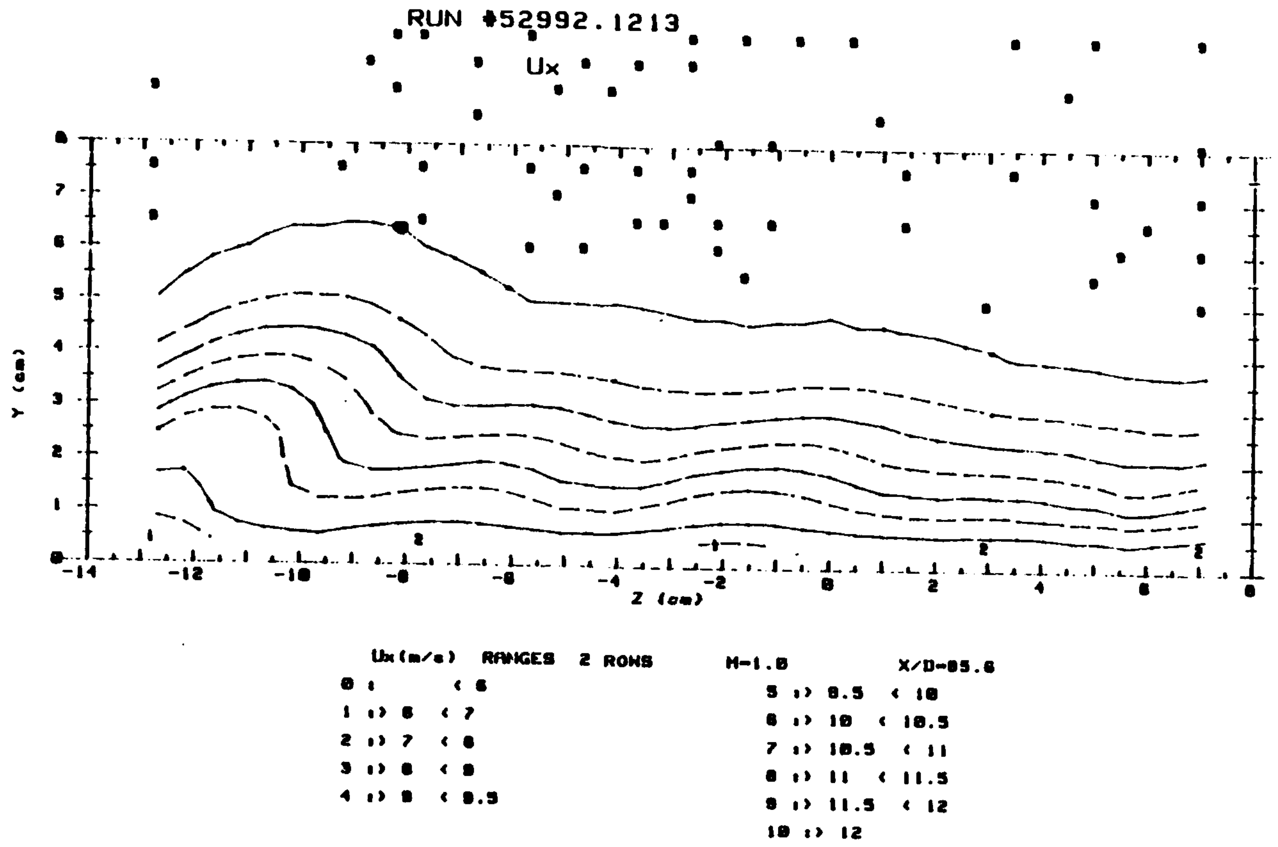

Figure 143. Streamwise Velocity Field, Compound Angle, 2 rows (8 holes), m=1.0, x/d=85.6

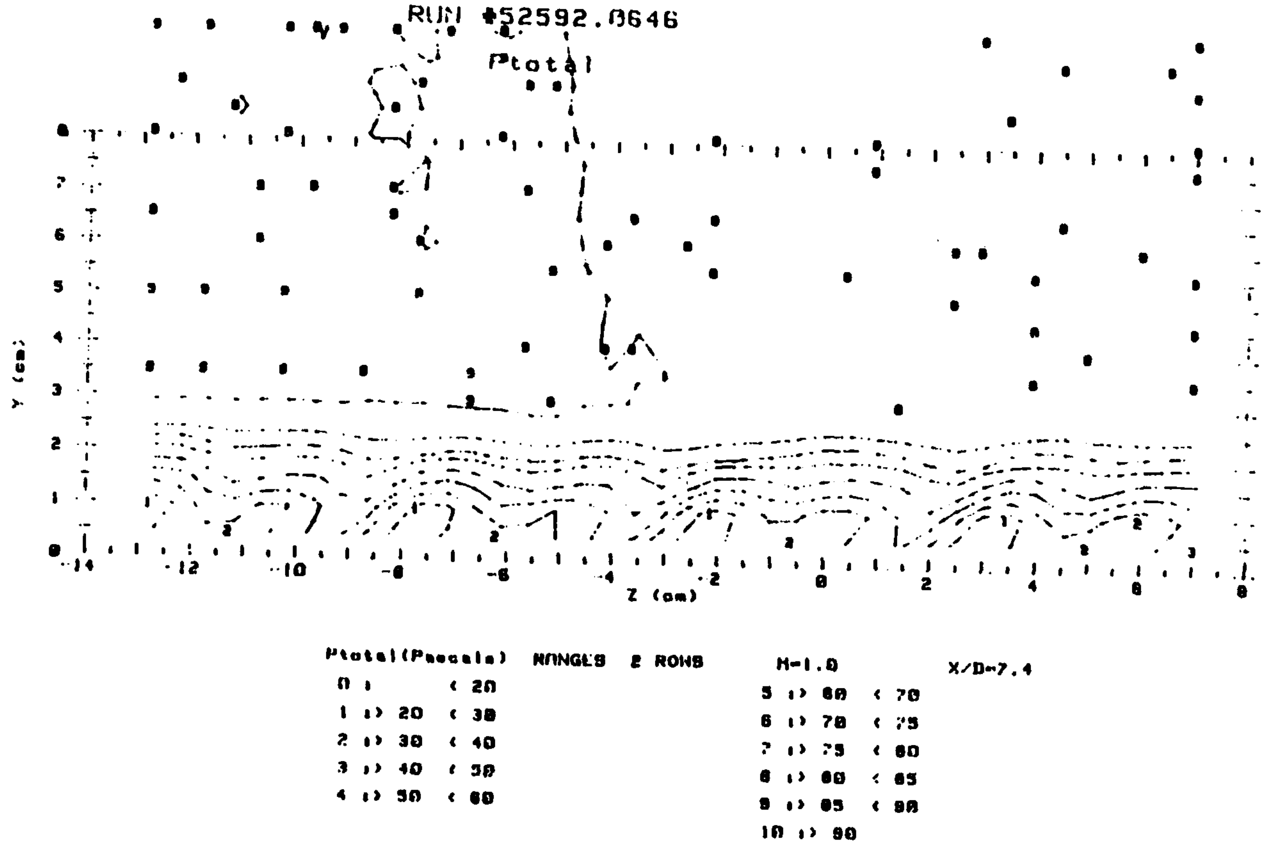

Figure 144. Streamwise Pressure Field, Compound Angle, 2 rows, m=1.0, x/d=7.4

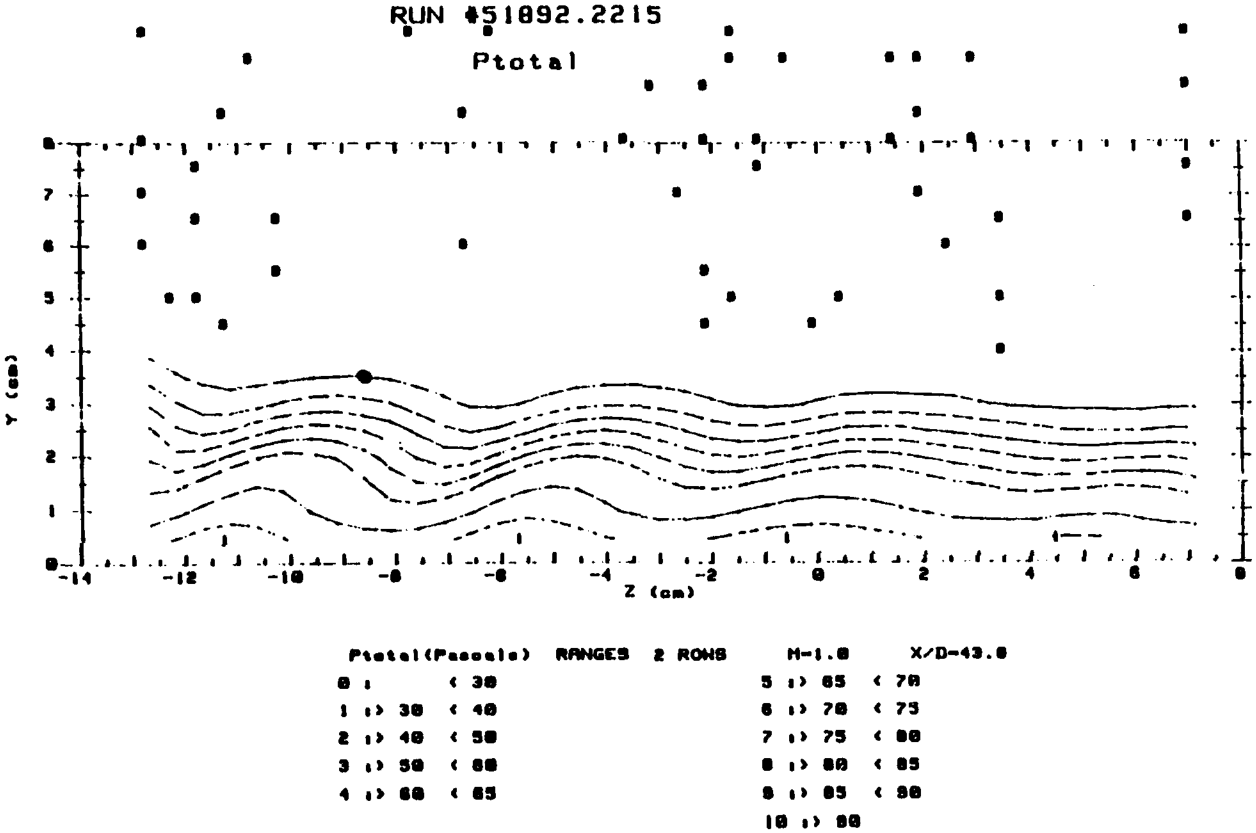

Figure 145. Streamwise Pressure Field, Compound Angle, 2 rows, m=1.0, x/d=43.8

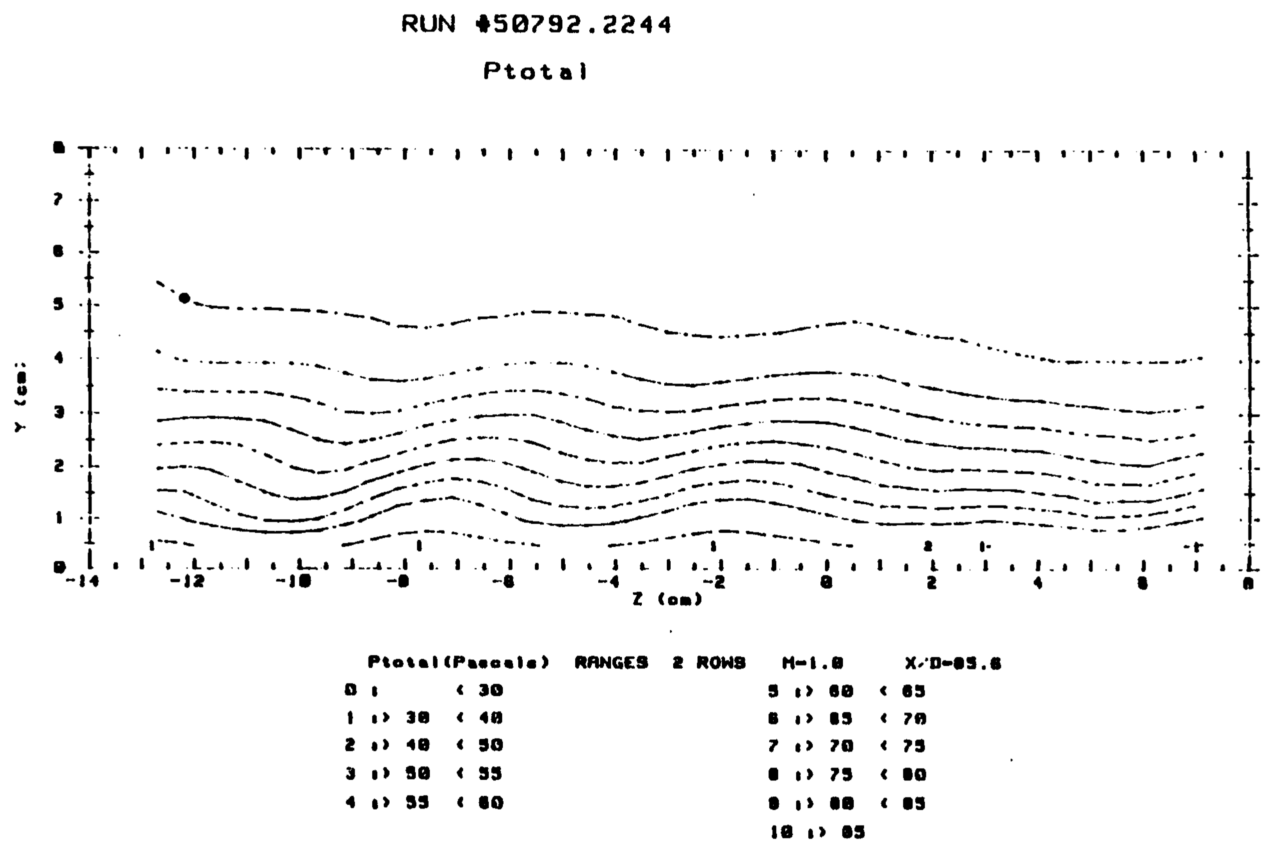

Figure 146. Streamwise Pressure Field, Compound Angle, 2 row, m=1.0, x/d=85.6

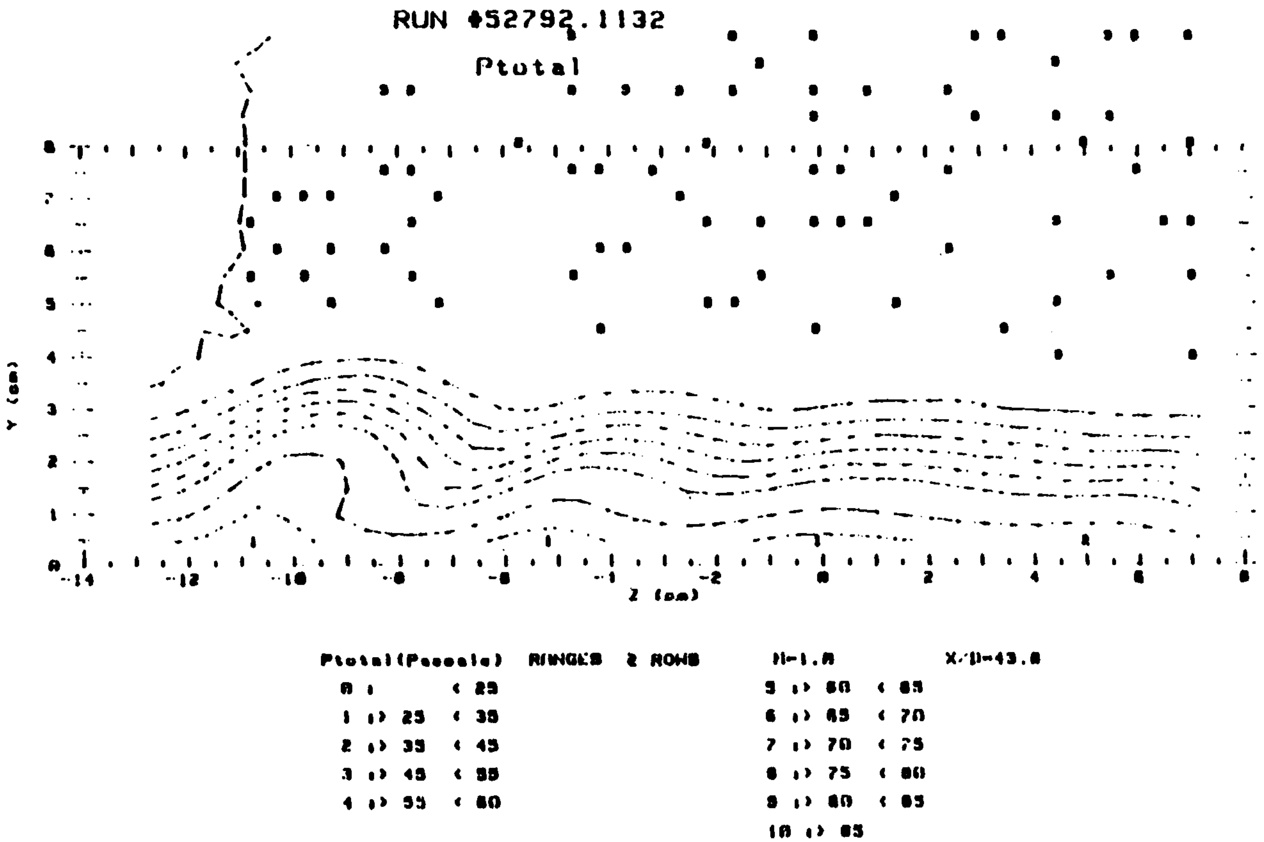

Figure 147. Streamwise Pressure Field, Compound Angle, 2 rows (8 holes), m=1.0, x/d=43.8

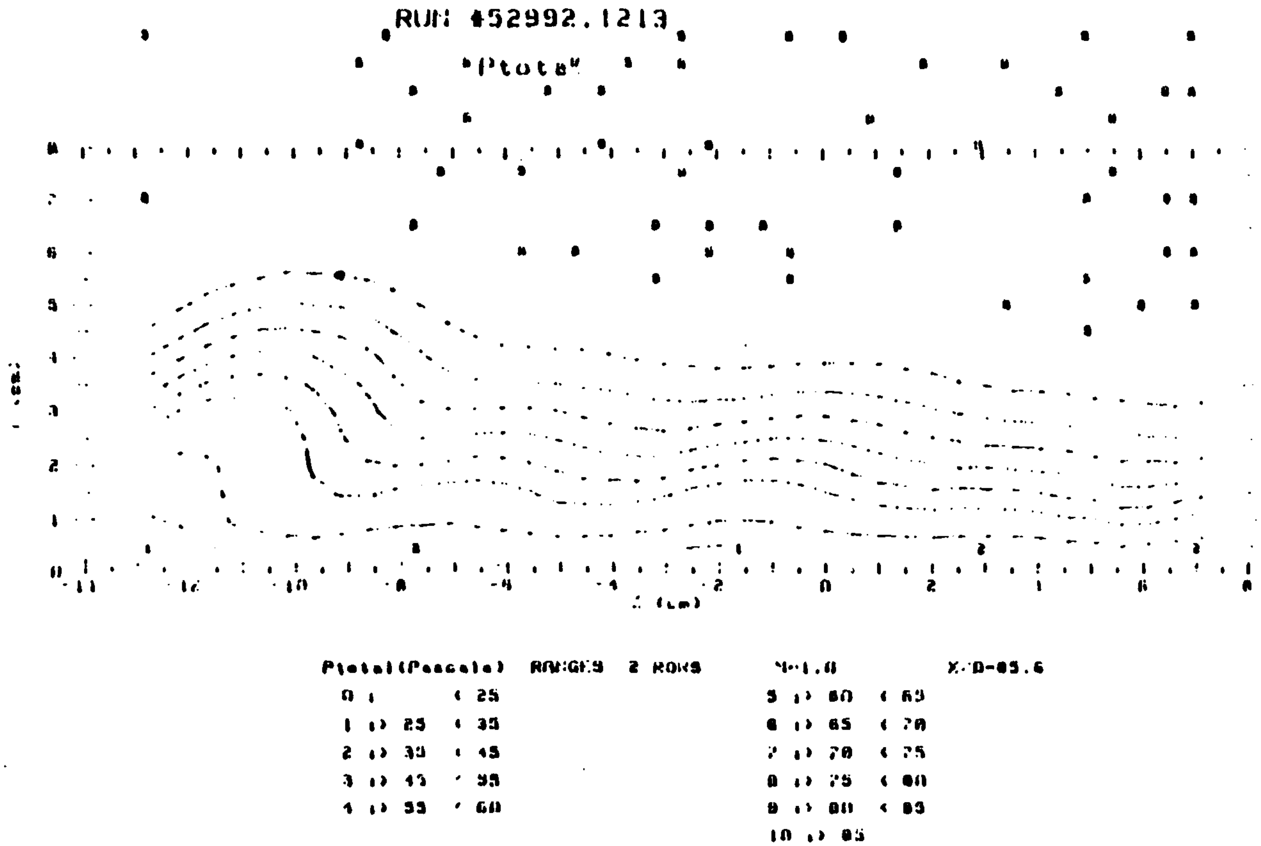

Figure 148. Streamwise Pressure Field, Compound Angle, 2 rows (8 holes), m=1.0, x/d=85.6

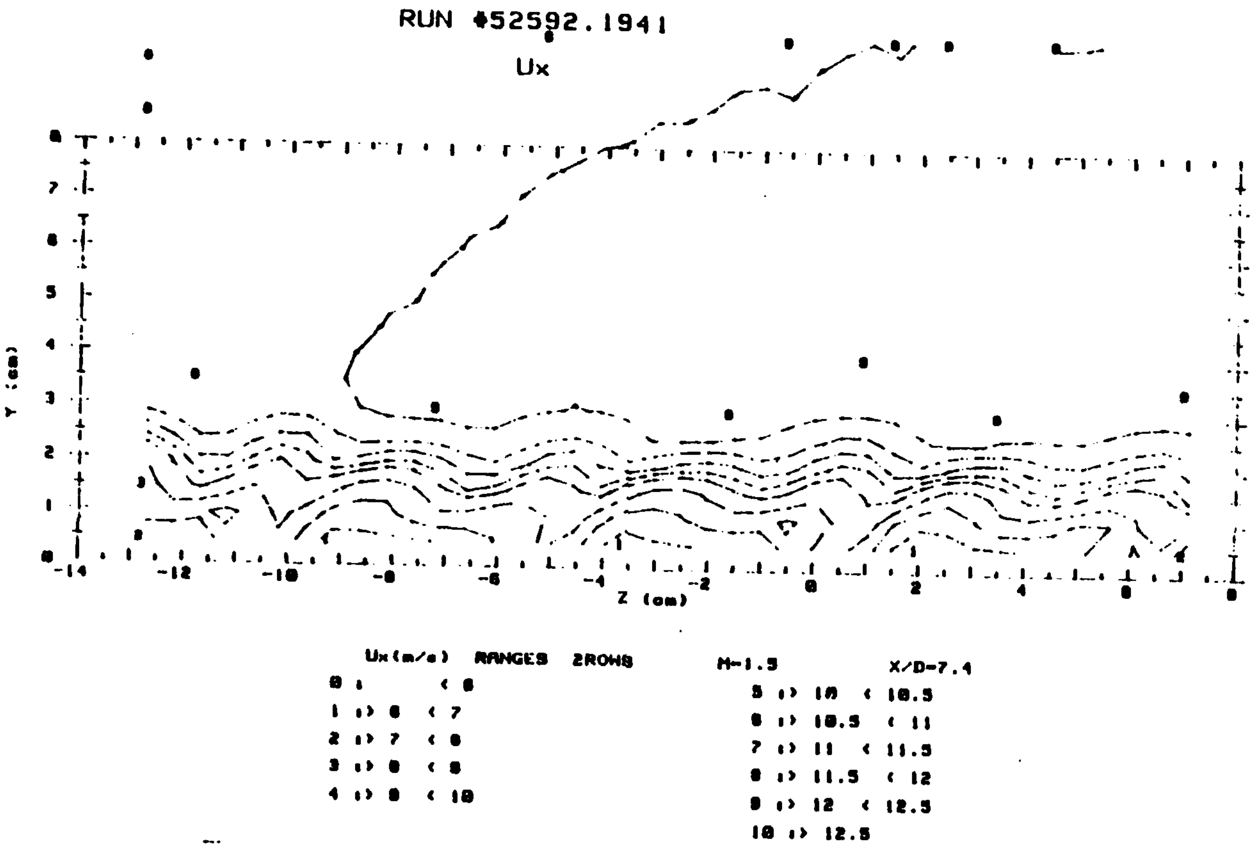

Figure 149. Streamwise Velocity Field, Compound Angle, 2 rows, m=1.5, x/d=7.4

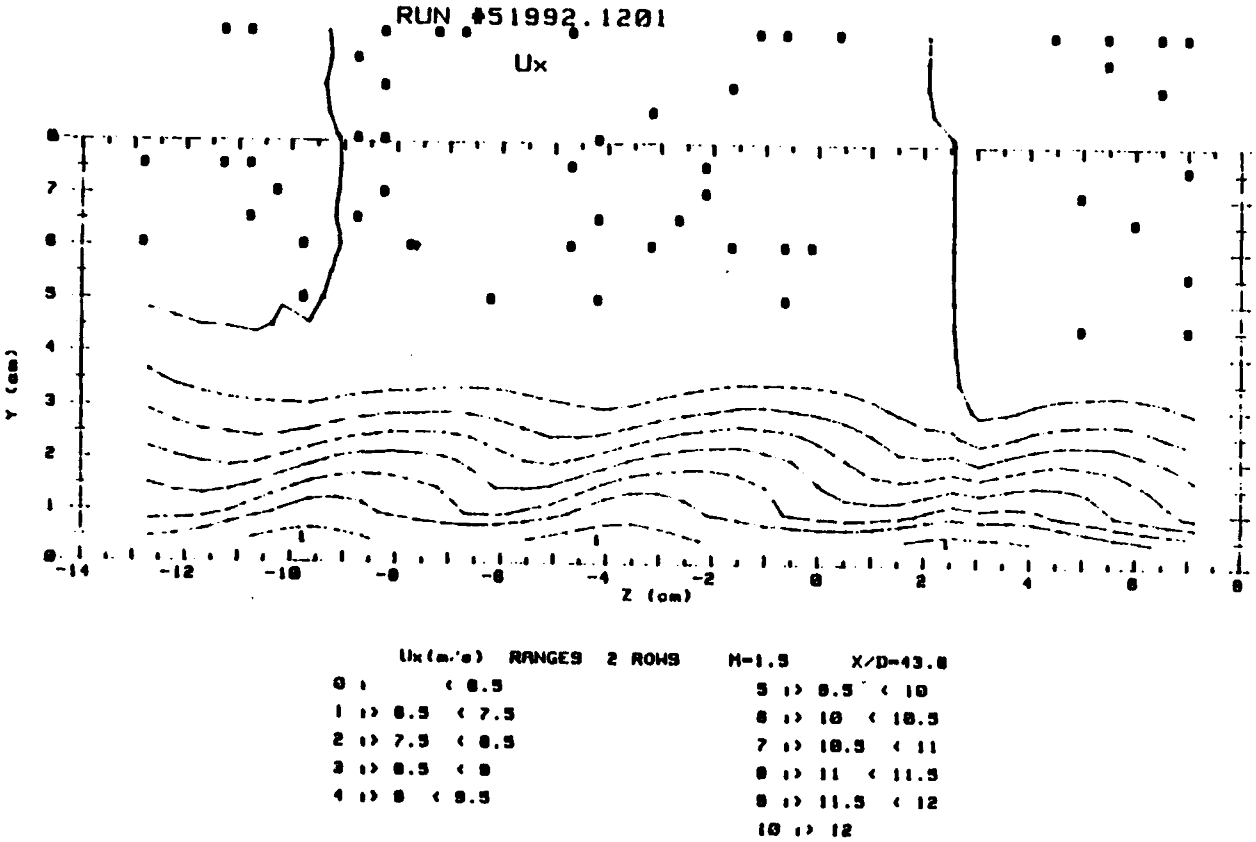

Figure 150. Streamwise Velocity Field, Compound Angle, 2 rows, m=1.5, x/d=43.8

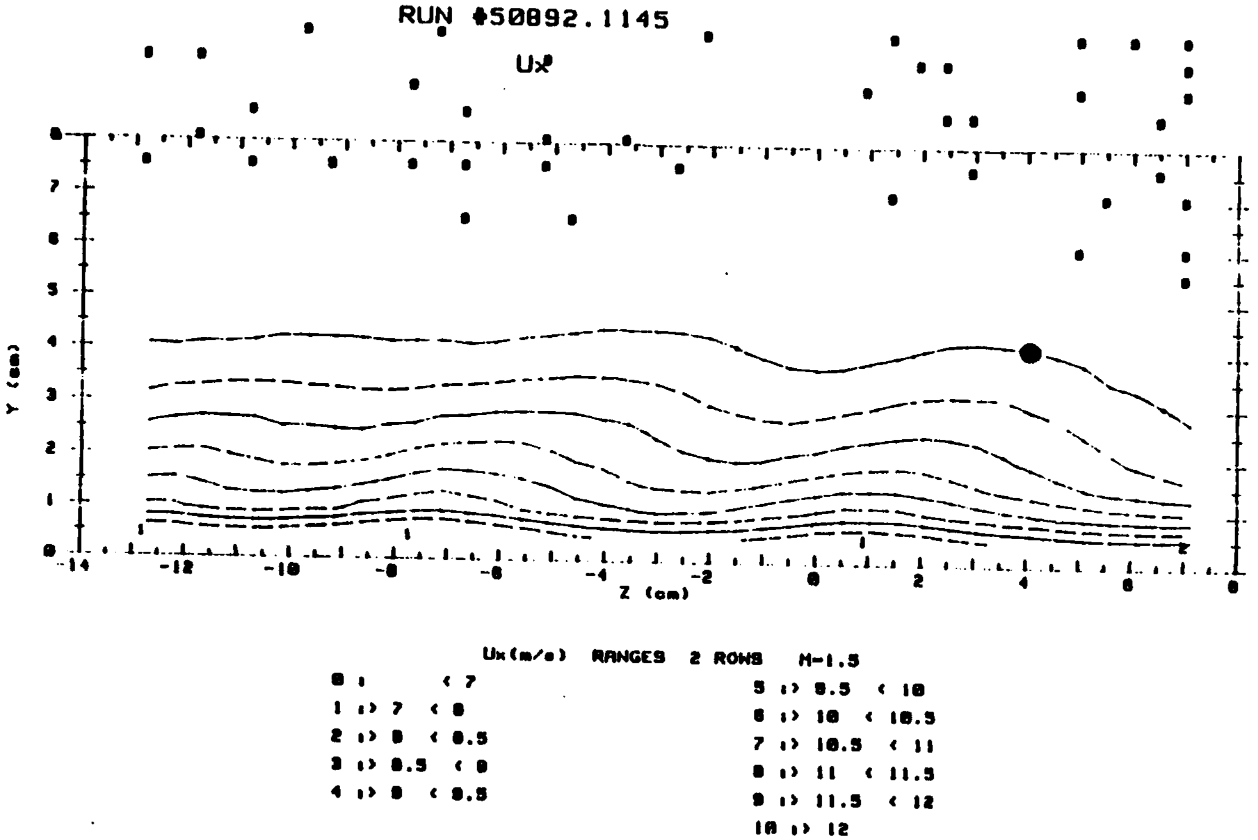

Figure 151. Streamwise Velocity Field, Compound Angle, 2 rows, m=1.5, x/d=85.6

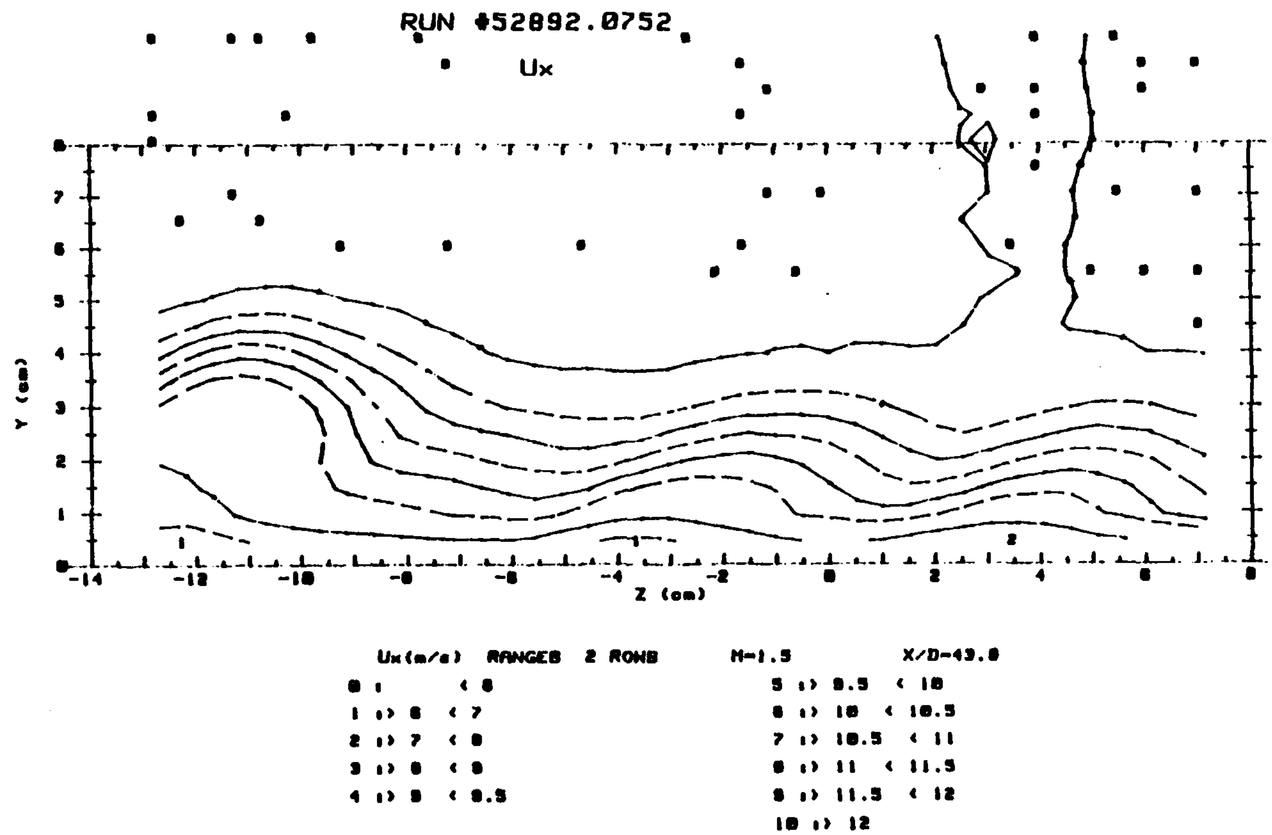

Figure 152. Streamwise Velocity Field, Compound Angle, 2 rows (8 holes), m=1.5, x/d=43.8

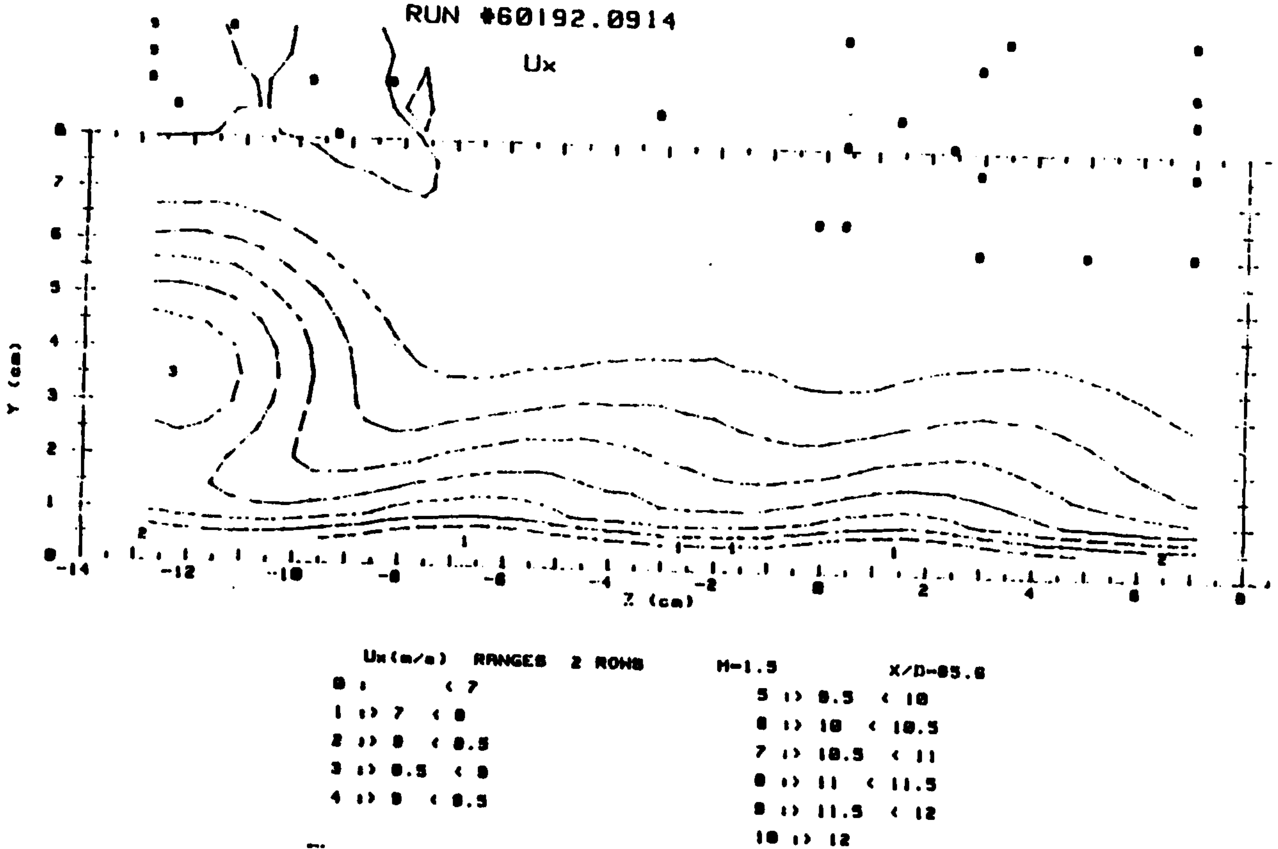

Figure 153. Streamwise Velocity Field, Compound Angle, 2 rows (8 holes), m=1.5, x/d=85.6

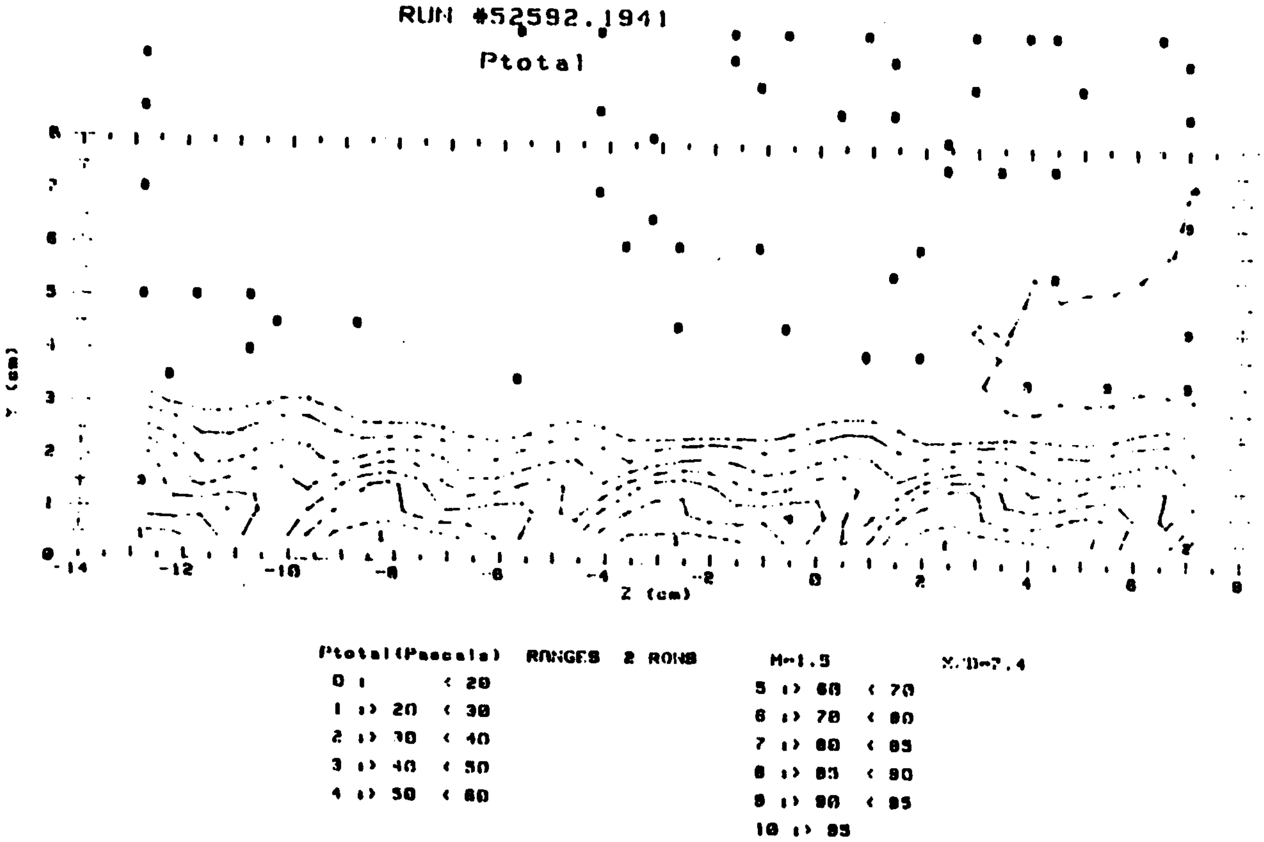

Figure 154. Streamwise Pressure Field, Compound Angle, 2 rows, m=1.5, x/d=7.4

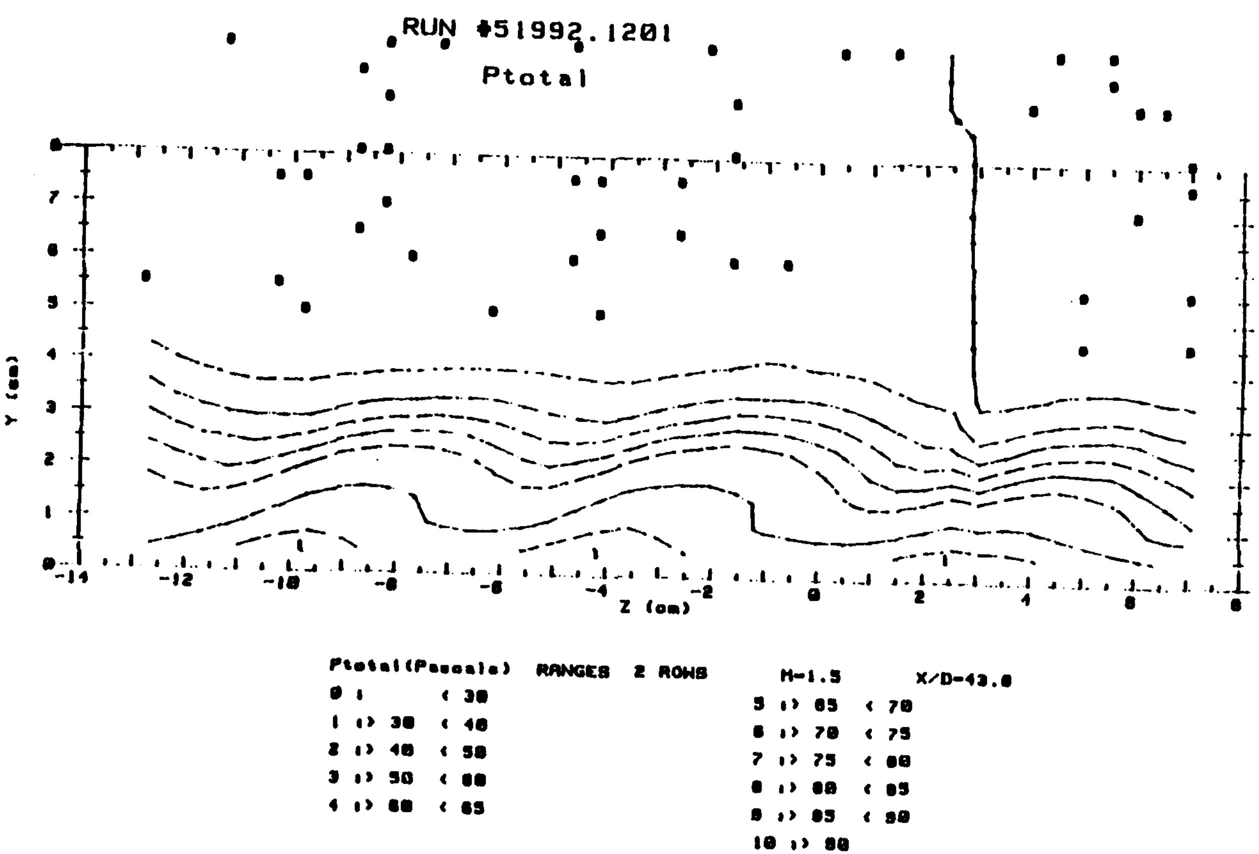

Figure 155. Streamwise Pressure Field, Compound Angle, 2 rows, m=1.5, x/d=43.8

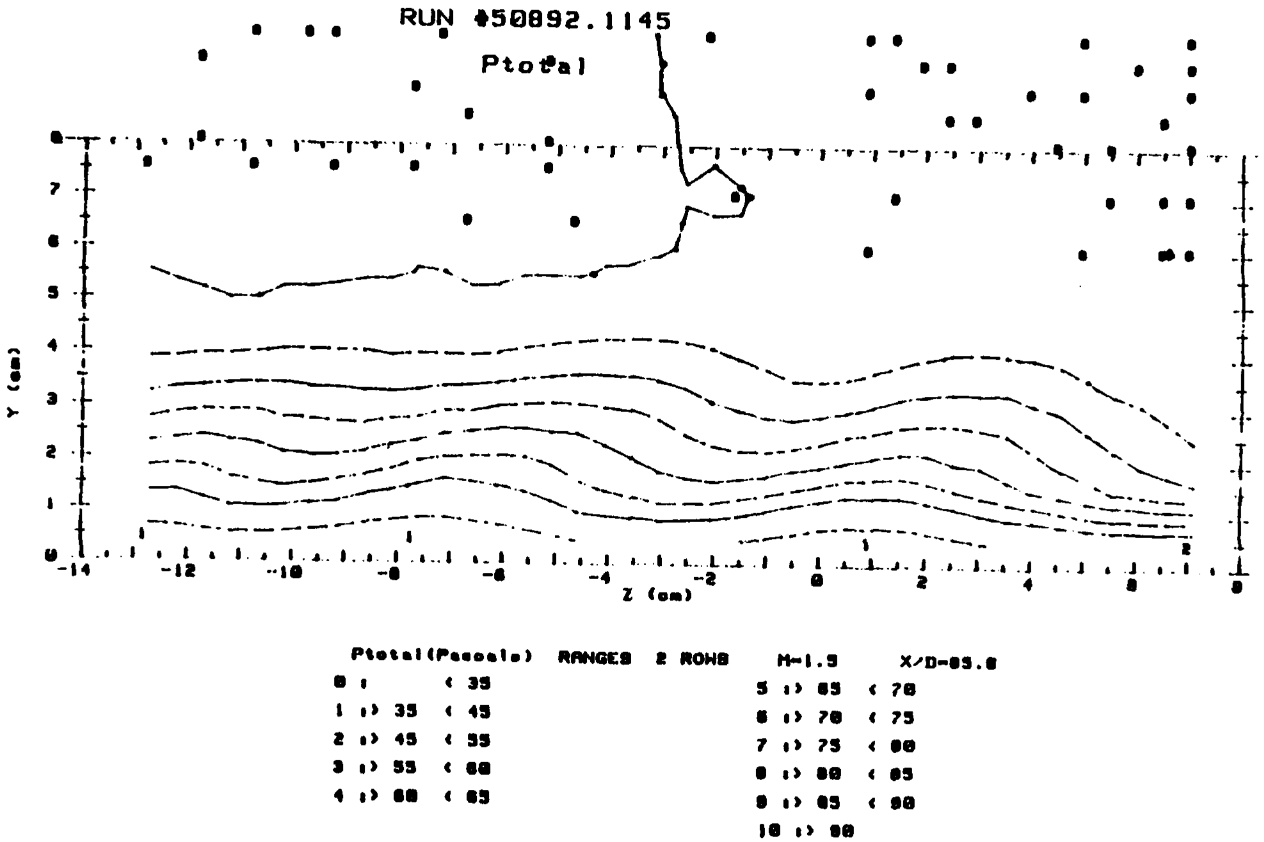

Figure 156. Streamwise Pressure Field, Compound Angle, 2 row, m=1.5, x/d=85.6

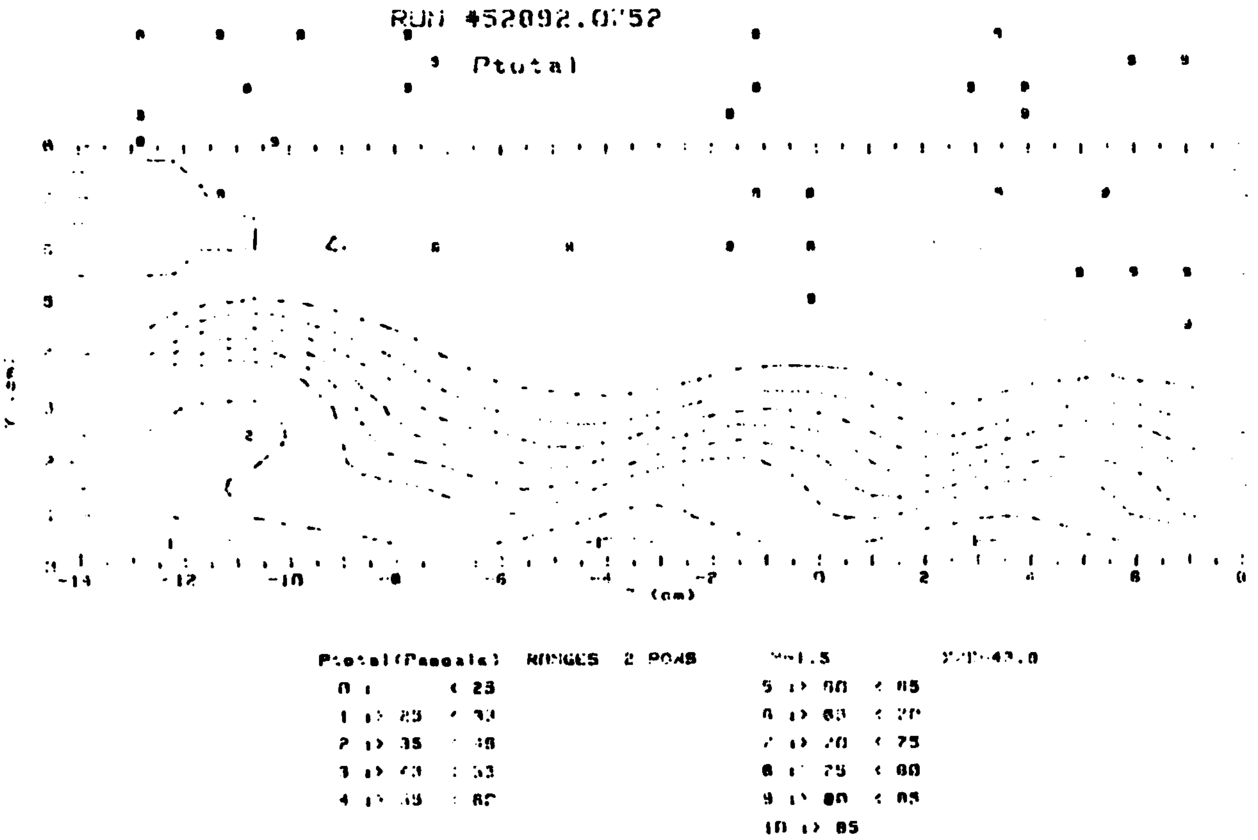

Figure 157. Streamwise Pressure Field, Compound Angle, 2 rows (8 holes), m=1.5, x/d=43.8

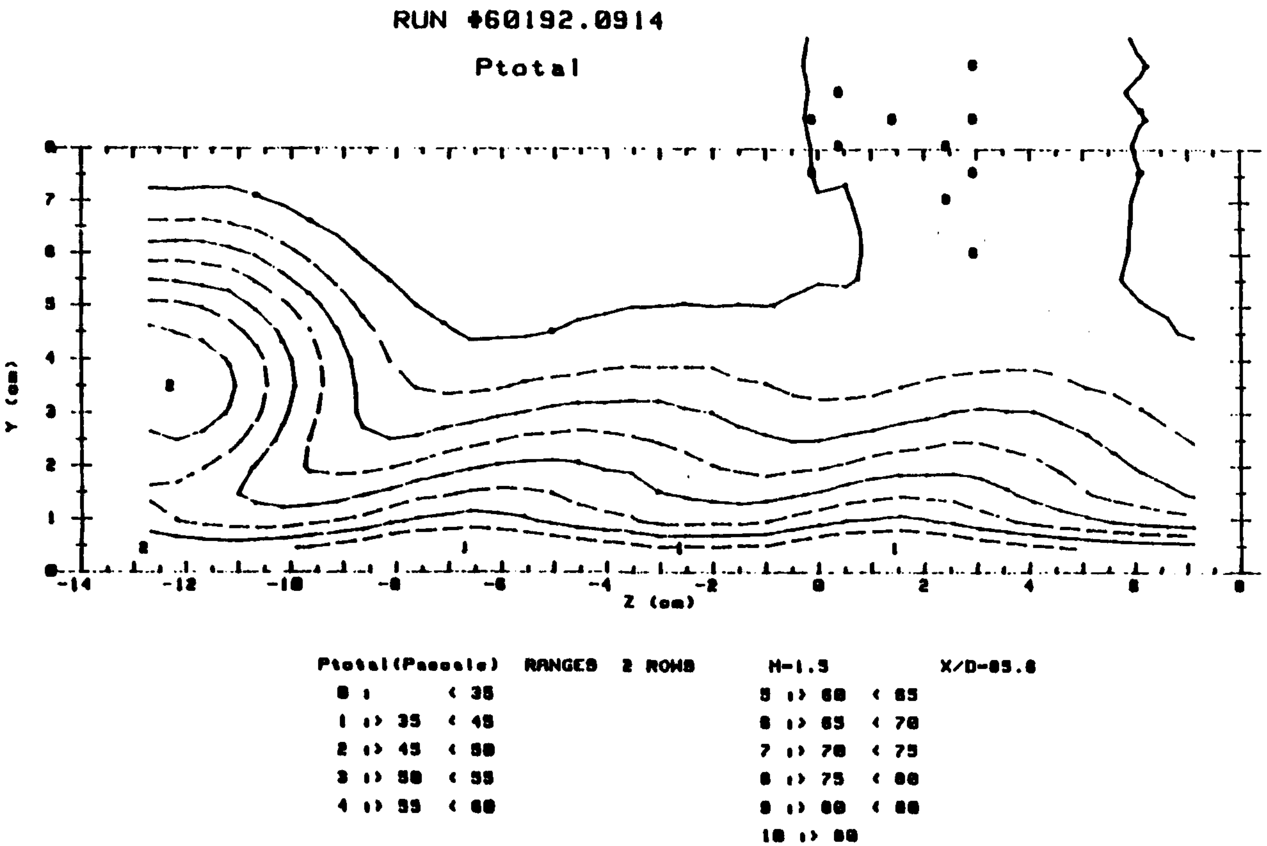

Figure 158. Streamwise Pressure Field, Compound Angle, 2 rows (8 holes), m=1.5, x/d=85.6

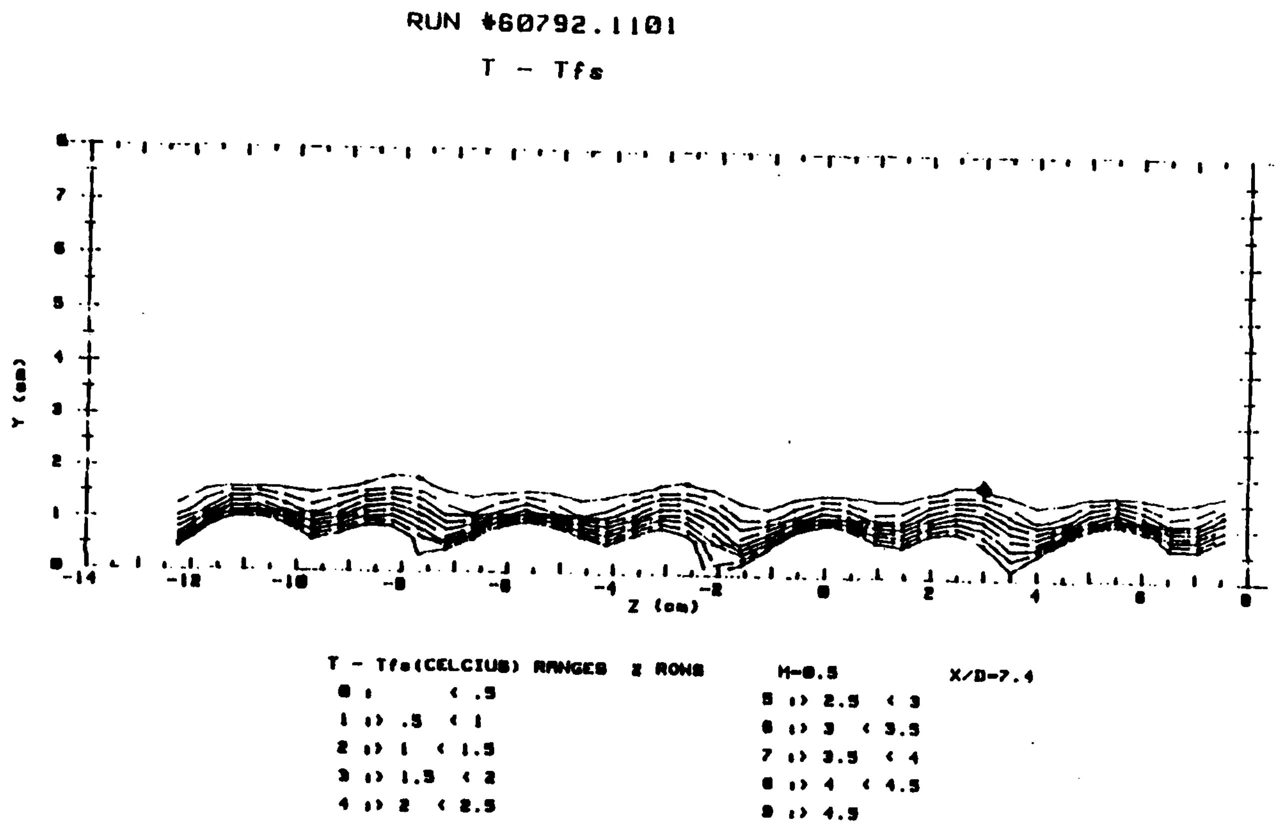

Figure 159. Streamwise Injectant Distribution, Compound Angle, 2 rows, m=0.5, x/d=7.4

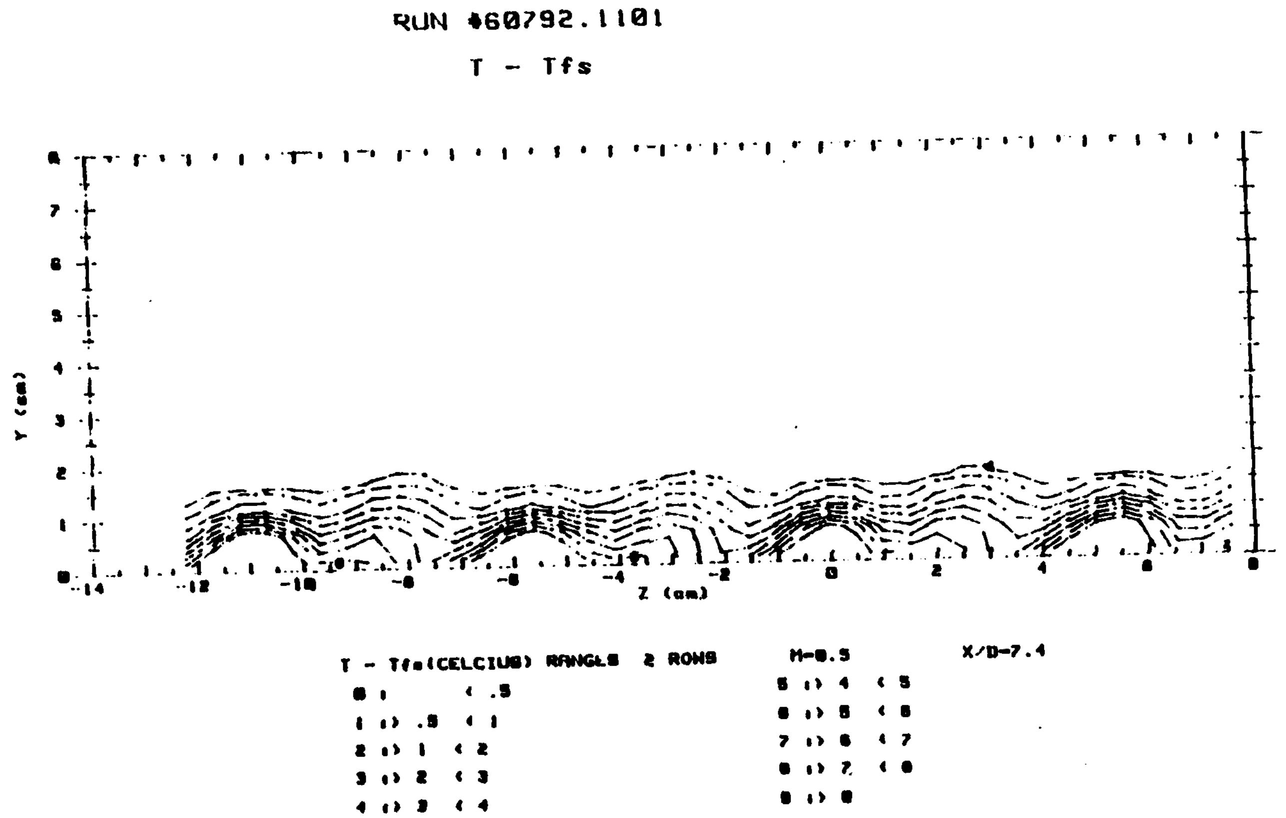

Figure 160. Streamwise Injectant Distribution, Compound Angle, 2 rows (larger range), m=0.5, x/d=7.4

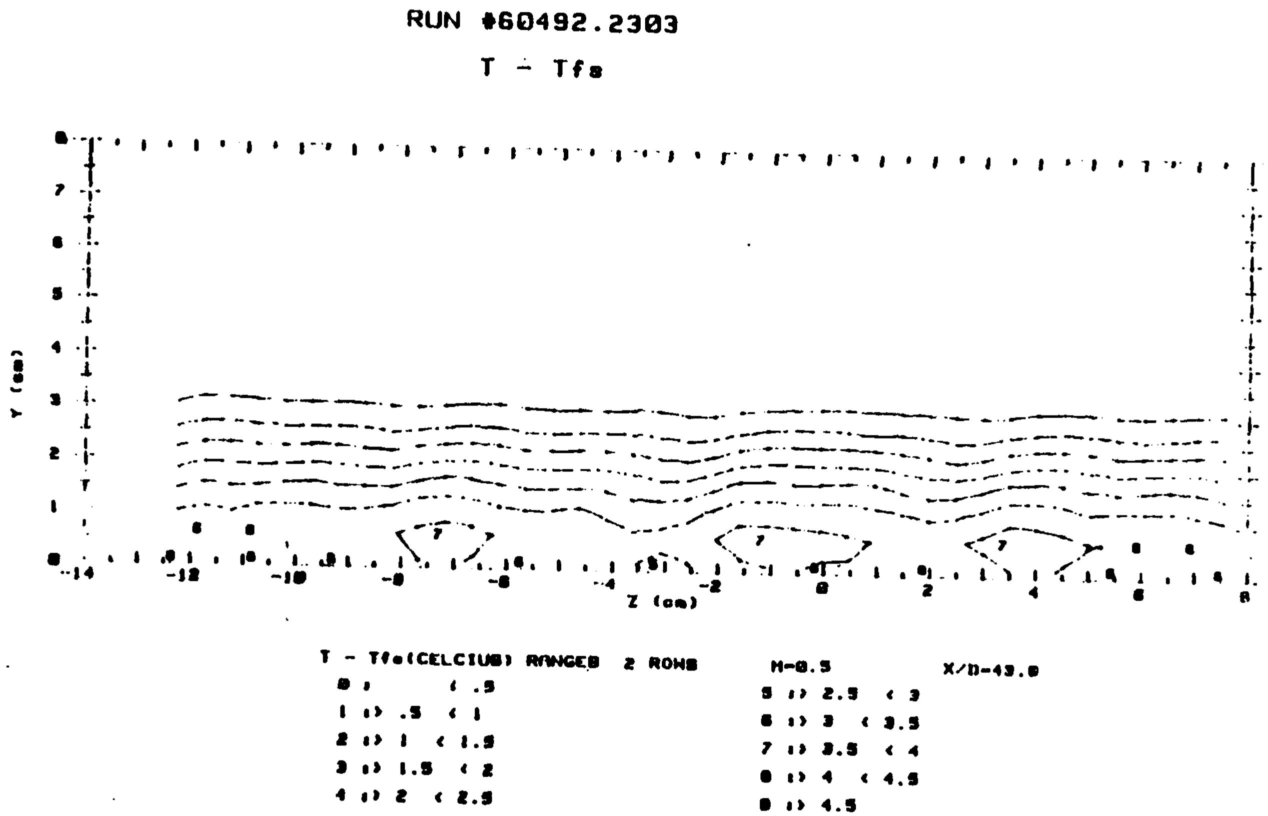

Figure 161. Streamwise Injectant Distribution, Compound Angle, 2 rows, m=0.5, x/d=43.8

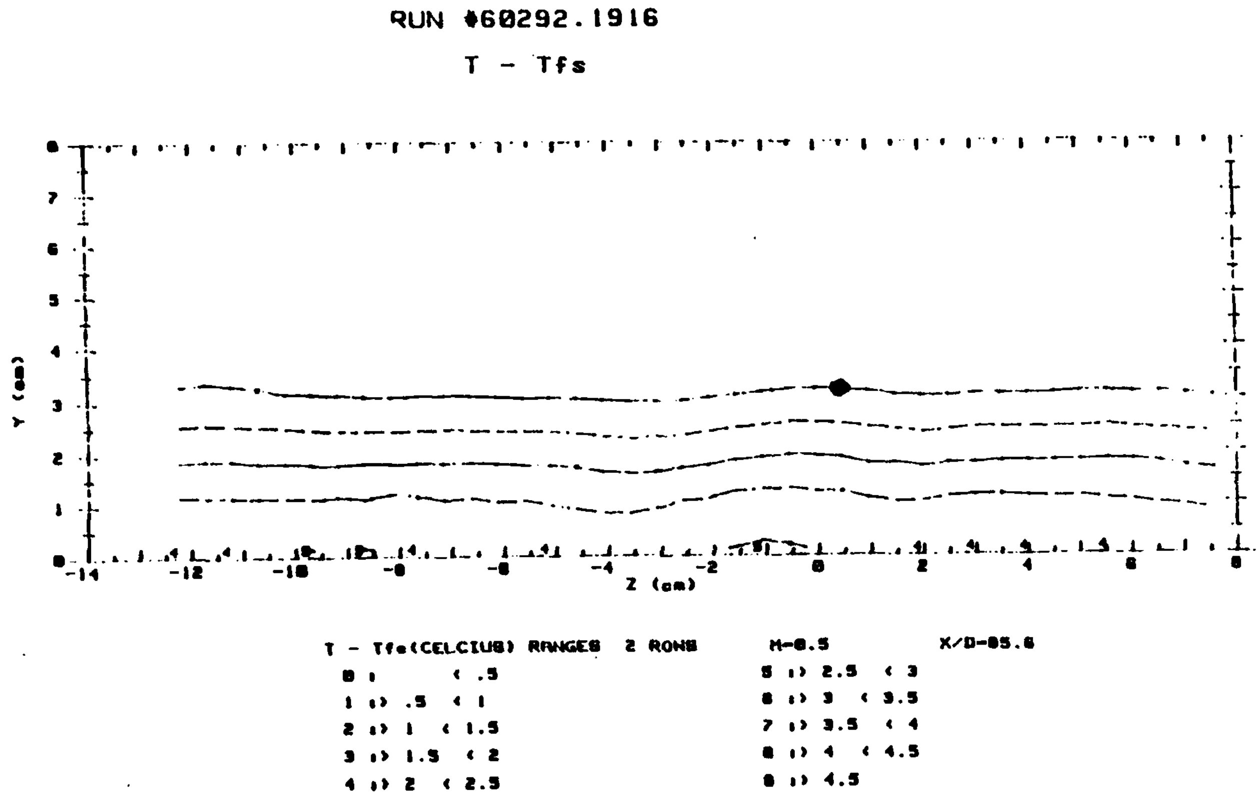

Figure 162. Streamwise Injectant Distribution, Compound Angle, 2 rows, m=0.5, x/d=85.6

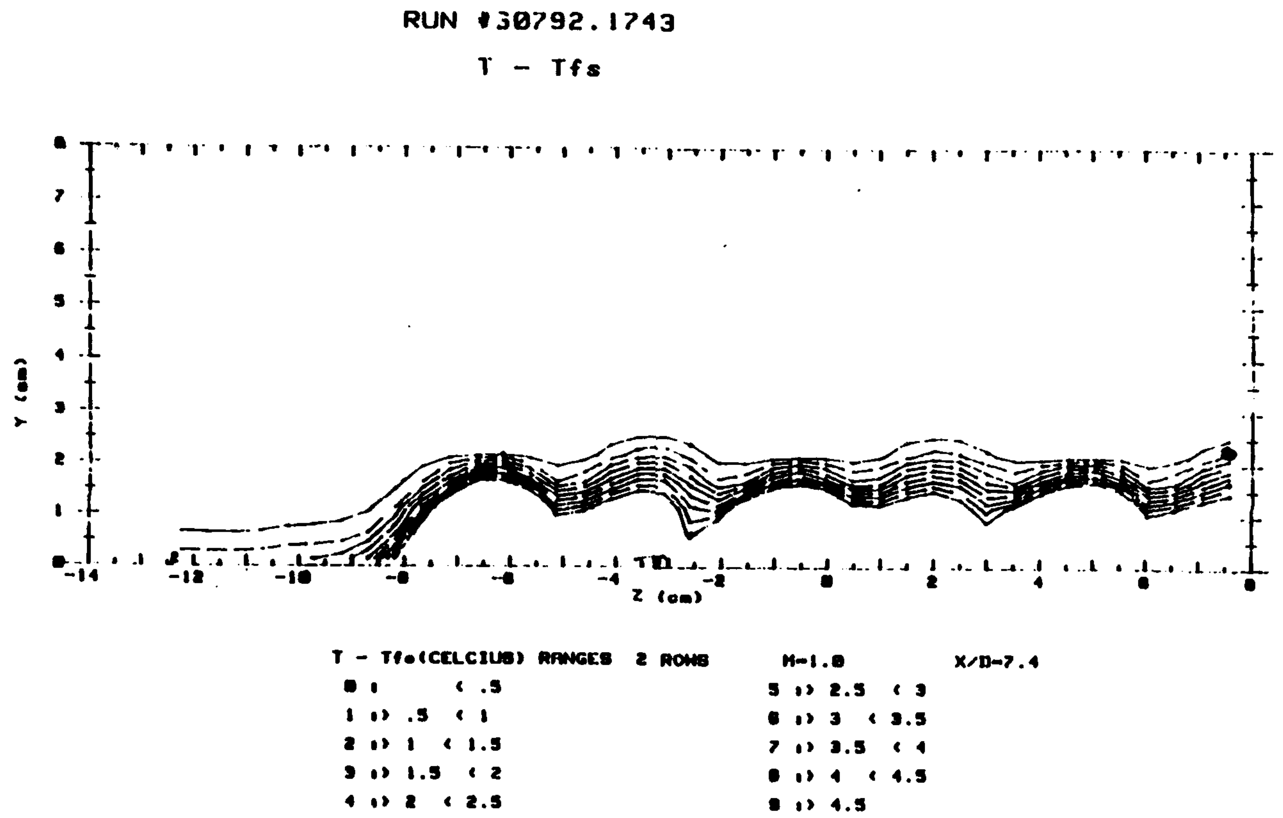

Figure 163. Streamwise Injectant Distribution, Compound Angle, 2 rows (8 holes), m=1.0, x/d=7.4

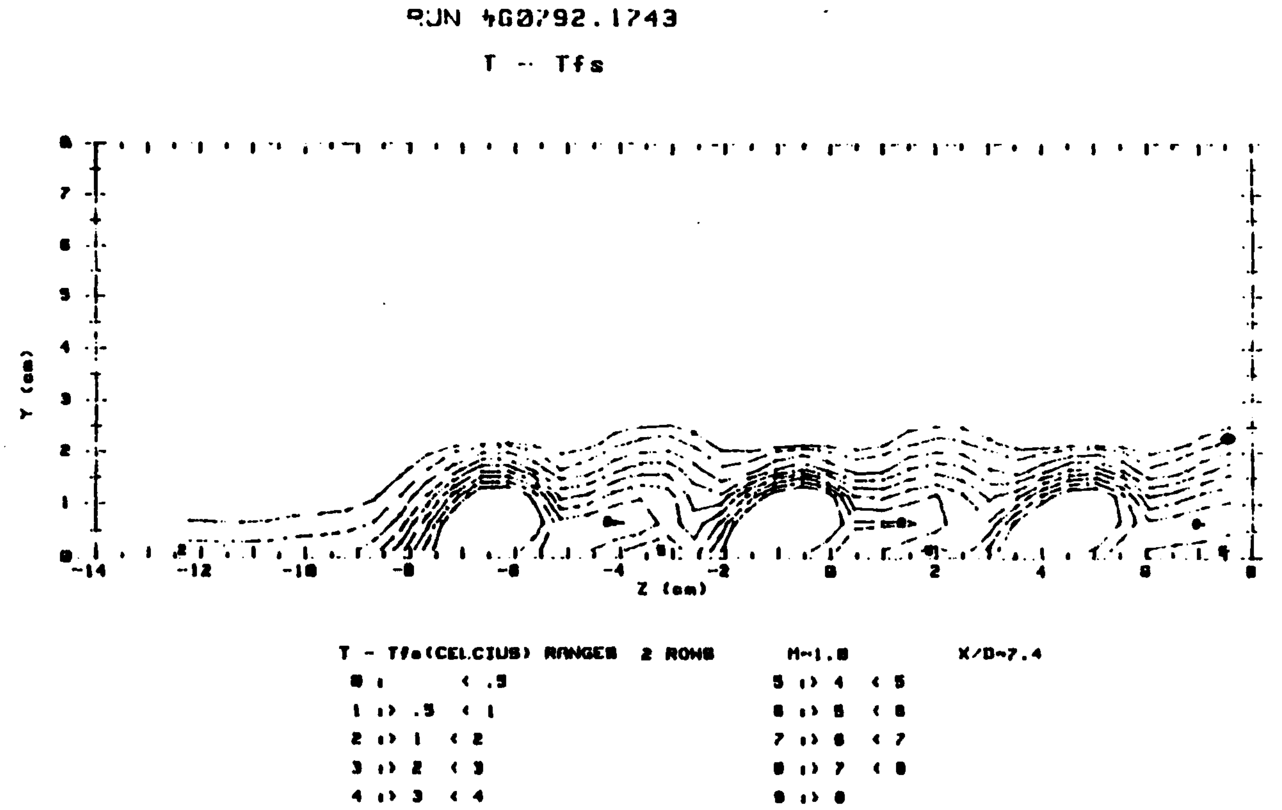

Figure 164. Streamwise Injectant Distribution, Compound Angle, 2 rows (8 holes, larger range), m=1.0, x/d=7.4

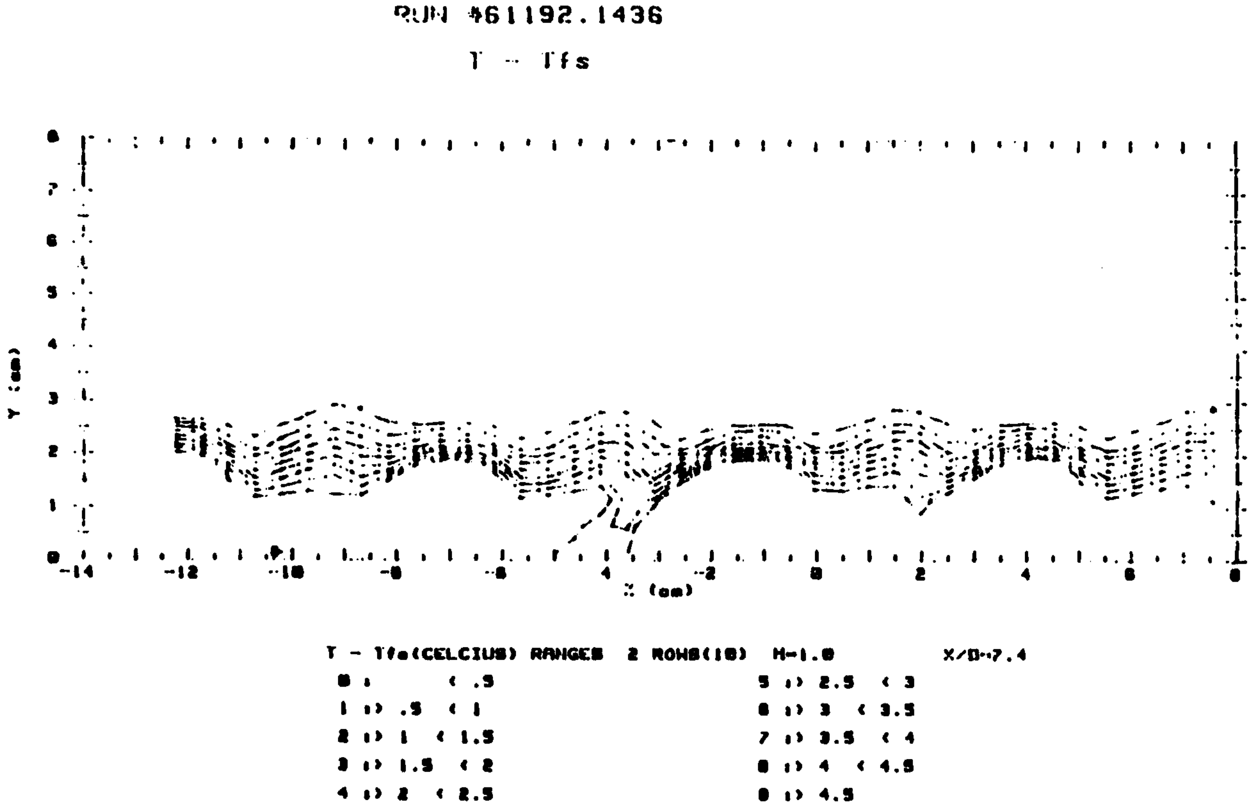

Figure 165. Streamwise Injectant Distribution, Compound Angle, 2 rows (10 holes), m=1.0, x/d=7.4

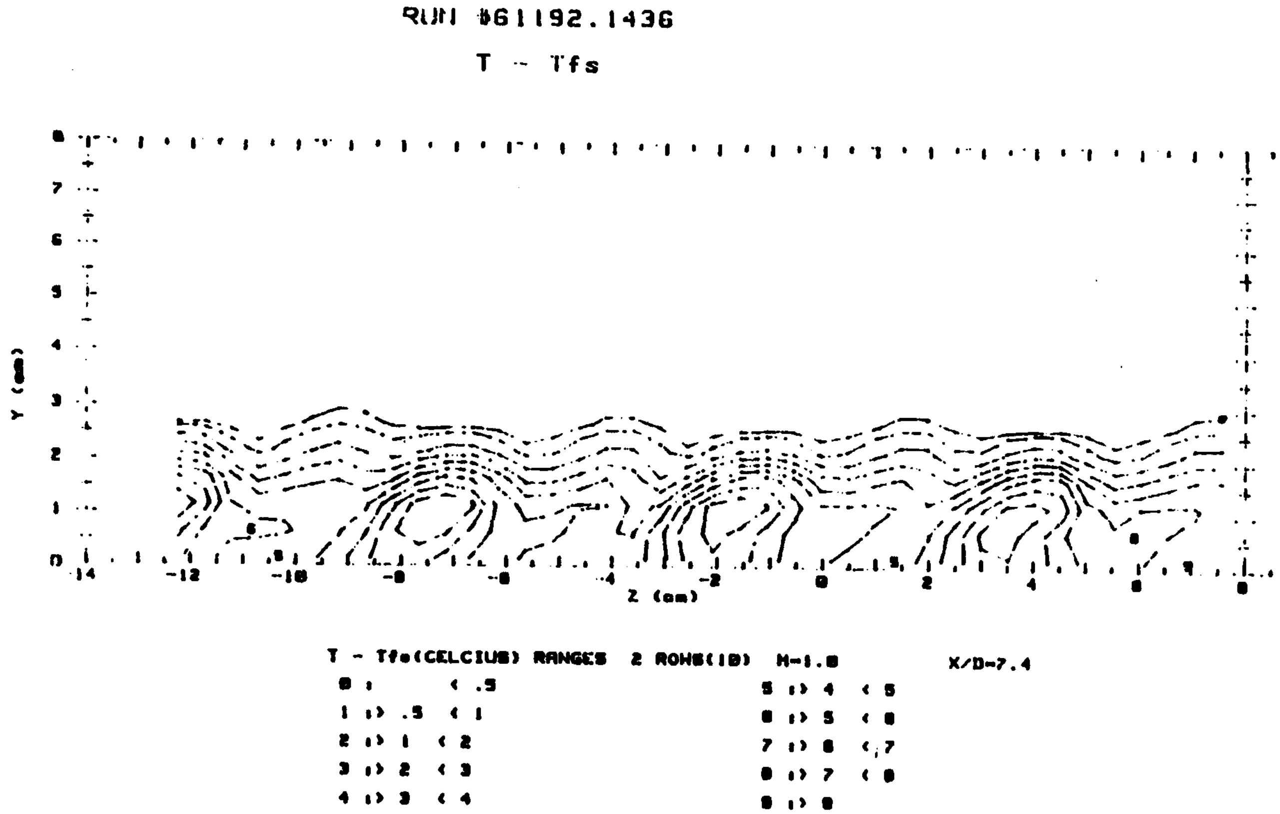

Figure 166. Streamwise Injectant Distribution, Compound Angle, 2 rows (10 holes, larger range), m=1.0, x/d=7.4

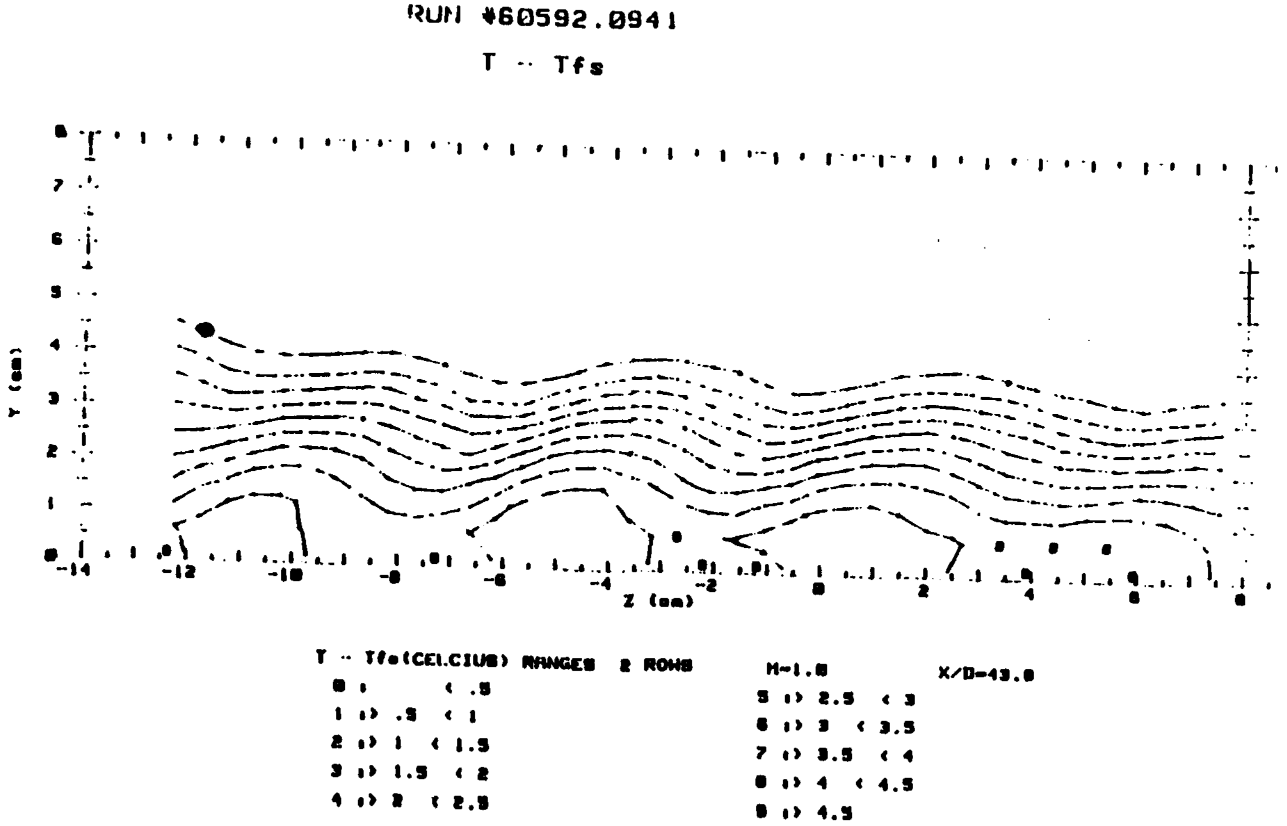

Figure 167. Streamwise Injectant Distribution, Compound Angle, 2 rows, m=1.0, x/d=43.8

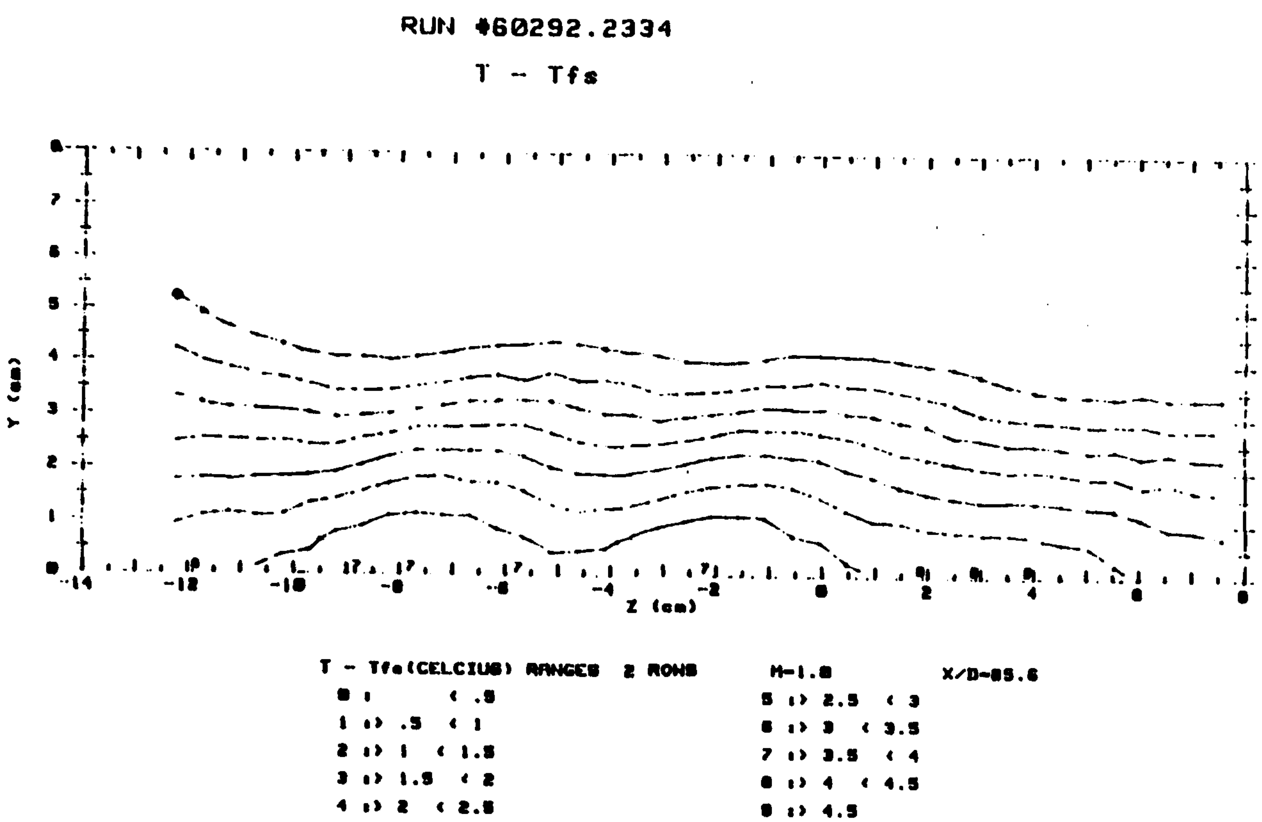

Figure 168. Streamwise Injectant Distribution, Compound Angle, 2 rows, m=1.0, x/d=85.6

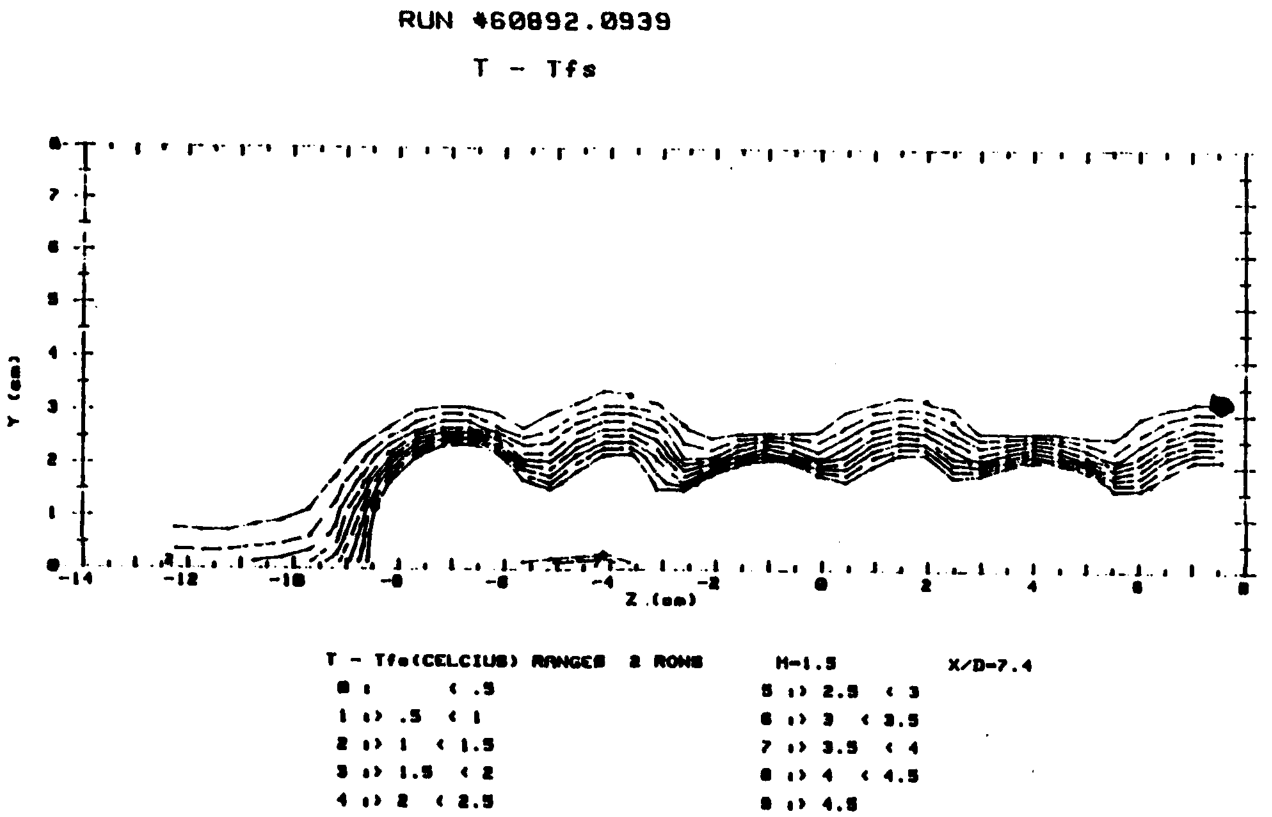

Figure 169. Streamwise Injectant Distribution, Compound Angle, 2 rows (8 holes), m=1.5, x/d=7.4

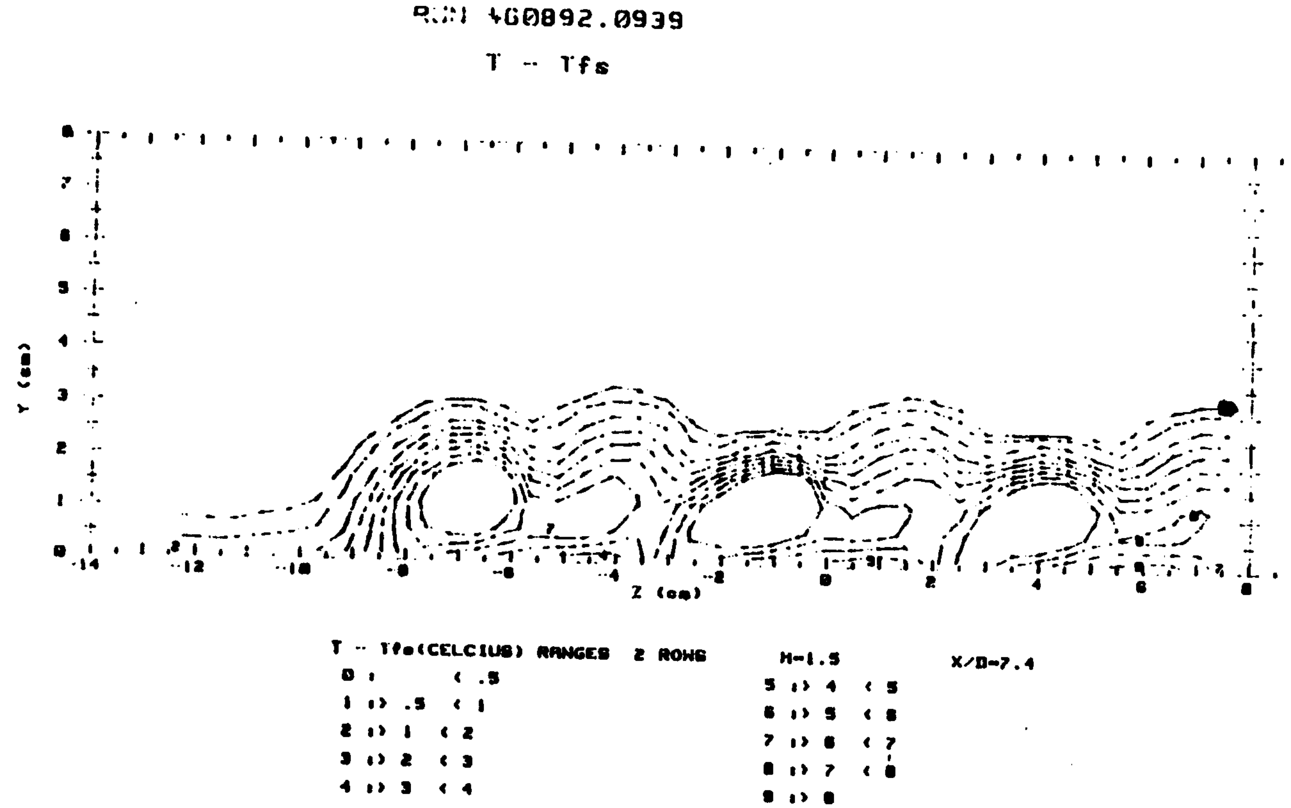

Figure 170. Streamwise Injectant Distribution, Compound Angle, 2 rows (8 holes, larger range), m=1.5, x/d=7.4

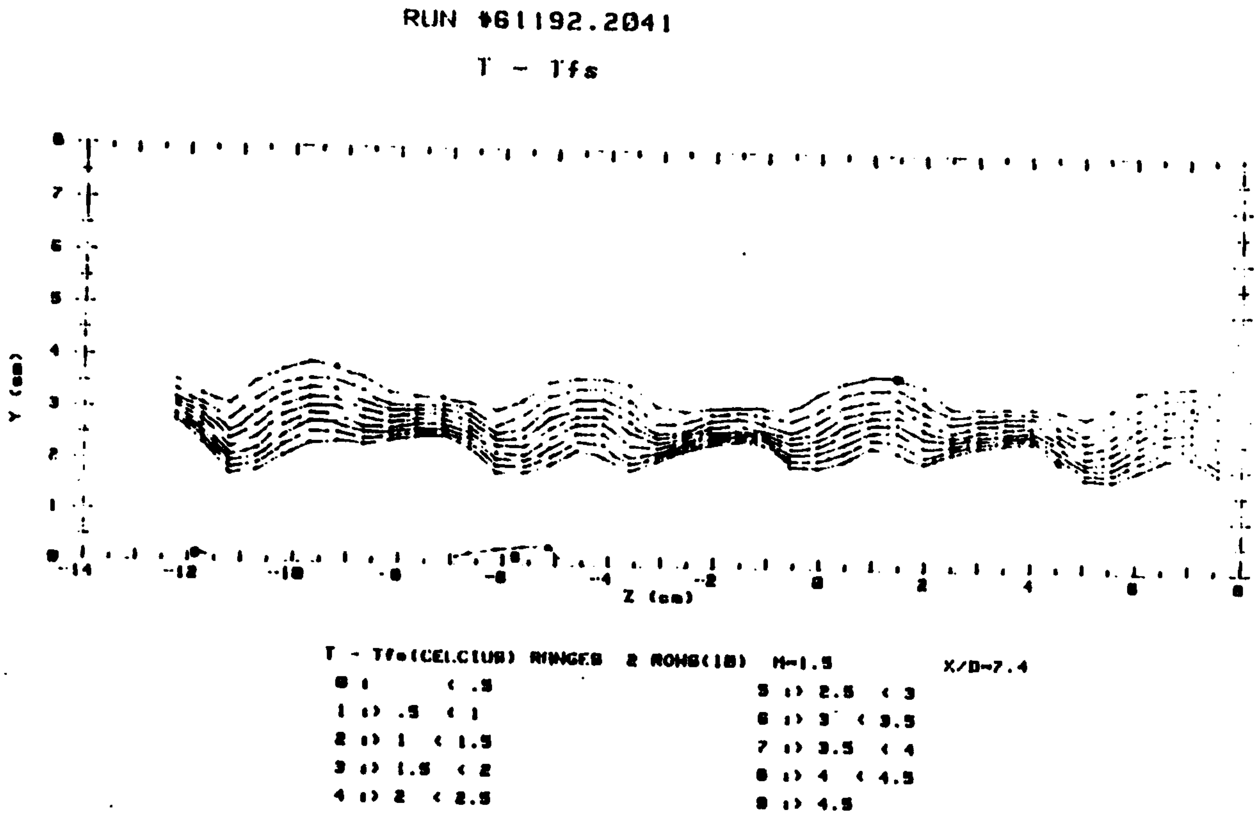

Figure 171. Streamwise Injectant Distribution, Compound Angle, 2 rows (10 holes), m=1.5, x/d=7.4

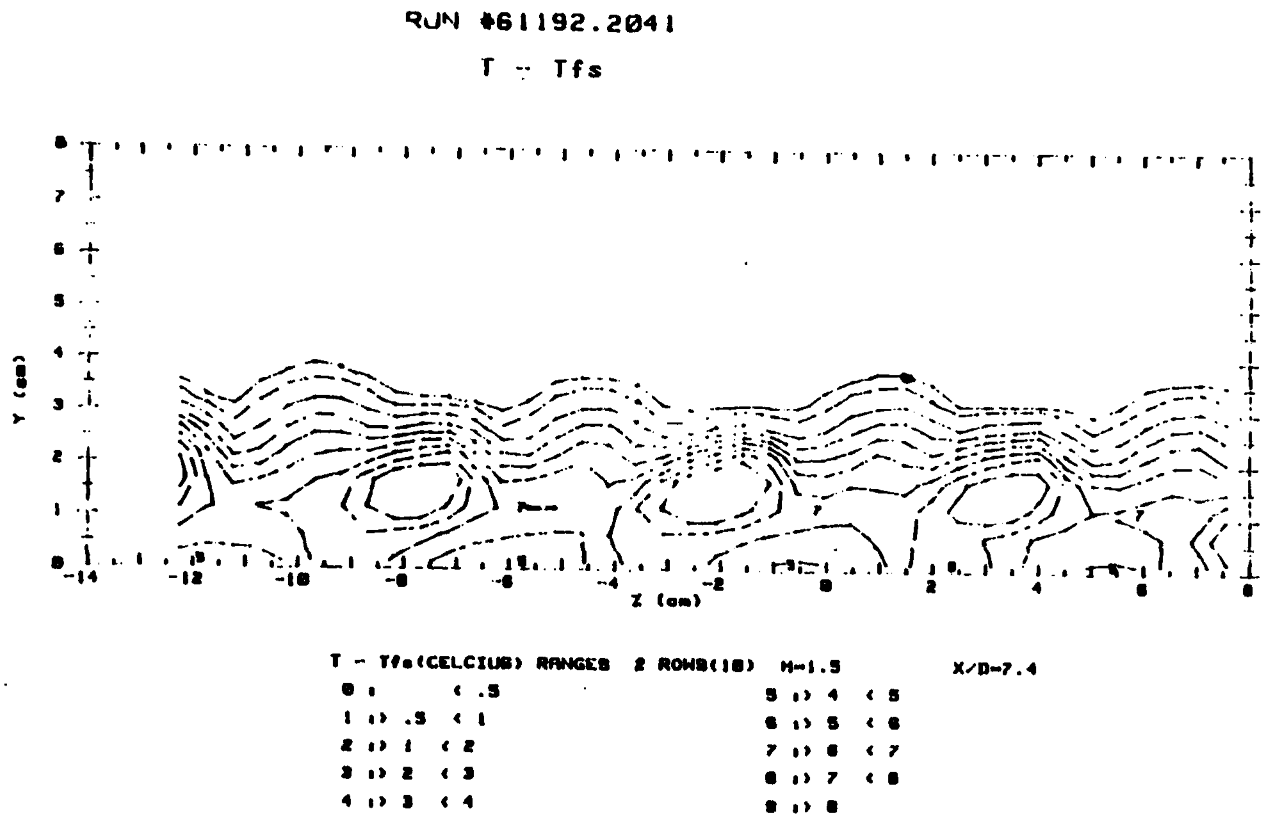

Figure 172. Streamwise Injectant Distribution, Compound Angle, 2 rows (10 holes, larger range), m=1.5, x/d=7.4

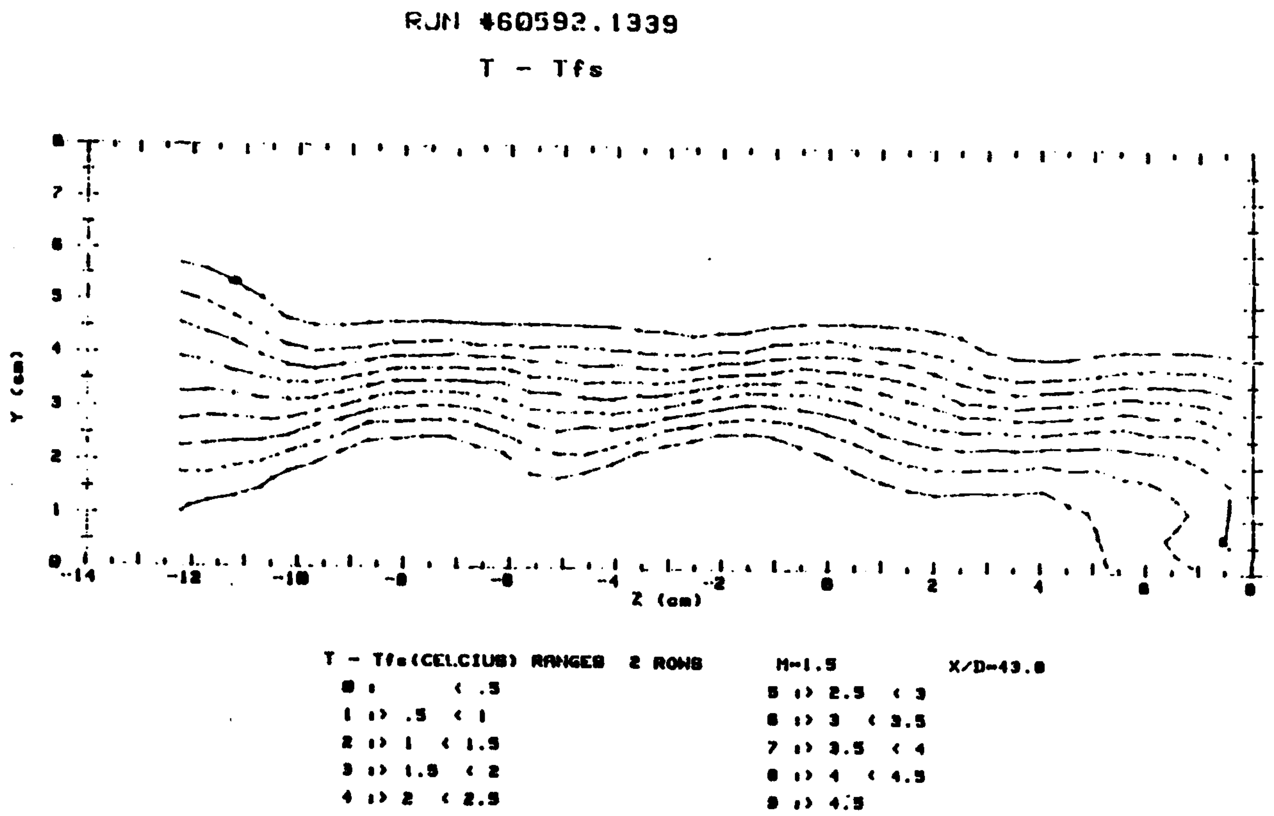

Figure 173. Streamwise Injectant Distribution, Compound Angle, 2 rows, m=1.5, x/d=43.8

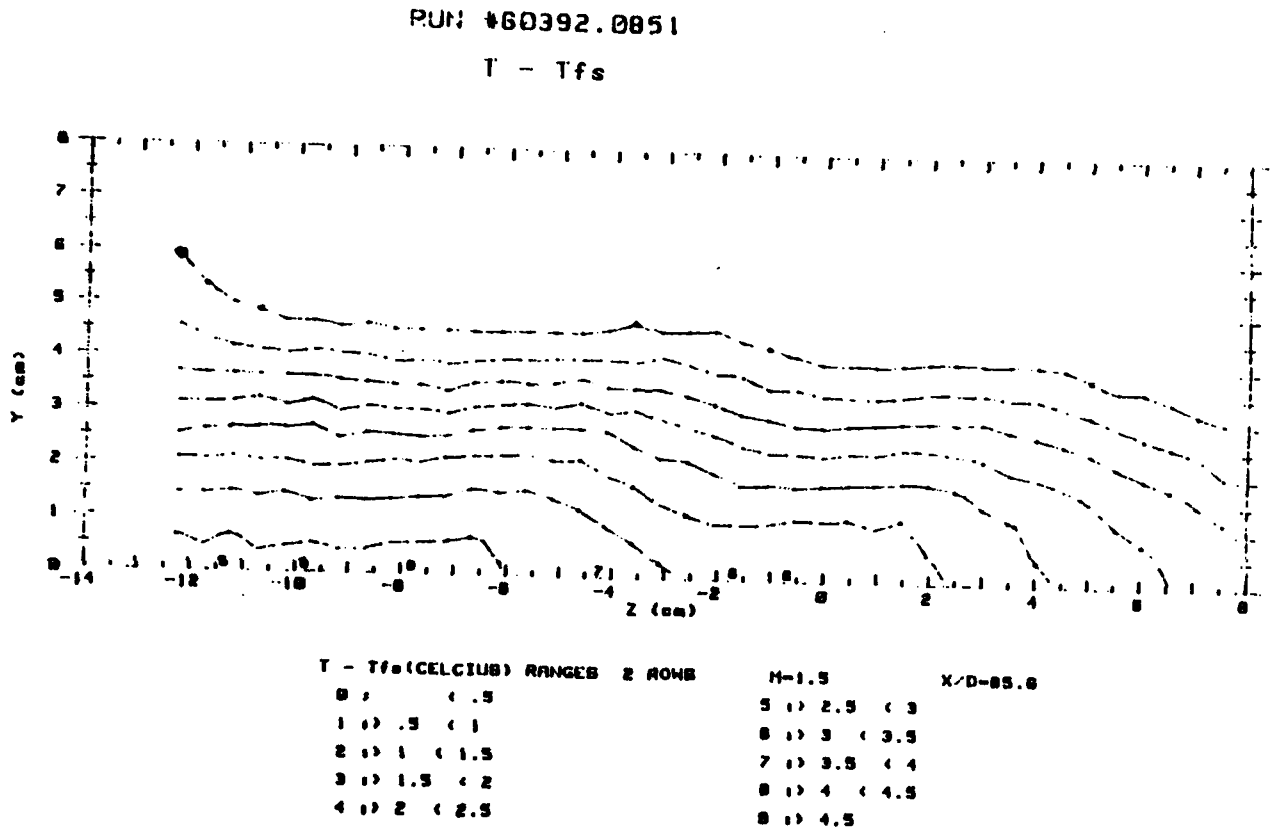

Figure 174. Streamwise Injectant Distribution, Compound Angle, 2 rows, m=1.0, x/d=85.6

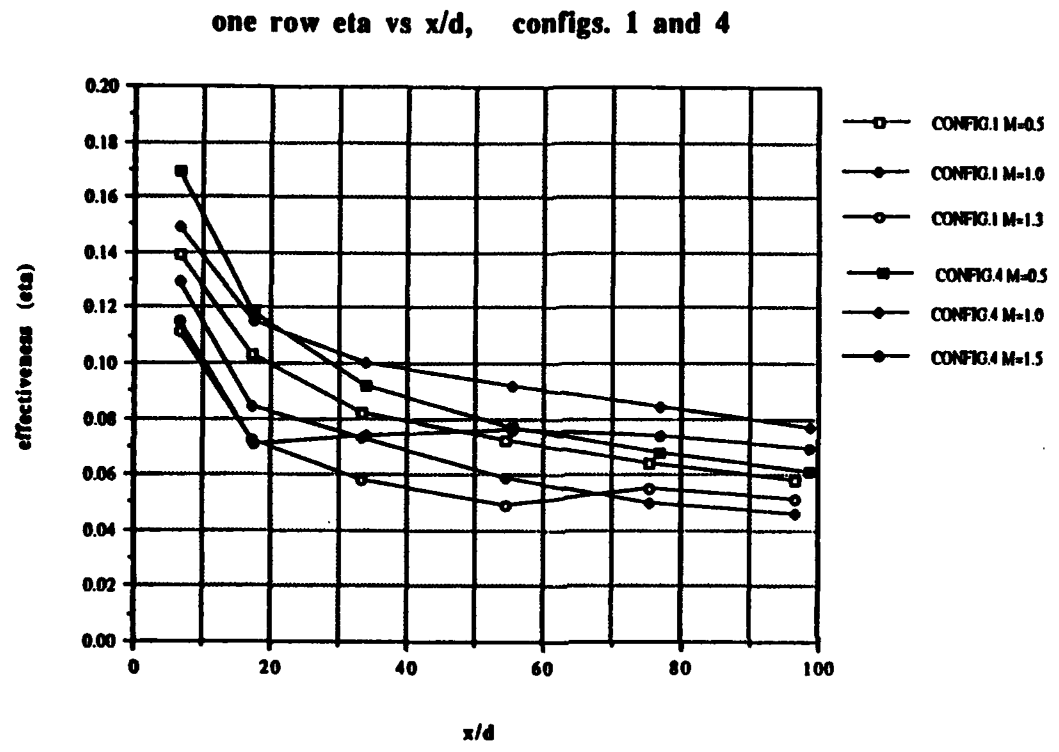

Figure 175. Spanwise Averaged $\overline{\eta}$ vs x/d, Comparison of Configuration 1 to Configuration 4, m=0.5, 1.0, and 1.5, 1 row

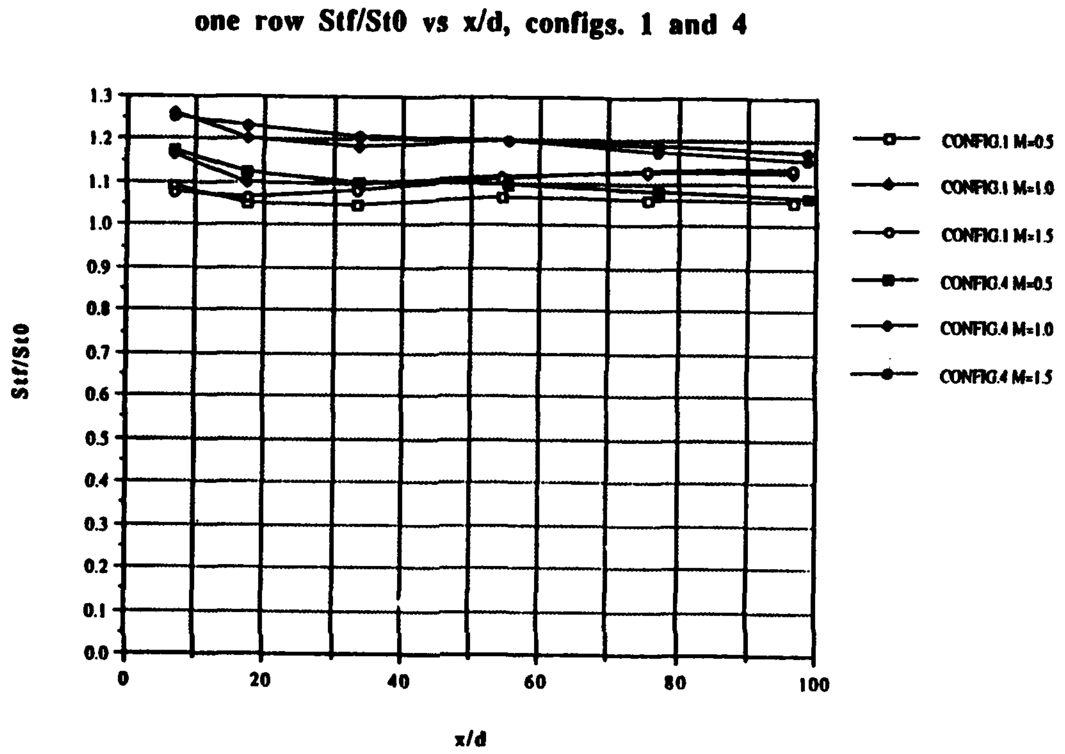

Figure 176. Spanwise Averaged $\overline{St_f / St_o}$ vs x/d, Comparison of Configuration 1 to Configuration 4, m=0.5, 1.0, and 1.5, 1 row

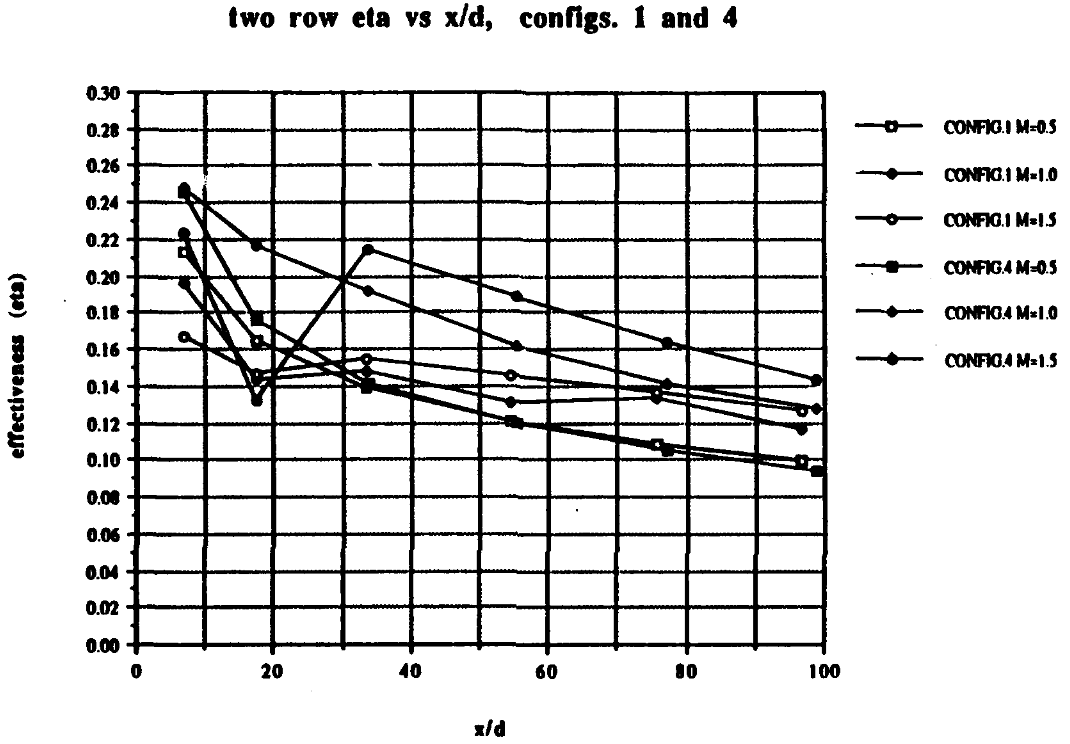

Figure 177. Spanwise Averaged $\overline{\eta}$ vs x/d, Comparison of Configuration 1 to Configuration 4, m=0.5, 1.0, and 1.5, 2 rows

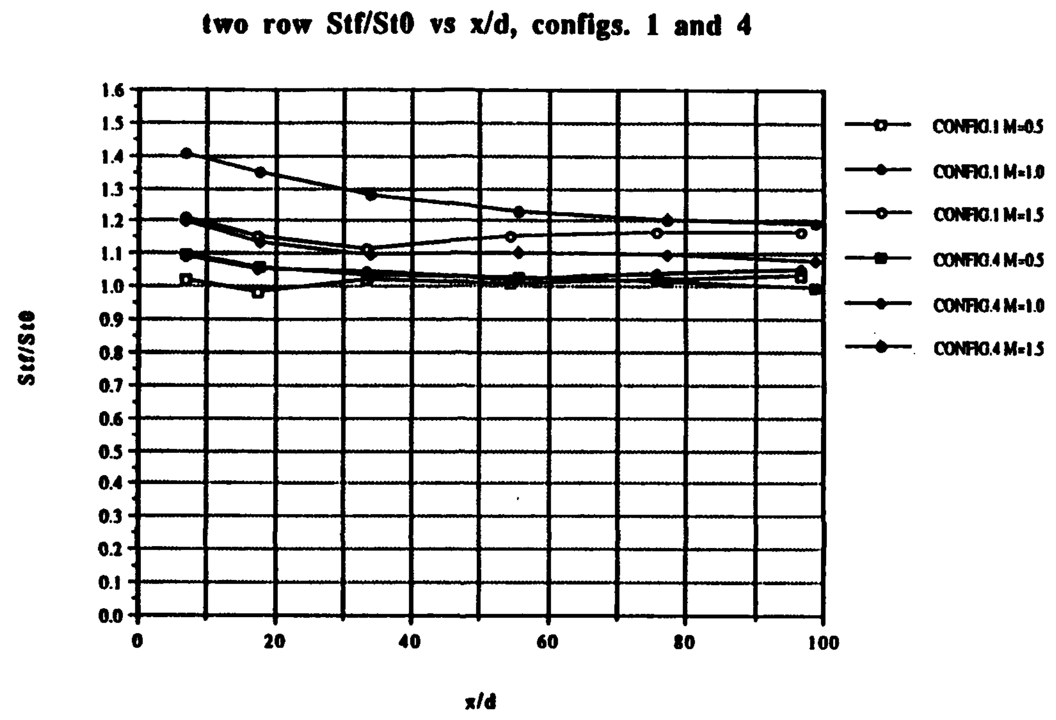

Figure 178. Spanwise Averaged $\overline{St_f / St_o}$ vs x/d, Comparison of Configuration 1 to Configuration 4, m=0.5, 1.0, and 1.5, 2 rows

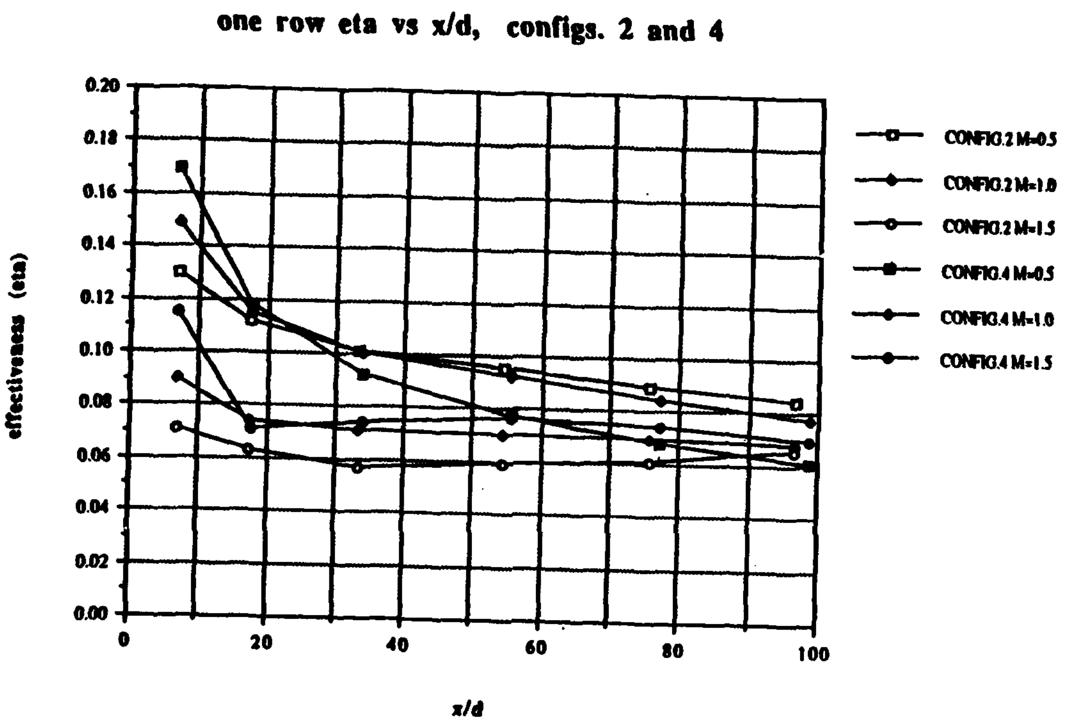

Figure 179. Spanwise Averaged $\overline{\eta}$ vs x/d, Comparison of Configuration 2 to Configuration 4, m=0.5, 1.0, and 1.5, 1 row

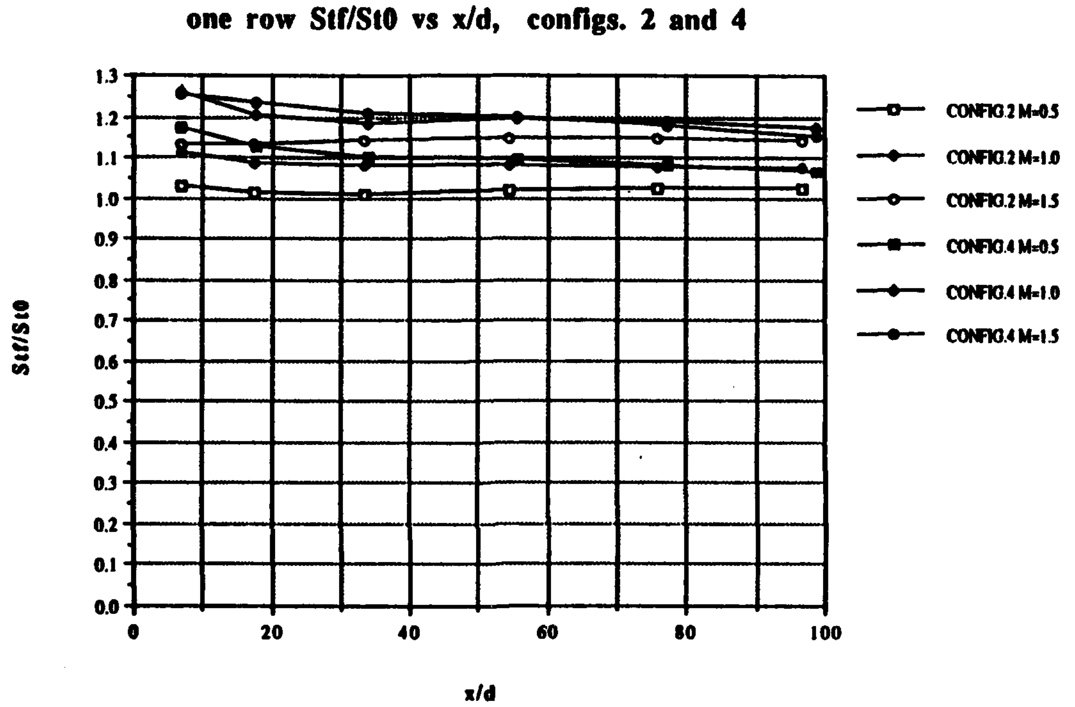

Figure 180. Spanwise Averaged $\overline{St_f / St_o}$ vs x/d, Comparison of Configuration 2 to Configuration 4, m=0.5, 1.0, and 1.5, 1 row

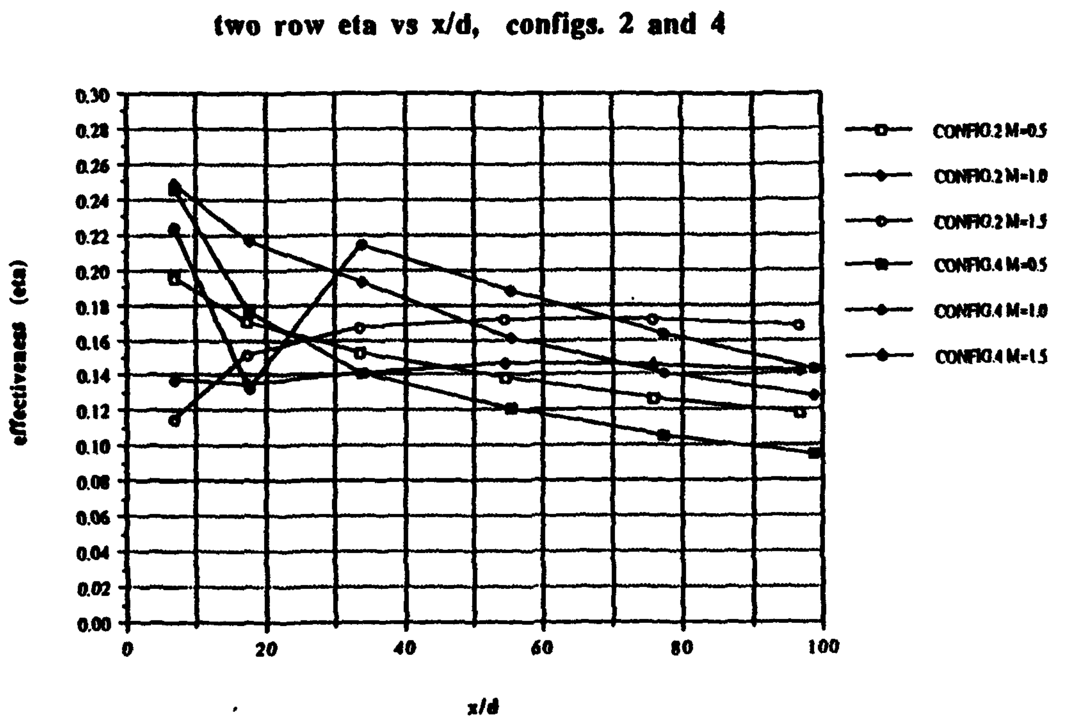

Figure 181. Spanwise Averaged $\overline{\eta}$ vs x/d, Comparison of Configuration 2 to Configuration 4, m=0.5, 1.0, and 1.5, 2 rows

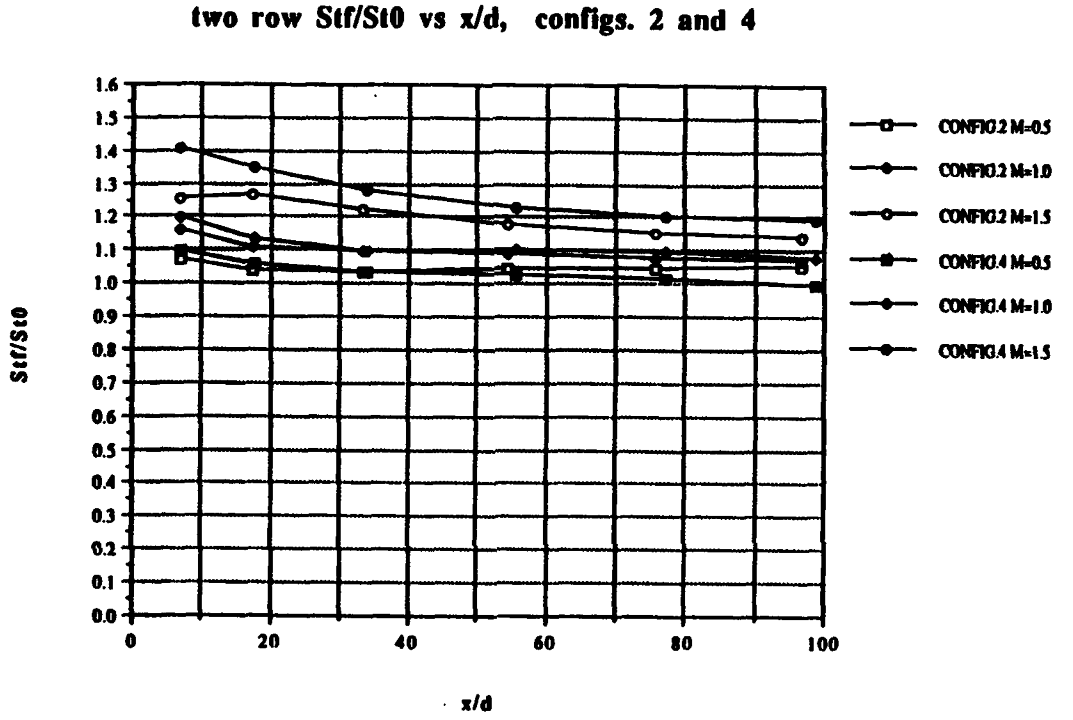

Figure 182. Spanwise Averaged $\overline{St_f / St_o}$ vs x/d, Comparison of Configuration 2 to Configuration 4, m=0.5, 1.0, and 1.5, 2 rows

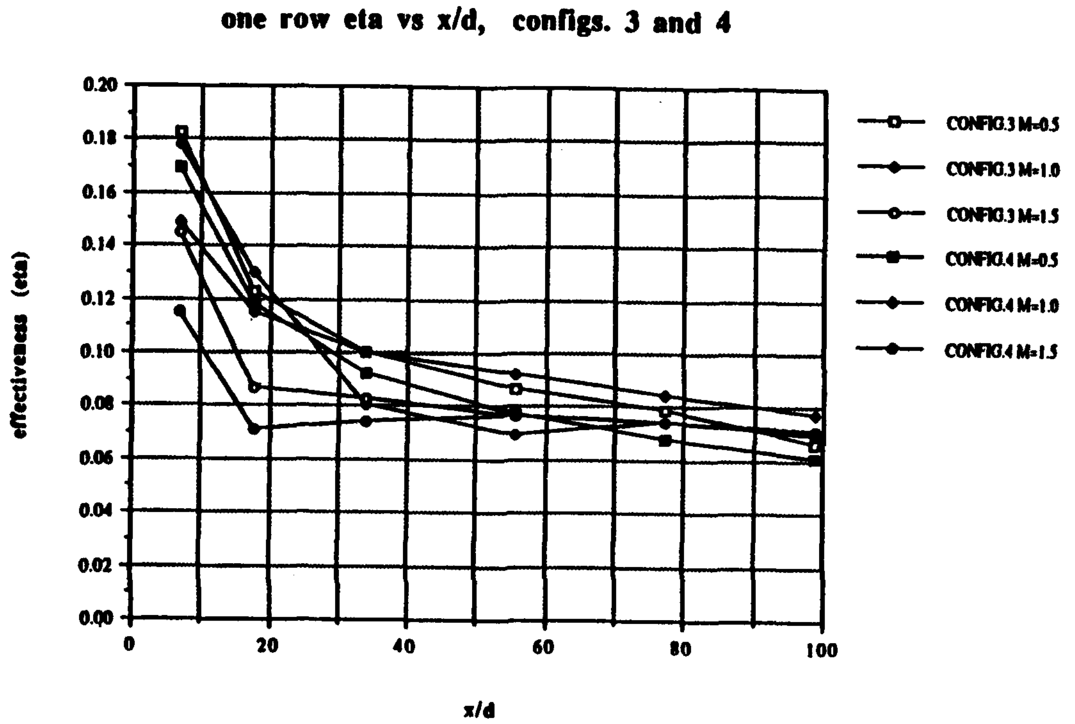

Figure 183. Spanwise Averaged $\bar{\eta}$ vs x/d, Comparison of Configuration 3 to Configuration 4, m=0.5, 1.0, and 1.5, 1 row

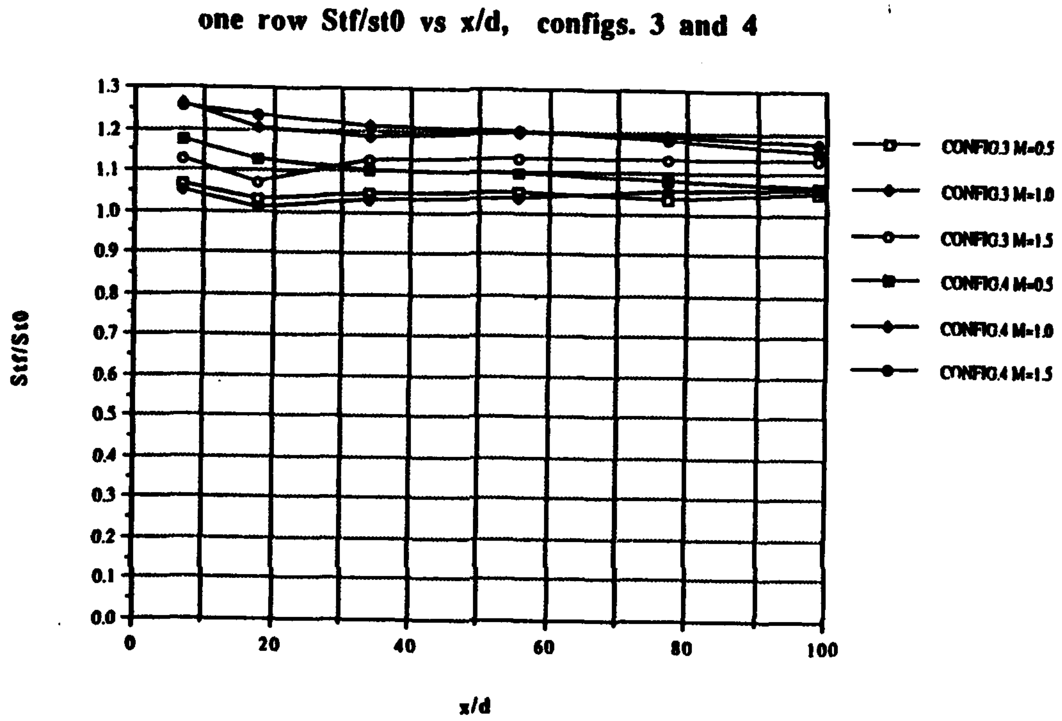

Figure 184. Spanwise Averaged $\overline{St_f / St_o}$ vs x/d, Comparison of Configuration 3 to Configuration 4, m=0.5, 1.0, and 1.5, 1 row

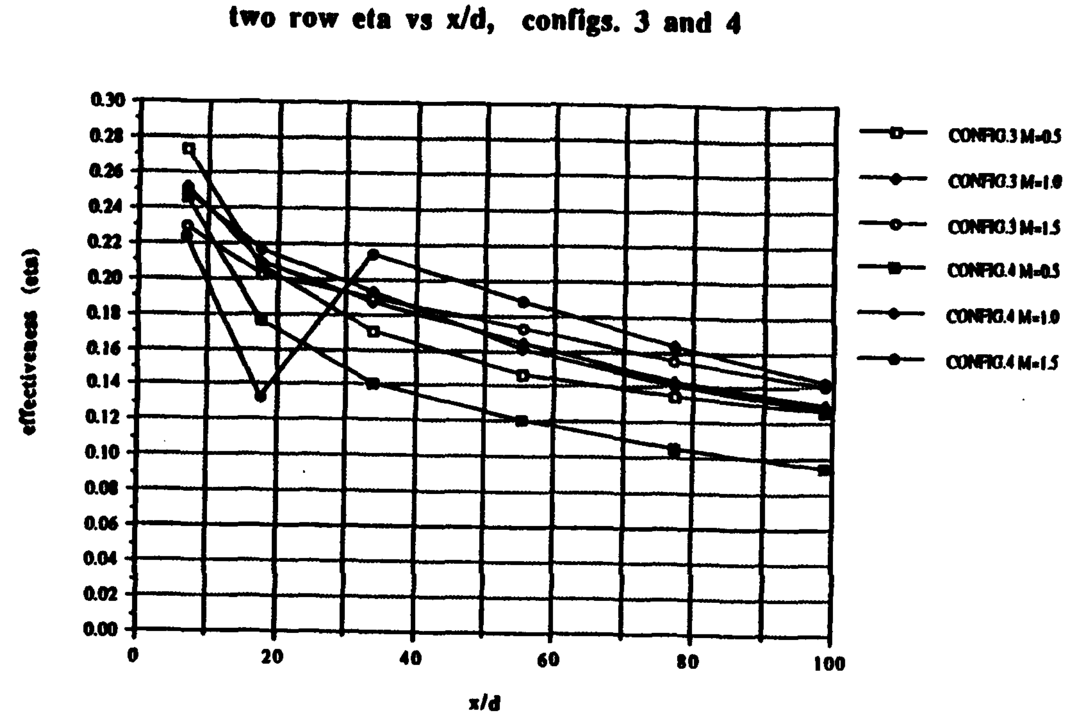

Figure 185. Spanwise Averaged $\overline{\eta}$ vs x/d, Comparison of Configuration 3 to Configuration 4, m=0.5, 1.0, and 1.5, 2 rows

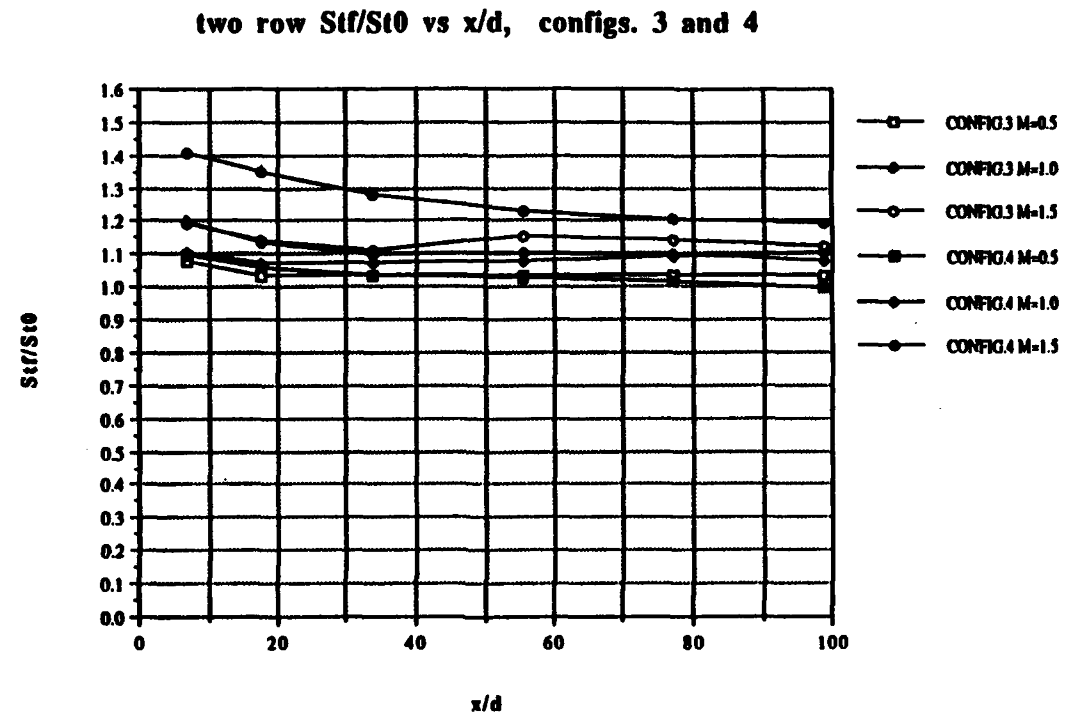

two row Stf/St0 vs x/d, configs. 3 and 4

Figure 186. Spanwise Averaged $\overline{St_f / St_o}$ vs x/d, Comparison of Configuration 3 to Configuration 4, m=0.5, 1.0, and 1.5, 2 rows

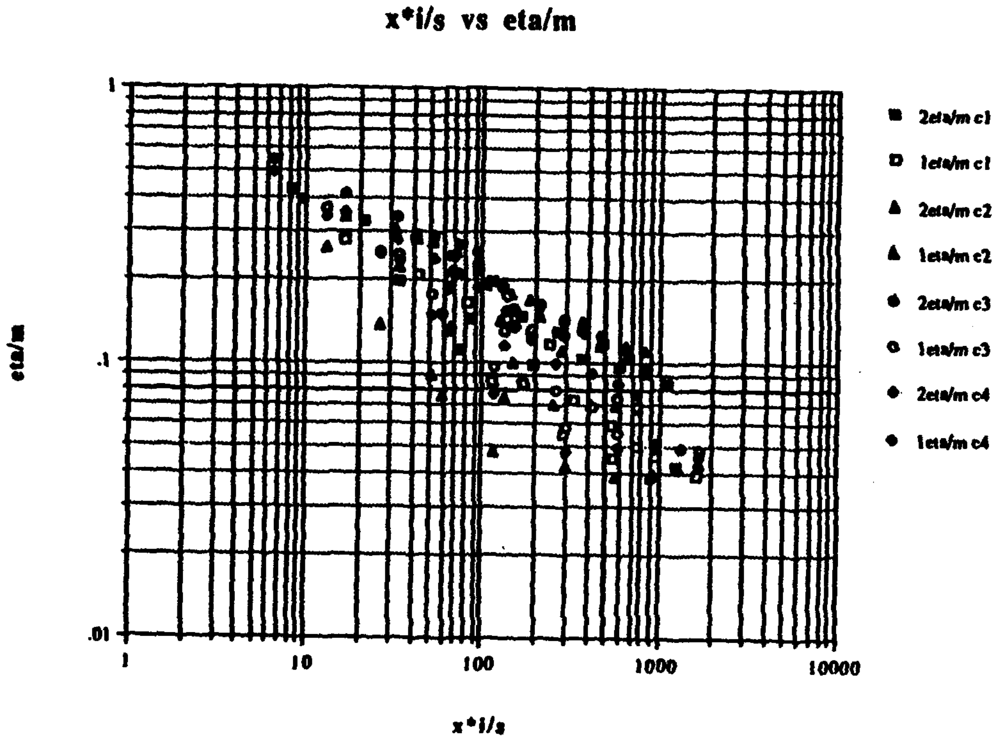

Figure 187. $\overline{\eta}/m$ vs x*I/s, Correlation plot of Configurations 1, 2, 3, and 4,m=0.5, 1.0, and 1.5, 1 row and 2 rows

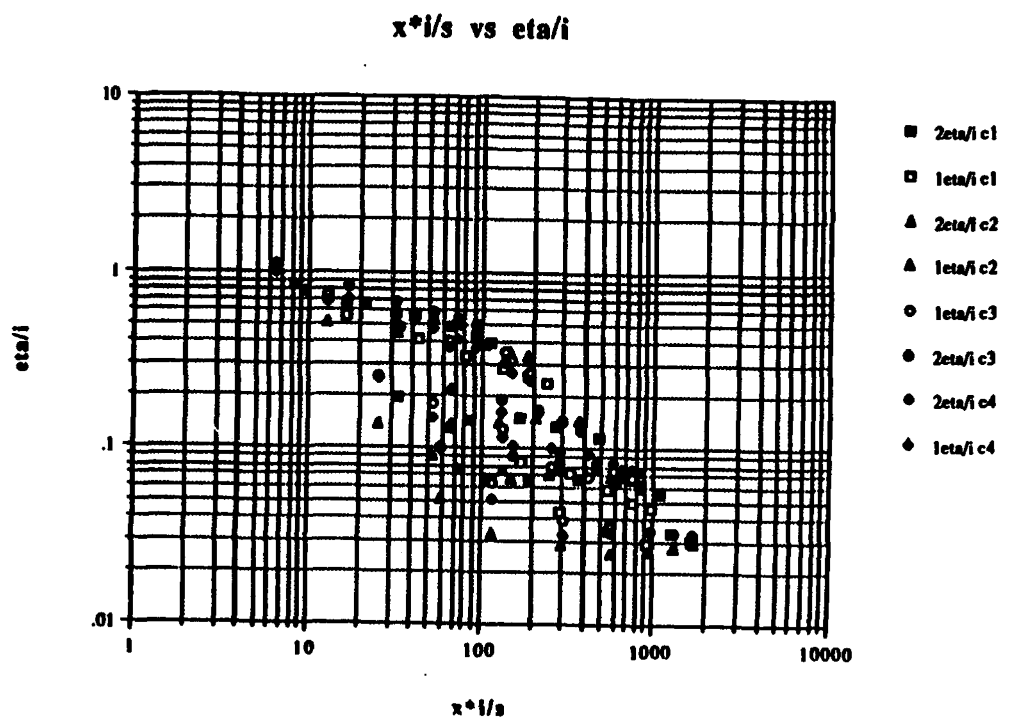

Figure 188. $\overline{\eta}$/I vs x∗I/s, Correlation plot of Configurations 1, 2, 3, and 4, m=0.5, 1.0, and 1.5, 1 row and 2 rows

APPENDIX B

DATA ACQUISITION, PROCESSING AND PLOTTING PROGRAMS

1. Mean Velocity Survey Software :

FIVEHOLE1 : This program acquires pressure data from each of the five transducers associated with the five hole pressure probe. The FIVEHOLE1 program controls the MITAS motor controller which, in turn, controls the automatic traversing device on which the five hole probe is mounted. An 800 point pressure survey is conducted in the Y-Z plane normal to the freestream flow. Two data files, FIVx and FIVPx, are created. The FIVx data file consists of mean velocity, center port pressure, average pressure of the four peripheral ports, and the yaw and pitch coefficients for each of the 800 locations sampled. The FIVx data file consists of the pressures P1 through P5 sensed by each of the five pressure probe sensing ports, the average pressure of the four peripheral ports and the mean velocity, for each of the 800 survey locations.

PADJUST : This program accesses the FIVPx data file created by FIVEHOLE1 and adjusts the pressures to account for spatial resolution problems. Pressure correction is performed using a curve fit to move the measurement location to the center sensing port location. The output file of PADJUST is FIVxA.

VELOCITY : This program accesses FIVxA, the data file created by

PADJUST, and computes Ux, Uy and Uz velocity components. The output file of VELOCITY is Vx.

UXJ : This program accesses Vx, the data file created by VELOCITY, and plots streamwise velocity (Ux) contours of the Y-Z plane surveyed by the five hole pressure probe.

PTOTJ : This program accesses Vx, data file created by VELOCITY, and plots total pressure contours of the surveyed Y-Z plane.

2. Mean Temperature Survey Software :

ROVER1 : This program acquires flow temperature data from the "roving" thermocouple mounted on the automatic traversing device. The traversing device is controlled by the MITAS controller which is, in turn, controlled by this program. The output data file consists of differential temperatures ($T_{rover} - T_{\infty}$) for each of the 800 survey locations in the Y-Z plane. The output file of ROVER1 is TEMx.

PLTMPJ : This program uses the differential temperature data file TEMx, created by ROVER1 and plots differential temperature contours of the surveyed Y-Z plane.

3. Heat Transfer Measurement Software (No Film Cooling) :

STANTON3 : This program acquires multiple channel thermocouple data for heat transfer measurements with no film cooling. It creates two output data files, TDATA and IDATA. The TDATA file consists of the 126 test plate thermocouple temperatures. The IDATA file records run number, test plate voltage and current, ambient pressure, pressure differential, ambient temperature, freestream velocity, air density and freestream temperature.

STANTONJ : STANTONJ uses as input TDATA and IDATA files created by STANTON3 and calculates heat transfer coefficients and Stanton numbers for each of the 126 thermocouple locations. The calculations of the local heat transfer coefficient and local Stanton number are updated using an energy balance which includes spanwise/streamwise conduction and the modified radiation heat flux calculations. STANTONJ creates a output file, the name of which is designated by the user, which consists of the Stanton number for each thermocouple. A printout is also produced which includes the local heat transfer coefficient, the Stanton number and the X and Z coordinates for each of the 126 test plate thermocouples.

4. Heat Transfer Measurement Software (with Film Cooling) :

SETCONDJ: This program is used to set conditions for heat transfer data acquisition when film cooling is employed. SETCONDJ determines injection velocity, Reynolds number, blowing ratio (m) and non-dimensional temperature (θ). It requires user input from the terminal of freestream conditions, rotometer percent flow and injection plenum differential pressure. This version is updated to include three different sized rotometers.

STANFC1J : This program is used when film cooling is employed to acquire multiple channel thermocouple data for heat transfer measurements. STANFC1J creates three data files : a temperature data file (Tx), a terminal input data file (Ix), and a film cooling data file (FCx). The temperature data file consists of the 126 test plate thermocouple temperatures. The terminal input data file records the identical information contained in the IDATA file of STANTON3, as discussed earlier. The film cooling data file contains the injection rotometer percent flow and the injection plenum differential pressure. This version is updated to include the larger sized rotometer.

STANFC2J : This program accesses the temperature, terminal input and film cooling data files created by STANFC1J. The program calculates Stanton number values for the 126 thermocouple locations and creates a single output file (FCx) containing these values. This version is updated to calculate the local heat transfer coefficients and Stanton numbers using an energy balance which includes spanwise/streamwise conduction and a modified radiation heat flux calculation.

STANR1 : This program reads two Stanton number data files and creates a single output file containing Stanton number ratios for each of the 126 thermocouple locations for a particular θ. The required input data files are : The user designated file created by STANTONJ containing baseline Stanton numbers for no film cooling and the FCx data file created by STANFC2J containing Stanton numbers with film cooling for a particular value of θ. The output file of STANR1 is STRx.

FLMEFFJ : This program processes Stanton number data and calculates the local and spanwise averaged film cooling effectiveness and iso-energetic Stanton number ratios. The program reads the output file created by STANTONJ which contains the baseline Stanton numbers for no film cooling, and up to six FCx, Tx and Ix files created by STANFC!J and STANFC2J. One of the two output data files contains the local effectiveness and iso-energetic Stanton number ratios and the other output file contains the spanwise averaged effectiveness and iso-energetic Stanton number ratios. This version of the program accounts for the use of two different baseline inputs (4 amp and 6 amp) and corrects the local θ calculation to account for convective heat flux when applying the thermal contact resistance to calculate the local plate surface temperature.

3DSTGETA : This program accesses the files created by FLMEFFJ and plots the spanwise variation of effectiveness in three-dimensional form.

3DSTGSTRIS : This program accesses the files created by FLMEFFJ and plots the spanwise variation of the iso-energetic Stanton number ratio in three-dimensional form.

3DSTRST : This program accesses STRx, the Stanton number ratio file created by STANR1, and plots the spanwise variations of the Stanton number ratios for a particular θ in three-dimensional form.

APPENDIX C

DATA FILE DIRECTORY

1. Heat Transfer Data:

A. STANTON3 / STANTONJ data files -- (no film cooling) :

xTDATA ---- temperature data file

xIDATA ---- user terminal input data file

STxABL ---- local Stanton number data file

Data Run #	Data File	Experimental Conditions
030892.1201	6TDATA	Compound Angle
	6IDATA	Tp-Tf=21.6 deg C
	ST6ABL	no film-cooling
030892.1721	4TDATA	Compound Angle
	4IDATA	Tp-Tf=9.6 deg C
	ST4ABL	no film cooling

B. STANFC1J/ STANFC2J data files -- (film-cooling)

TpABxx ---- temperature data file

IpABxx ---- user terminal input data file

FCpABxx ---- film-cooling parameters data file

STpABxx ---- local Stanton number data file

COMPOUND ANGLE, 1 ROW

Data Run #	Data File	Experimental Conditions
033092.1206	T16A5B1 I16A5B1 FC16A5B1 ST16A5B1	Compound Angle 1 row, m=0.5, theta=0.42
033092.1301	T16AB52 I16AB52 FC16AB52 ST16AB52	Compound Angle 1 row, m=0.5, theta=0.67
033092.1421	T16AB53 I16AB53 FC16AB53 ST16AB53	Compound Angle 1 row, m=0.5, theta=1.82
033092.1532	T16AB54 I16AB54 FC16AB54 ST16AB54	Compound Angle 1 row, m=0.5, theta=2.74
033092.1845	T14AB56 T14AB56 FC12AB56 ST14AB56	Compound Angle 1 row, m=0.5, theta=3.21
033092.2006	T14AB57 I14AB57 FC14AB57 ST14AB57	Compound Angle 1 row, m=0.5, theta=4.94
033192.1233	T16AB101 I16AB101 FC16AB101 ST16AB101	Compound Angle 1 row, m=1.0, theta=0.075

033192.1332	T16AB102 I16AB102 FC16AB102 ST16AB102	Compound Angle 1 row, m=1.0, theta=0.63
033192.1432	T16AB103 I16AB103 FC16AB103 ST16AB103	Compound Angle 1 row, m=1.0, theta=1.51
033192.1532	T16AB104 I16AB104 FC16AB104 FC16AB104	Compound Angle 1 row, m=1.0, theta=2.34
033192.1914	T14AB105 I14AB105 FC14AB105 ST14AB105	Compound Angle 1 row, m=1.0, theta=2.86
033192.2017	T14AB106 I14AB106 FC14AB106 ST14AB106	Compound Angle 1 row, m=1.0, theta=4.25
040192.1211	T16AB151 I16AB151 FC16AB151 ST16AB151	Compound Angle 1 row, m=1.5, theta=0.19
040192.1305	T16AB152 I16AB152 FC16AB152 ST16AB152	Compound Angle 1 row, m=1.5, theta=0.61

040192.1413	T16AB153 I16AB153 FC16AB153 ST16AB153	Compound Angle 1 row, m=1.5, theta=1.42
040192.1517	T16AB154 I16AB154 FC16AB154 ST16AB154	Compound Angle 1 row, m=1.5, theta=2.17
040292.0749	T14AB155 I14AB155 FC14AB155 ST14AB155	Compound Angle 1 row, m=1.5, theta=2.90
040292.0857	T14AB156 I14AB156 FC14AB156 ST14AB156	Compound Angle 1 row, m=1.5, theta=4.41
040892.2119	T16AB2011 I16AB2011 FC16AB2011 ST16AB2011	Compound Angle 1 row, m=2.0, theta=0.35
040892.1728	T16AB202 I16AB202 FC16AB202 ST16AB202	Compound Angle 1 row, m=2.0, theta=0.69
040892.1831	T16AB2O3 I16AB203 FC16AB203 ST16AB203	Compound Angle 1 row, m=2.0, theta=1.37

040892.1933	T16AB204 I16AB204 FC16AB204 ST16AB204	Compound Angle 1 row, m=2.0, theta=2.07
040992.1127	T14AB205 I14AB205 FC14AB205 ST14AB205	Compound Angle 1 row, m=2.0, theta=2.72
040992.1233	T14AB206 I14AB206 FC14AB206 ST14AB206	Compound Angle 1 row, m=2.0, theta=3.86
041592.1422	T16AB251 I16AB251 FC16AB251 ST16AB251	Compound Angle 1 row, m=2.5, theta=0.43
041592.1521	T16AB252 I16AB252 FC16AB252 ST16AB252	Compound Angle 1 row, m=2.5, theta=0.75
041592.1621	T16AB253 I16AB253 FC16AB253 ST16AB253	Compound Angle 1 row, m=2.5, theta=1.25
041592.1718	T16AB254 I16AB254 FC16AB254 ST16AB254	Compound Angle 1 row, m=2.5, theta=1.86

041692.0815	T14AB255 I14AB255 FC14AB255 ST14AB255	Compound Angle 1 row, m=2.5, theta=2.70
041692.1019	T16AB256 I14AB256 FC14AB256 ST14AB256	Compound Angle 1 row, m=2.5, theta=3.76

COMPOUND ANGLE, 2 ROWS

031292.1159	T6A5BR1 I6A5BR1 FC6A5BR1 ST6A5BR1	Compound Angle 2 rows, m=0.5, theta=0.22
031792.1639	T6A5BR3 I6A5BR3 FC6A5BR3 ST6A5BR3	Compound Angle 2 rows, m=0.5, theta=0.61
031792.1854	T6A5BR5 I6A5BR5 FC6A5BR5 ST6A5BR5	Compound Angle 2 rows, m=0.5, theta=1.33
031792.2024	T6A5BR6 I6A5BR6 FC6A5BR6 ST6A5BR6	Compound Angle 2 rows, m=0.5, theta=1.98
032592.1215	T4A5BR7 I4A5BR7 FC4A5BR7 ST4A5BR7	Compound Angle 2 rows, m=0.5, theta=2.52

032592.1336	T4A5BR8 I4A5BR8 FC4A5BR8 ST4A5BR8	Compound Angle 2 rows, m=0.5, theta=3.46
031692.1812	T6ABR10 I6ABR10 FC6ABR10 ST6ABR10	Compound Angle 2 rows, m=1.0, theta=0.28
031692.2013	T6AB101 I6AB101 FC6AB101 ST6AB101	Compound Angle 2 rows, m=1.0, theta=0.66
031692.2126	T6AB102 I6AB102 FC6AB102 ST6AB102	Compound Angle 2 rows, m=1.0, theta=1.18
031692.2239	T6AB103 I6AB103 FC6AB103 ST6AB103	Compound Angle 2 rows, m=1.0, theta=1.74
031792.1121	T4AB101 I4AB101 FC4AB101 ST4AB101	Compound Angle 2 rows, m=1.0, theta=2.08
031792.1301	T4AB102 I4AB102 FC4AB102 ST4AB102	Compound Angle 2 rows, m=1.0, theta=2.80

032692.1205	T6AB151 I6AB151 FC6AB151 ST6AB151	Compound Angle 2 rows, m=1.5, theta=0.56
032692.1309	T6AB152 I6AB152 FC6AB152 ST6AB152	Compound Angle 2 rows, m=1.5, theta=0.74
032692.1427	T6AB153 I6AB153 FC6AB153 ST6AB153	Compound Angle 2 rows, m=1.5, theta=1.17
032692.1528	T6AB154 I6AB154 FC6AB154 ST6AB154	Compound Angle 2 rows, m=1.5, theta=1.67
032692.1856	T4AB155 I4AB155 FC4AB155 ST4AB155	Compound Angle 2 rows, m=1.5, theta=2.21
032692.2021	T4AB156 I4AB156 FC4AB156 ST4AB156	Compound Angle 2 rows, m=1.5, theta=2.90

C. FILM EFFECTIVENESS DATA

Generating Program : FLMEFFJ

STRxxx ---- local effectiveness data file

SPExxx ---- spanwise average effectiveness data file

COMPOUND ANGLE, 1 ROW

Data Run #	Data File	Experimental Conditions
033092.1206	STR511	Compound Angle.
033092.1301	SPE511	1 row, m=0.5
033092.1421		
033092.1532		
033092.1845		
033092.2006		
033192.1233	STR1011	Compound Angle
033192.1332	SPE1011	1 row, m=1.0
033192.1432		
033192.1532		
033192.1914		
033192.2017		
040192.1211	STR1511	Compound Angle
040192.1305	SPE1511	1 row, m=1.5
040192.1413		
040192.1517		
040292.0749		
040292.0857		

040892.2119	STR2011	Compound Angle
040892.1728	SPE2011	1 row, m=2.0
040892.1831		
040892.1933		
040992.1127		
040992.1233		

041592.1422	STR2511	Compound Angle
041592.1521	SPE2511	1 row, m=2.5
041592.1612		
041592.1718		
041692.0815		
041692.1019		

COMPOUND ANGLE, 2 ROWS

031292.1159	STR5112	Compound Angle
031792.1639	SPE5112	2 row, m=0.5
031792.1854		
031792.2024		
032592.1215		
032592.1336		

031692.1812	STR1012	Compound Angle
031692.2013	SPE1012	2 rows, m=1.0
031692.2126		
031692.2239		
031792.1121		
031792.1301		

032692.1205	STR1512	Compound Angle
032692.1309	SPE1512	2 rows, m=1.5
032692.1427		
032692.1528		
032692.1856		
032692.2021		

D. STANTON NUMBER RATIO FILES

Generating Program : STANR1

pSTRxx ---- Film-cooling data file

COMPOUND ANGLE, 1 ROW

Data Run #	Data File	Experimental Conditions
033092.1421	4STR15	1 row, m=0.5, theta=1.82
033192.1432	4STR11	1 row, m=1.0, theta=1.51
040192.1413	4STR115	1 row, m=1.5, theta=1.42
040892.1831	4STR12	1 row, m=2.0, theta=1.37
041592.1621	4STR13	1 row, m=2.5, theta=1.25

COMPOUND ANGLE, 2 ROWS

Data Run #	Data File	Experimental Conditions
031792.1854	4STR22	2 rows, m=0.5, theta=1.33
031692.2126	4STR23	2 rows, m=1.0, theta=1.18
032692.1427	4STR24	2 rows, m=1.5, theta=1.17

E. MEAN VELOCITY DATA :

COMPOUND ANGLE, 1 ROW

Data Run #	Data File	Generating Program	Experimental Conditions
052192.2054	FIV1	FIVEHOLE1	1 row, m=0.5
	FIVP1	FIVEHOLE1	x/d = 7.4
	FIV19	PADJUST	
	V19	VELOCITY	
051992.1114	FIV1	FIVEHOLE1	1 row, m=0.5
	FIVP1	FIVEHOLE1	x/d = 43.8
	FIV09	PADJUST	
	V9	VELOCITY	
050492.1044	FIV0	FIVEHOLE1	1 row, m=0.5
	FIVP0	FIVEHOLE1	x/d = 85.6
	FIV00	PADJUST	
	V0	VELOCITY	
052292.1016	FIV0	FIVEHOLE1	1 row, m=1.0
	FIVP0	FIVEHOLE1	x/d = 7.4
	FIV18	PADJUST	
	V18	VELOCITY	
052092.1032	FIV2	FIVEHOLE1	1 row, m=1.0
	FIVP2	FIVEHOLE1	x/d = 43.8
	FIV10	PADJUST	
	V10	VELOCITY	

050592.1134	FIV0	FIVEHOLE1	1 row, m=1.0
	FIVP0	FIVEHOLE1	x/d = 85.6
	FIV01	PADJUST	
	V1	VELOCITY	
052392.1947	FIV2	FIVEHOLE1	1 row, m=1.5
	FIVP2	FIVEHOLE1	x/d = 7.4
	FIV17	PADJUST	
	V17	VELOCITY	
052092.2221	FIV2	FIVEHOLE1	1 row, m=1.5
	FIVP2	FIVEHOLE1	x/d = 43.8
	FIV11	PADJUST	
	V11	VELOCITY	
050692.1151	FIV1	FIVEHOLE1	1 row, m=1.5
	FIVP1	FIVEHOLE1	x/d = 85.6
	FIV08	PADJUST	
	V8	VELOCITY	

COMPOUND ANGLE, 2 ROWS

Data Run #	Data File	Generating Program	Experimental Conditions
052492.1102	FIV2	FIVEHOLE1	2 row, m=0.5
	FIVP2	FIVEHOLE1	x/d = 7.4
	FIV16	PADJUST	
	V16	VELOCITY	
051892.1112	FIV0	FIVEHOLE1	2 row, m=0.5
	FIVP0	FIVEHOLE1	x/d = 43.8
	FIV12	PADJUST	
	V12	VELOCITY	

050792.1113	FIV0	FIVEHOLE1	2 row, m=0.5
	FIVP0	FIVEHOLE1	x/d = 85.6
	FIV07	PADJUST	
	V7	VELOCITY	
052592.0646	FIV1	FIVEHOLE1	2 rows, m=1.0
	FIVP1	FIVEHOLE1	x/d = 7.4
	FIV14	PADJUST	
	V14	VELOCITY	
051892.2215	FIV0	FIVEHOLE1	2 rows, m=1.0
	FIVP0	FIVEHOLE1	x/d = 43.8
	FIV13	PADJUST	
	V13	VELOCITY	
050792.2244	FIV2	FIVEHOLE1	2 rows, m=1.0
	FIVP2	FIVEHOLE1	x/d = 85.6
	FIV04	PADJUST	
	V4	VELOCITY	
052792.2215	FIV01	FIVEHOLE1	2 rows, m=1.0
	FIVP01	FIVEHOLE1	x/d = 43.8
	FIV43	PADJUST	
	V43	VELOCITY	
052992.1213	FIV02	FIVEHOLE1	2 rows, m=1.0
	FIVP02	FIVEHOLE1	x/d = 85.6
	FIV40	PADJUST	
	V40	VELOCITY	
052592.1941	FIV1	FIVEHOLE1	2 rows, m=1.5
	FIVP1	FIVEHOLE1	x/d = 7.4
	FIV15	PADJUST	
	V15	VELOCITY	

051992.1201	FIV0	FIVEHOLE1	2 rows, m=1.5
	FIVP0	FIVEHOLE1	x/d = 43.8
	FIV06	PADJUST	
	V6	VELOCITY	
050892.1145	FIV2	FIVEHOLE1	2 rows, m=1.5
	FIVP2	FIVEHOLE1	x/d = 85.6
	FIV05	PADJUST	
	V5	VELOCITY	
052892.0752	FIV06	FIVEHOLE1	2 rows, m=1.5
	FIVP06	FIVEHOLE1	x/d = 43.8
	FIV46	PADJUST	
	V46	VELOCITY	
060192.0914	FIV20	FIVEHOLE1	2 rows, m=1.5
	FIVP20	FIVEHOLE1	x/d = 85.6
	FIV50	PADJUST	
	V50	VELOCITY	

F. Mean Temperature Survey Data :

Generating Program : ROVER1

COMPOUND ANGLE

Data Run #	Data File	Experimental Conditions
060892.1506	TEM12	1 row, m=0.5, x/d=7.4
060892.1506	TEM12	1 row, m=0.5, x/d=7.4
060492.0854	TEM11	1 row, m=0.5, x/d=43.8

060392.1312	TEM0	1 row, m=0.5, x/d=85.6
060892.1932	TEM13	1 row, m=1.0, x/d=7.4
060892.1932	TEM13	1 row, m=1.0, x/d=7.4
060492.1339	TEM10	1 row, m=1.0, x/d=43.8
060392.1755	TEM1	1 row, m=1.0, x/d=85.6
060992.0829	TEM14	1 row, m=1.5, x/d=7.4
060992.0829	TEM14	1 row, m=1.5, x/d=7.4
060492.1751	TEM9	1 row, m=1.5, x/d=43.8
060392.2252	TEM2	1 row, m=1.5, x/d=85.6

COMPOUND ANGLE, 2 ROW

Data Run #	Data File	Experimental Conditions
060792.1101	TEM15	2 row, m=0.5, x/d=7.4
060792.1101	TEM15	2 row, m=0.5, x/d=7.4
060492.2303	TEM8	2 row, m=0.5, x/d=43.8
060292.1916	TEM3	2 row, m=0.5, x/d=85.6
060792.1743	TEM16	2 rows, m=1.0, x/d=7.4
060792.1743	TEM16	2 rows, m=1.0, x/d=7.4
061192.1436	TEM20	2 rows, m=1.0, x/d=7.4
061192.1436	TEM20	2 rows, m=1.0, x/d=7.4
060592.0941	TEM7	2 rows, m=1.0, x/d=43.8

060292.2334	TEM4	2 rows, m=1.0, x/d=85.6
060892.0939	TEM17	2 rows, m=1.5, x/d=7.4
060892.0939	TEM17	2 rows, m=1.5, x/d=7.4
061192.2041	TEM21	2 rows, m=1.5, x/d=7.4
061192.2041	TEM21	2 rows, m=1.5, x/d=7.4
060592.1339	TEM6	2 rows, m=1.5, x/d=43.8
060392.0851	TEM5	2 rows, m=1.5, x/d=85.6

REFERENCES

1. Metzger, D. E., Carper, H. J., and Swank, L. R., "Heat Transfer With Film Cooling Near Nontangential Injection Slots," *ASME Transactions-Journal of Engineering for Power*, pp. 157-163, April, 1968.

2. Ligrani, P. M., and Camci, C., "Adiabatic Film Cooling Effectiveness from Heat Transfer Measurements in Compressible, Variable Property Flow," *ASME Transactions-Journal of Heat Transfer*, Vol. 107, No. 2, pp. 313-320, 1985.

3. Ligrani, P. M., "Comment on Behavior of a Coolant Film With Two Rows of Holes Along the Pressure Side of a High Pressure Nozzle Guide Vane," *ASME Transactions-Journal of Turbomachinery*, Vol. 112, No. 3, pp. 520-521, 1990.

4. Ligrani, P. M., Ortiz, A., Joseph, S. L., and Evans, D. L., "Effects of Embedded Vortices on Film-Cooled Turbulent Boundary Layers," *ASME Transactions-Journal of Turbomachinery*, Vol. 111, No. 1, pp. 71-77, 1989.

5. Ligrani, P. M., Subramanian, C. S., Craig, D. W. and Kaisuwan, P., "Effect of Vortices with Different Circulations on Heat Transfer and Injectant Downstream of a Row of Film-Cooling Holes in a Turbulent Boundary Layer," *ASME Transactions-Journal of Heat Transfer*, Vol. 113, No. 1, pp.79-90, 1991.

6. Bishop, D. T., *Heat Transfer, Adiabatic Effectiveness and Injectant Distributions Downstream of Single and Double Rows of Film-Cooling Holes With Compound Angles,* M. S. Thesis, Naval Postgraduate School, Monterey, California, September 1990.

7. Ciriello, S., *Heat Transfer, Adiabatic Effectiveness and Injectant Distributions Downstream of Single and Double Rows of Film-Cooling Holes With Simple and Compound Angles,* M. S. Thesis, Naval Postgraduate School, Monterey, California, March 1991.

8. Wigle, J. M., *Heat Transfer, Adiabatic Effectiveness and Injectant Distributions Downstream of Single and Double Rows of Film-Cooling Holes with Compound Angles*, M.S. Thesis, Naval Postgraduate School, Monterey, California, December 1991.

9. Ortiz, A., *The Thermal Behavior of Film Cooled Turbulent Boundary Layers as Affected by Longitudinal Vortices*, M. E. Thesis, Naval Postgraduate School, Monterey, California, September 1987.

10. Williams, W., *Effects of an Embedded Vortex on a Single Film-Cooling Jet in a Turbulent Boundary Layer*, M. S. Thesis, Naval Postgraduate School, Monterey, California, June 1988.

11. Kays, W. M., and Crawford, M. E., *Convective Heat and Mass Transfer*, Second Edition, p.216, McGraw-Hill Book Company, 1980.

INITIAL DISTRIBUTION LIST

		No. Copies
1.	Defense Technical Information Center Cameron Station Alexandria, Virginia 22304-6145	2
2.	Library, Code 52 Naval Postgraduate School Monterey, California 93943-5002	2
3.	Professor P.M. Ligrani Department of Mechanical Engineering MEB 3209 University of Utah Salt Lake City, Utah 84112	2
4.	Department Chairman, Code ME Department of Mechanical Engineering Naval Postgraduate School Monterey, California 93943-5000	1
5.	Dr. Dan Groghan Naval Sea Systems Command Code 56X3 Washington, D:C 20362	3
6.	Naval Engineering Curricular Officer, Code 34 Department of Mechanical Engineering Naval Postgraduate School Monterey, California 93943-5000	1
7.	LT. Anthony E. Ramsey 5221 W. Race Ave. Chicago, Illinois 60644	2
8.	Dr. Bill Troka Department of the Air Force Air Force Wright Aeronautical Laboratories Wright-Patterson Air Force Base, Ohio 45433	2